REPORT DOCUMENTATION PAGE

Form Approved OMB No. 0704-0188

1. REPORT DATE *(DD-MM-YYYY)*	2. REPORT TYPE	3. DATES COVERED *(From – To)*
13-03-2002	Final Report	22 September 2000 - 22-Sep-01

4. TITLE AND SUBTITLE

Analysis and modeling of AFRL 'Gap 98' balloon-borne measurements

5a. CONTRACT NUMBER
F61775-00-WE072

5b. GRANT NUMBER

5c. PROGRAM ELEMENT NUMBER

6. AUTHOR(S)

Dr. Yolande Louvet

5d. PROJECT NUMBER

5d. TASK NUMBER

5e. WORK UNIT NUMBER

7. PERFORMING ORGANIZATION NAME(S) AND ADDRESS(ES)
Office of National Establishment for Aerospace Research (ONERA)
Chemin de la Huniere
PALAISEAU 91761
FRANCE

8. PERFORMING ORGANIZATION REPORT NUMBER
N/A

9. SPONSORING/MONITORING AGENCY NAME(S) AND ADDRESS(ES)

EOARD
PSC 802 BOX 14
FPO 09499-0014

10. SPONSOR/MONITOR'S ACRONYM(S)

11. SPONSOR/MONITOR'S REPORT NUMBER(S)
SPC 00-4072

12. DISTRIBUTION/AVAILABILITY STATEMENT

Approved for public release; distribution is unlimited.

13. SUPPLEMENTARY NOTES

14. ABSTRACT

This report results from a contract tasking Office of National Establishment for Aerospace Research (ONERA) as follows: The objective of this project is to validate data collected on a French research balloon ("SPIRALE") successfully flown from Gap on 29 June 99. SPIRALE was funded by CNES / ONERA / INSU and developed by ONERA / LPCE to measure atmospheric trace gases (CO, O3, CH4, N2O, NO2, NO, CO2, H2O, HF, and others) from 13 to 35 km. Another test campaign ("Gap 98") was conducted during June 98 with AFRL balloon-borne sensors above the Gap-Tallard Aerodrome, in southern France. The contractor shall evaluate previously collected data from both balloon experiments and determine if the measured data validates turbulence and radiance propagation codes at middle altitudes and latitudes.

The contractor will complete the following tasks:
- Determine the ozone profile structure as a function of air mass temperature
- Evaluate the possible correlation of measured data with local wind shear and ozone measurements from other instruments
- Model the luminance fluctuation and optical turbulence derived from the temperature fluctuation data.

15. SUBJECT TERMS
EOARD, Turbulence Modeling, Atmospheric Propagation, Optical systems

16. SECURITY CLASSIFICATION OF:			17. LIMITATION OF ABSTRACT	18, NUMBER OF PAGES	19a. NAME OF RESPONSIBLE PERSON
a. REPORT	b. ABSTRACT	c. THIS PAGE			David M. Burns, Lt Col, USAF
UNCLAS	UNCLAS	UNCLAS	UL	171	19b. TELEPHONE NUMBER *(Include area code)* +44 (0)20 7514 4955

ONERA

BORDEREAU DE DIFFUSION

DÉPARTEMENT OPTIQUE THÉORIQUE ET APPLIQUÉE

Palaiseau le 16 octobre 2001
N° : DOTA/B-n° 2210/01
Copies Intérieures : DSAC/ADV, DOTA/SC (2)

Titre : **Analysis and modeling of AFRL "Gap 98" balloon-borne measurements**
Auteur(s) : **Y. Louvet ; L. Rousset-Rouvière ; V. Michau ; P. Simoneau, F. Dalaudier (CNRS/Sce d'Aéronomie).**
Contrat : **F61775-00-WEO72 du 27/09/00.**

Document : **RTS 2/05199 DOTA**
Nature : **Concluding Technical Report**
Date : **September 2001**
Client : **EOARD**

Destinataires du document (22)

■ **Extérieurs à l' ONERA :**

EOARD Liaison Officer	Dr. Lt. Col. D. Burns	1 ex.
	Major T. Lawrence	1 ex.
CNRS/Sce d'Aéronomie	J.P. Pomereau, A. Garnier, C. Vialle	3 ex.
CNRS/Sce d'Aéronomie	S. Godin, F. Goutail, F. Dalaudier, G. Ancellet	4 ex.
CNRS/Sce d'Aéronomie	A. Hauchecorne	1 ex.

■ **Intérieurs à l' ONERA :**

DOTA/SC		1 ex.
DOTA/Adj.	J.M. Maisonneuve, M. Séchaud	2 ex.
DOTA/CMMO	B. Rosier	1 ex.
DOTA/LOE	J.P. Cariou, Y. Louvet	2 ex.
DOTA/MPSO	P. Simoneau	1 ex.
DOTA/ASO	V. Michau, L. Rousset-Rouvière	2 ex.
DMPH	R. Ramaroson	1 ex.
ISP	Documentation (original document électronique)	
ISP	Documentation (original document papier + 1 ex.)	

Destinataires de la fiche d'identification seule (24)

■ **Extérieurs à l' ONERA :**

CEDOCAR		1 ex.

■ Intérieurs à l' ONERA :

DOTA/CMIR	J. Deschamps	2 ex.
DOTA/G	A. Raffard	1 ex.
DOTA/Adj.	B. Moreau, G. Rousset,	2 ex.
DOTA/R.U.	X. Briottet, Y. Fazilleau	2 ex.
DOTA/R.U.	E. Georges, M. Girard,	2 ex.
DOTA/R.U.	V. Michau, J. Primot, A. Roblin	3 ex.

Diffusion systématique : D, DSG, DAJ, DTG, DSAC, MM. les directeurs de MFE, PHY, MAS, TIS, GMT

Le Directeur du Département
Optique Théorique et Appliquée
R. Jalin

p.o

BP 72 - 29, avenue de la Division Leclerc
92322 Châtillon Cedex - France
Tél. : 01 46 73 40 40 Fax : 01 46 73 41 41
Office National d'Études et de Recherches Aérospatiales

ONERA

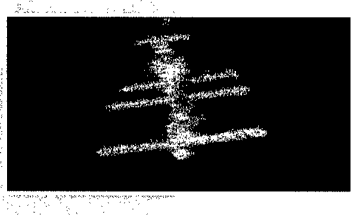

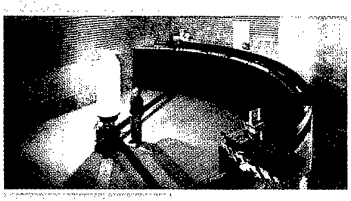

THEORETICAL AND APPLIED OPTICS DEPARTMENT

Concluding Technical Report

Analysis and modeling of AFRL "Gap 98" balloon-borne measurements

RTS 2/05199 DOTA - September 2001

Y. Louvet ; L. Rousset-Rouvière ; V. Michau
P. Simoneau ; F. Dalaudier (CNRS/Service d'Aéronomie).

SANS MENTION DE PROTECTION

PHYSICS

ONERA

THEORETICAL AND APPLIED OPTICS DEPARTMENT

Concluding Technical Report N° RTS 2/05199 DOTA

September 2001

Analysis and modeling of AFRL "Gap 98" balloon-borne measurements

Written by :

Y. Louvet ; L. Rousset-Rouvière ; V. Michau ; P. Simoneau ; F. Dalaudier (CNRS/Sce d'Aéronomie).

Verified by :

Bernard Rosier, Chargé de Mission "Modélisation optique des cibles et des fonds"

Approved by :

Director
Theoretical and Applied Optics Department
R. Jalin

P.o

This document comprises 171 pages

SANS MENTION DE PROTECTION

BP 72 - 29, avenue de la Division Leclerc
92322 Châtillon Cedex - FRANCE
Tél. : 01 46 73 40 40 - Fax : 01 46 73 41 41
Office National d'Études et de Recherches Aérospatiales

SMP

AQ F02-10-2173

SANS MENTION DE PROTECTION

SMP

IDENTIFICATION CARD of ONERA REPORT N° RTS 2/05199 DOTA

Issued by : **THEORETICAL AND APPLIED OPTICS DEPARTMENT**	Contracting Agency : **EOARD**	Contract Number : **F61775-00-WEO72 du 27/09/00.**
	Programme card number : **OTA 910 A**	Date : **September 2001**

Title : **Analysis and modeling of AFRL "Gap 98" balloon-borne measurements**

Author(s) : **Y. Louvet ; L. Rousset-Rouvière ; V. Michau ; P. Simoneau ; F. Dalaudier (CNRS/Sce d'Aéronomie).**

SECURITY CLASSIFICATION : **Civile**	Timing Classification Off
Title : **SANS MENTION PROTECTION**	Title : **Sans objet**
ID card : **SANS MENTION PROTECTION**	ID card : **Sans objet**
Report : **SANS MENTION PROTECTION**	Report : **Sans objet**

Abstract : The objective is the validation of turbulence and propagation codes at middle altitudes/latitudes and the proof of principle for flight of U.S. ozone sondes and thermosondes on a major French research balloon called SPIRALE (SPectrometre InfraRouge Atmosphérique à Laser Embarqué), successfully flown from Gap on June 29, 1999 and June 20, 2001. SPIRALE, funded by CNES (Centre National d'Etudes Spatiales), Onera and INSU (Institut National des Sciences de l'Univers), was developed by Onera and LPCE (Laboratoire de Physique et Chimie de l'Evironnement) to measure atmospheric trace gases (CO, O_3, CH_4, N_2O, NO_2, NO, CO_2, H_2O, HF, etc.) from 13 to 35 km.

A test campaign ("Gap 98") was conducted in June 1998 by the AFRL (Air Force Research Laboratory) team with AFRL balloon-borne ozone sondes and thermosondes above the Gap-Tallard Airfield, in southern France.
The AFRL proposed to Onera to join efforts to analyze these data.
Onera proposed [3] and carried out the following tasks presented in this report:

- analysis of AFRL data for possible correlation with measurements made by the Service d'Aéronomie (S.A.) (see Section 2),
- an example of atmospheric stability analysis in collaboration with Dr. Dalaudier from the Service d'Aéronomie. This work is presented in Section 3,
- analysis of Gap Cn^2 profile measurements and study of the effects of atmospheric turbulence on optical propagation in the stratosphere. This optical propagation study is reported in Section 4,
- an analysis of the ozone profile structure related to air mass temperature and modeling of luminance fluctuation using AFRL and S.A. data is given in Section 5.

We collected available measurements from S.A. for June 98. The date and location measurements of the AFRL data did not satisfactorily match those of the S.A. data, so it was difficult to make a reliable comparison.
The analysis of AFRL data established the existence of predominant monochromatic gravity waves. Possible cases of dynamic effects and sheets have been observed. Suggestions for future work are given.
Numerical experiments were conducted to simulate the effects of atmospheric turbulence on the propagation of optical beams over a long path (500 km) in the upper atmosphere (10 to 25 km). The study showed that the propagation could be analyzed using the weak perturbation model (Rytov approximation) in most cases. Future work can be proposed to take into account the influence of refraction index fluctuations caused, for instance, by gravity waves.
In this study, the ozone profiles measured during the Gap campaign which hold in June 1998 have been used for estimating their impact on atmospheric radiance computations. Some important variations can be observed for specific geometries, when using the high fluctuating Lidar profiles measurements. Nevertheless, it is difficult to compare radiance variations induced by the choice of the profile measurement device because the available data have not been recorded on the same site location or at the same time.

Key words :

OZONE ; TEMPERATURE MEASUREMENT ; ATMOSPHERIC MEASUREMENT ; BALLOON-BORNE ; PAYLOAD ; ATMOSPHERIC STABILITY ; CN2 ; TURBULENCE , RADIANCE.

BP 72 - 29, avenue de la Division Leclerc
92322 Châtillon Cedex - FRANCE
Tél. : 01 46 73 40 40 - Fax : 01 46 73 41 41
Office National d'Études et de Recherches Aérospatiales

ONERA

SANS MENTION
DE PROTECTION

SMP

DISTRIBUTION LIST of ONERA REPORT N° RTS 2/05199 DOTA

Distribution of report

■ Outside ONERA :

EOARD Liaison Officer	Dr. Lt. Col. D. Burns	1 ex.
	Major T. Lawrence	1 ex.
CNRS/Sce d'Aéronomie	J.P. Pomereau, A. Garnier, C. Vialle	3 ex.
CNRS/Sce d'Aéronomie	S. Godin, F. Goutail, F. Dalaudier, G. Ancellet	4 ex.
CNRS/Sce d'Aéronomie	A. Hauchecorne	1 ex.

■ Inside ONERA :

DOTA/SC		1 ex.
DOTA/Adj.	J.M. Maisonneuve, M. Séchaud	2 ex.
DOTA/CMMO	B. Rosier	1 ex.
DOTA/LOE	J.P. Cariou, Y. Louvet	2 ex.
DOTA/MPSO	P. Simoneau	1 ex.
DOTA/ASO	V. Michau, L. Rousset-Rouvière	2 ex.
DMPH	R. Ramaroson	1 ex.
ISP	Documentation (original document électronique)	
ISP	Documentation (original document papier + 1 ex.)	

Distribution of identification card only

■ Outside ONERA :

CEDOCAR		1 ex.

■ Inside ONERA :

DOTA/CMIR	J. Deschamps	2 ex.
DOTA/G	A. Raffard	1 ex.
DOTA/Adj.	B. Moreau, G. Rousset,	2 ex.
DOTA/R.U.	X. Briottet, Y. Fazilleau	2 ex.
DOTA/R.U.	E. Georges, M. Girard,	2 ex.
DOTA/R.U.	V. Michau, J. Primot, A. Roblin	3 ex.

Systematic Distribution : D, DSG, DAJ, DTG, DSAC, MM. les directeurs de MFE, PHY, MAS, TIS, GMT

BP 72 - 29, avenue de la Division Leclerc
92322 Châtillon Cedex - FRANCE
Tél. : 01 46 73 40 40 - Fax : 01 46 73 41 41
Office National d'Études et de Recherches Aérospatiales

ONERA

TABLE OF CONTENTS

1. SCIENTIFIC OBJECTIVE

The objective is the validation of turbulence and propagation codes at middle altitudes/latitudes and the proof of principle for flight of U.S. ozone sondes and thermosondes on a major French research balloon called SPIRALE (**SP**ectrometre **I**nfraRouge **A**tmosphérique à **L**aser **E**mbarqué), successfully flown from Gap on June 29, 1999 and June 20, 2001. SPIRALE, funded by CNES (Centre National d'Etudes Spatiales), Onera and INSU (**I**nstitut **N**ational des **S**ciences de l'**U**nivers), was developed by Onera and LPCE (Laboratoire de Physique et Chimie de l'Evironnement) to measure atmospheric trace gases (CO, O_3, CH_4, N_2O, NO_2, NO, CO_2, H_2O, HF, etc.) from 13 to 35 km.

A test campaign ("Gap 98") was conducted in June 1998 by the AFRL team with AFRL balloon-borne ozone sondes and thermosondes above the Gap-Tallard Airfield, in southern France.

The town of Gap is located approximately 160 km due north of Toulon, France. The Gap-Tallard Airfield is situated in the Alps of Southeastern France on a flat plateau 600 m above sea level. Small 1200-gram balloons were launched to obtain *in situ* vertical profiles of ozone, wind speed, wind direction, humidity, temperature and temperature fluctuations.

Dual ozone sonde [1]/thermosonde [2] payloads were employed in some of the measurements. This campaign is the first in which both ozone and temperature fluctuation (turbulence) data were simultaneously measured *in situ* from the same small balloon platform at altitudes from ground level to 30 km.

Several nights of sequential ozone altitude profiles obtained from these *in situ* measurements showed interesting patterns above and below the tropopause level (at 12.5 km) suggestive of gravity waves.

The data are unique in that they give insights into not only the structure, but also the variability of that structure over one- to three-hour periods. The integrated ozone concentration agrees well with the totals and trends observed by the TOMS (Total Ozone Mapping Satellite) satellite for a nearby reporting location for the same period (the altitude-corrected balloon data are within 4-5% of the TOMS data.)

The AFRL proposed to Onera to join efforts to analyze these data.

The following tasks, presented in this report were proposed to and carried out by Onera [3]:

- analysis of AFRL data for possible correlation with measurements made by the Service d'Aéronomie (S.A.) (see Section 2),
- an example of atmospheric stability analysis in collaboration with Dr. Dalaudier from the Service d'Aéronomie. This work is presented in Section 3,
- analysis of Gap Cn^2 profile measurements and study of the effects of atmospheric turbulence on optical propagation in the stratosphere. This optical propagation study is reported in Section 4,
- an analysis of the impact of ozone profiles measured during the Gap campaign on the spectral radiance in the 8-12 μm band.

2. DATA r. Louvet)

2.1. AFRL data

The data transfer process was completed on April 23, 2001.

The AFRL campaign was conducted in June 1998. The list of AFRL flights including the date, time and type of each balloon payload is given in Figure 1.

The data files received (see Figure 2) included:

- wind data from the first flight to flight 17 on June 27, 1998,
- simultaneous ozone and Cn^2 data measurements from flight 9 (on June 24) and flights 10, 11 and 14 (on June 26),
- ozone data from flights 12, 15 and 16.

A sample of available measurements as a function of the date is given in Figure 3.

The file format is explained in the dataform file given by AFRL (see Appendix 1).
This file provides angular data and wind data as a function of altitude according to meteorological convention.

The ozone and temperature files provide measurements as a function of altitude. The altitude is calculated from the hydrostatic equation using Vaisala pressure data. The aspect and acquisition frequency of the data were unusual, so considerable additional information was requested from AFRL. The two sets of questions and the answers are given in Appendix 2.

2.1.1. Sets of data graphs

Two sets of graphs have been plotted.

The first set is presented in Appendix 3. It is intended to assist the investigation of each flight.

The second set of graphs (Appendix 4) is dedicated to a more complex analysis in relation with a stability study. Here we focused on runs 9, 10, 11, and 14 which provided the simultaneous O3/T/Cn^2 data necessary for the stability analysis.
In particular, we calculated the Richardson number and presented an analysis of the principal parameters in the three altitude ranges: [14-18] km [18-22] km and [22-26] km.
We investigated the missing data link which induced incorrect shear values (flat values).
We detected some missing link on data wind:

- run 9 from 15 to 17 km,
- run 10 none,
- run 11 from 3 to 7 km, from 18.5 to 19.3 and 19.7 km and 27 km,
- run 14 at 19.3 km and 18.7 km).

2.1.2. Remarks

The best data with no missing link data seem to be from run 10. Since atmospheric stability studies require very good data correlation, run 10 was chosen first to observe stability processes.

(For this work, see Section 3)

2.2. Available measurements provided by the Service d'Aéronomie

Several contacts were established with researchers of the Service d'Aéronomie in order to identify common scientific interest and possible correlation measurements. A description of Service d'Aéronomie's activities is available on web site: http://www.aero.jussieu.fr/SA.

Measurements were provided by five instruments available in June 1998: SAOZ, ozone lidar, wind lidar, Rayleigh temperature lidar, and ozone sonde. A short description of these measurements is given in Appendix 5 and references [4-12].

The list of available S.A. data as a function of the date and time is shown in Figures 3 and 4.

Only SAOZ flights were made from the Gap launch base. All other measurements were made from the OHP (Observatoire de Haute Provence). The OHP is located about 100 km south of Gap.

2.2.1. Comparison between AFRL and SA data

Looking at Figures 1, 3 and 4, we can see that it was unfortunately difficult to provide a reliable comparison between AFRL data and S.A. data. Data were from different dates, e.g. SAOZ, or from different locations (AFRL from Gap and S.A. from OHP).

A comparison between different ozone data profiles is given in Section 6.

3. ANALYSIS OF ATMOSPHERIC STABILITY (Dr. Dalaudier AND Dr. Louvet)

3.1. Detection of predominant gravity waves

AFRL surveys (wind, O_3, H_2O) revealed the essential structures of the local dynamics, dominated by gravity waves. The wind zonal and meridian profiles clearly show the typical oscillations associated with these waves.

As an example, during flight 10 in the altitude range between 18 and 22 km (see Figures 5 and 6), the profiles of two wind components show the signature of a predominant wave. A diagram of 3D wind data clearly shows the helicoidal variation.

Remark: outside the 18-22 km range, the main part of the fluctuation, which does not have a clear oscillating character, undoubtedly corresponds to a random combination of many gravity waves ("not a single dominant wave but a mixture of many waves").

To confirm this assumption of a predominant gravity wave in the 18-22 km range, we plotted the gradients of the two available tracers (passive parameters with respect to dynamics in this altitude range), i.e. the potential temperature and the mixing ratio of ozone.

In fact, the vertical gradient of logarithmic potential temperature is proportional to the Brunt-Väisälä frequency.

Figure 7 shows that the correlation between the ozone gradient (grad03) and the Brunt-Vaisala pulsation (N2) and the wind is excellent. Excellent but not perfect (see 18 km) because the O_3 gradient is locally variable whereas the potential temperature variations are always positive. The same characteristic periods but out of phase can be observed on two wind components and the tracers. The characteristic associated wavelengths are kilometric in the lower stratosphere.

3.2. Study of local stability conditions

The fluctuations induced by the waves determine areas of more or less great stability.

A distinction can be made between:

Static stability (with respect to convective phenomena) according to a positive Brunt-Vaisala pulsation (N2>0), and

Dynamic stability, characterized by the Richardson number ($Ri=N2/shear^2$), occurring when Ri>0.25. This does not eliminate the possible presence of decreasing mode turbulence in stable zones (see below), or in the opposite case of areas becoming dynamically unstable where turbulence does not have time to develop.

A few interesting typical cases were observed:

a) Possible contribution of atmospheric layer (sheets) [13].

Flight 10 at 19.2 km (see Appendix 4, Figure 8-2, Run 10), we observed a Cn^2 maximum correlated with a shear minimum and an N2 maximum. This could be the contribution of a sheet [13] to the temperature probe signal, but the origin of the layer cannot be determined from the data.

b) Turbulence associated with a dynamic instability

Flight 11 at an altitude of around 21 km (see Appendix 4, Figure 8-2, Run 11), we observed a Cn^2 peak, with a high value of N2 and a shear maximum which could be a dynamic instability

c) Fluctuation in a neutralized layer

Flight 9 at around 18.1 km (see Appendix 4, Figure 8-2, Run 9), a negative or weak N2 was associated with fluctuation of cn^2. Two explanations are possible:

The existence of fluctuation in a stable layer neutralized by a mixing process.

A possible artefact (see [14]) or fluctuation on a small scale not observed by the main Vaisala temperature sensor.

3.3. Conclusion of the atmospheric stability study

Sample cases of analysis and interpretation with emphasis on the dynamical state of the atmosphere were presented. The general domination of large scale dynamics by gravity wave was confirmed, and a short case study of a predominant monochromatic gravity waves was presented. Various typical atmospheric stability cases were observed within this short example of stability analysis. The numerous peaks observed with the thermosonde are not necessarily associated with atmospheric turbulence [14].

3.4. Prospects

This work is a preliminary example of possible investigation. The following future work is proposed.

A more detailed and more complete analysis of the existing layers (sheets), with investigation of their origin and their influence on the Cn^2, could be carried out.

An analysis of the horizontal structure and its variation over time could be made by correlation between the closed flights as well as an investigation of the variation of gravity waves and turbulent layers.

A statistical stability analysis of the static and dynamic layer with a high Cn^2 level would make it possible to better identify the real contribution of turbulence on the signal.

4. OPTICAL PROPAGATION (Dr. Michau and Rousset-Rouvière)

This chapter is aimed at describing the effects of atmospheric turbulence on the propagation of optical beams over a long path (500 km) in the upper atmosphere (10 to 25 km).

This study was made by conducting numerical experiments under various conditions of propagation. The first part of this section describes the model used for the numerical experiments. The second part presents the conditions of the different experiments. The results of the numerical experiments are presented in the last part of this section.

4.1. Description of wave propagation through atmospheric turbulence

4.1.1. Plane wave propagation

The model describing propagation of a plane wave through atmospheric turbulence is based on a method widely described in the literature [15]. In this method, the phase delays induced by the spatial variations of the refraction index are described using phase screens placed regularly along the propagation axis. The statistical properties of the optical delay map of each phase screen has a stationary Gaussian distribution, deduced from Kolmogorov's law. The electromagnetic field EMF is propagated along the distance between each phase screen using the propagation equation in a vacuum, i.e. with a Fresnel transform.

For a plane wave, the propagation between phase screen q and phase screen q+1 is written (see Figure 8):

$$\tilde{U}_{q+1}\left(\vec{\omega}\right)=\tilde{U}'_{q+1}\left(\vec{\omega}\right)\exp(-i\pi\lambda h\omega^2).\exp(ikh)$$

where $\tilde{U}_q\left(\vec{\omega}\right)$ is the Fourier transform of the EMF complex amplitude $U_q\left(\vec{\rho}\right)$ in plane q before phase screen q and $U'_q\left(\vec{\rho}\right)$ is the EMF complex amplitude after phase screen q, denoted $\varphi_{turb,q}$:

$$U'_q\left(\vec{\rho}\right)=U_q\left(\vec{\rho}\right)\exp\left(i\varphi_{turb,q}\left(\vec{\rho}\right)\right)$$

h denotes the distance between phase screens q and q+1, λ the wavelength and $k=\frac{2\pi}{\lambda}$.

4.1.2. Spherical wave propagation

The model presented in Section 4.1.1 was modified to simulate spherical wave propagation. The EMF complex amplitude is then broken down as:

$$U\left(\vec{\rho}\right)=m\left(\vec{\rho}\right)U_{sw}\left(\vec{\rho}\right)$$

where $U_{sw}\left(\vec{\rho}\right)$ represents the EMF complex amplitude corresponding to a perfect spherical wave and m a modulation term taking into account the perturbations due to turbulence effects. With this definition, the modulation term obeys the following propagation equation:

$$\tilde{m}_{q+1}\left(\vec{\omega}\right)=\tilde{m}'_q\left(\vec{\omega}\right)\exp\left(-ik\lambda\omega^2 h_{eq}\right)$$

where $h_{eq}=\frac{h}{1-h/z}$, h is the distance between phase screens q and q+1, and z is the distance from the source to phase screen q+1. This allows propagation of a spherical wave to be described in the same way as propagation of a plane wave. The beam geometry is shown in Figure 9. Note that the sizes of the phase screens increase linearly with the propagation distance. Turbulence effects between the source and the first phase screen are not taken into account in our model.

Using these models, a software code was developed at Onera to describe propagation of plane and spherical waves through atmospheric turbulence. The phase screens are drawn randomly. The main input parameters of this code are:

- the conditions defining turbulence along the optical path: the C_n^2 profile, the outer scale (L_0), the inner scale (l_0),
- the beam characteristics: wavelength, distance between the source and the receiver plane, width of the receiver plane,
- the numerical parameters: spatial sampling of the phase screens, number of pixels in a screen phase, position of the phase screens along the propagation axis.

The first output of the software is the EMF complex amplitude in the receiver plane. For a wave propagated through turbulence, the EMF complex amplitude in the receiver plane can be written:

$$E(\vec{r}) = E_0(\vec{r})\exp[i\psi(\vec{r})]$$

E_0 is the EMF complex amplitude without perturbations and $\exp[i\psi(\rho)]$ represents the perturbation term due to turbulence effects. ψ is a complex number whose real part represents the phase perturbations denoted φ and whose imaginary part, the so-called log-amplitude, represents the amplitude perturbations, i.e. the scintillation effects:

$$\psi(\vec{r}) = \varphi(\vec{r}) + i\chi(\vec{r})$$

A numerical experiment was conducted by processing a set of EMF complex amplitudes, E_i, obtained in the receiver plane with the same set of input parameters but with different drawings of the phase screens. Then, the statistical properties of φ and ψ are determined from the set of E_i values:

- the spatial power spectral density (PSD) of φ,
- the spatial variance of ψ as a function of the propagation distance,
- the spatial PSD of ψ,
- the spatial PSD of $I=|E|^2$.

4.2. Propagation conditions

This part describes the different propagation conditions that were simulated for the numerical experiments. The propagation geometry is shown in Figure 10:

- the receiver plane was 15 km high,
- the source height varied between 10 and 25 km,
- the propagation distance was 500 km.

The outer scale was assumed to be 50 meters and the inner scale 2 mm. We studied propagation at the following wavelengths: 1.06, 1.55, 5 and 10 µm. Turbulence was represented by 20 phase screens sampled with a 256 by 256 grid. The size of the last screen was 50 meters.

The C_n^2 profile used in the numerical experiment was obtained by a log-linear fit of the data given in the GAP9811.txt file. The equation of fitted profile is:

$$C_n^2 = \alpha.10^{(-\beta h)}$$

where h is the altitude and α and β are constants. The fit was made in the [5; 25] km range.

The figure 11 shows the C_n^2 profile corresponding to the GAP9811.txt file and the result of the fit.

4.3. Results

Table 1 shows the main parameters characterizing optical propagation for the numerical experiments:

- the geometry of the optical path,
- the Fresnel distance ($\sqrt{\lambda L}$),
- the Fried parameter r_0,
- the standard deviation of log-amplitude χ in the Rytov regime (weak perturbations),
- the standard deviation of log-amplitude χ estimated with the numerical experiment.

As indicated in table 1, the log-amplitude standard deviation σ_χ obtained from the Rytov approximation and the one obtained from the numerical experiment are very similar, except for the worst case i.e. for h_{source} = 10 km, λ = 1.06 µm. In this case, the standard deviation σ_χ obtained from the numerical experiment is smaller than the Rytov one, $\sigma_{\chi\,Rytov}$. This result indicates the beginning of the saturation regime of scintillation. In the other cases, the numerical experiments were conducted in the weak perturbation regime. This behavior might be able to be predicted by comparing r_0 with the Fresnel distance $\sqrt{\lambda L}$.

Table 1

Source height (km) – Wavelength (µm)	$\sqrt{\lambda L}$ (m)	r_0 (m)	σ_χ	$\sigma_{\chi\,Rytov}$
10 – 1.06	0.73	0.39	0.74	0.84
10 – 1.55	0.88	0.61	0.68	0.67
10 – 5.00	1.58	2.51	0.35	0.34
10 – 10.0	2.23	5.76	0.22	0.22
15 – 1.06	0.73	0.47	0.65	0.63
15 – 1.55	0.88	0.74	0.54	0.51
15 – 5.00	1.58	3.05	0.26	0.25
15 – 10.0	2.23	7.0	0.17	0.17
20 – 1.06	0.73	0.56	0.47	0.45
20 – 1.55	0.88	0.88	0.41	0.40
20 – 5.00	1.58	3.60	0.20	0.20
20 – 10.0	2.23	8.26	0.13	0.13
25 – 1.06	0.73	0.64	0.39	0.39
25 – 1.55	0.88	1.01	0.31	0.31
25 – 5.00	1.58	4.13	0.15	0.16
25 – 10.0	2.23	9.5	0.10	0.10

The results obtained from the numerical experiments are given in Figure 12 to Figure 27. Each figure shows:

- an example of intensity distribution in the receiver plane,

- the spatial power spectral density (PSD) of φ,
- the spatial standard deviation χ as a function of the propagation distance or as a function of the value obtained from the Rytov approximation,
- the spatial PSD of χ,
- the spatial PSD of $I=|E|^2$.

For the weak perturbation case, the PSD of χ and I and the standard deviations obtained from the numerical experiments were fitted with analytical results obtained from the Rytov model. Saturation of the intensity fluctuations can be seen in Figure 12. The PSD of I obtained from the numerical experiment is lower than the Rytov one mainly for intermediate spatial frequencies [16, 17].

The examples of intensity distribution in the pupil plane of the receiver also illustrate this behavior. A single characteristic structure size (the Fresnel distance) can be seen in the weak perturbation case. In the saturation regime (Figure 12) filaments appear and two structure sizes can be distinguished: the width and the length of these filaments.

4.4. Conclusion

Numerical experiments were conducted to simulate the effects of atmospheric turbulence on the propagation of optical beams over a long path (500 km) in the upper atmosphere (10 to 25 km). The study showed that propagation could be analyzed using the weak perturbation model (Rytov approximation) in most cases. In the worst case, (λ= 1.06 µm, h_{source}= 10 km, $h_{receiver}$ = 15 km, $distance_{source\text{-}receiver}$ = 500 km), the intensity fluctuations entered the saturation regime. The PSD of the phase and log-amplitude were characterized.

This study was made using a phase perturbation model based on the perturbation of the refraction index in the inertial range. This model is probably valid for describing the intensity variations inside the receiver pupil. However, it does not take into account large scale fluctuations of the refraction index along the optical path such as gravity waves. These variations can substantially modify the amplitude of the variations of the total intensity in the receiver pupil.

5. ANALYSIS OF THE OZONE PROFILE AND RADIANCE COMPUTATIONS (Dr. Simoneau)

The goal of this study is to analyze the impact of ozone profiles measured during the Gap campaign on the spectral radiance in the 8-12 μm band. In this work, we run the radiative transfer code MATISSE developed at Onera, using ozone, temperature and water vapor profiles measured during the campaign as input data.

The 5.1. paragraph contains a brief description of MATISSE. It is followed by a discussion on profiles measurements in section 5.2. Computation results are finally discussed in paragraph 5.3.

5.1. MATISSE code

MATISSE 1.1 (MATISSE stands for "Advanced Earth Modeling for Imaging and Scene Simulation") is the first version of a new program currently under development at Onera [18], whose purpose is to compute background radiance images by taking into account atmospheric, clouds and ground radiation as well as the variability of atmospheric properties along the lines of sight. The development is planned for the code to be delivered by the mid year 2002. Before MATISSE 1.1 development phase, a prototype has been realized whose first objective was to compute transmission and atmospheric radiance along an optical path in an atmosphere exhibiting geographically variable thermodynamic properties with a fast computing method for the radiation propagation (band model with 1 cm^{-1} spectral resolution). This prototype has been used for this study. Accordingly, it allows computations in atmospheres defined by a large number of atmospheric layers, which is not the case for most of the available radiative transfer codes. We use MATISSE in the 8-12 μm spectral band without taking into account aerosols, and by computing atmospheric thermal emission only. Refraction effects are also taken into account.

5.2. The atmospheric profiles

Figure 28 and Figure 29 show the ozone profiles versus altitude measured during gap campaign. Four ozone profiles measured by the Air Force Research Laboratory (AFRL) during the 24th, 25th and 26th of June 1998 and the MidLatitude Summer profile (MLS) [19] are plotted on the Figure 28. As can be seen, the measured profiles are close to the MLS profile, though exhibiting small variations in the vicinity of 15 km. Figure 29 shows ozone profiles measured by the ozone Lidar (22nd, 23rd, 25th, 26th and 29th of June), the ECC probe (24th of June) and SAOZ (23th of June) instruments (see Section 2 and Figure 3, measurements of Service d'Aeronomie). Huge variations of the Lidar measurements are observed between 40 and 50 km, so the major part of this work is devoted to the radiance variations induced by the use of these atmospheric ozone profiles as input data. The striking evolution of the SAOZ profile below 15 km is a modeling artifact due to the absence of measurement for these altitudes.

Moreover, the profiles are only available for a restricted section of the atmosphere, so they have been extrapolated from the ground to the top of the atmosphere, and the missing atmospheric molecules have been added by using the PRFL code [20]. The deduced profiles are plotted on the Figure 30 as well as the MLS profile and the climatological profile used in the PRFL code (so called Climato 20/06 on the figure). It can be seen that the large fluctuations of the Lidar profiles induce artifacts in the extrapolated data around 50 km.

5.3. Results

The figure 31 shows radiance computations performed by using ozone Lidar measurements and the MLS profile as input data. The following observational conditions are used : the observer, located at an altitude of 50 km is looking towards the ground and the path length is 10 km. The figure put in evidence a high variability of the radiance. The largest gap between Lidar measurements and MLS profile corresponds to the data of the 23rd of June, where the value at 50 km is close to zero. Nevertheless, this altitude is the upper limit of the Lidar range, so this result has to be taken with care.

Figure 32 shows radiance computations using the reverse geometry : the observer is now located at an altitude of 40 km and is looking upward. The same conclusions as previously can be drawn, but it appears a less pronounced radiance variability.

Figure 33 to Figure 36 show radiance computations for an horizontal line of sight, a path length of 1 km and an observer located at different altitudes on each figure. The data used for the computations are again the Lidar profiles measurements. The aim of these computations is to study the radiance variations induced by using various atmospheric profiles as they could be measured by an observer in the atmosphere looking at a target flying at the same altitude. For Figure 33 the observer is located at an altitude of 50 km. As expected, the lowest radiance value is for measurements performed on the 23rd of June where the ozone concentration measurement is close to zero. It can be seen that in all cases, the MLS profile induce the highest radiance value. This result could be unexpected regarding the ozone value for this altitude in comparison with the other Lidar measurements, but it appears that the temperature value in the MLS case is higher than the data recorded during the campaign. This last point explains the higher radiance value for these wavelengths.

For the case treated in the Figure 34, the observer is located at an altitude of 48 km, which is the altitude of the ozone peak value for the 22nd of June. As expected, the radiance reaches its higher value for this day. For the other days, the MLS profile always induces the higher radiance value for the same reasons as previously discussed.

Figure 35 exhibits a less pronounced variability in correlation with the ozone profile fluctuations for this altitude, and has a low value at an altitude of 40 km where the Lidar measurements are smoother (Figure 36).

Figure 37 shows radiance computation using similar observation geometry as for the Figure 35, but the path length is 100 km. In this case, the ozone concentrations are averaged over the optical path due to the sphericity of the atmospheric layers inducing, as can be observed, a lower variability for the computed radiance.

The results plotted on the Figure 38 are obtained with another geometrical conditions: in this case, the observer is located at an altitude of 46 km (in the validity domain of the Lidar measurements) looking at the ground with a zenithal angle of 135°. The final altitude of the line of sight is 3.7 km. The SAOZ artifact already mentioned, induces the high radiance value in the ozone emission band. Nevertheless, a line structure of radiance values appears, which is due to the presence of water vapor at low altitude. This phenomenon is well marked for the AFRL measurement as it can be expected, because this profile (measured at the same time) is the most humid as can be seen on the Figure 39.

The last two figures (Figure 40 and Figure 41) show a comparison of the computed radiance from measurements performed in the same period and with two different devices (Lidar/SAOZ and AFRL/ECC sounds). It appears a marked gap between Lidar and SAOZ measurements, nevertheless it is not possible to conclude because measurements have been performed on two sites separated by 100 km.

5.4. Conclusion

In this study the ozone profiles measured during the Gap campaign which hold in June 1998 have been used for estimating their impact on atmospheric radiance computations. Some important variations can be observed for particular geometries, when using the high fluctuating Lidar profiles measurements. Nevertheless, it is difficult to compare radiance variations induced by the choice of the profile measurement device because the available data have not been recorded on the same site location or at the same time.

6. CONCLUSION

We collected available measurements from S.A. for June 98. The date and location measurements of the AFRL data did not satisfactorily match those of the S.A. data, so it was difficult to make a reliable comparison.

The analysis of AFRL data established the existence of predominant monochromatic gravity waves and possible cases of dynamic effects and sheets have been observed. Suggestions for future work are given.

Numerical experiments were conducted to simulate the effects of atmospheric turbulence on the propagation of optical beams over a long path (500 km) in the upper atmosphere (10 to 25 km). The study showed that the propagation could be analyzed using the weak perturbation model (Rytov approximation) in most cases Future work can be proposed to take into account the influence of refraction index fluctuations caused, for instance, by gravity waves.

The Gap98 ozone profiles measured have been used for estimating their impact on atmospheric radiance computations. Nevertheless, it is difficult to compare radiance variations induced by the choice of the profile measurement device because the available data have not been recorded on the same site location or at the same time.

7. ACKNOWLEDGMENTS

We wish to thank all the researchers of the Service d'Aéronomie involved in this study for their advice and the experimental data provided. We would especially like to thank Dr. Dalaudier for his active participation in the stability study. We wish to thank Dr. Jumper and Murphy for all additional information about GAP98 data.

8. BIBLIOGRAPHY

[1] W.D. Komhyr, R. A. Barnes, G. B. Brothers
J. A. Lathrop and D. P. Opperman, Electrochemical concentration cell ozone sonde performance evaluation during STOIC 1989
J. Geophys. Res., 100, 9231-9244,1995.

[2] J.H. Brown, R. E. Good, P. M. Bench, and G. Faucher
Sonde Measurements for Comparative Measurements of Optical Turbulence
Air Force Geophysics Laboratory, AFGL-TR-82-0079, ADA 118740, National Technical Information service, Springfield, VA., 1982.

[3] Y. Louvet, B. Rosier, V. Michau, P. Simoneau
Analysis and modelling of AFRL "GAP98" balloon-borne measurements: task definition
Intermediate Onera Report n° RTI 1/05199, March 2001.

[4] F. Goutail, J.P. Pomereau, C. Philips, F. Lefèvre, E. Kyro, and al
Ozone depletion in the Arctic during winter 94-95
J. Atm Chem, 1996.

[5] J.P. Pomereau, F. Goutail, J. Piquard, L. Denis, C. Philips
The AOAZ Balloon optical sonde for atmospheric chemistry study
Proc 11th ESA symposium EUR.Rocket &Balloon prog. ESA SP 355, 87, 1994.

[6] S. Godin , G. Mégie, J. Pelon
Systematic Lidar Measurements of the Stratospheric Ozone vertical Distribution
Geophys. Res. Letters, vol. 16, n° 16, 547-550, 1989.

[7] S. Godin., V. Bergeret, S. Bekki, C. David, G. Mégie
Study of the interannual ozone loss and the permeability of the Antarctic Polar Vortex from long-term aerosol and ozone lidar measurements in Dumont d'Urville (66.4°, 140°S)
J. Geophys. Res., 106, 1311-1330, 2001.

[8] A. Hauchecorne, M.L. Chanin
Density and temperature profiles obtained by lidar between 35 and 70 km
Geophys. Res. Lett., 7, 565-568, 1980.

[9] A. Hauchecorne, M.L. Chanin, P. Keckhut
Climatology and trends of the middle atmospheric temperature (33-87 km) as seen by Rayleigh lidar above south of France
J. Geophys. Res., 96, 15297-15309, 1991.

[10] P. Keckhut, A. Hauchecorne, M.L. Chanin
A critical review of the data base acquired for the long term surveillance of the middle atmosphere by Rayleigh lidar
J. Atm. Ocean. Tech., 10, 850-867, 1993.

[11] A. Hauchecorne
Lidar temperature measurements in the middle atmosphere
Rev. Laser Engineering, 23, 119-123, 1995.

[12] T. Leblanc, I.S. McDermid, A. Hauchecorne, P. Keckhut
Evaluation of optimization of lidar temperature analysis algorithms using simulated data
J. Geophys. Res., 103, 6177-6187, 1998.

[13] F. Dalaudier, C. Sidi, M. Crochet, J. Vernin
Direct Evidence of "sheets" in the Atmospheric Temperature Field
Journal of the Atmospheric Sciences, Vol 51, N°2, 15 January 1994.

[14] G.Y. Jumper, R. R. Beland and P. Tracy
Investigating Sources of Error in Balloon-Borne Optical Turbulence Measurements
American Institute of Aeronautics and Astronautics.

[15] J. M. Martin, S. M. Flatté
Intensity images and statistics from numerical simulation of wave propagation in 3-d random media
Appl. Opt., 27(11): 2111-2126, 1988.

[16] L. C. Andrews, R. L. Phillips, C. Y. Hopen, and M. A. Alhabash,
Theory of optical scintillation
J. Opt. Soc. Am., 16(6):1417-1429, 1999.

[17] F. Mahé
Application d'un modèle atmosphérique à l'étude des fluctuations d'indice de réfraction dans la couche limite. Influence de la scintillation sur l'analyse de front d'onde
Thèse de doctorat, Université de Nice-Sophia Antipolis, fév. 2000.

[18] P. Simoneau, R. Berton, K. Caillault, G. Durand, T. Huet, L. Labarre, C. Malherbe, C. Miesch, A. Roblin, B. Rosier
MATISSE, Advanced Earth Modeling for Imaging and Scene Simulation
8th International Remote Symposium on Remote Sensing, Toulouse, France, September 2001.

[19] G. P. Anderson, S. A. Clough, F. X. Kneizys, J. H. Chetwynd, E. P. Shettle
AFGL Atmospheric Constituent Profiles (0-120km)
AFGL-TR-86-0110, May 1986.

[20] F. Karcher
Détermination des profils atmosphériques de référence par la mesure de constituants par spectrométrie d'absorption
CNRM Internal Report, 1990.

9. KEY ONERA PEOPLE INVOLVED IN THE STUDY

Yolande Louvet was born in France in 1955. She received a PhD in Physical Sciences from the University of Orsay (Paris XI) in 1986. She joined Onera in 1988. She has worked in the field of high power gas lasers. From 1992, she has headed the Tunable Diode Laser Spectroscopy activity. She was Onera's project manager on the SPIRALE balloon-borne experiment. Yolande Louvet has published about 10 papers and co-directed 3 theses.

Vincent Michau was born in 1961. He received a PhD in Physical Sciences from the University of Orsay (Paris XI) in 1987. He joined Onera in 1987.

He has worked on tunable solid lasers and the Raman effect. Since 1998, he has been in charge of the "Wave front analysis and image restoration" research unit. He leads fundamental and applied research in the field of turbulence studies and atmospheric transmission problems. **Vincent Michau** has published more than 20 papers.

Bernard Rosier was born in 1960. He received his degree in Advanced Physics from "Ecole Centrale de Paris" in 1982. He joined Onera in 1983.

He has worked on Tunable Laser Spectroscopy and Missile Plume Signature. In 1989 he was in charge of the Infrared Instrument Design and Modeling team, in 1994 of the Earth and Atmosphere Observation team, and in 1997 of the Optical Signature Modeling research team. Since 1999 he has been in charge of coordinating the Background and Target Optical Signature Modeling activities in the Applied and Theoretical Optics Department.

Laurent Rousset-Rouvière was born in 1967. He received his degree from "Ecole Nationale Supérieure de Physique de Marseille" in 1992. He joined Onera in 1994.

He has worked on experimental wave front analysis of atmospheric turbulence and experimental adaptive optic systems. Since 1999, he has been in charge of the simulations of adaptive optic systems and optical propagations through atmospheric turbulence.

Pierre Simoneau was born in 1958. He received a PhD in Physical Sciences from the University of Orsay (Paris XI) in 1986 where he worked on nonlinear optical effects and atomic spectroscopy in gases (saturated absorption, four-wave mixing, etc.).

He joined Onera in 1990. Since then, he has worked on atmospheric codes and is responsible for atmospheric effect modeling (radiance computation, transmission, NETL, clouds, etc.) in the Optical Signature Modeling research team. Since 1999 he has been project manager for development of a new atmospheric radiative transfer code called MATISSE. Pierre Simoneau directed two theses: one on high altitude effects and the second on fire detection from satellites.

SANS MENTION
DE PROTECTION

SMP

GAP98 PRELIMINARY DATA REPORT

Launch #	Date	Time	Payload	Cn_2	GPS Winds	Ozone	P, T, %RH	Comments
gap9801	06/20/98	2215 LT	T/GPS	Good 30 Km	Good 30 Km	N/A	Good 30 Km	
gap9802	06/21/98	0025 LT	T/GPS	Good 28 Km	Good 27.5 Km	N/A	Good 28 Km	
gap9803	06/21/98	2133 LT	T/GPS	Good 29 Km	No Winds	N/A	Good 29 Km	failed to record wind data
gap9804	06/21/98	2332 LT	T/GPS	Good 30 Km	Good 30 Km	N/A	Good 30 Km	
gap9805	06/22/98	2130 LT	T/GPS	Good 29 Km	Good 30 Km	N/A	Good 29 Km	
gap9806	06/22/98	2320 LT	T/GPS	Good 22 Km	Good 28 Km	N/A	Good 30 Km	
gap9807	06/23/98	1548 LT	O_3/GPS	Good 27 Km	No Winds	Yes	Good 27 Km	failed to record wind data
gap9808	06/24/98	2140 LT	TO_2/GPS	Good 30 Km	Good 19.5 Km	Yes	Good 30 Km	some noise on O_3 channels
gap9809	06/24/98	2345 LT	TO_2/GPS	Good 22.7Km	Good 23.4 Km	Yes	Good 27 Km	O_3 BG slightly high
gap9810	06/25/98	2130 LT	TO_2/GPS	Good 29 Km	Good 27.6 Km	Yes	Good 29 Km	2 channels agree on O_3, BG high
gap9811	06/25/98	0003 LT	TO_2/GPS	Good 30 Km	Good 27.5 Km	Yes	Good 30 Km	all 3 O_3 channels differ
gap9812	06/26/98	1935 LT	O_3/GPS	N/A	Good 30 Km	Yes	Good 30 Km	O_3 good all channels, BG good
gap9813	06/26/98	2133 LT	T/GPS	Awaiting data	Good 9.4 Km	N/A	Good 9.4 Km	balloon burst at 9.4 Km
gap9814	06/26/98	2241 LT	TO_2/GPS	Good 30 Km	Good 28 Km	Yes	Good 30 Km	O_3 good all channels, BG good
gap9815	06/27/98	1730 LT	O_3/GPS	N/A	Good 22 Km	Yes	Good 22 Km	O_3 good all channels, BG good
gap9816	06/27/98	1926 LT	O_3/GPS	N/A	Good 29.8 Km	Yes	Good 30 Km	O_3 good all channels, BG good
gap9817	06/27/98	2130 LT	T/GPS	Good 30 Km	Good 30 Km	N/A	Good 30 Km	

Figure 1 - List of flights from the GAP98 campaign provided by AFRL.

ONERA

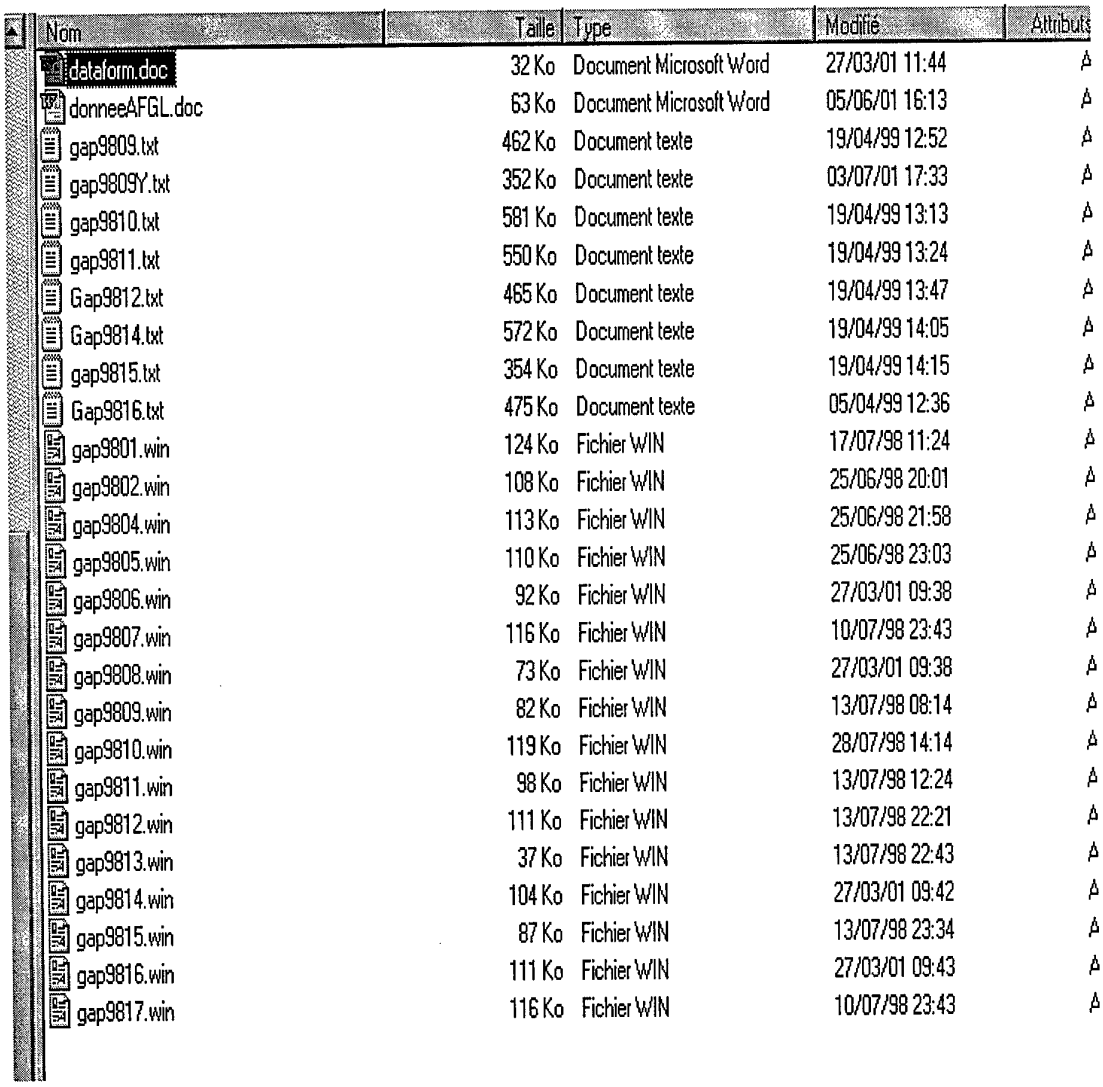

Nom	Taille	Type	Modifié	Attributs
dataform.doc	32 Ko	Document Microsoft Word	27/03/01 11:44	A
donneeAFGL.doc	63 Ko	Document Microsoft Word	05/06/01 16:13	A
gap9809.txt	462 Ko	Document texte	19/04/99 12:52	A
gap9809Y.txt	352 Ko	Document texte	03/07/01 17:33	A
gap9810.txt	581 Ko	Document texte	19/04/99 13:13	A
gap9811.txt	550 Ko	Document texte	19/04/99 13:24	A
Gap9812.txt	465 Ko	Document texte	19/04/99 13:47	A
Gap9814.txt	572 Ko	Document texte	19/04/99 14:05	A
gap9815.txt	354 Ko	Document texte	19/04/99 14:15	A
Gap9816.txt	475 Ko	Document texte	05/04/99 12:36	A
gap9801.win	124 Ko	Fichier WIN	17/07/98 11:24	A
gap9802.win	108 Ko	Fichier WIN	25/06/98 20:01	A
gap9804.win	113 Ko	Fichier WIN	25/06/98 21:58	A
gap9805.win	110 Ko	Fichier WIN	25/06/98 23:03	A
gap9806.win	92 Ko	Fichier WIN	27/03/01 09:38	A
gap9807.win	116 Ko	Fichier WIN	10/07/98 23:43	A
gap9808.win	73 Ko	Fichier WIN	27/03/01 09:38	A
gap9809.win	82 Ko	Fichier WIN	13/07/98 08:14	A
gap9810.win	119 Ko	Fichier WIN	28/07/98 14:14	A
gap9811.win	98 Ko	Fichier WIN	13/07/98 12:24	A
gap9812.win	111 Ko	Fichier WIN	13/07/98 22:21	A
gap9813.win	37 Ko	Fichier WIN	13/07/98 22:43	A
gap9814.win	104 Ko	Fichier WIN	27/03/01 09:42	A
gap9815.win	87 Ko	Fichier WIN	13/07/98 23:34	A
gap9816.win	111 Ko	Fichier WIN	27/03/01 09:43	A
gap9817.win	116 Ko	Fichier WIN	10/07/98 23:43	A

Figure 2 - Available AFRL data files.

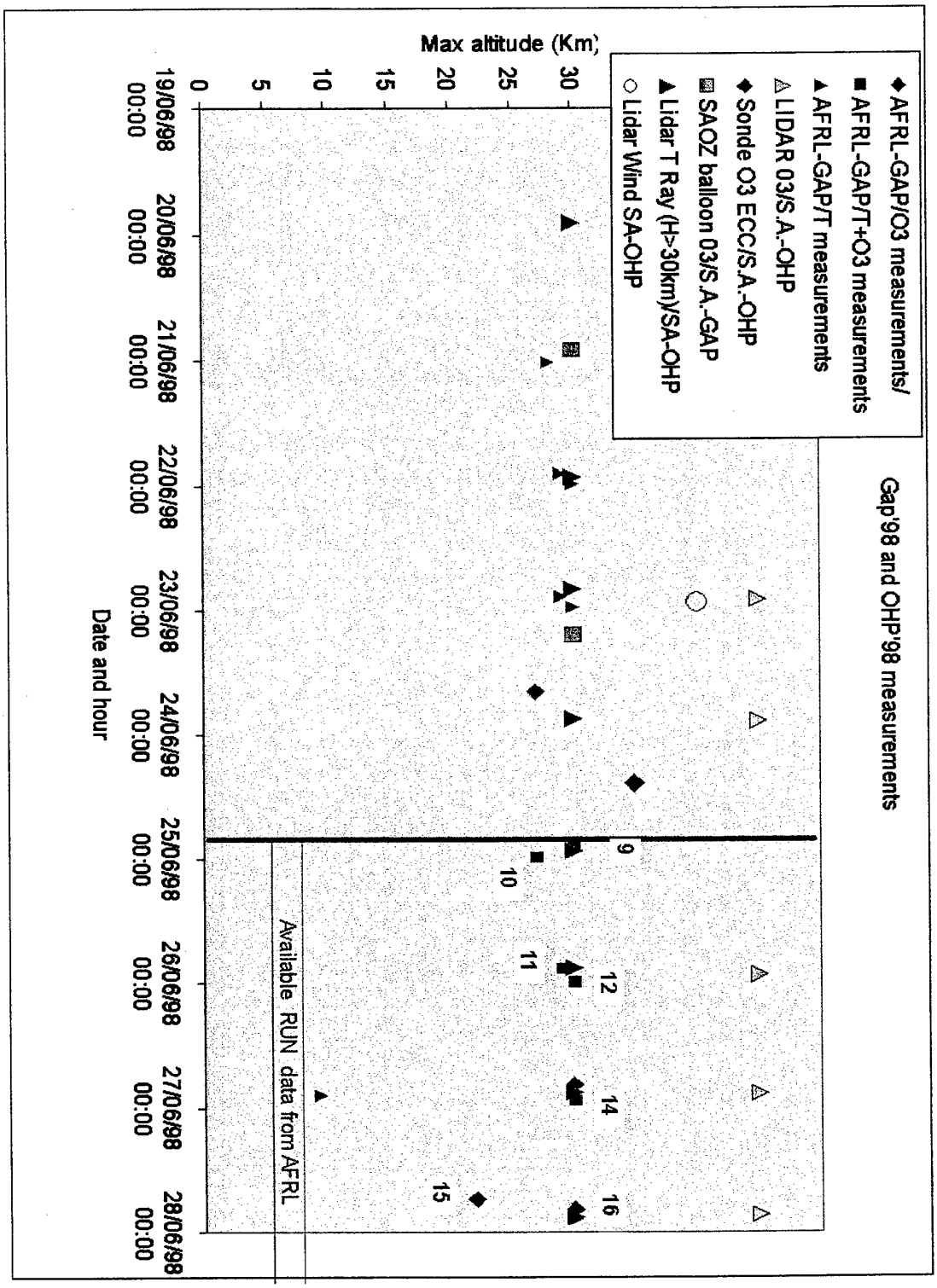

Figure 3 - Available data from AFRL and S.A. as a function of date.

ONERA

Device Name	Launch Base	Date	Launch (hh/mm)	Born facili	Instrument	method	Altitude field	DATA	Contact
		1998	Beginning end						
SAOZ	GAP	20-juin	sunset	Stratosphel	Spectrometer	UV-Visible spectrometer Screening solar light	0-33 km	available	Dr. GOUTAIL
		23-juin	sunrise	Balloon					
C3/ECC	OHP	24-juin	9H26 TU	smal balo	Sonde C3 ECC	Eletro-chemical	0-35 km	available	Dr. YIALLE
Wind LIDAR	OHP			ground			5 to 45 km	Possible	Dr. GARNIER
Lidar C3 Strato	OHP	22-juin	21H50	OH51	ground	Lidar C3	Two wavelengths	10-45 km	available	Dr. GODIN
		23-juin	21H20	2H52		DIAL UV	feedback detection			
		25-juin	22H33	2H52			flight time			
		26-juin	21H16	2H52						
		28-juin	20H40	2H00						
Lidar Rayleigh		19-juin	21h37	03H03						
		21-juin	22H21	03H03						
		22-juin	20H01	00H43			Feedback lidar			
		23-juin	21H05	03H04	ground	Lidar Rayleigh	Atmospheric density	30 to 70km	available	M. HAUCHECORNE
		24-juin	22H25	03H04						
		25-juin	21H09	03H05			to convert in Temperature			
		26-juin	20H58	03H05			using hydrostatic coefficient			P hilippe Keckhut
		27-juin	20H58	03H05						
		28-juin	20h	03H06						
Lidar C3 Troposphere ALTO	OHP	??						No available dates	M. ANCELLET	

Figure 4 - Measurements from S.A. in June 98.

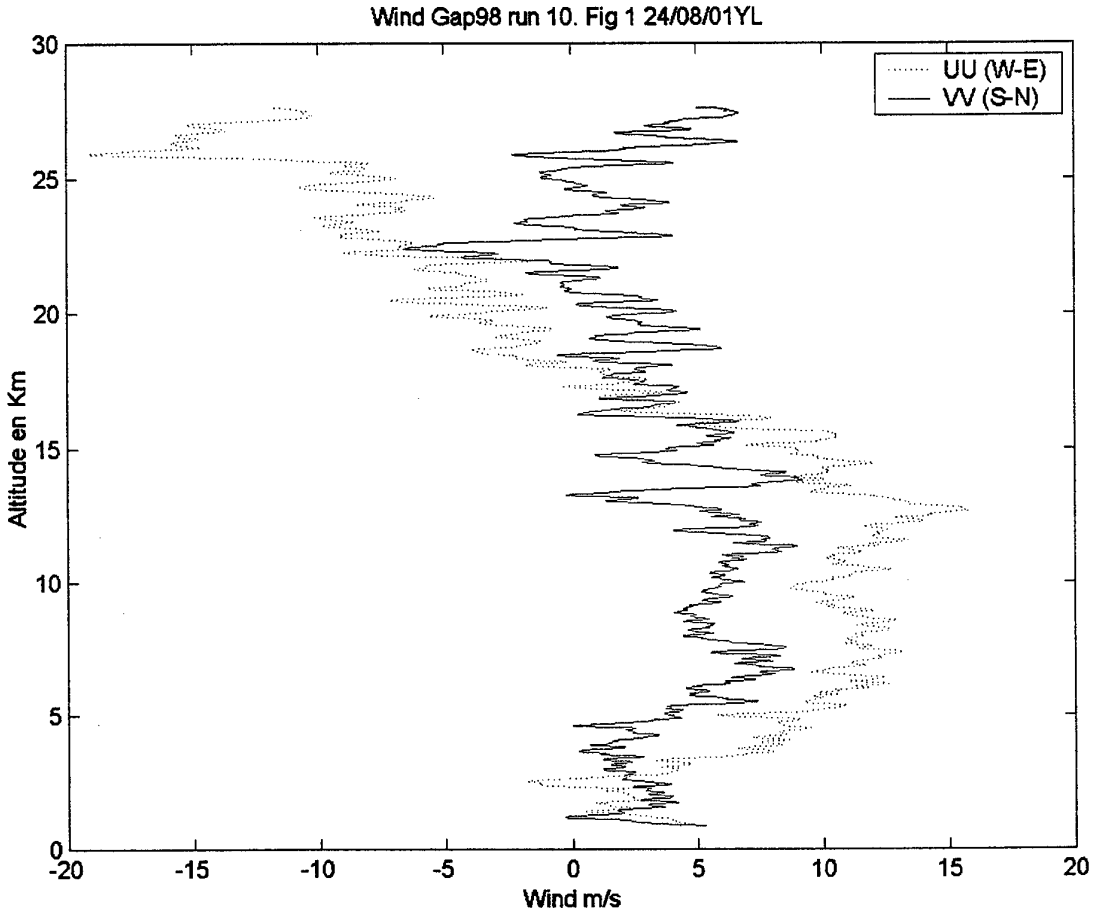

Figure 5 - Two wind components of RUN 10 as a function of altitude.

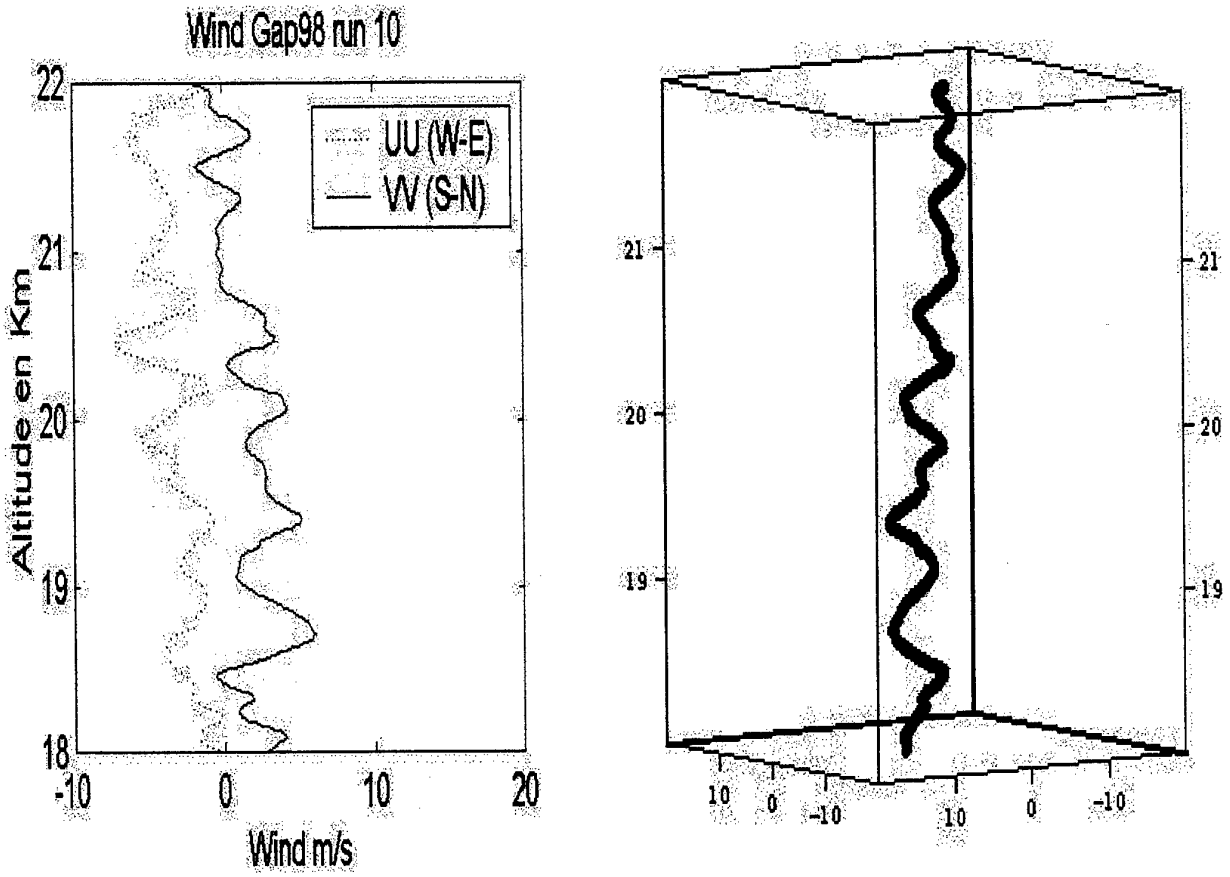

Figure 6 - Wind representation of RUN 10 in the [18-22] km altitude range.

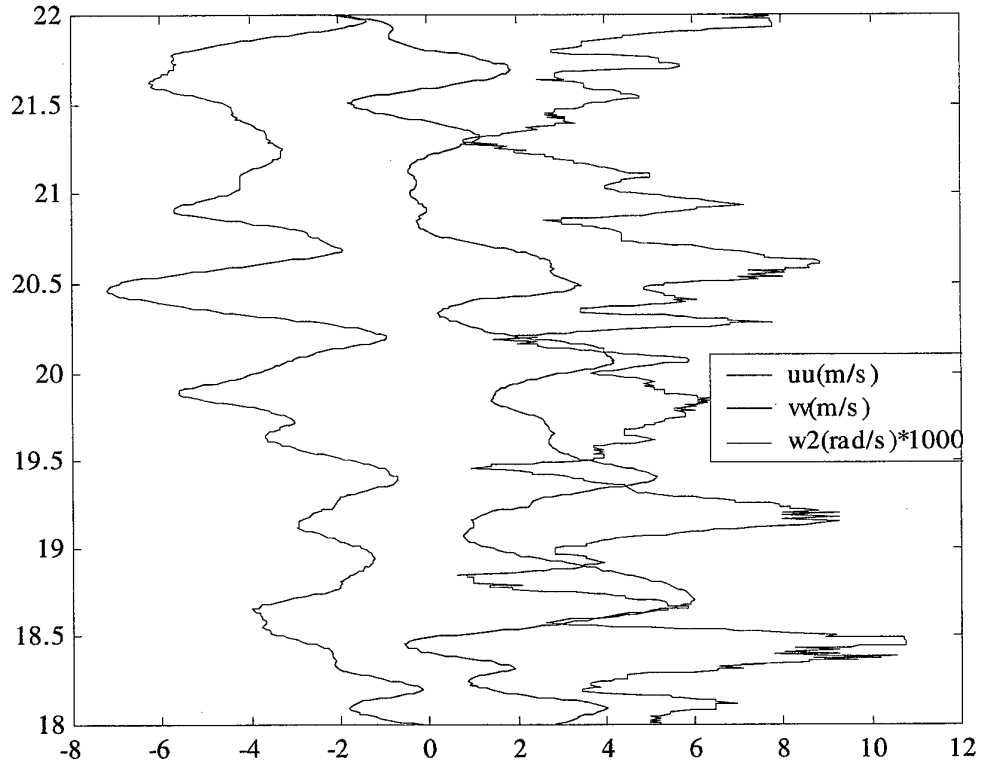

Figure 7 - RUN 10. Correlation between ozone gradient, Brunt Vaisala pulsation square (N2) and wind components in the [18-22] km altitude range

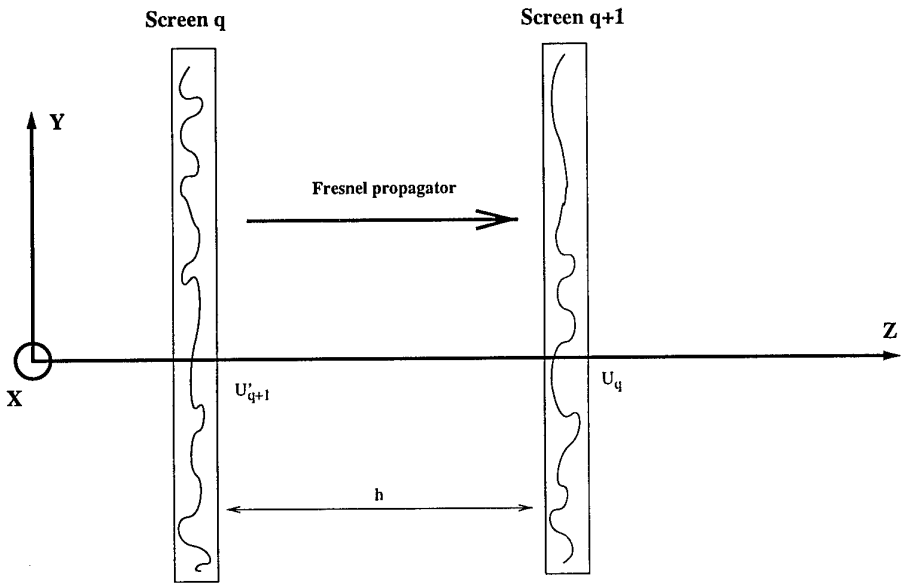

Figure 8 - Diagram of plane wave propagation along z between phase screens q and q+1. U'_q is the EMF complex amplitude after phase screen q and U_{q+1} is the complex amplitude before phase screen q+1.

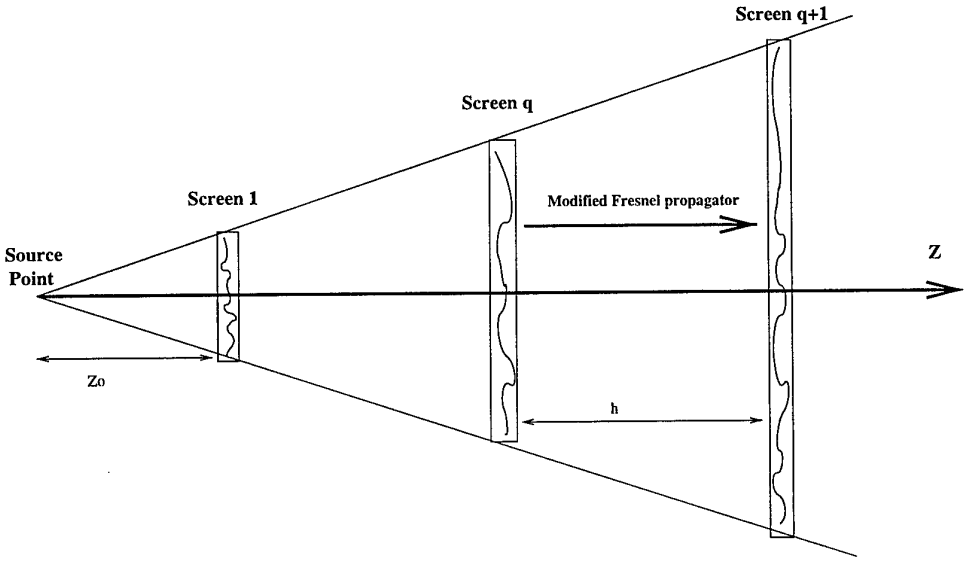

Figure 9 - Diagram of spherical wave propagation along z. Z_0 is distance between the first phase screen and the source.

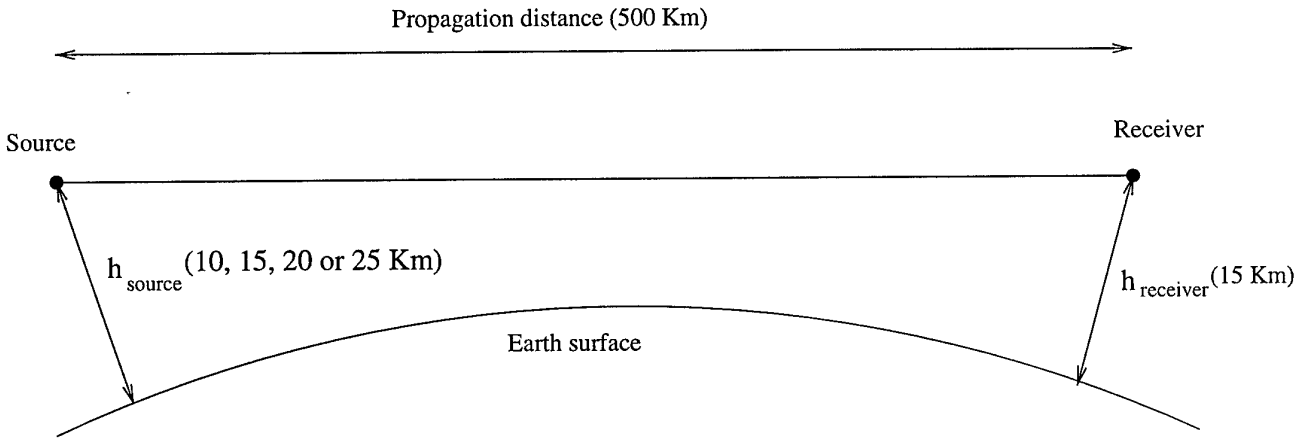

Figure 10 - Propagation geometry.

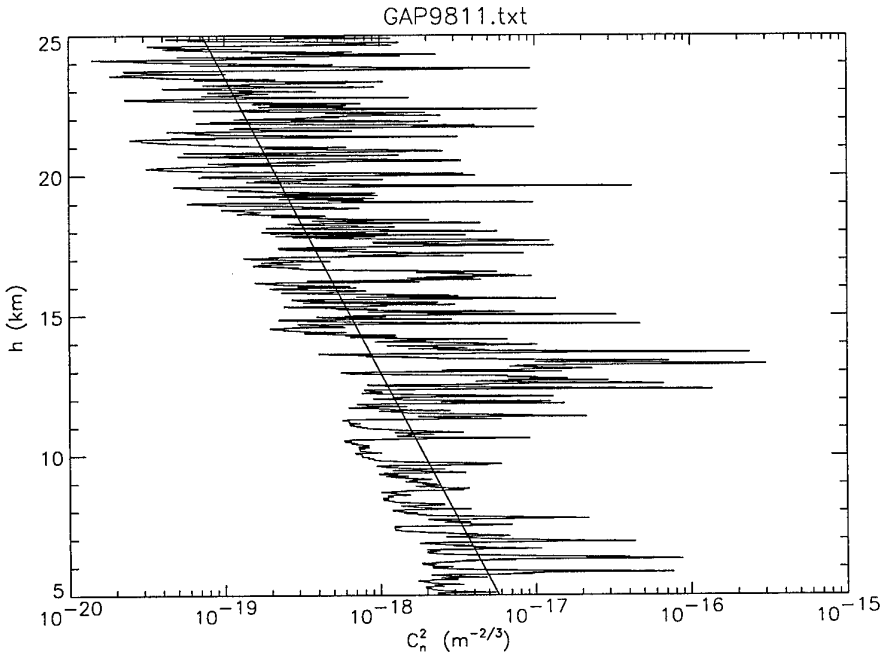

Figure 11 - Measured (GAP9811.txt file) and fitted C_n^2 profiles between 5 and 25 km.

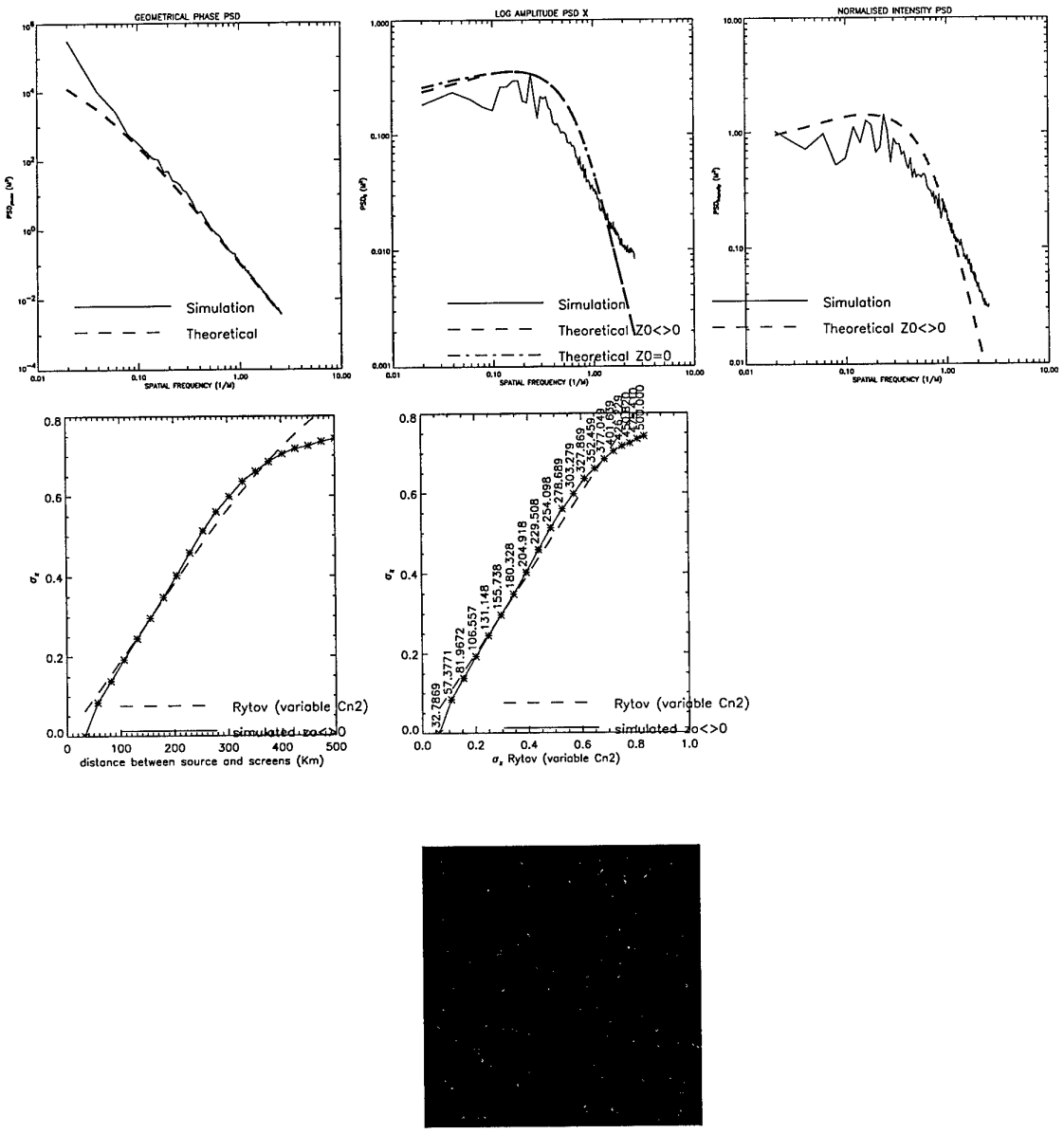

Figure 12 - Result of the numerical experiment (h_{source} = 10 km, λ = 1.06 μm)

Upper left	:	*PSD of φ (phase of the EMF complex amplitude)*
Upper middle	:	*PSD of χ (log-amplitude of the EMF complex amplitude)*
Upper right	:	*PSD of I (square modulus of the EMF complex amplitude)*
Middle left	:	*Variance of χ as function of the propagation distance*
Middle right	:	*Variance of χ as function of the theoretical variance of χ (Rytov approximation)*
Bottom	:	*Example of intensity distribution in the receiver plane*

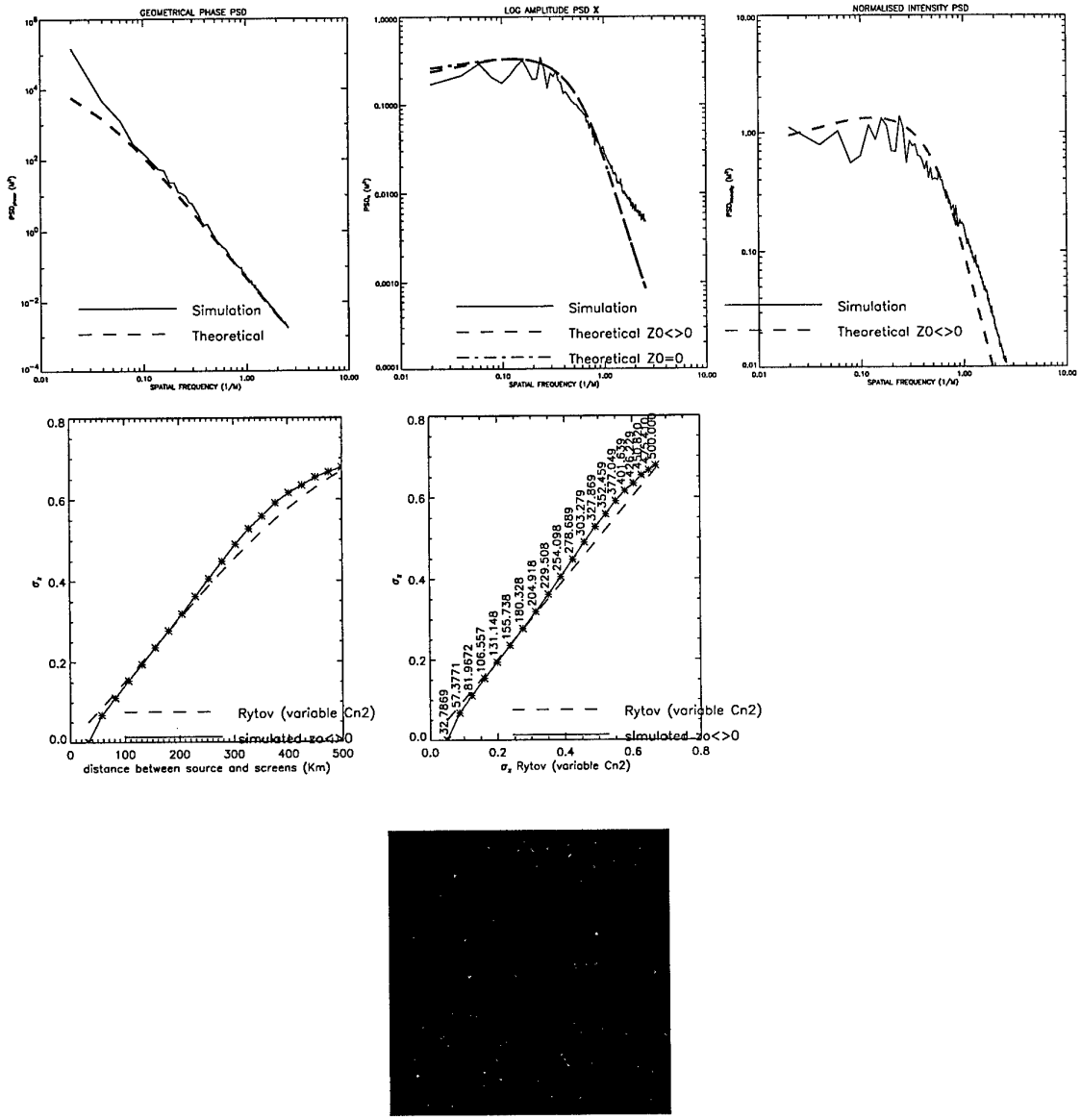

Figure 13 - Result of the numerical experiment (h_{source} = 10 km, $\lambda = 1.55\ \mu m$).

Upper left	:	*PSD of φ (phase of the EMF complex amplitude)*
Upper middle	:	*PSD of χ (log-amplitude of the EMF complex amplitude)*
Upper right	:	*PSD of I (square modulus of the EMF complex amplitude)*
Middle left	:	*Variance of χ as function of the propagation distance*
Middle right	:	*Variance of χ as function of the theoretical variance of χ (Rytov approximation)*
Bottom	:	*Example of intensity distribution in the receiver plane*

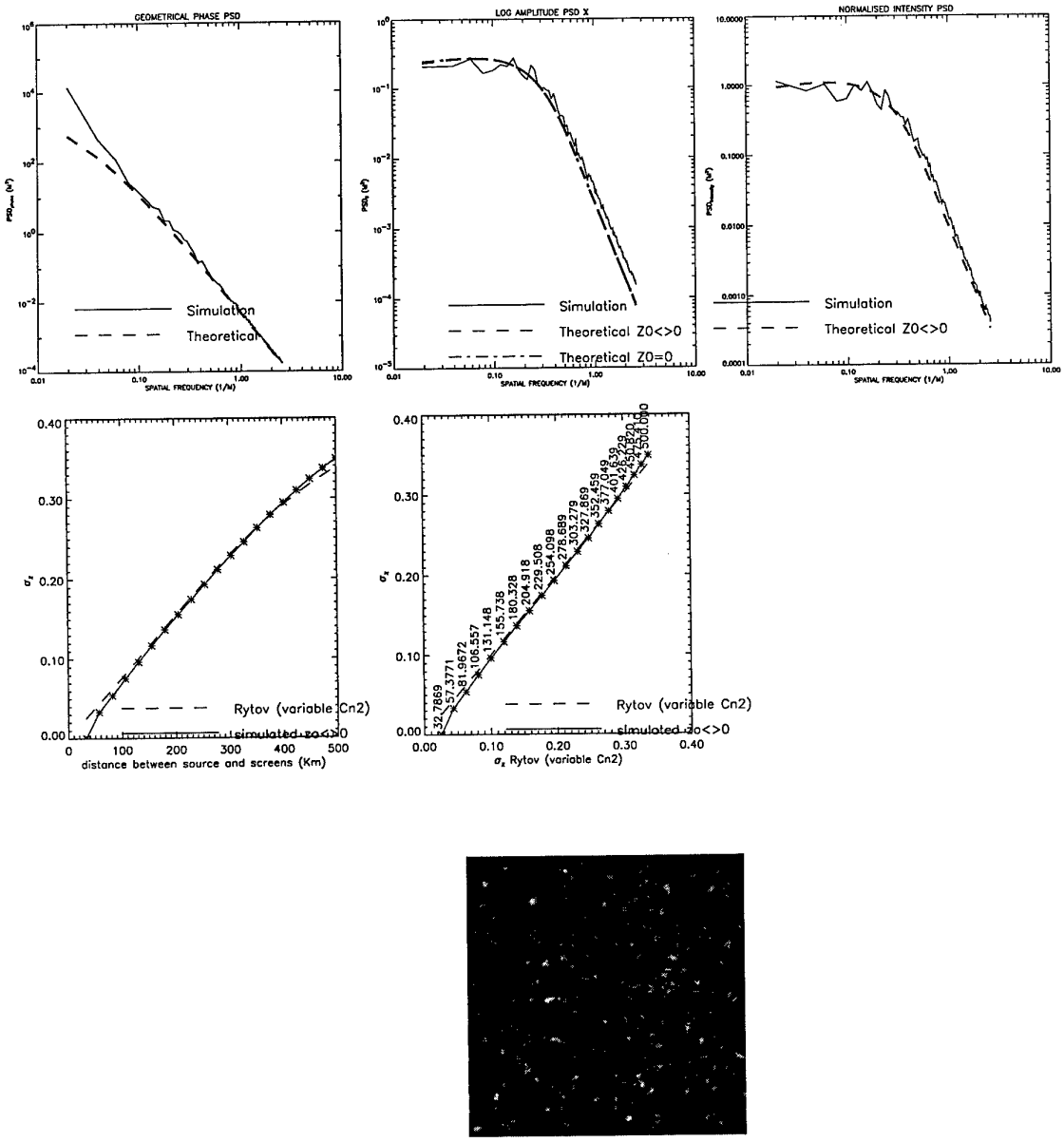

Figure 14 - Result of the numerical experiment (h_{source} = 10 km, λ = 5.0 μm).

Upper left	:	*PSD of φ (phase of the EMF complex amplitude)*
Upper middle	:	*PSD of χ (log-amplitude of the EMF complex amplitude)*
Upper right	:	*PSD of I (square modulus of the EMF complex amplitude)*
Middle left	:	*Variance of χ as function of the propagation distance*
Middle righ	:	*Variance of χ as function of the theoretical variance of χ (Rytov approximation)*
Bottom	:	*Example of intensity distribution in the receiver plane*

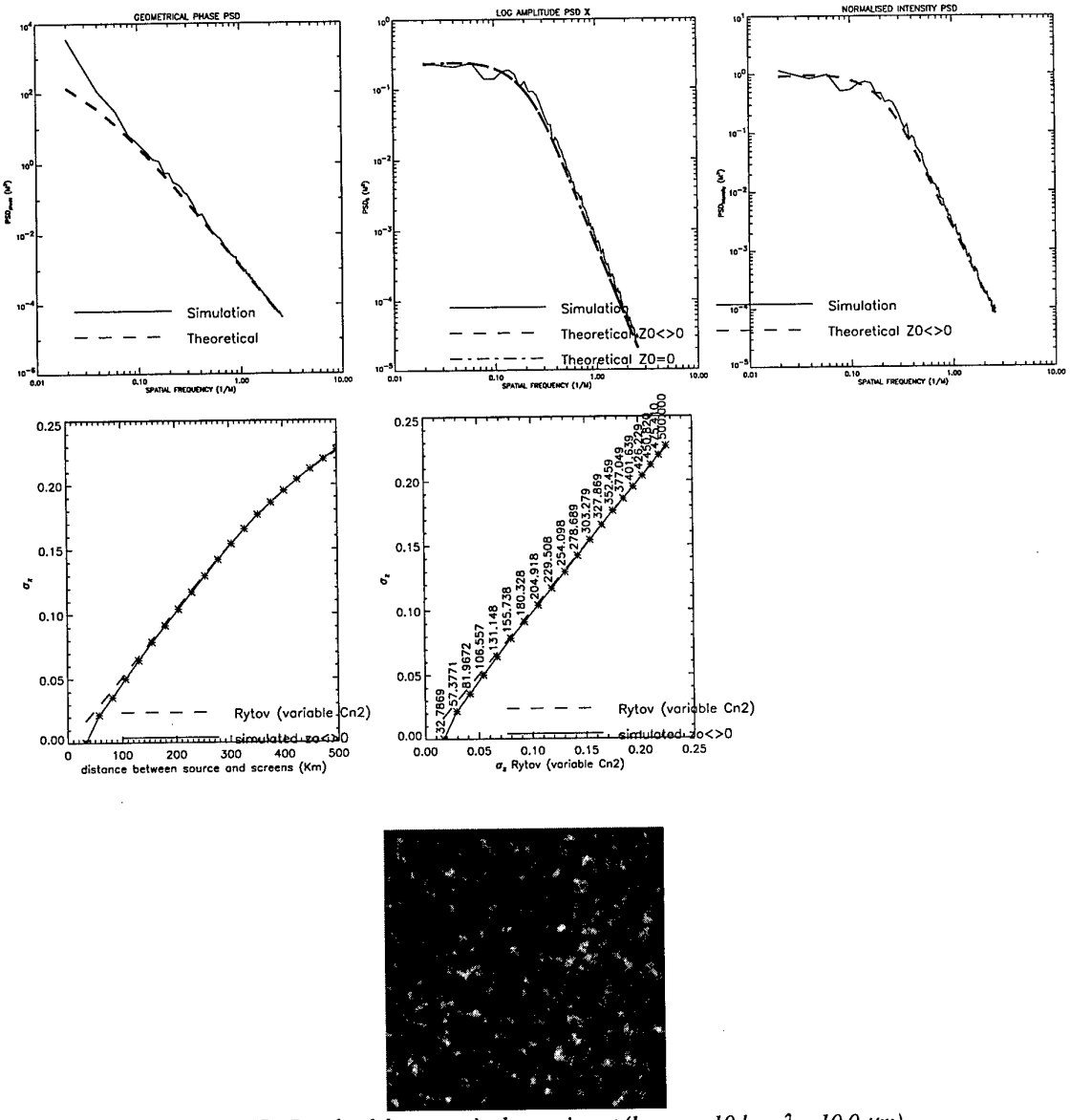

Figure 15 - Result of the numerical experiment (h_{source} = 10 km, $\lambda = 10.0\ \mu m$).

Upper left	:	*PSD of φ (phase of the EMF complex amplitude)*
Upper middle	:	*PSD of χ (log-amplitude of the EMF complex amplitude)*
Upper right	:	*PSD of I (square modulus of the EMF complex amplitude)*
Middle left	:	*Variance of χ as function of the propagation distance*
Middle right	:	*Variance of χ as function of the theoretical variance of χ (Rytov approximation)*
Bottom	:	*Example of intensity distribution in the receiver plane*

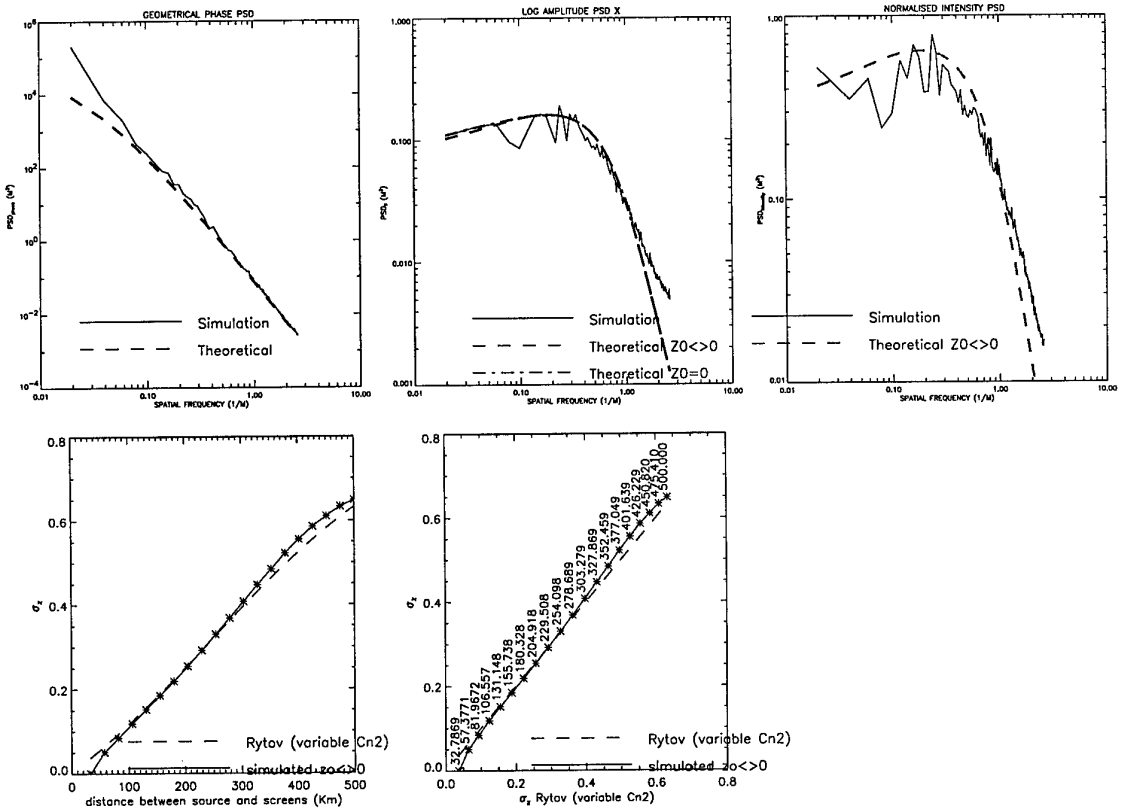

Figure 16 - Result of the numerical experiment (h_{source} = 15 km, $\lambda = 1.06$ µm).

Upper left	:	*PSD of φ (phase of the EMF complex amplitude)*
Upper middle:		*PSD of χ (log-amplitude of the EMF complex amplitude)*
Upper right	:	*PSD of I (square modulus of the EMF complex amplitude)*
Middle left	:	*Variance of χ as function of the propagation distance*
Middle right	:	*Variance of χ as function of the theoretical variance of χ (Rytov approximation)*
Bottom	:	*Example of intensity distribution in the receiver plane*

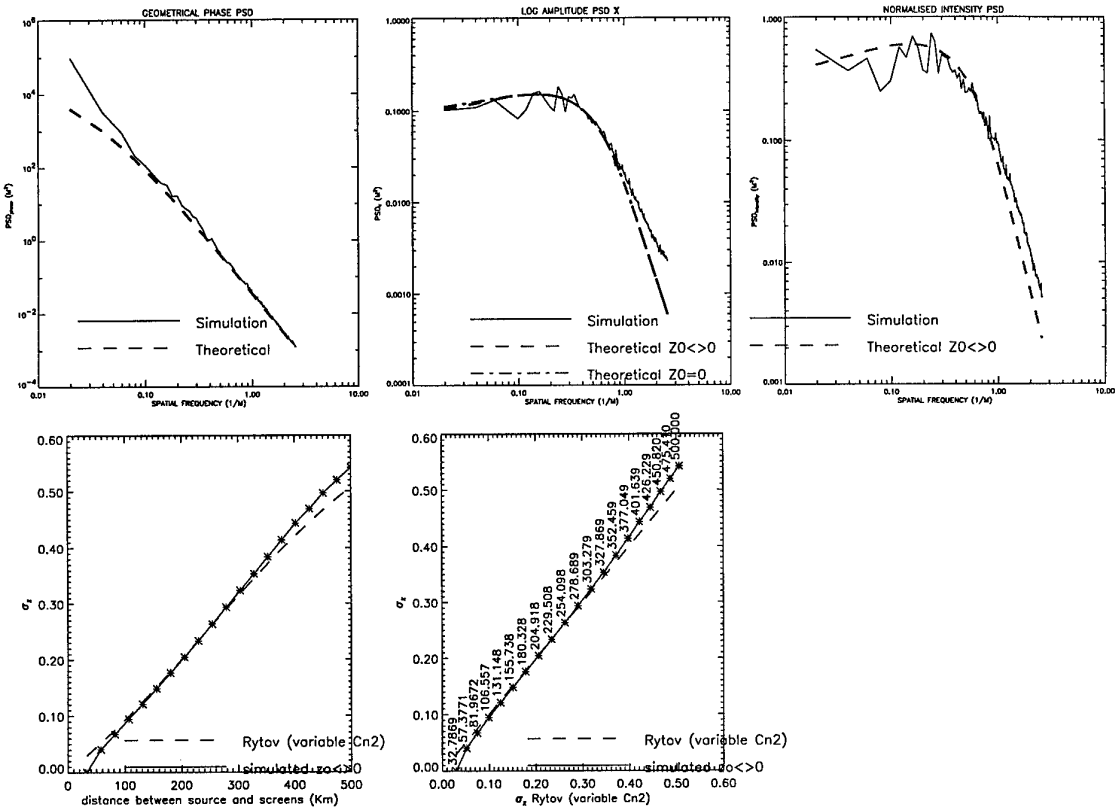

Figure 17 - Result of the numerical experiment (h_{source} = 15 km, $\lambda = 1.55\ \mu m$).

Upper left	*:*	*PSD of φ (phase of the EMF complex amplitude)*
Upper middle	*:*	*PSD of χ (log-amplitude of the EMF complex amplitude)*
Upper right	*:*	*PSD of I (square modulus of the EMF complex amplitude)*
Middle left	*:*	*Variance of χ as function of the propagation distance*
Middle righ t:		*Variance of χ as function of the theoretical variance of χ (Rytov approximation)*
Bottom	*:*	*Example of intensity distribution in the receiver plane*

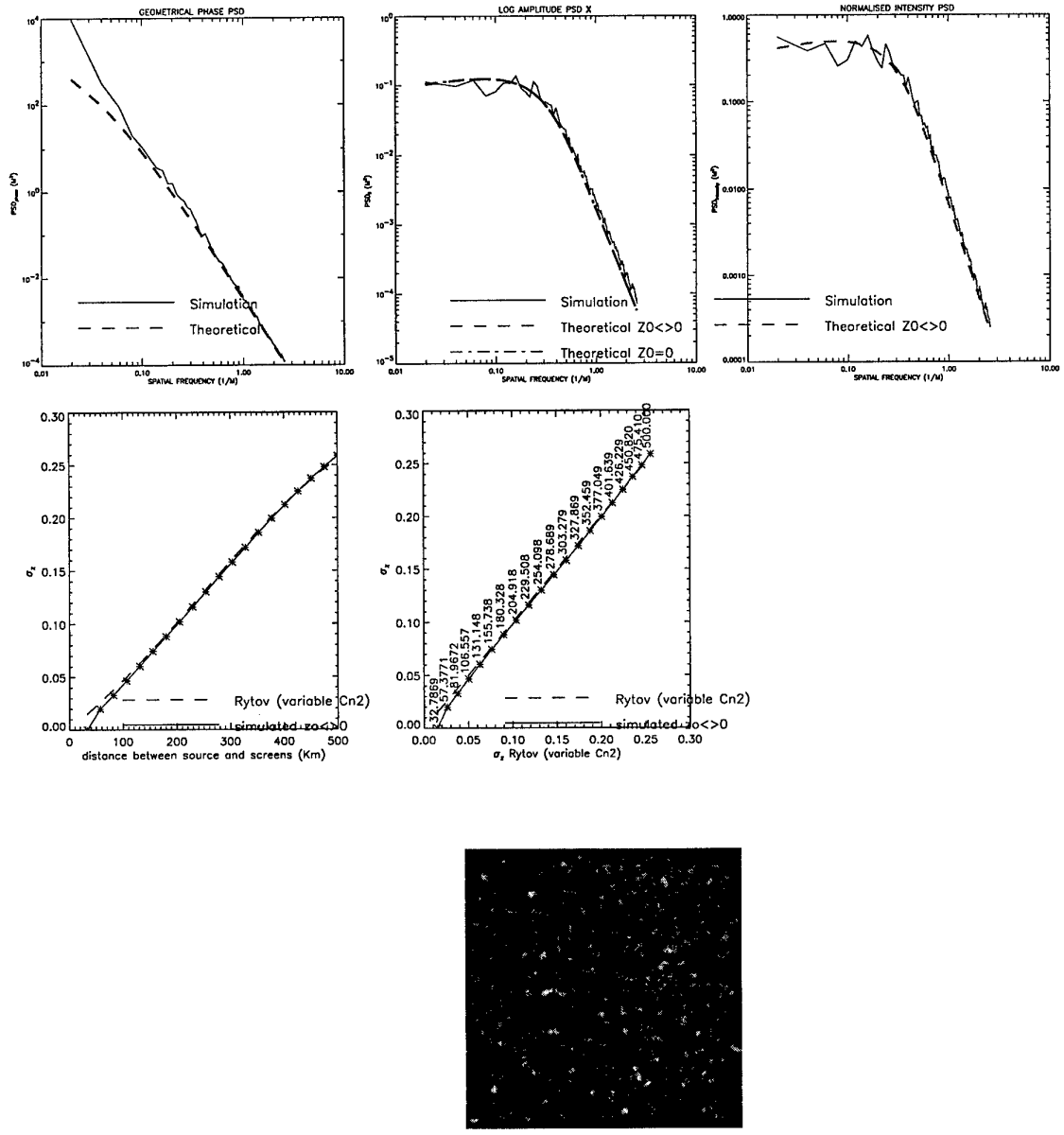

Figure 18 - Result of the numerical experiment (h_{source} = 15 km, λ = 5.0 µm).

Upper left : *PSD of φ (phase of the EMF complex amplitude)*
Upper middle : *PSD of χ (log-amplitude of the EMF complex amplitude)*
Upper right : *PSD of I (square modulus of the EMF complex amplitude)*
Middle left : *Variance of χ as function of the propagation distance*
Middle right : *Variance of χ as function of the theoretical variance of χ (Rytov approximation)*
Bottom : *Example of intensity distribution in the receiver plane*

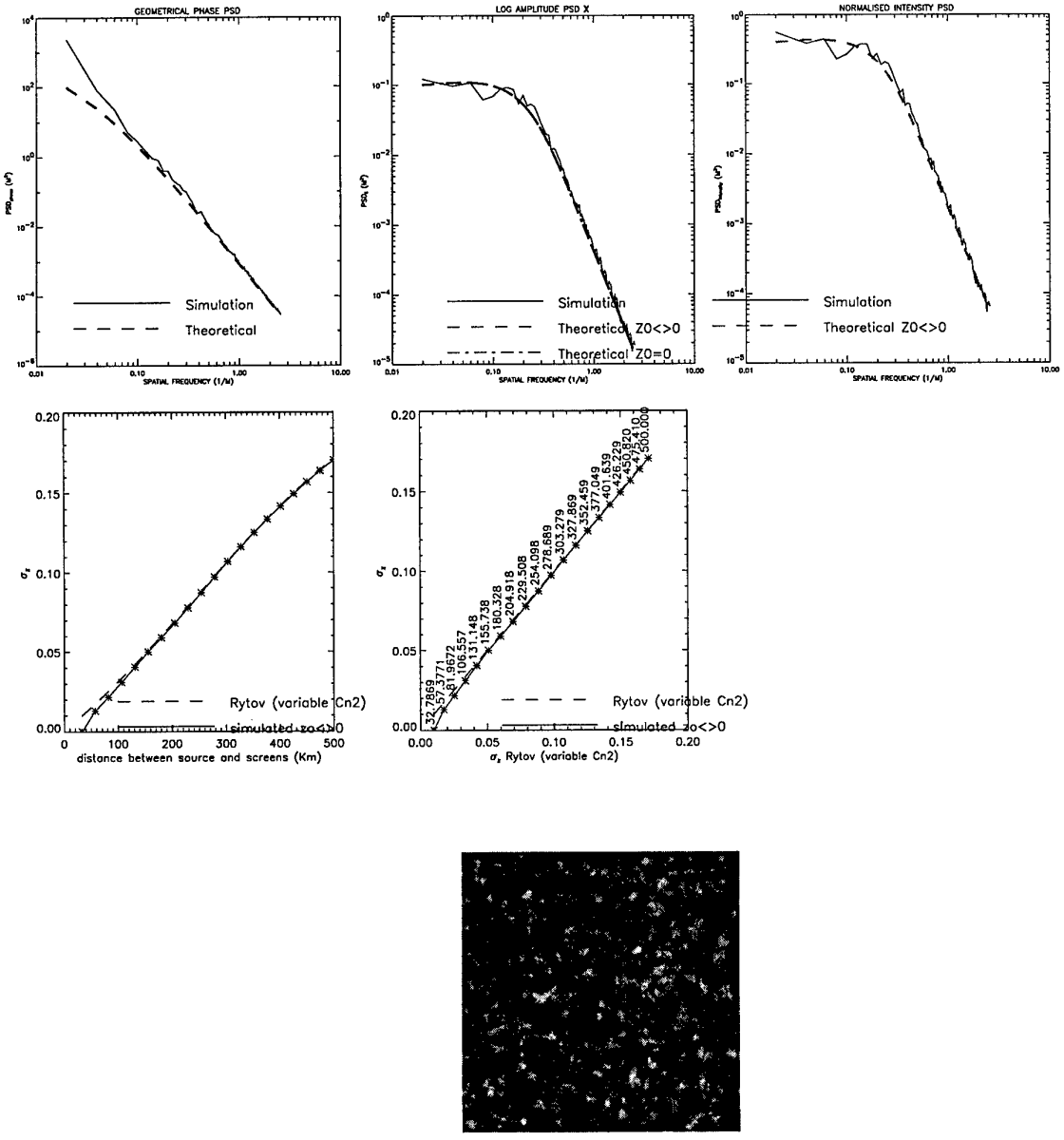

Figure 19: Result of the numerical experiment (h_{source} = 15 km, $\lambda = 10.0\ \mu m$).

Upper left : *PSD of φ (phase of the EMF complex amplitude)*
Upper middle : *PSD of χ (log-amplitude of the EMF complex amplitude)*
Upper right : *PSD of I (square modulus of the EMF complex amplitude)*
Middle left : *Variance of χ as function of the propagation distance*
Middle right : *Variance of χ as function of the theoretical variance of χ (Rytov approximation)*
Bottom : *Example of intensity distribution in the receiver plane*

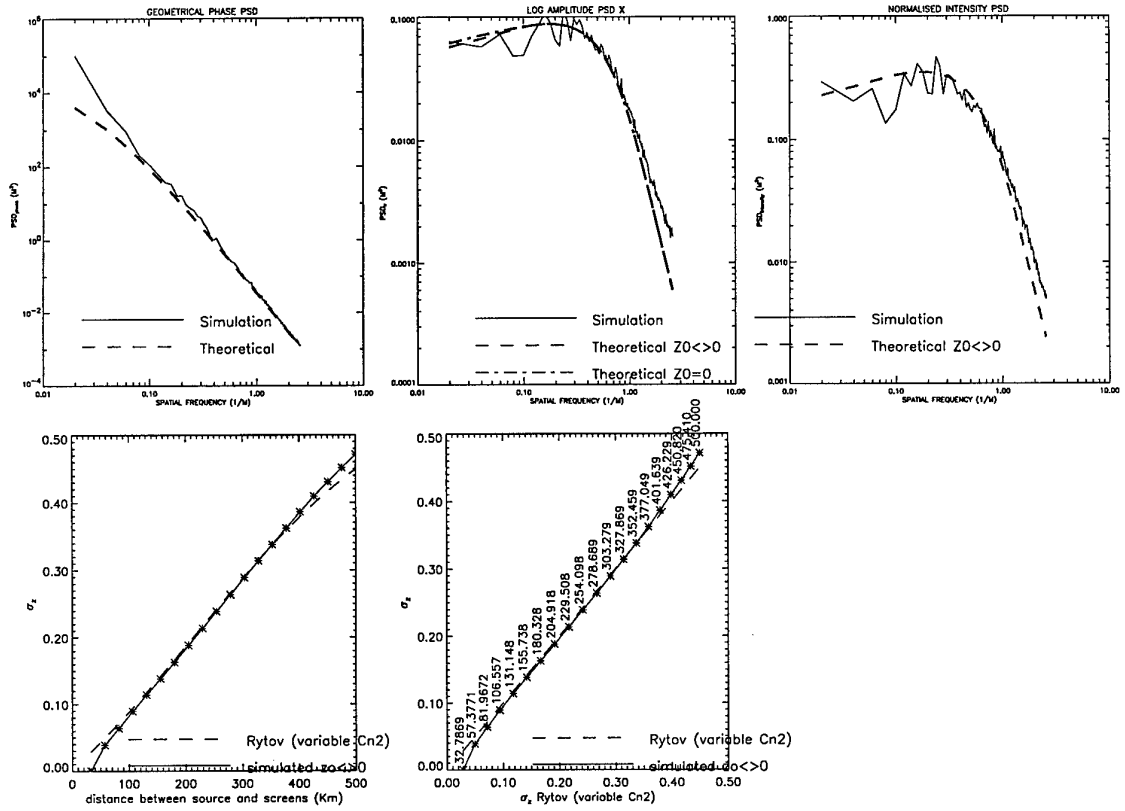

Figure 20 - Result of the numerical experiment (h_{source} = 20 km, $\lambda = 1.06\ \mu m$).

Upper left : PSD of φ (phase of the EMF complex amplitude)
Upper middle : PSD of χ (log-amplitude of the EMF complex amplitude)
Upper right : PSD of I (square modulus of the EMF complex amplitude)
Middle left : Variance of χ as function of the propagation distance
Middle right : Variance of χ as function of the theoretical variance of χ (Rytov approximation)
Bottom : Example of intensity distribution in the receiver plane

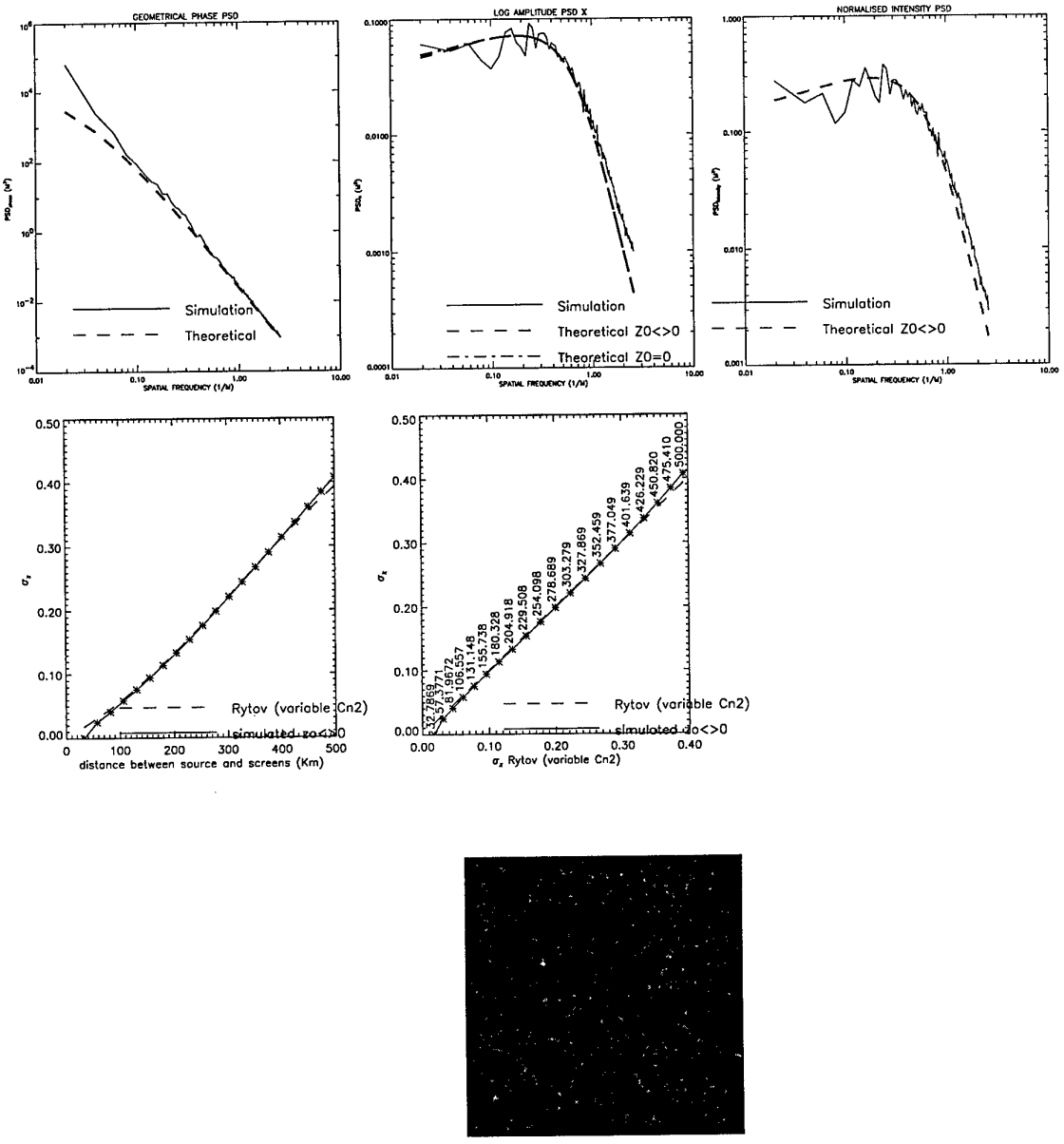

Figure 21 - Result of the numerical experiment (h_{source} = 15 km, $\lambda = 1.55$ µm).

Upper left : PSD of φ (phase of the EMF complex amplitude)
Upper middle : PSD of χ (log-amplitude of the EMF complex amplitude)
Upper right : PSD of I (square modulus of the EMF complex amplitude)
Middle lef t: Variance of χ as function of the propagation distance
Middle right : Variance of χ as function of the theoretical variance of χ (Rytov approximation)
Bottom : Example of intensity distribution in the receiver plane

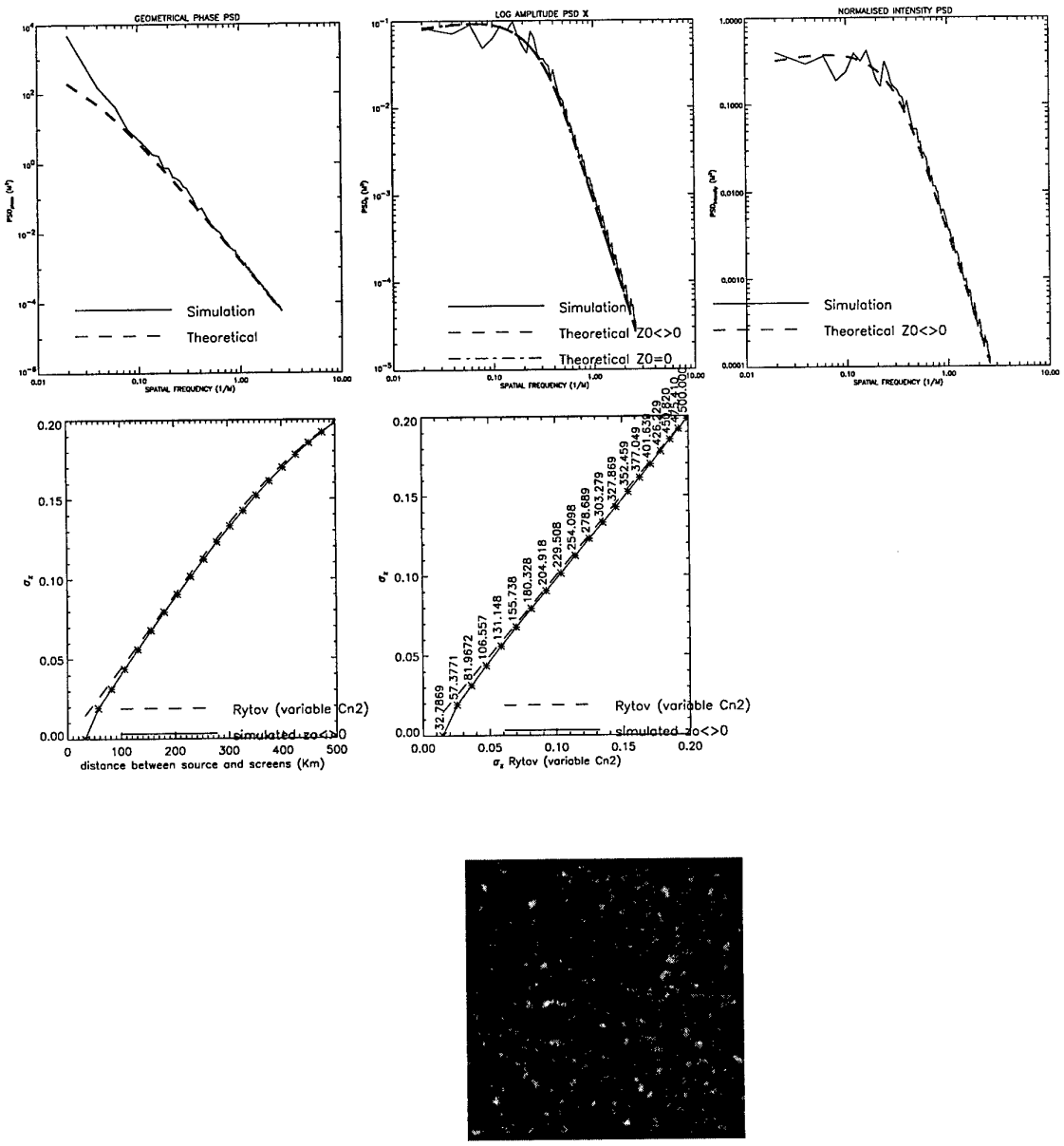

Figure 22: Result of the numerical experiment (h_{source} = 15 km, $\lambda = 5.0$ µm).

Upper left : PSD of φ (phase of the EMF complex amplitude)
Upper middle : PSD of χ (log-amplitude of the EMF complex amplitude)
Upper right : PSD of I (square modulus of the EMF complex amplitude)
Middle left : Variance of χ as function of the propagation distance
Middle right : Variance of χ as function of the theoretical variance of χ (Rytov approximation)
Bottom : Example of intensity distribution in the receiver plane

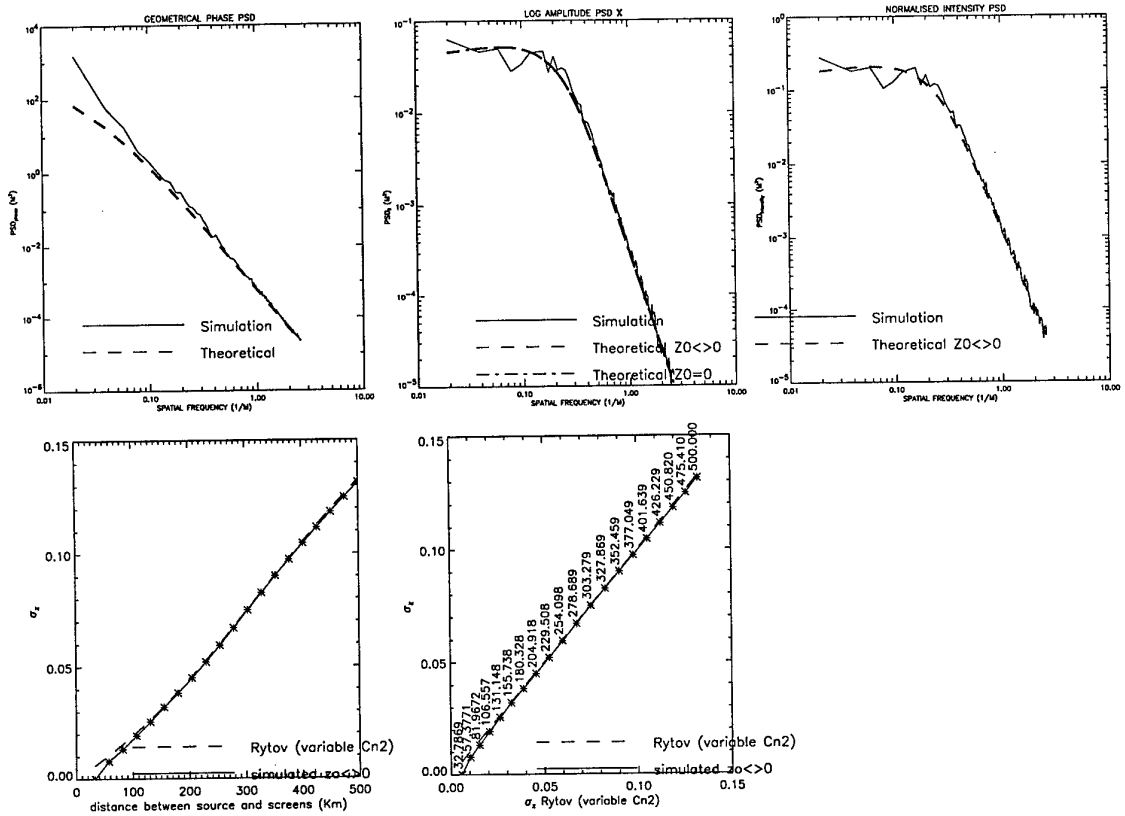

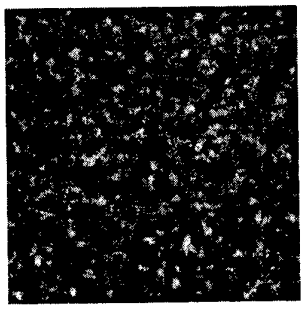

Figure 23 - Result of the numerical experiment (h_{source} = 15 km, $\lambda = 10.0\ \mu m$).

Upper left : *PSD of φ (phase of the EMF complex amplitude)*
Upper middle : *PSD of χ (log-amplitude of the EMF complex amplitude)*
Upper right : *PSD of I (square modulus of the EMF complex amplitude)*
Middle left : *Variance of χ as function of the propagation distance*
Middle right : *Variance of χ as function of the theoretical variance of χ (Rytov approximation)*
Bottom : *Example of intensity distribution in the receiver plane*

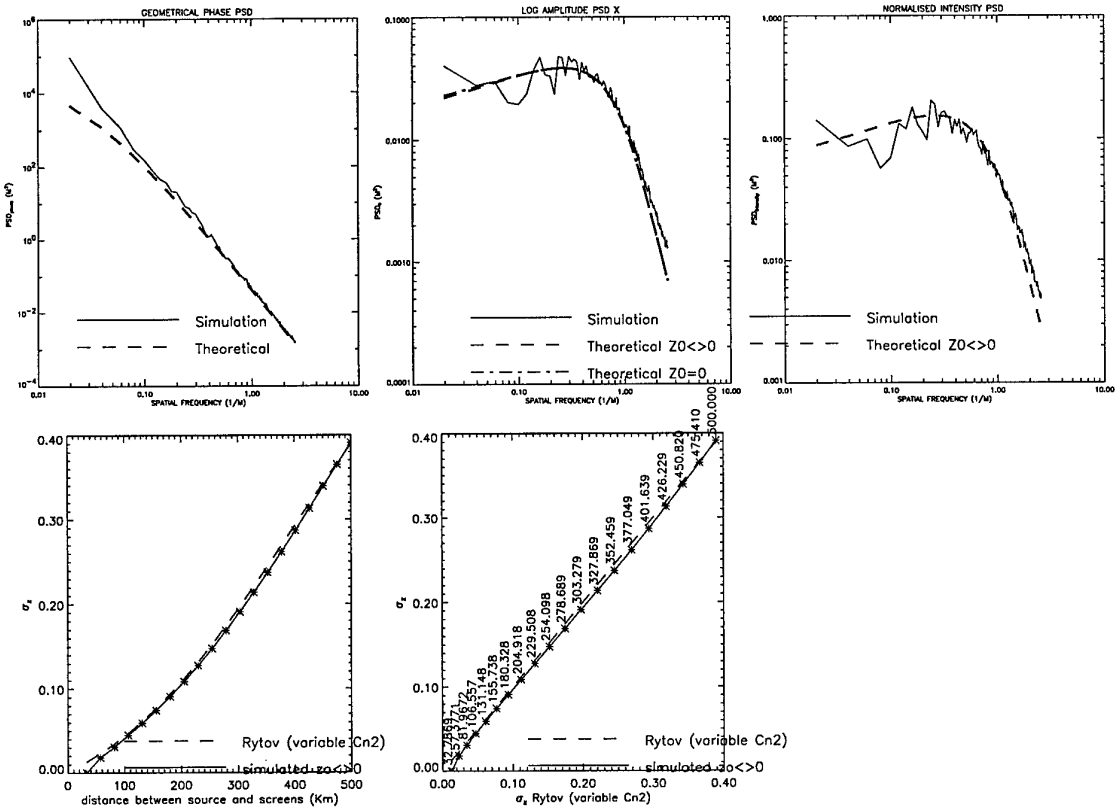

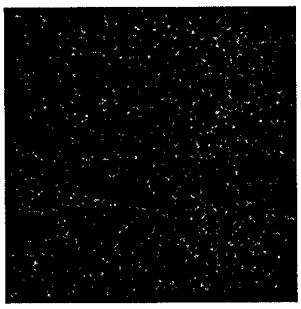

Figure 24 - Result of the numerical experiment (h_{source} = 25 km, $\lambda = 1.06\ \mu m$).

Upper left : PSD of φ (phase of the EMF complex amplitude)
Upper middle: PSD of χ (log-amplitude of the EMF complex amplitude)
Upper right : PSD of I (square modulus of the EMF complex amplitude)
Middle left : Variance of χ as function of the propagation distance
Middle right : Variance of χ as function of the theoretical variance of χ (Rytov approximation)
Bottom : Example of intensity distribution in the receiver plane

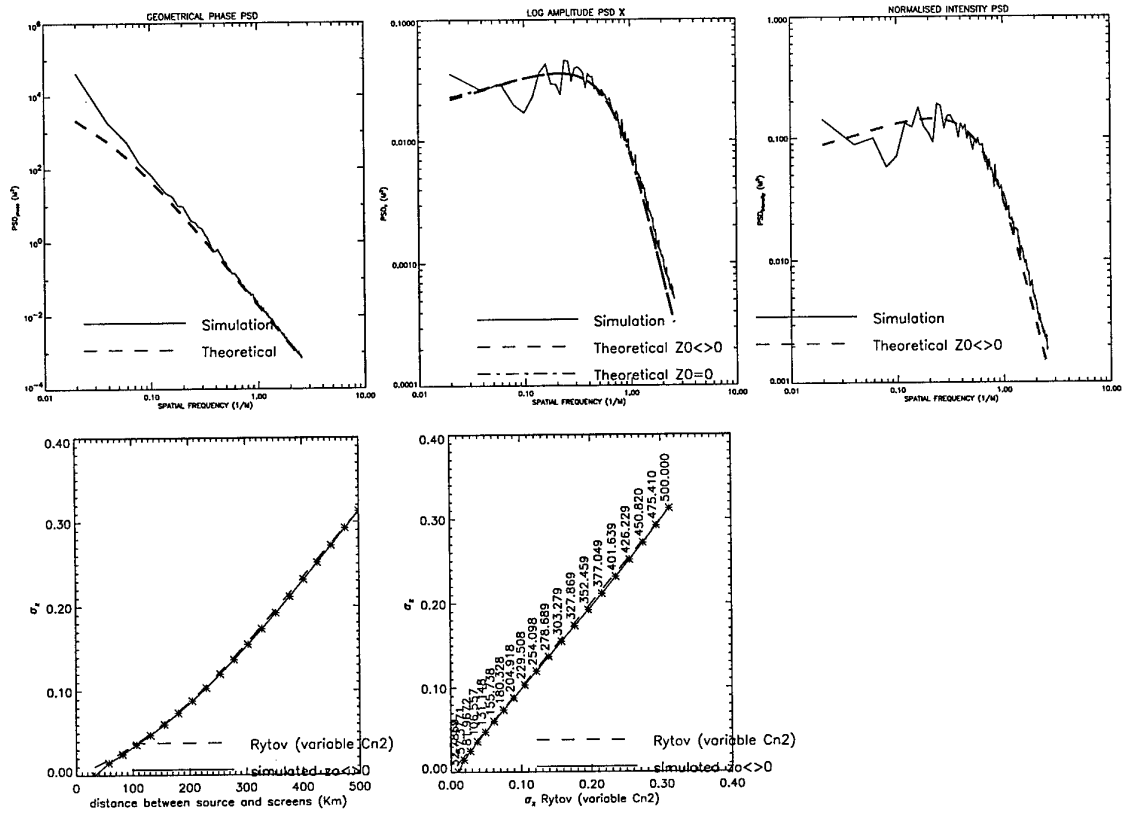

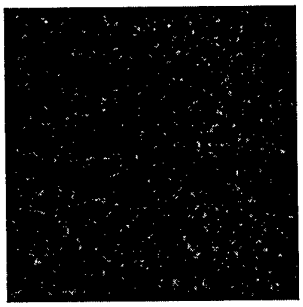

Figure 25 - Result of the numerical experiment (h_{source} = 25 km, $\lambda = 1.55\ \mu m$).

Upper lef t: PSD of φ (phase of the EMF complex amplitude)
Upper middle: PSD of χ (log-amplitude of the EMF complex amplitude)
Upper right : PSD of I (square modulus of the EMF complex amplitude)
Middle left : Variance of χ as function of the propagation distance
Middle right : Variance of χ as function of the theoretical variance of χ (Rytov approximation)
Bottom : Example of intensity distribution in the receiver plane

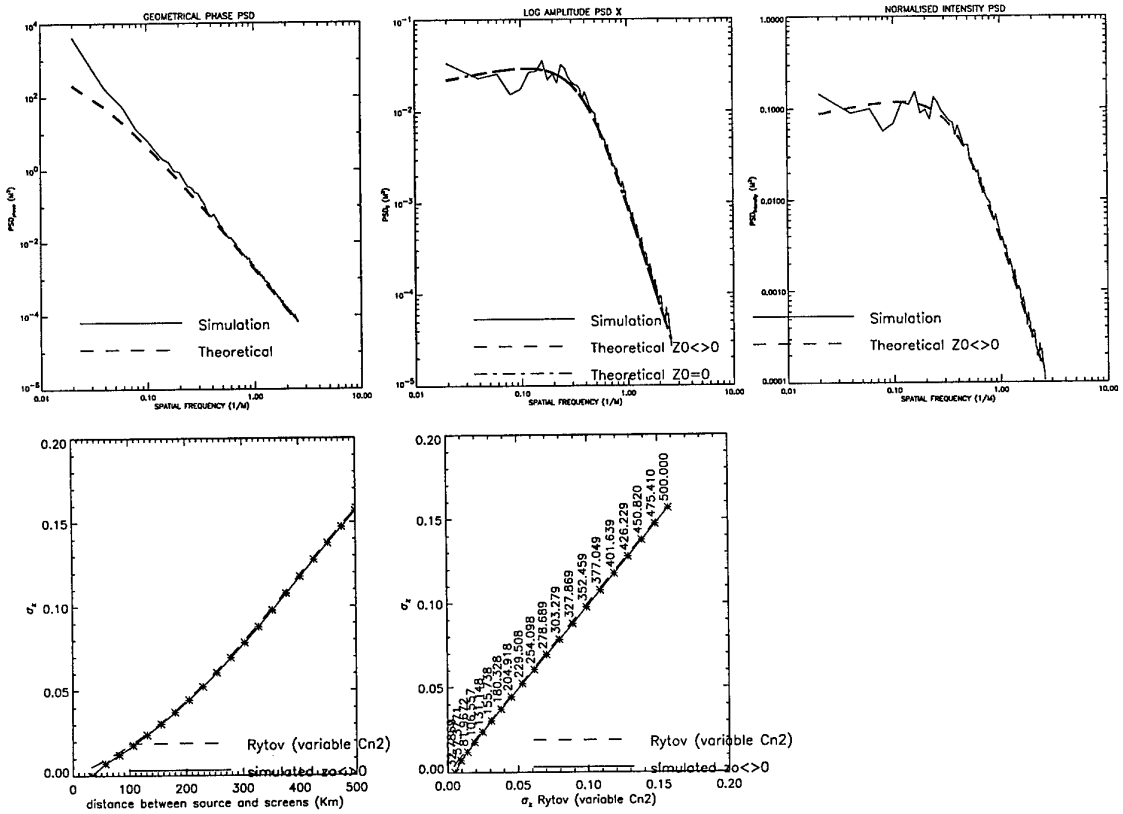

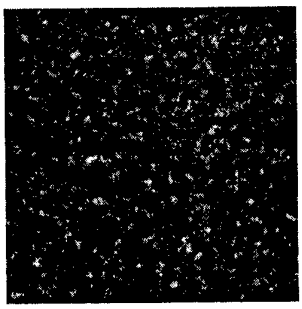

Figure 26 - Result of the numerical experiment (h_{source} = 25 km, λ = 5.0 μm).

Upper left : PSD of φ (phase of the EMF complex amplitude)
Upper middle : PSD of χ (log-amplitude of the EMF complex amplitude)
Upper right : PSD of I (square modulus of the EMF complex amplitude)
Middle left : Variance of χ as function of the propagation distance
Middle right : Variance of χ as function of the theoretical variance of χ (Rytov approximation)
Bottom : Example of intensity distribution in the receiver plane

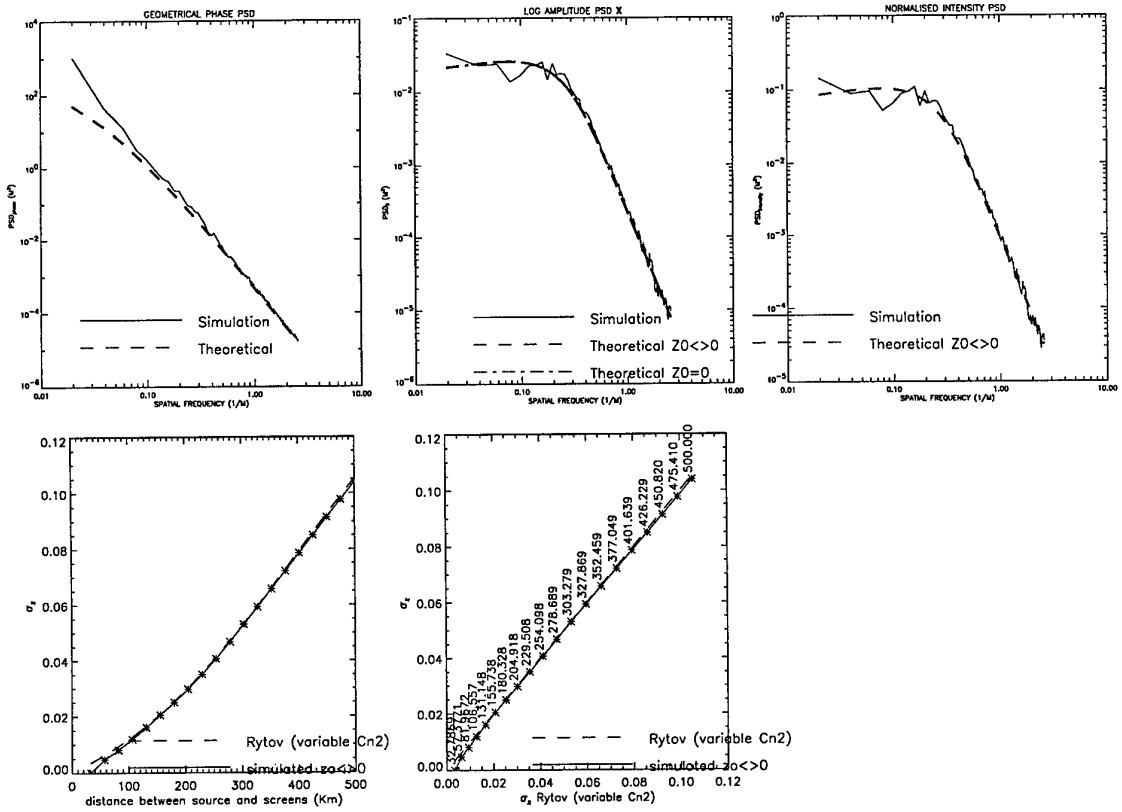

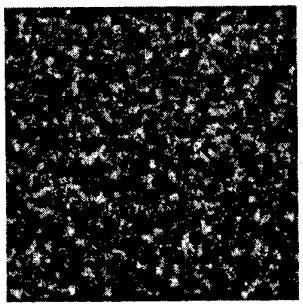

Figure 27 - Result of the numerical experiment (h_{source} = 25 km, $\lambda = 10.0\ \mu m$).

Upper left : *PSD of φ (phase of the EMF complex amplitude)*
Upper middle: *PSD of χ (log-amplitude of the EMF complex amplitude)*
Upper right : *PSD of I (square modulus of the EMF complex amplitude)*
Middle left : *Variance of χ as function of the propagation distance*
Middle right : *Variance of χ as function of the theoretical variance of χ (Rytov approximation)*
Bottom : *Example of intensity distribution in the receiver plane*

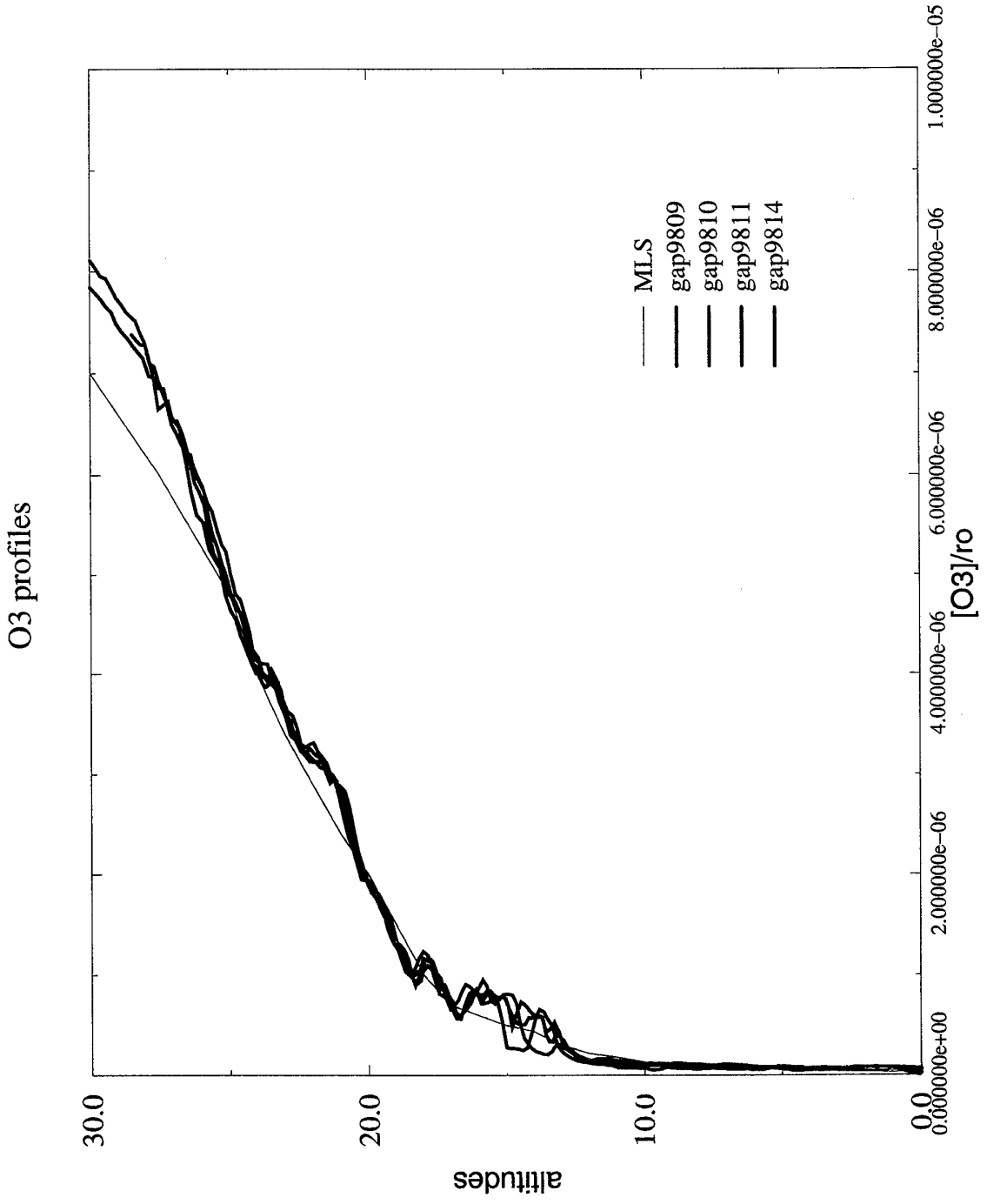
O3 profiles
MLS
gap9809
gap9810
gap9811
gap9814
30.0
20.0
10.0
0.0
altitudes
0.000000e+00
2.000000e-06
4.000000e-06
6.000000e-06
8.000000e-06
1.000000e-05
[O3]/ro

Figure 28.

SANS MENTION
DE PROTECTION

SMP

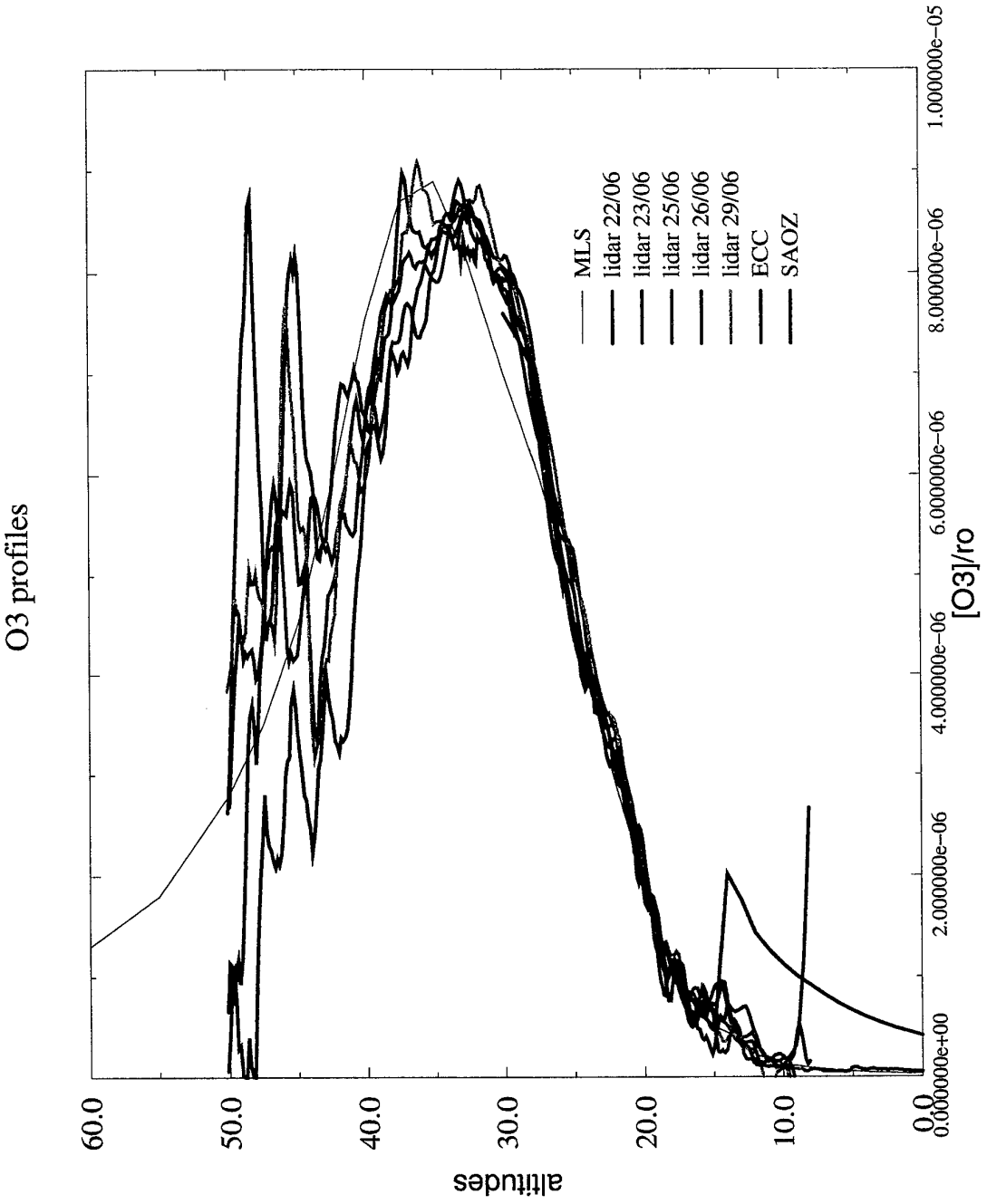

Figure 29.

ONERA

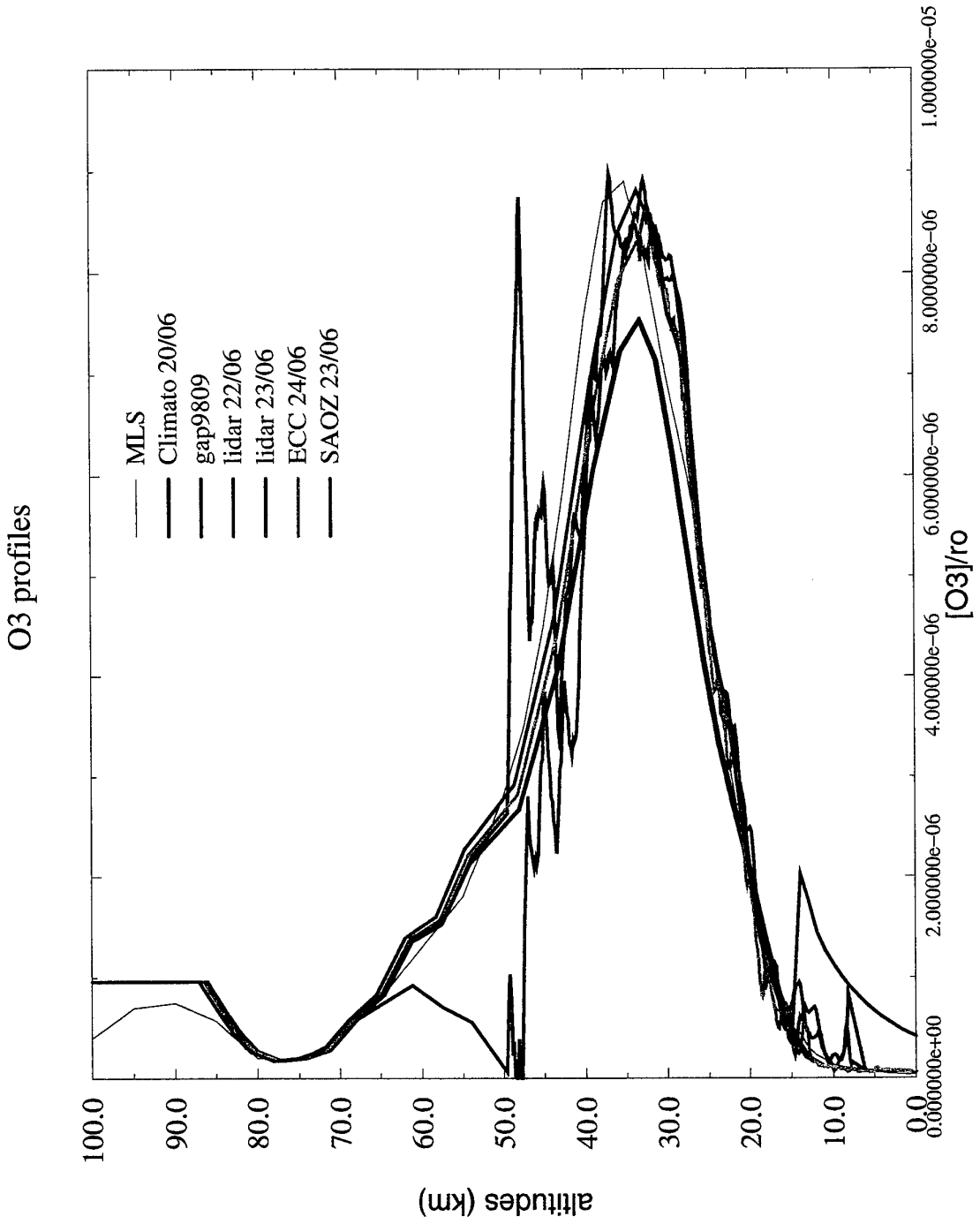
O3 profiles
MLS
Climato 20/06
gap9809
lidar 22/06
lidar 23/06
ECC 24/06
SAOZ 23/06
altitudes (km)
100.0
90.0
80.0
70.0
60.0
50.0
40.0
30.0
20.0
10.0
0.0
0.000000e+00
2.000000e-06
4.000000e-06
6.000000e-06
8.000000e-06
1.000000e-05
[O3]/ro

Figure 30.

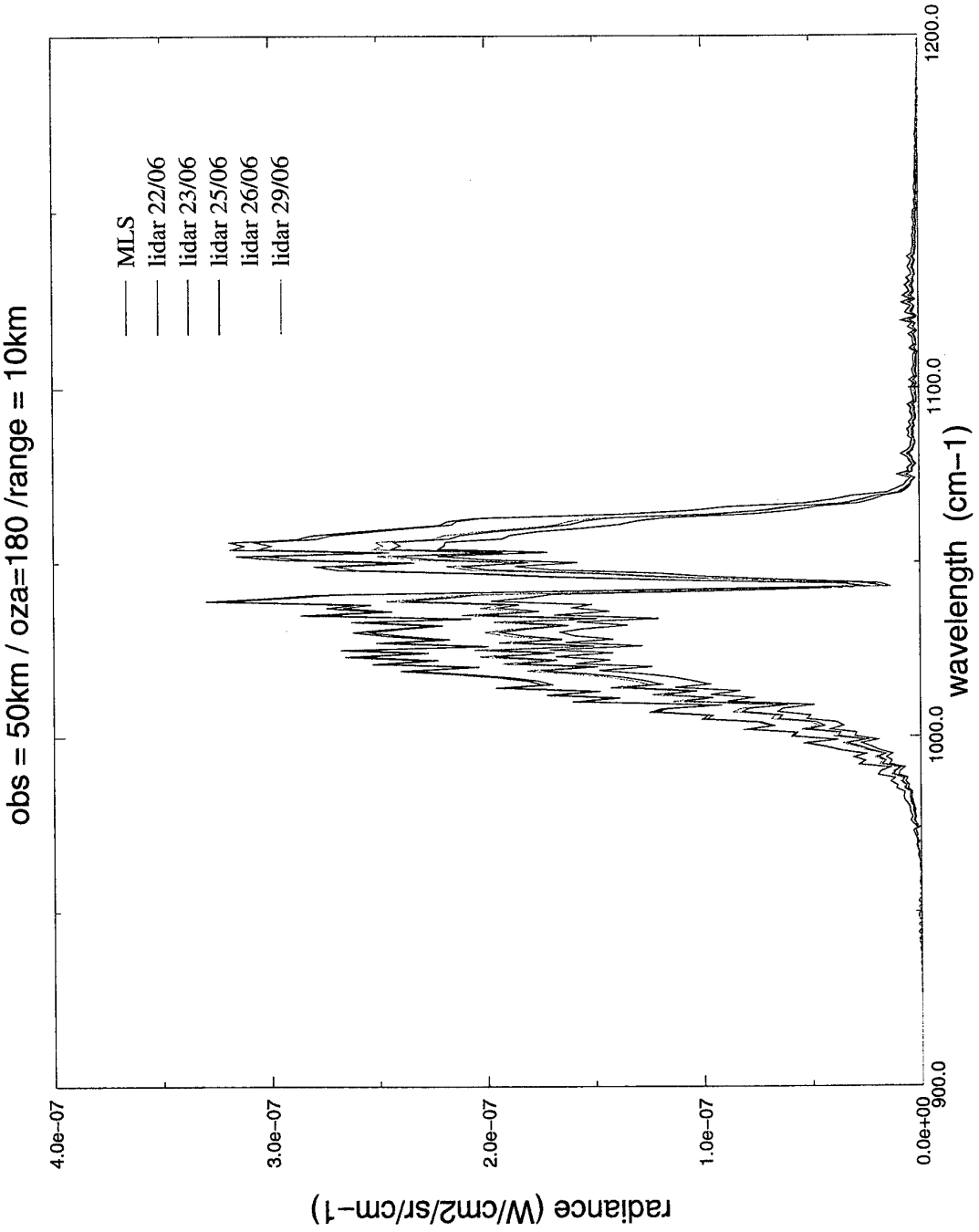

Figure 31.

ONERA

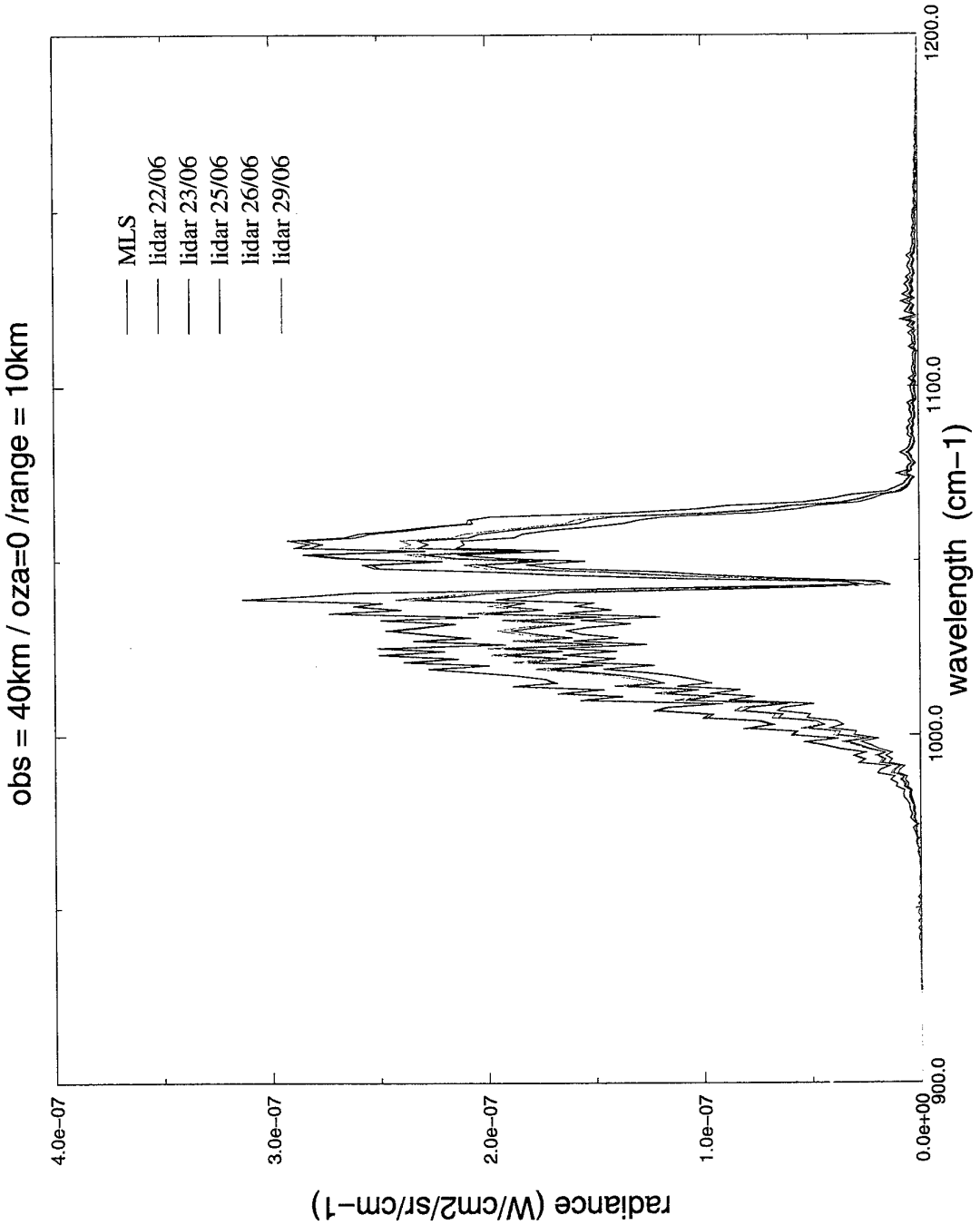
obs = 40km / oza=0 /range = 10km
MLS
lidar 22/06
lidar 23/06
lidar 25/06
lidar 26/06
lidar 29/06
radiance (W/cm2/sr/cm-1)
4.0e-07
3.0e-07
2.0e-07
1.0e-07
0.0e+00
900.0
1000.0
1100.0
1200.0
wavelength (cm-1)

Figure 32.

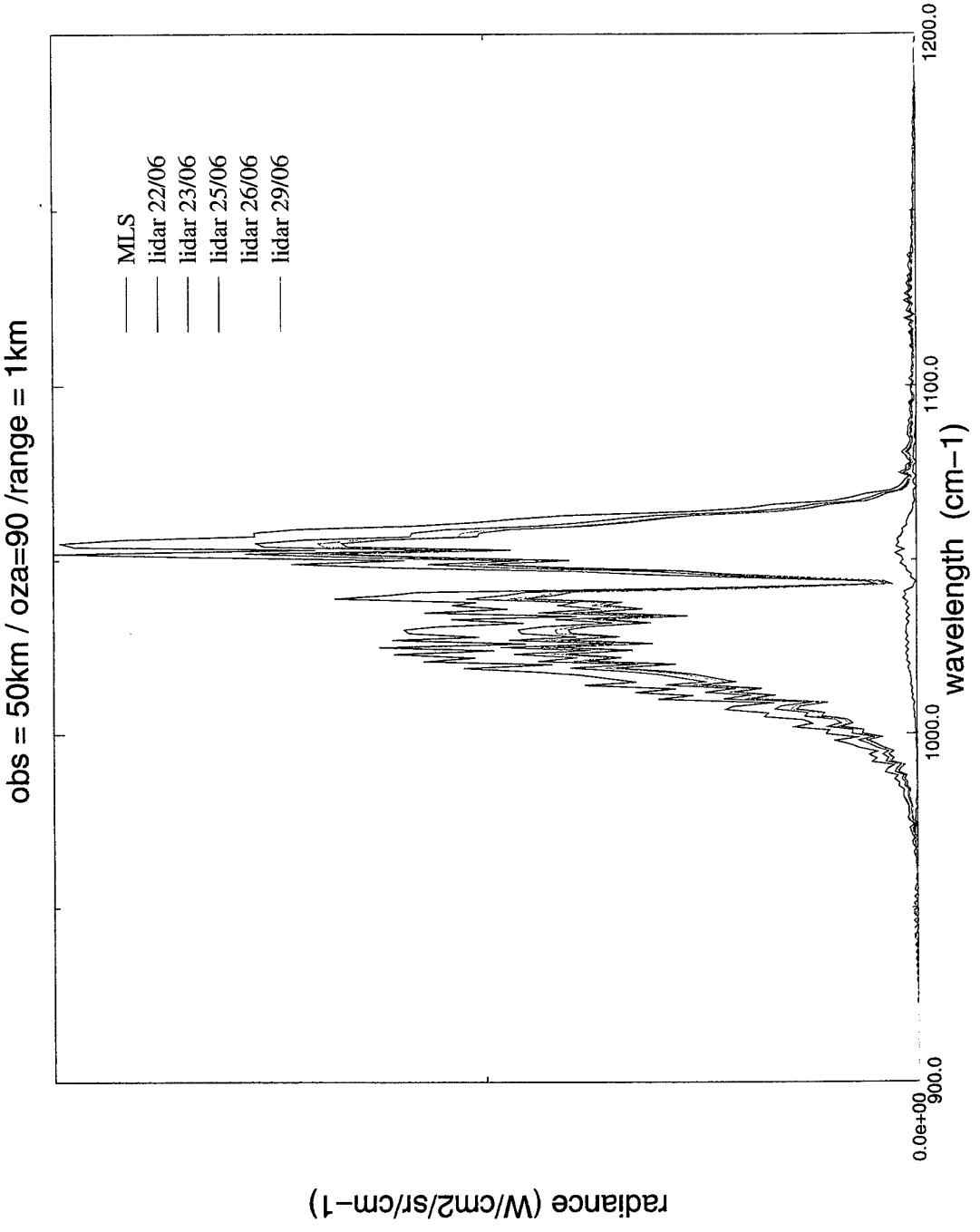
MLS
lidar 22/06
lidar 23/06
lidar 25/06
lidar 26/06
lidar 29/06
obs = 50km / oza=90 /range = 1km
wavelength (cm-1)
radiance (W/cm2/sr/cm-1)
1200.0
1100.0
1000.0
900.0
0.0e+00

Figure 33.

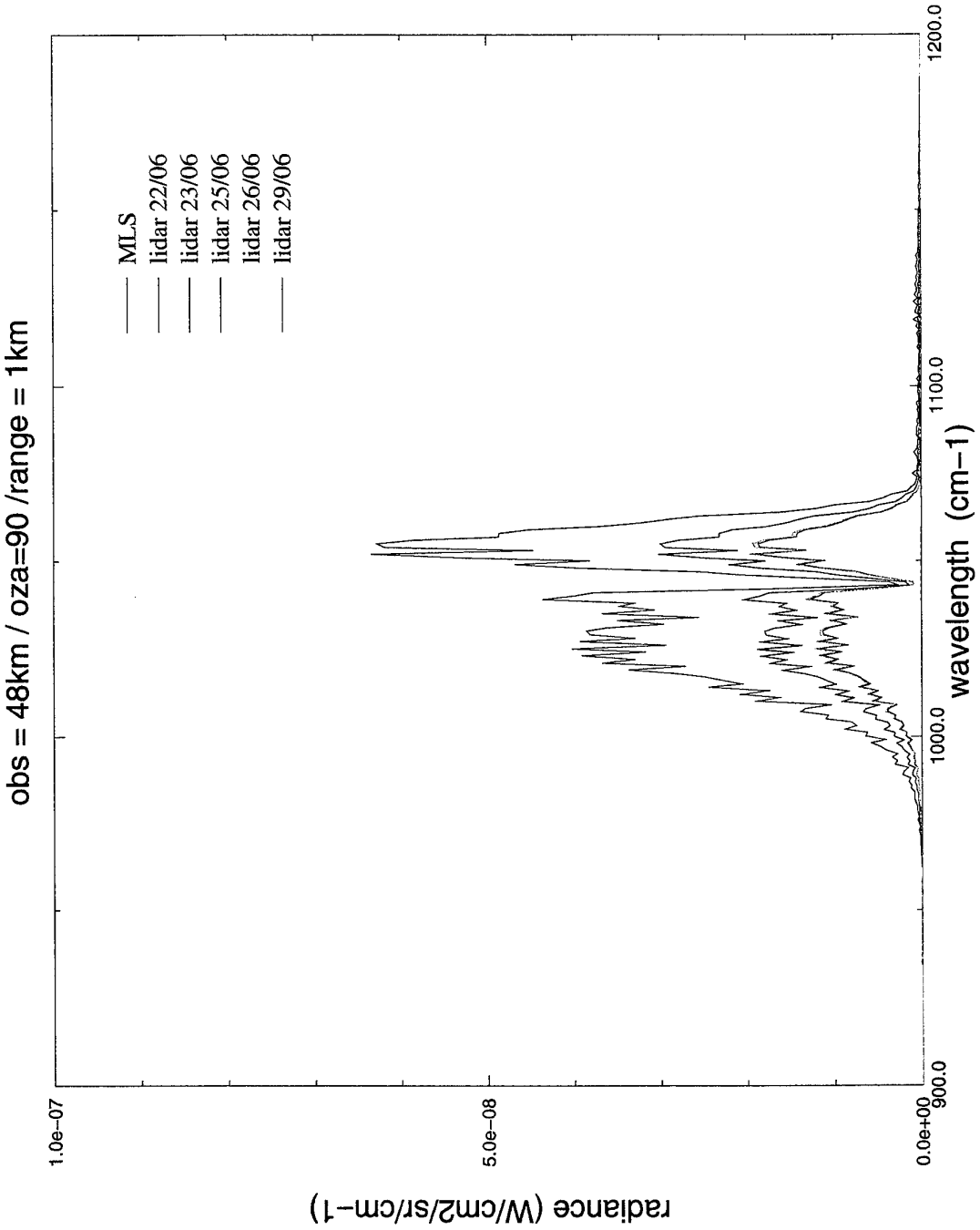

Figure 34.

ONERA

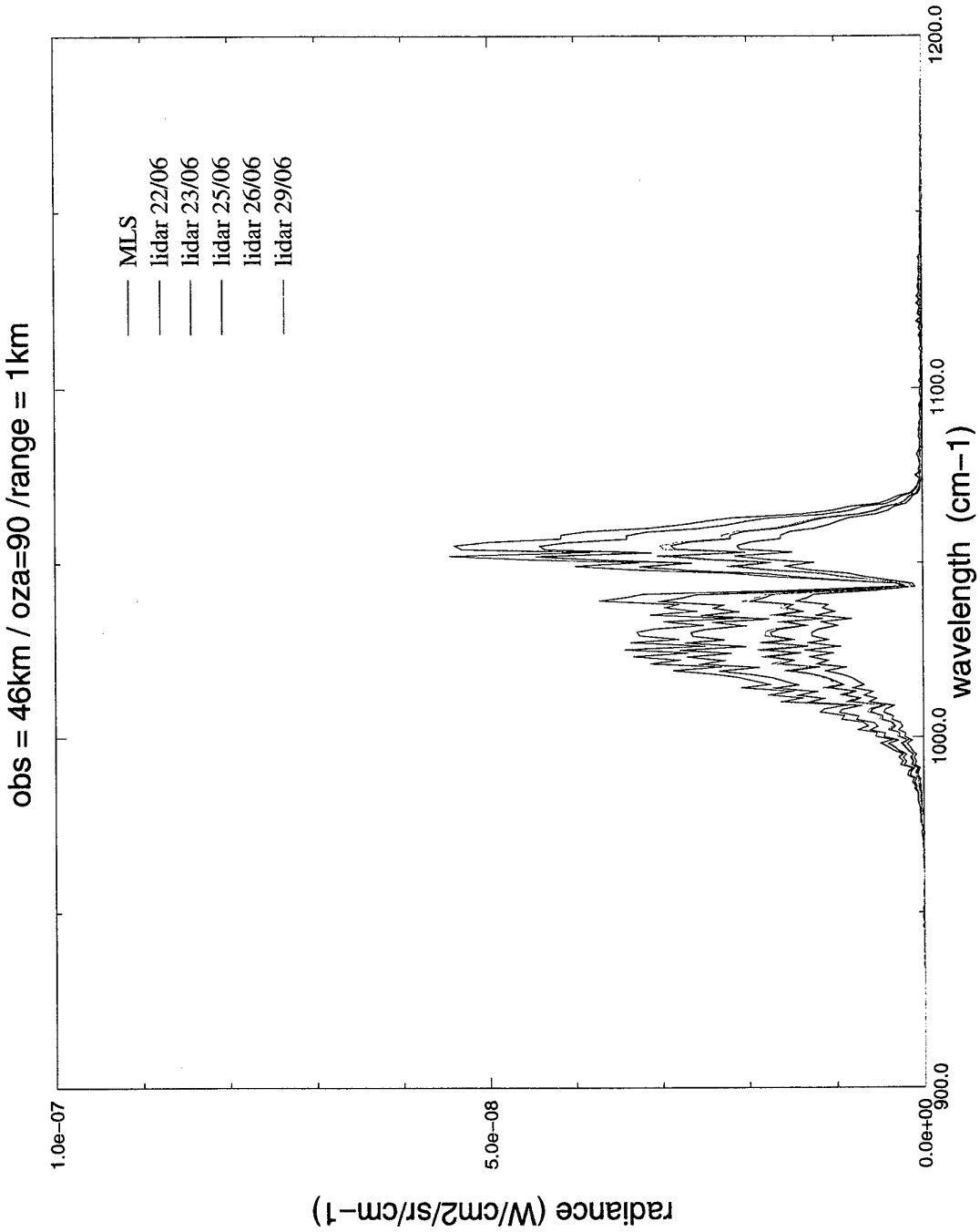

Figure 35.

ONERA

SANS MENTION
DE PROTECTION

SMP

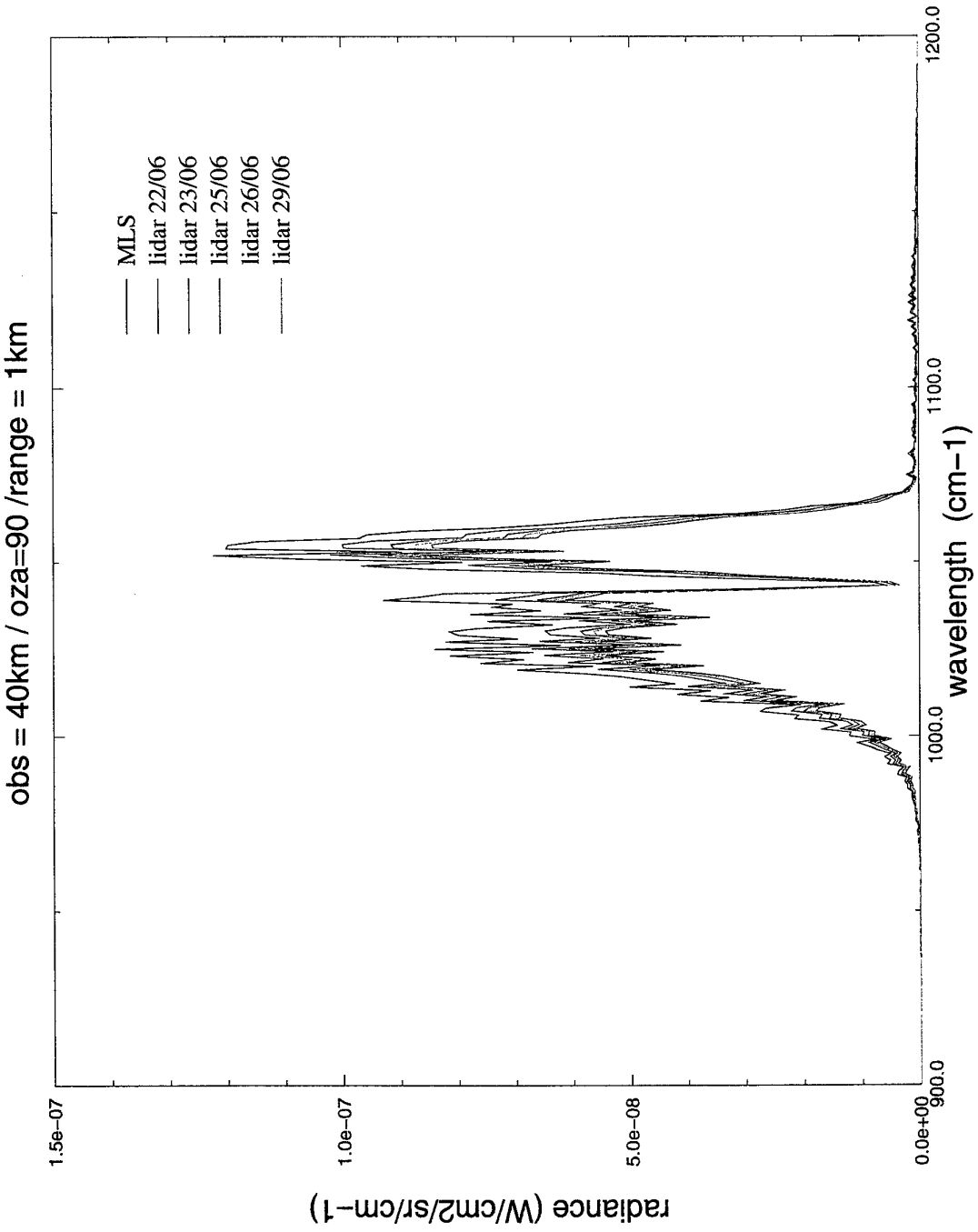

Figure 36.

ONERA

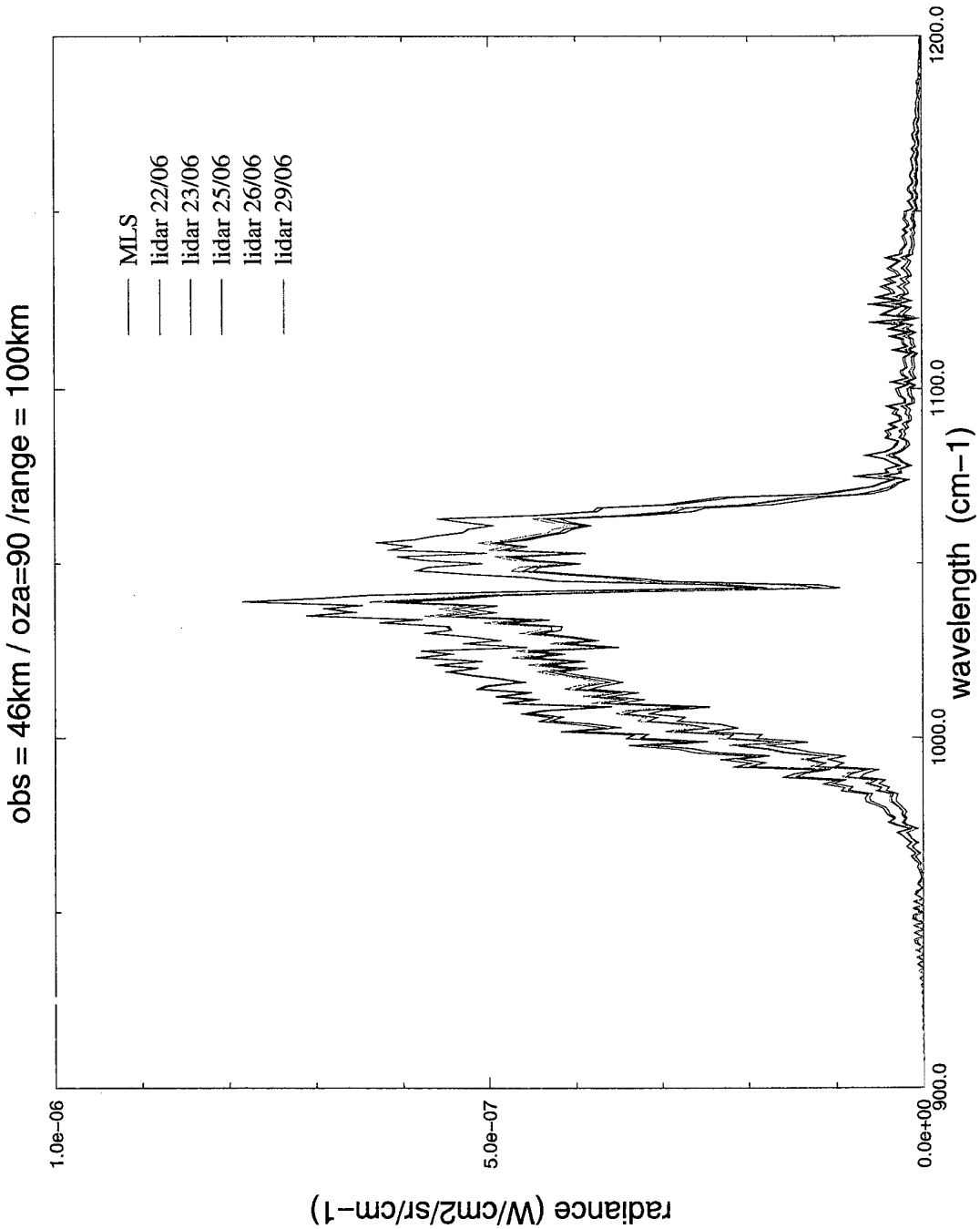
obs = 46km / oza=90 /range = 100km
MLS
lidar 22/06
lidar 23/06
lidar 25/06
lidar 26/06
lidar 29/06
radiance (W/cm2/sr/cm-1)
1.0e-06
5.0e-07
0.0e+00
900.0
1000.0
1100.0
1200.0
wavelength (cm-1)

Figure 37.

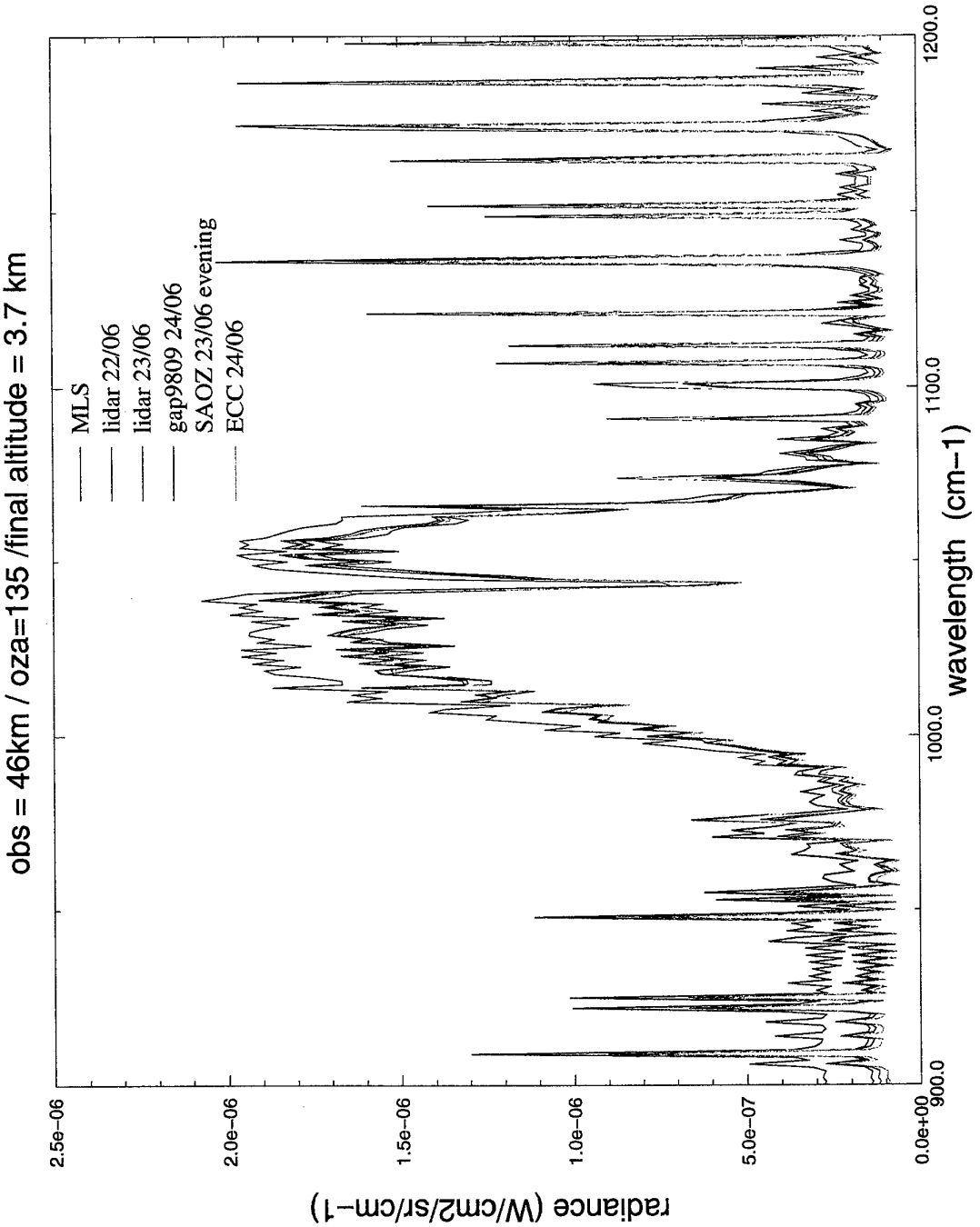

Figure 38.

ONERA

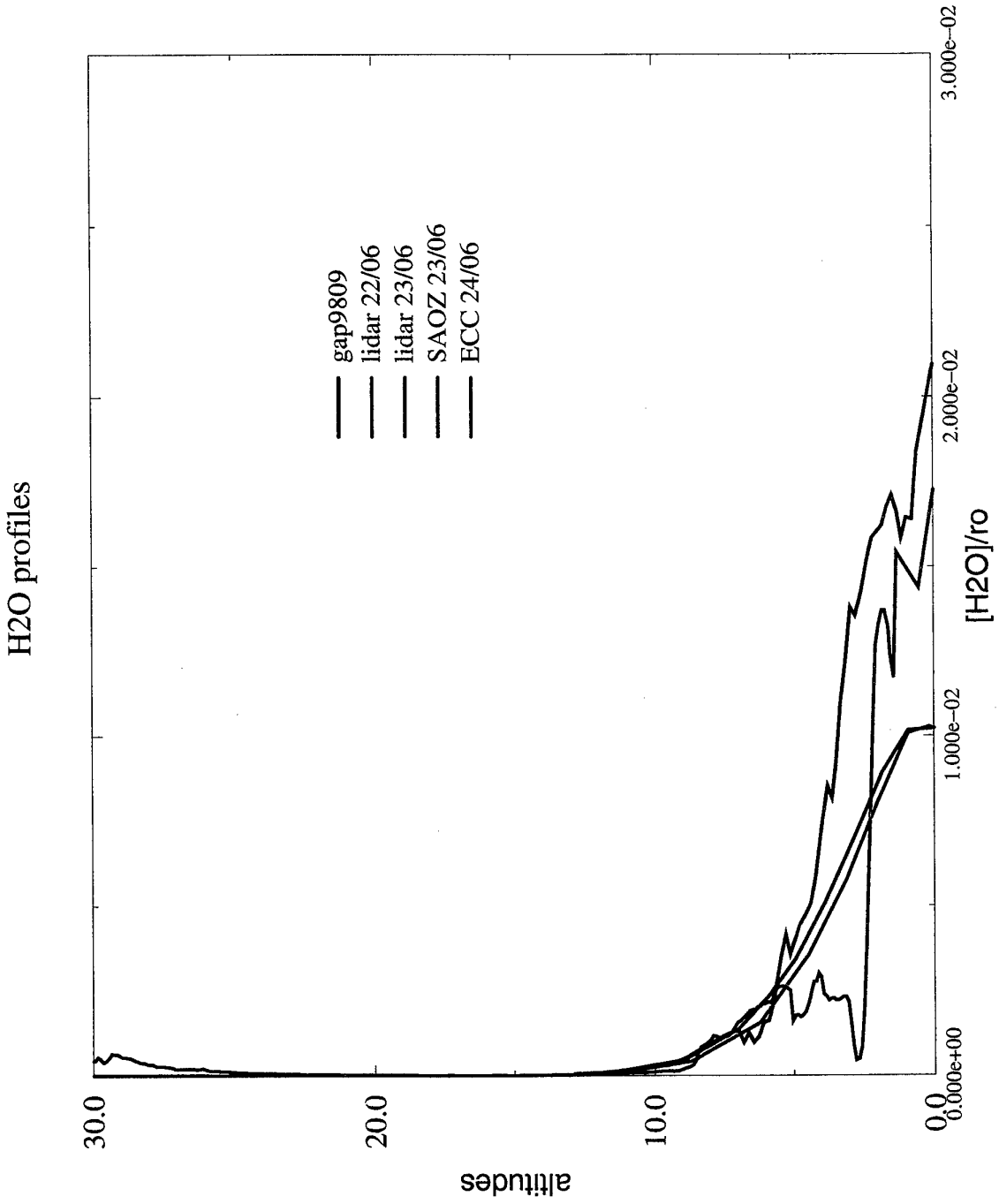

Figure 39.

ONERA

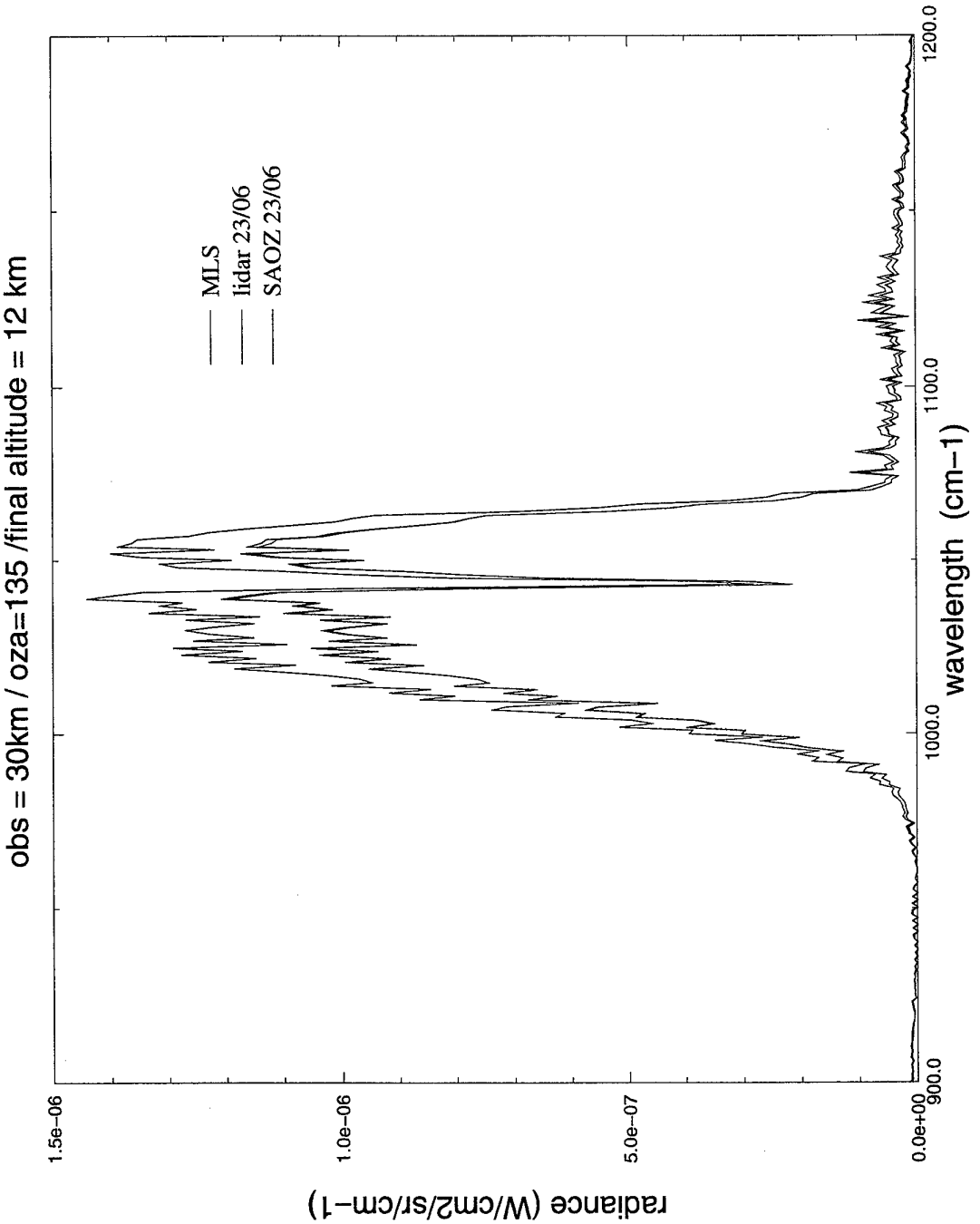

Figure 40.

ONERA

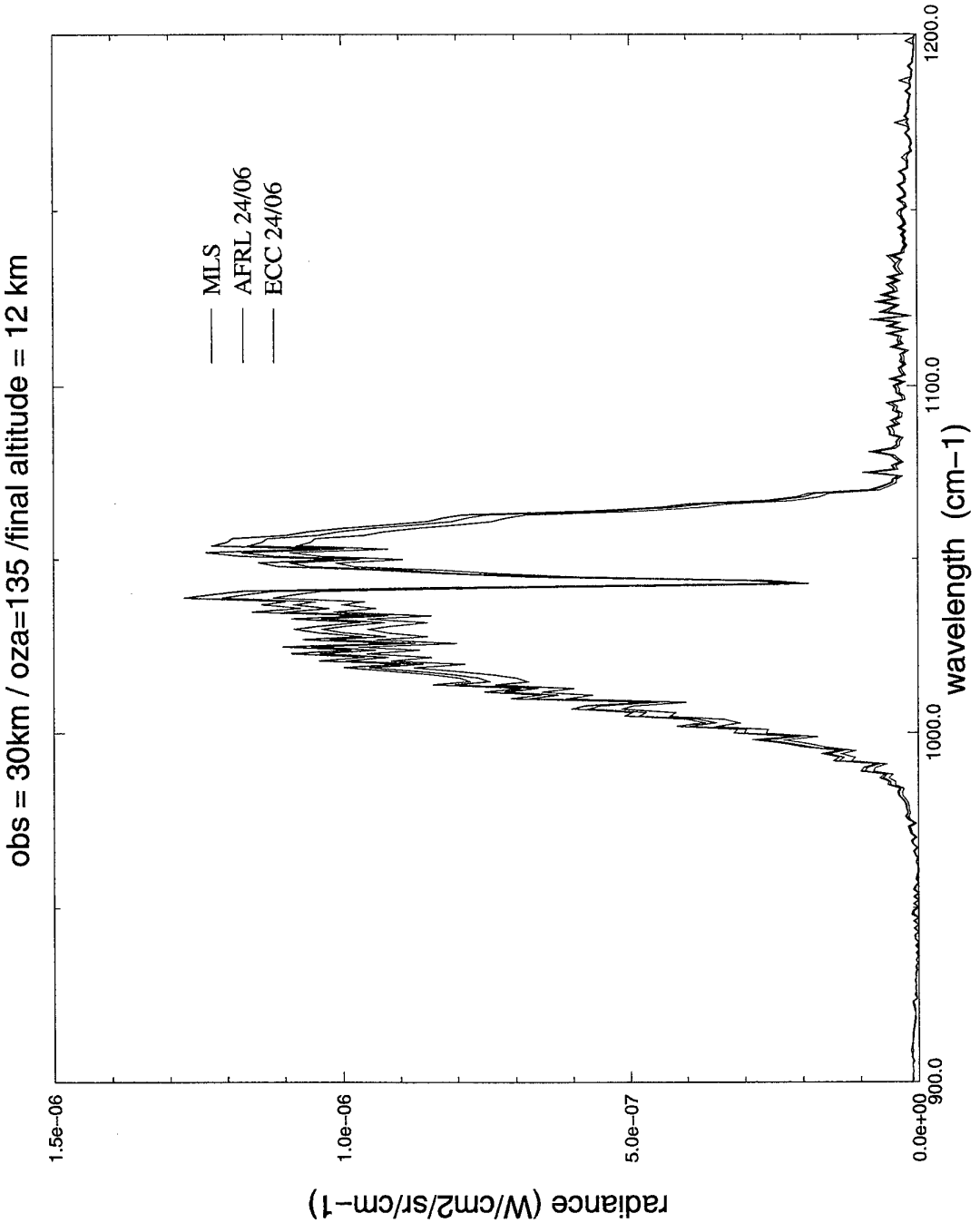

Figure 41.

ONERA

APPENDIX 1
FORMAT OF AFRL DATA FILE

Gap, France 1998 Data to be sent to France under the Bilateral US/France Data Exchange Agreement

Prepared by Edmund A. Murphy/ AFRL/VSBL, 29 Randolph Rd., Hanscom AFB, MA 01731, Tel: (781)377 4403, e-mail Edmund.Murphy@hanscom.af.mil

27 March 2001

NOTE! - The following information explains the output formats for each of two balloon payload configurations launched during the Gap, France 1998 ozone/ thermosonde program. The flights consisted of either a dual payload for the measurement of ozone and turbulence or just the ozone experiment. The thermosonde data is the temperature difference across two fine wire probes spaced one meter apart. The output data name cn2 is the value of the atmospheric structure parameter calculated from the temperature difference across the probes. Ozone is given in the output file as Partial pressure as well as number density.

There are seven Ozone payloads:

1.) gap9809 obtained on 06/24/98 at 2345 GMT to a height of 26.6 km is a dual payload.
2.) gap9810 obtained on 06/25/98 at 2130 GMT to a height of 28.6 km is a dual payload.
3.) gap9811 obtained on 06/25/98 at 2359 GMT to a height of 30.6 km is a dual payload.
4.) gap9812 obtained on 06/26/98 at 1935 GMT to a height of 30.6 km is an ozone payload only.
5.) gap9814 obtained on 06/26/98 at 2241 GMT to a height of 30.6 km is a dual payload.
6.) gap9815 obtained on 06/27 98 at 1730 GMT to a height of 21.6 km is an ozone payload only.
7.) gap9816 obtained on 06/27/98 at 1926 GMT to a height of 30.6 km is an ozone payload only.
8.)

The following lines of code are are taken from the data reduction programs to better explain the data output files [gap98xx.txt]

```
pro va_du09g

; Ver oct 98 created by EAM to process Vaisala Thermosondes/Ozonesondes
;*********************************************************************
; NOTE!! THIS PROGRAM IS USED TO REDUCE A DUAL (THERMOSONDE/OZONE) PAYLOAD
; INPUT TO THIS PROGRAM IS OUTPUT FROM FULLxxg.PRO
;*********************************************************************

;Create a data .TXT file
;***********************
close,4
```

```
      openw,4,txtfileout
          for i=0,fin do begin
            printf,4,format="(4(f12.4,1x),4(e15.4,1x),3(e13.5,1x))",zz(i),pr(i),te(i),h
u(i),ecn2(i),$
                  parp3(i),parp4(i),parp5(i),numd3(i),numd4(i),numd5(i)
          endfor
      close,4
```

```
      pro va_oz12g

      ; Ver oct 98 created by EAM to process Vaisala Ozonesonde only
      ;*************************************************************
      ; NOTE!! THIS PROGRAM IS USED TO REDUCE An OZONE PAYLOAD
      ; INPUT TO THIS PROGRAM IS OUTPUT FROM ozxxg.PRO
      ;*************************************
      ; NOTE! -  All five channels are Ozone *
      ;Calculate the Ozone concentration
      ;*********************************
      numd1 = (7.24313*parp1/kte)*1.e+12

      ;This is from Komhyr's paper and is in (1/cm^3) - mult. by 10e+06 for (1/m^3)
      ;********************
      numd1 = numd1*1.0e+06

      ;********************
      ;Create a data .TXT file
      ;***********************
      close,4
      openw,4,txtfileout
          for i=0,fin do begin
            printf,4,format="(4(f12.4,1x),6(e13.5,1x))",zz(i),pr(i),te(i),hu(i),$
                  parp1(i),parp2(i),parp3(i),parp4(i),parp5(i),numd1(i)
          endfor
      close,4
```

VARIABLE NAME	**PARAMETER**	**UNITS**
zz	Altitude	km
pr	Pressure	mbars
te	Ambient temperature	Deg. C
hu	Relative humidity	%
cn2	Atmospheric Structure Function	m^-(2/3)
parp1	Ozone partial pressure (channel #1)	Nanobars
numd1	Ozone number density (channel #1)	/m^3

10. WIND DATA

Column #1 – Altitude in km
Column #2 – Velocity in m/sec
Column #3 - Direction in degrees from true north

File name	Launch Date	Launch time LT	Max Altitude
Gap9801.win	06/20/98	2215	31.08
Gap9802.win	06/21/98	0025	32.35
Gap9804.win	06/21/98	2332	30.07
Gap9805.win	06/22/98	2130	30.09
Gap9806.win	06/22/98	2320	28.12
Gap9807.win	06/23/98	1548	30.27
Gap9808.win	06/24/98	2140	19.50
Gap9809.win	06/24/98	2345	23.44
Gap9810.win	06/25/98	2130	27.63
Gap9811.win	06/25/98	2359	30.03
Gap9812.win	06/26/98	1935	30.02
Gap9813.win	06/26/98	2133	9.43
Gap9814.win	06/26/98	2241	30.18
Gap9815.win	06/27/98	1730	22.24
Gap9816.win	06/27/98	1926	29.79
Gap9817.win	06/27/98	2130	30.27

APPENDIX 2
Data Additional information

Question from Y. Louvet on 19th June 2001 and answer from Dr. Jumper

>As you know it is always very difficult to interpret measurements when
>haven't to take part in the trial measurements, so we have again a lot of
>questions from Dr. Dalaudier.
>
>1- The data are difficult to correlate because we do not have the exact
>dating of the measurement. Have you kept the dating of measurements and
>could you send it to us?
>We have all dates and times of launch. The balloon goes up at 5 to 7 m/s,
>so there is a lag as it progresses. I have attached the time sheet summary
>below (GAP98T.pdf). The time and date are "Local" Gap time, NOT Universal
>Time. If you have a problem with the Adobe PDF document, let me know and I
>will send you a text copy. (In fact, I noticed the math fonts are not very
>good - if anyone wants a good copy, I can send it by mail.)
>2- In addition we have some difficulties in correlation of the altitude
>data. How is calculated the data of altitude from the file *.win? is it
>altitude coming from data GPS or is it from calculated altitude by
>integration of vertical winds measurements of the Vaisala probe?
>Altitudes are computed the standard way for a radiosonde. The
"hypsometric"
>equation is used, that is, the hydrostatic equation with humidity
considered
>in the equation. The radiosonde measures pressure, temperature, and
>humidity (and we get wind speed).
>3- The probe Vaisala gives a frequency of measurements which is not usual
>acts of a probe RS90?
>
> 4- In the *.text file, how is measured or calculated the pressure ?
>Pressure is measured. Altitude is computed.
>5- It is always interesting to know the processing of the signal carried
>out of differential measurement with the electronics bandwidths. How the
>differential temperature signal is it treated and how much is the
bandwidth
>of electronic used?.
>The attached paper "AIAA Sources of Error" below discusses the instrument
>and the measurements along with references. (It also discusses possible
>sources of error). The differential temperature is measured with some very
>fine wire probes, 3.45 micro meters in diameter. The time constant of the
>wires are nominally above 250 hz at maximum altitude - faster on the
ground.
>The band pass of the filters is between 1000Hz and 0.5Hz. The amplified
and
>filtered signal is then passed through an RMS chip with a nominal time
>constant of 3.75s. As discussed in the paper, this was found to actually
>depend on whether the signal was rising or falling. When falling, the time
>constant increases to 7.5s.
>

Question from Dr. Louvet on 12th July 2001
Answer from Dr. Jumper on 27th July
1) Firstly about very interesting publication AIAA Sources of Error.pdf unfortunately as you be afraid of a numerous problems happened on math fonts. Please can you send a text copy, see below address. Thank

.....See attached .pdf file. Hopefully the equations will be readable this time...

As you know atmospheric stability study requires very good data correlation between measurements. So we try to understand time acquisition, pressure measurement and calculated hydrostatic altitude correlation. We are a little bit surprise by data can you help us.

2) The ratio of pressure variation by pressure seems excellent and constant as altitude. What is the sensor reference?
What is VAISAL probe reference and work mode acquisition choosing

... It is the Vaisala pressure sensorfor the RS80. We will FAX the specifications to you along with the specifications on the Ozone sensor (FAX to Laurent)...

3) The dat files show that time acquisition is not constant and is very different as time difference products from cutting time. (for exemple if time is only measured in seconds and if acquisition frequency is 1,2s we have time data recorded steps of 1 and 2 seconds).

... For some strange reason, Vaisala rounds the times in the files to the nearest second, even though it shows several decimal places. Those times can be used as is, accepting a +/- .5 second error, or the times can be replaced by multiples of the sample interval. If you do the latter, you have to be careful, because sometimes a line is lost in the transmission .....

In txt file it seems
that measurements are taken one or two or three time of fundamental acquisition frequency as we see in *.dat file. Please do you know why ?

... In the .txt file, we present data for approximately equal values of time, and interpolate if required. There is no time given, only altitude in km ...

4) In *.TXT we have several values of Ozone pressures (P3O3, P4O3, ..) can you remenber me what is the difference and where come from these different values?

...The radiosonde actually has 5 spare channels that we can use for the additional data, and a couple of reference voltages . All the 03 data comes from the same instrument, it is just sampled 5 times if it is the only instrument. If we have the thermosonde also attached to 2 or 3 of the spare channels, we show 2 or 3 O3 data points and 3 or 2 thermosonde data points. Typically we then use only one of the channels for analysis ...

5) About wind angle we have supposed it is right to meteo convention which gives angles where the wind come from and not the angle of wind vector goes.

...You are correct, the meteo convention is used, it is the angle the wind is coming from. 0 is from the North, 90 is from the East....

6) About time. In your mail of the 19 th June you have confirmed according to GAP98T.pdf file that the time is in Local Time. Unfortunetly in dataform.doc file send with txt and win file it is write GMT time and it is the same values ? Can you confirm the right time?

... In the table of all launches, we give the local date and time at launch. It is local time that is sometimes shown on graphs. There is no time in the .txt and .win files - the first column is altitude (km). The .met file does have time to the nearest second, with an arbitrary zero time near the actual launch time. We sent the .dat files so that you could tell what time (seconds after launch) was associated with each altitude. You can add those seconds to launch time to get actual time. Remember any launch time we provide is local. I do not know why someone said there was GMT in the .txt and .win files. There is no time at all in those files ...

7) If possible we are very interested of all data from the descent . We know that at the beginning descent the data are certainly no right, but have you any think ?

... We do not know much about the descent of that one flight. The ozone concentrations agree fairly well, so we showed them in the paper...

8) Have you the geographic path as a function of time for each launch. Can you send it.

... We did not compute it. We sometimes assume that we are totally in equilibrium with the horizontal wind and compute the position from the wind file, but we did not accomplish that for these flights ...

9)Good new. Preliminary analysis of ozone gradient shows a very good correlation between potential temperature. It means that spatial resolution of O3 sensor was better than 100 m in the altitude range of 18 to 22 km high. have you some idea about time response of o3 probe as function of altitude.

... I do not remember the time response as a function of altitude. I thought that it was associated with the volume of the pump, which does not change, but I might be wrong. We will look into this and get back to you if we find anything....

APPENDIX 3
FIRST SET OF GRAPHS
RUNS 9,10, 11, 12, 14, 15 AND 16

For each run we plotted 9 figures, in the following order:

Figure 1 : Wind components UU (West –East) et VV (South-North) in the [0-35] km altitude range.
Figure 2 : Zoom in the [15-18] km, [18-22] km and [22-30] km altitude ranges.
Figure 3 : Plots of UU, VV, measured (T) and potential (Tpotent) temperatures, ozone concentration in the [0-35] km altitude range.
Figure 3bis : Same as 3 in the [15-18] km, [18-22] km and [22-30] km altitude ranges.
Figure 4 : Wind components UU (W-E) et VV (S-N); O3 concentration and gradient and N2 (square Brunt-Vaisala pulsation multiplied by 10000) in the [18-22] km altitude range.
Figure 5 : Same as Figure 4 but on two graphs.
Figure 6 : Curves of P (pressure), T, Tpotent, O3 and %humidity in the [0-35] km altitude range.
Figure 7 : Graphs of shear (wind gradient), N2 et cn2 (runs 9, 10, 11, and 14) in the [0-35] km altitude range.
Figure 8 : Same as Figure 7 but shear, N2 et cn2 (runs 9, 10, 11, and 14) in the [18-22] km altitude range.

APPENDIX 3
GAP98- Graphs RUN n°9

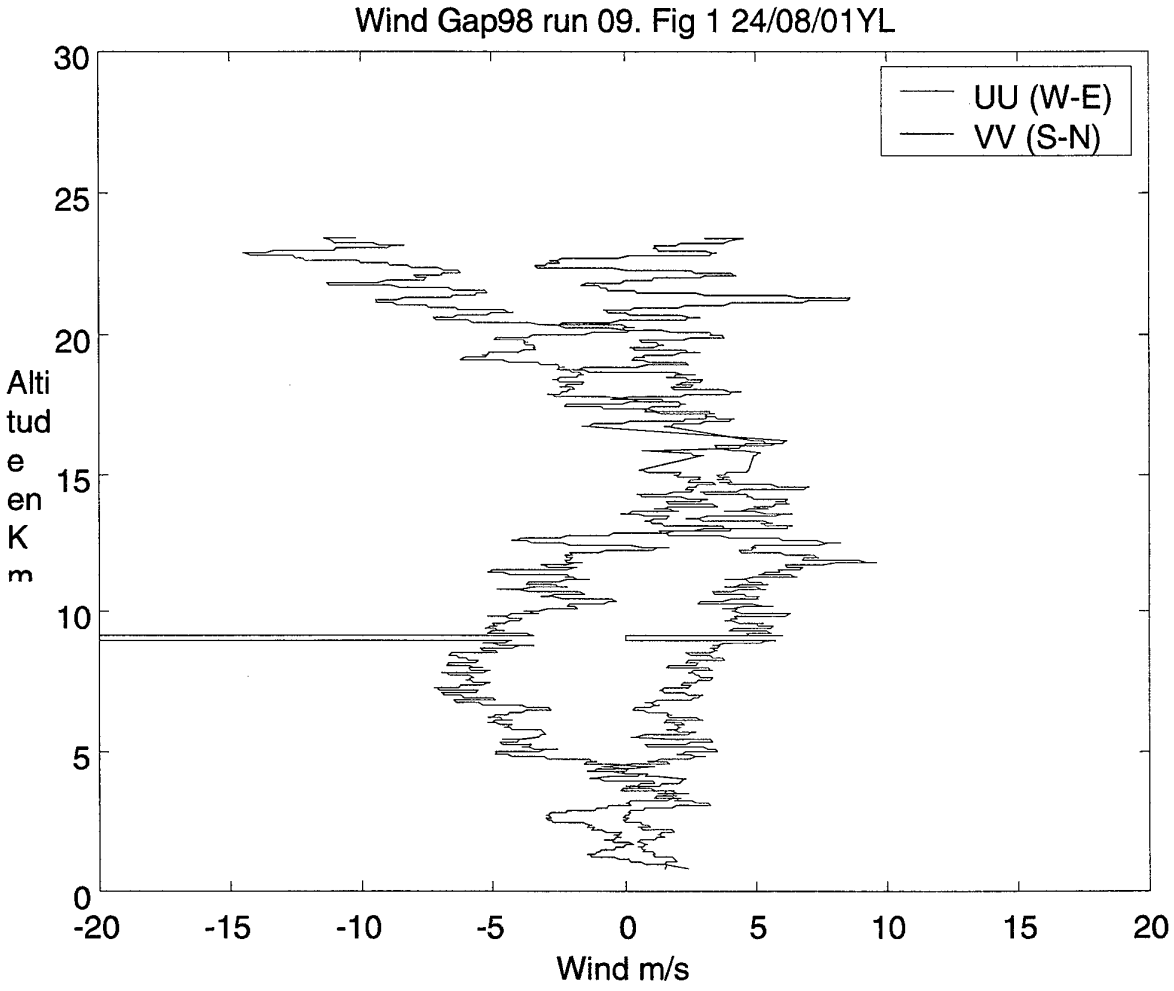
Wind Gap98 run 09. Fig 1 24/08/01YL
UU (W-E)
VV (S-N)
Altitude en Km
Wind m/s
30
25
20
15
10
5
0
-20
-15
-10
-5
0
5
10
15
20

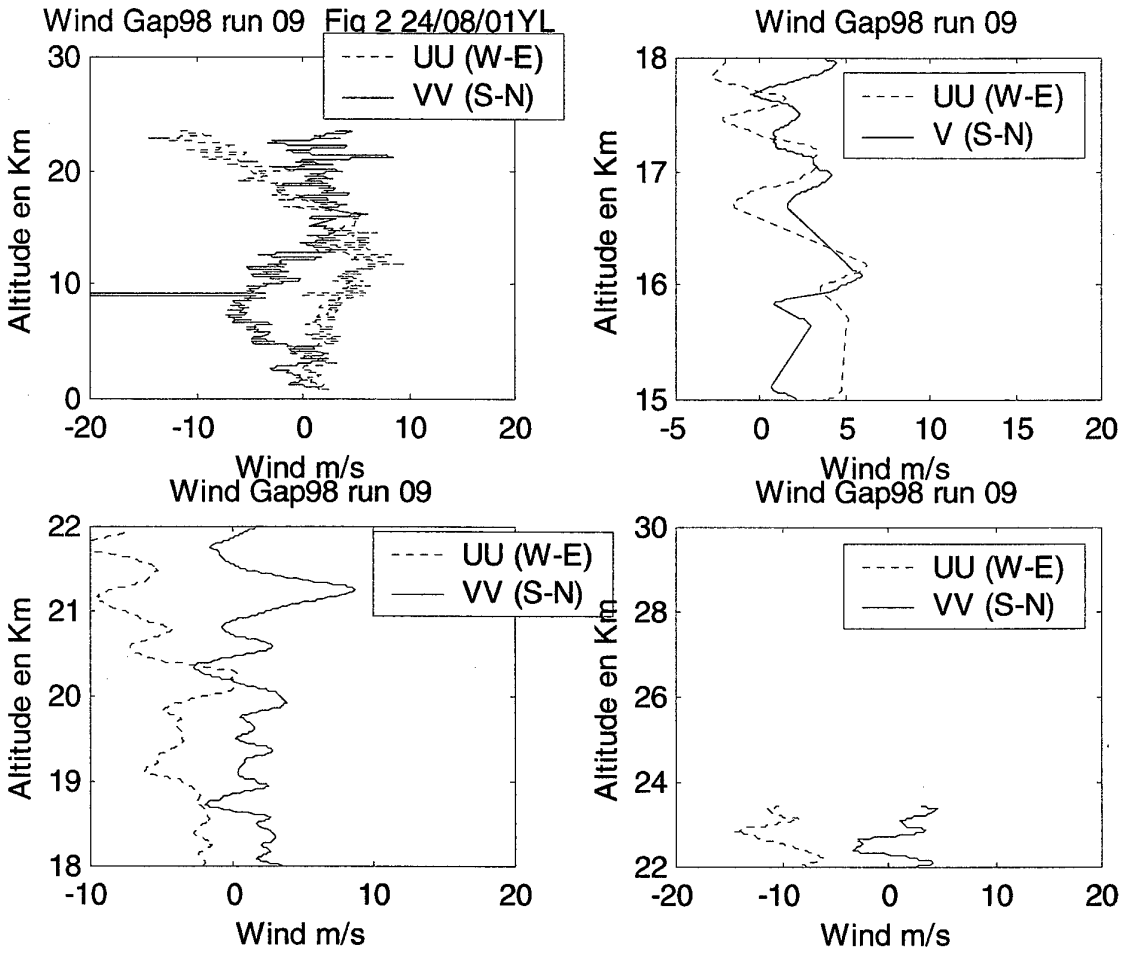
Wind Gap98 run 09 Fig 2 24/08/01YL
UU (W-E)
VV (S-N)
Altitude en Km
Wind m/s
Wind Gap98 run 09
UU (W-E)
V (S-N)
Altitude en Km
Wind m/s
Wind Gap98 run 09
UU (W-E)
VV (S-N)
Altitude en Km
Wind m/s
Wind Gap98 run 09
UU (W-E)
VV (S-N)
Altitude en Km
Wind m/s

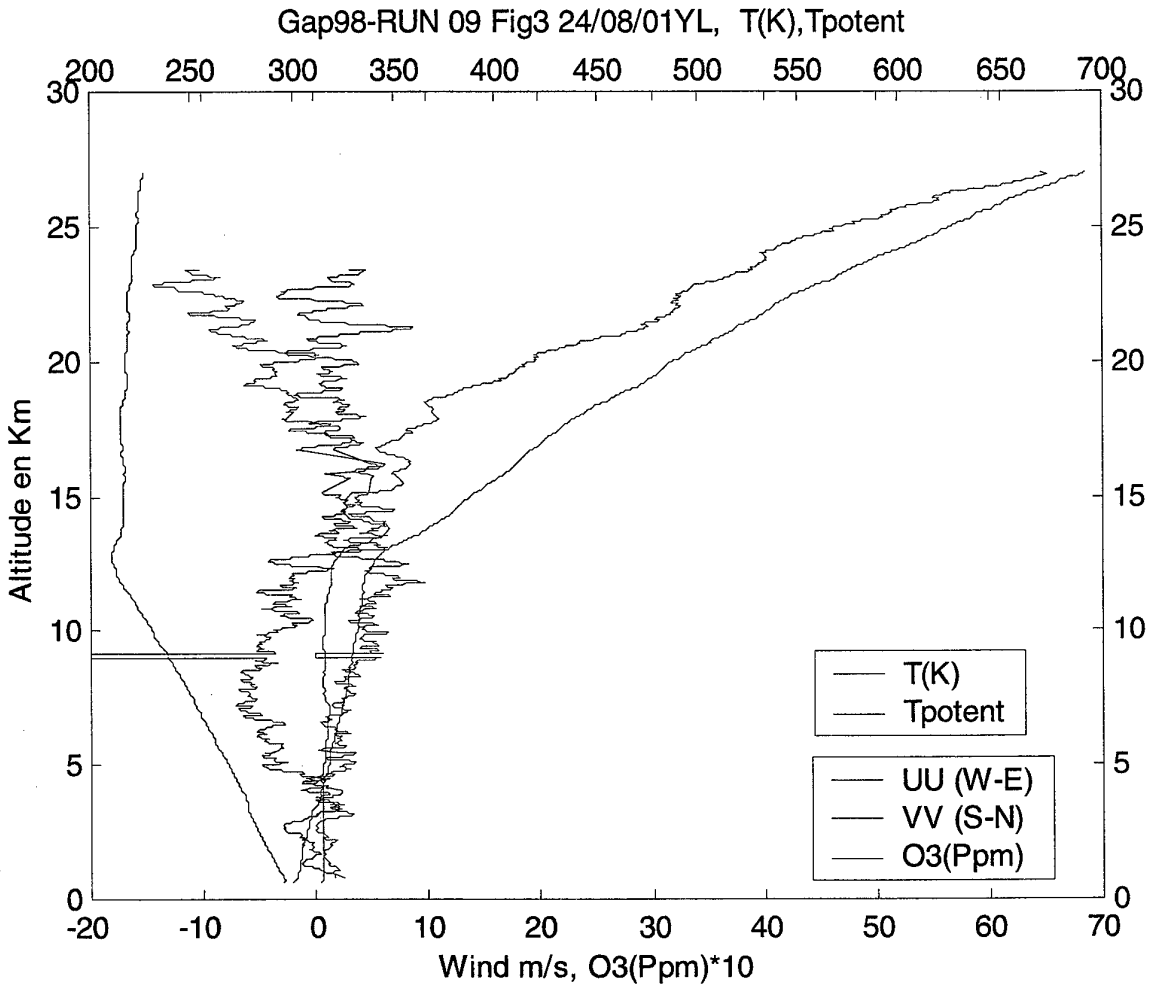
Gap98-RUN 09 Fig3 24/08/01YL, T(K),Tpotent
Altitude en Km
Wind m/s, O3(Ppm)*10
T(K)
Tpotent
UU (W-E)
VV (S-N)
O3(Ppm)

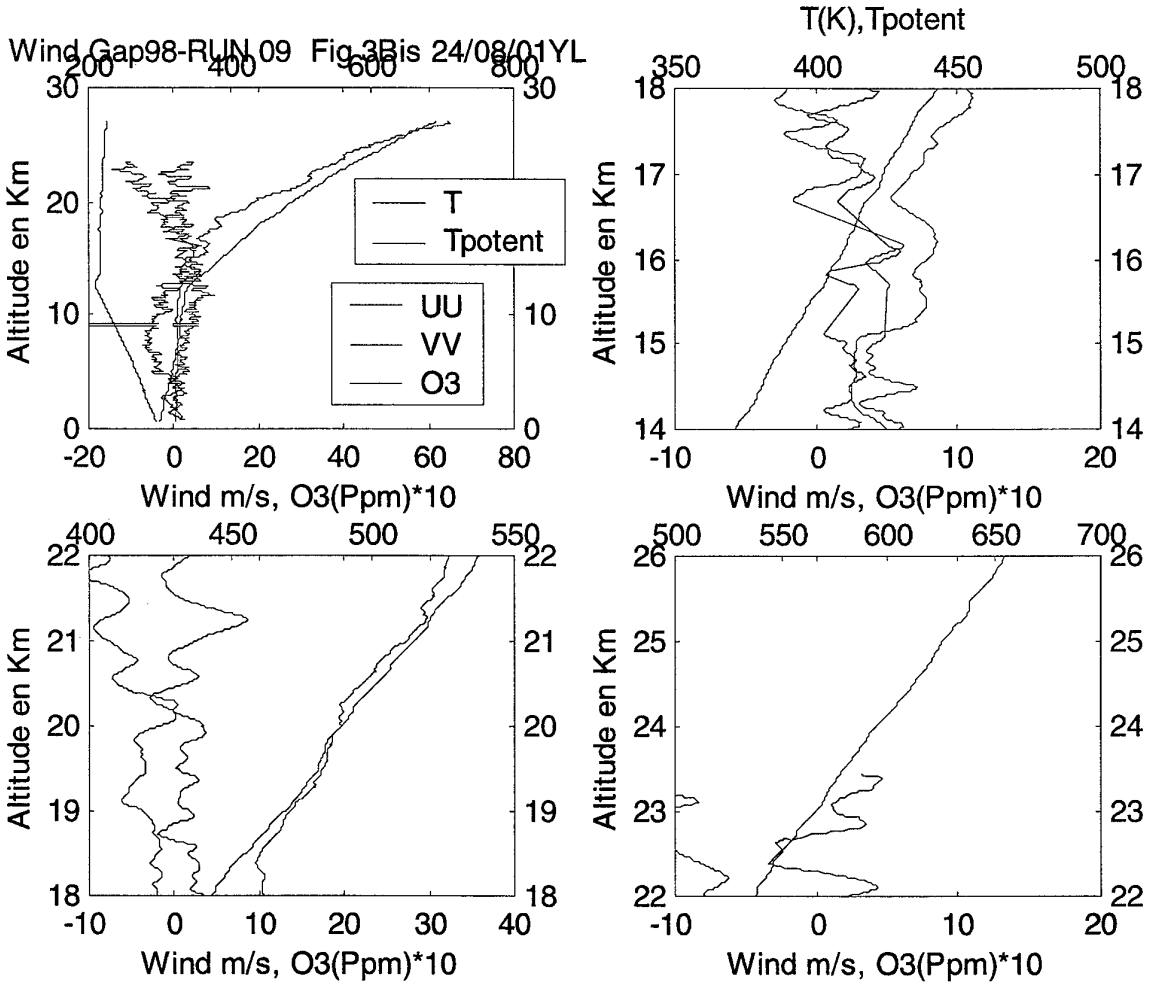
Wind Gap98-RUN 09 Fig 3Bis 24/08/01YL
T(K),Tpotent
Altitude en Km
Wind m/s, O3(Ppm)*10
T
Tpotent
UU
VV
O3

SANS MENTION
DE PROTECTION

SMP

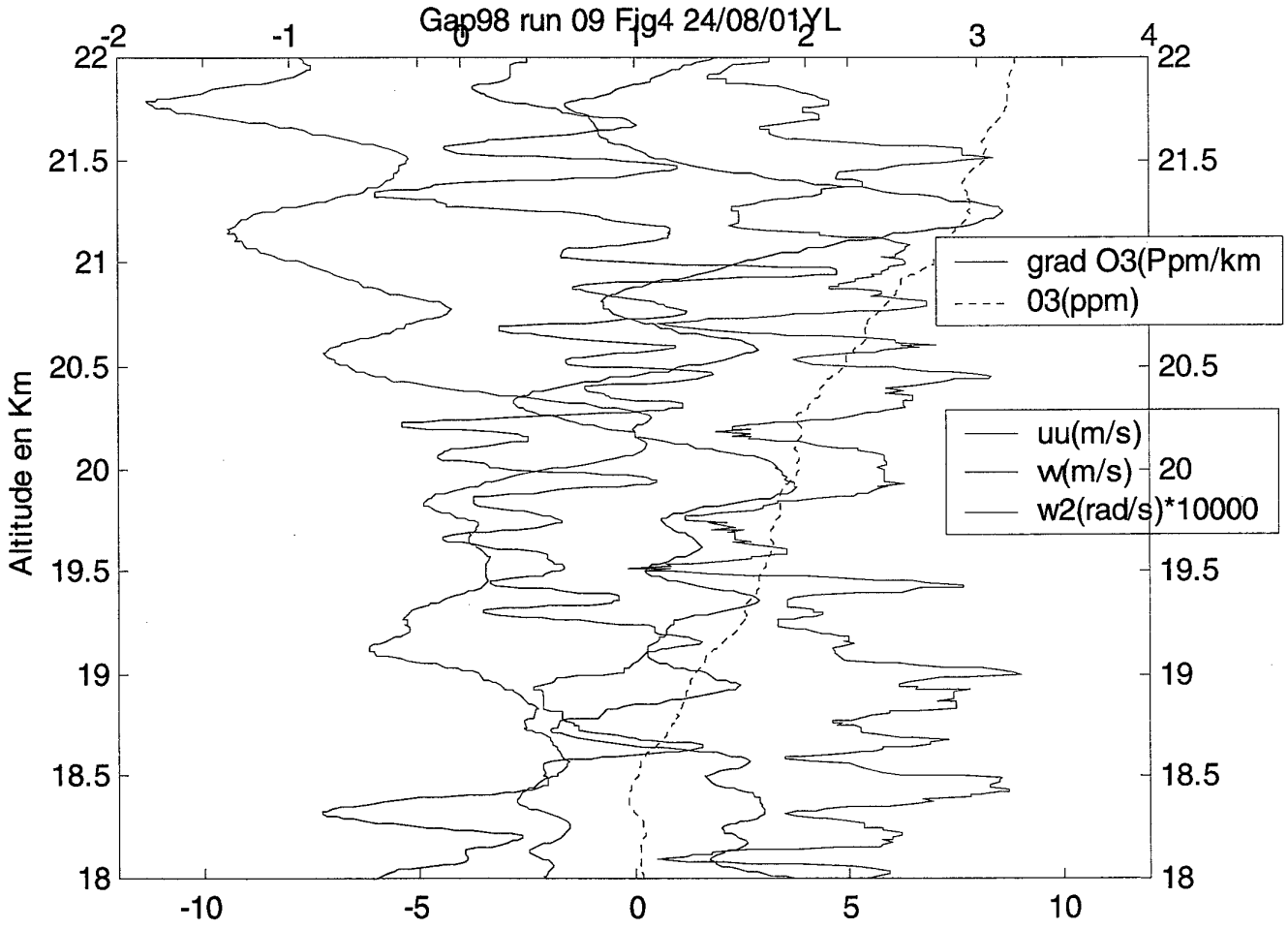

ONERA

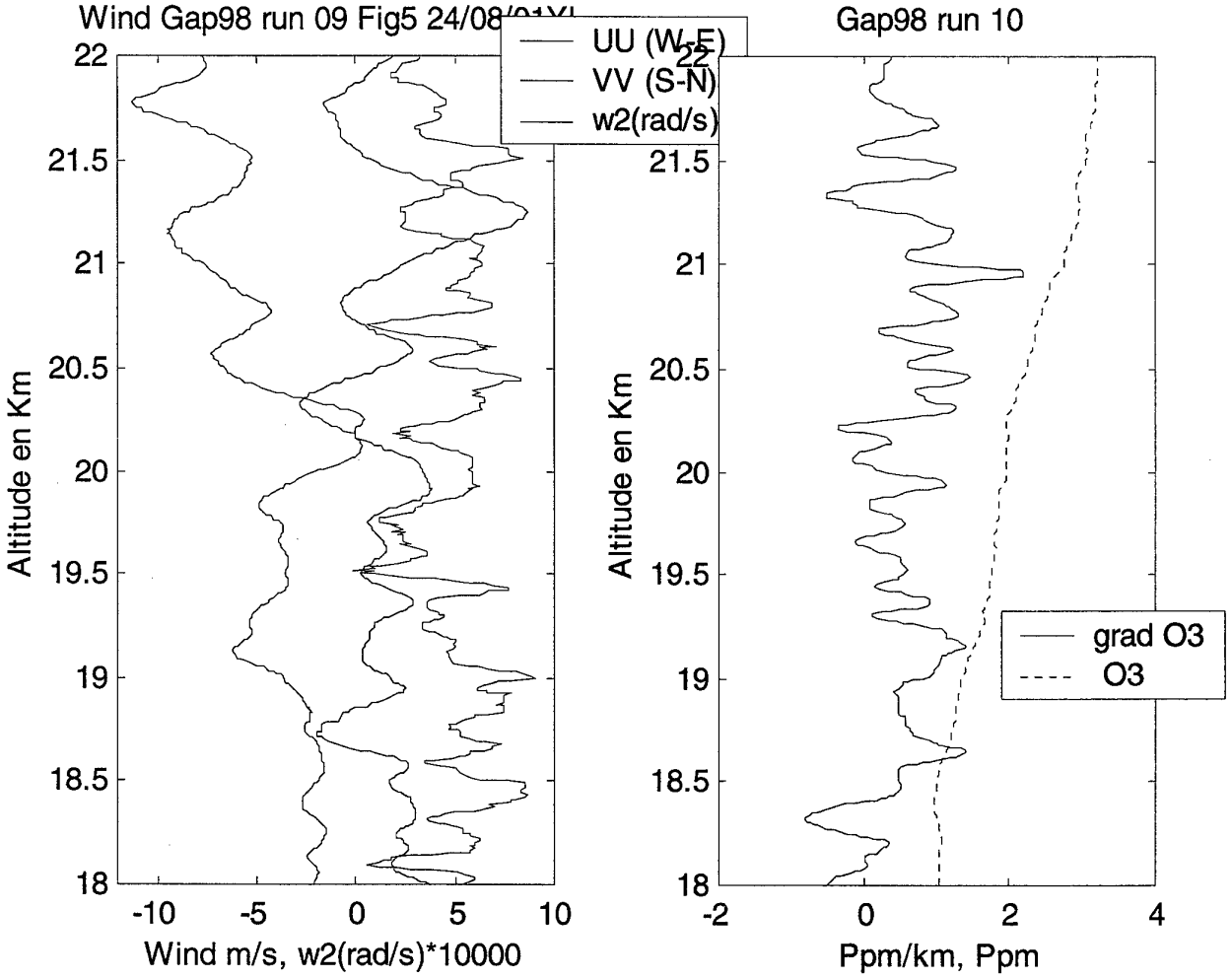
Wind Gap98 run 09 Fig5 24/08/01Y
UU (W-E)
VV (S-N)
w2(rad/s)
Altitude en Km
22
21.5
21
20.5
20
19.5
19
18.5
18
-10
-5
0
5
10
Wind m/s, w2(rad/s)*10000
Gap98 run 10
grad O3
O3
-2
0
2
4
Ppm/km, Ppm

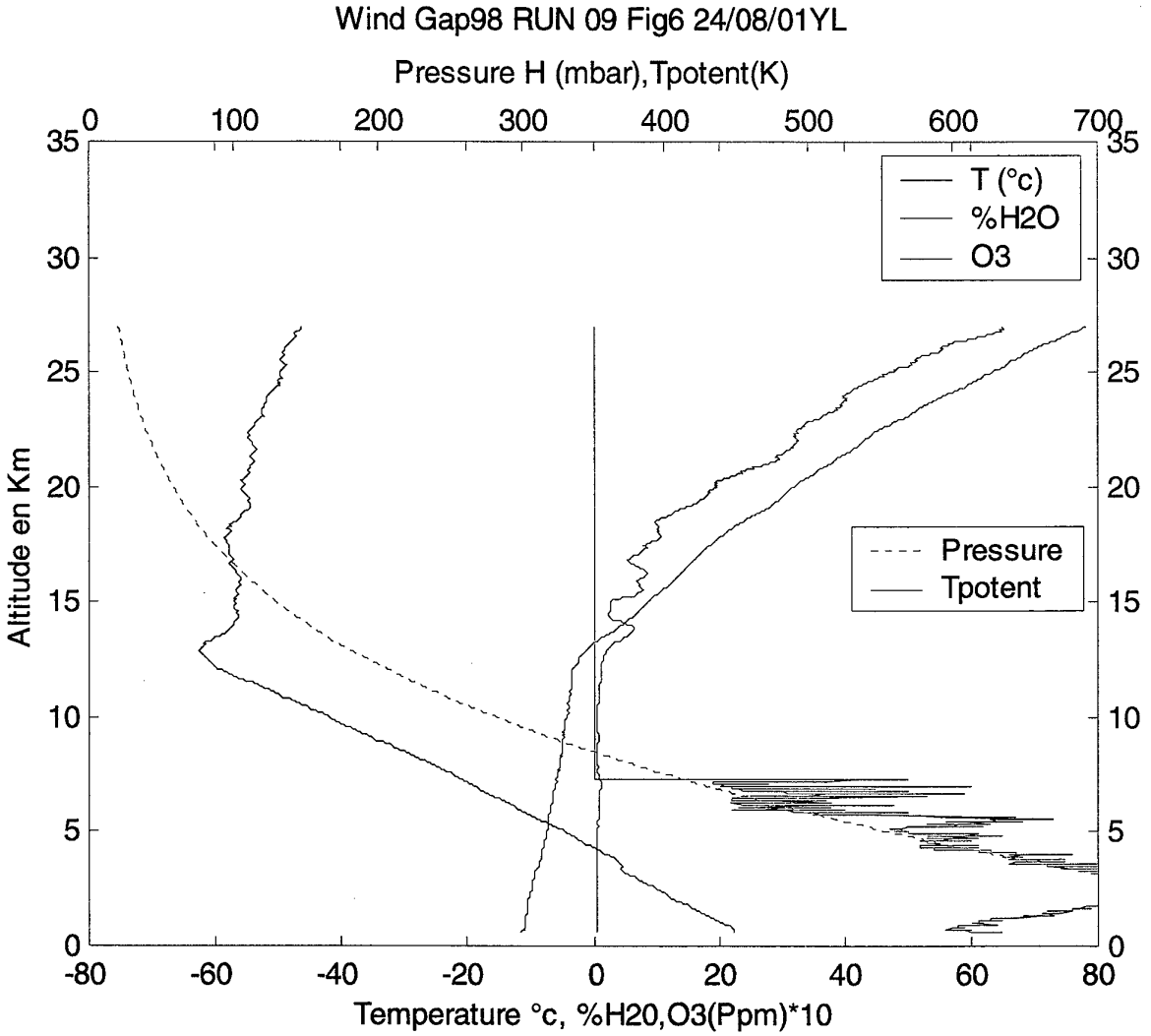
Wind Gap98 RUN 09 Fig6 24/08/01YL
Pressure H (mbar),Tpotent(K)
0
100
200
300
400
500
600
700
T (°c)
%H2O
O3
Pressure
Tpotent
Altitude en Km
0
5
10
15
20
25
30
35
-80
-60
-40
-20
0
20
40
60
80
Temperature °c, %H20,O3(Ppm)*10

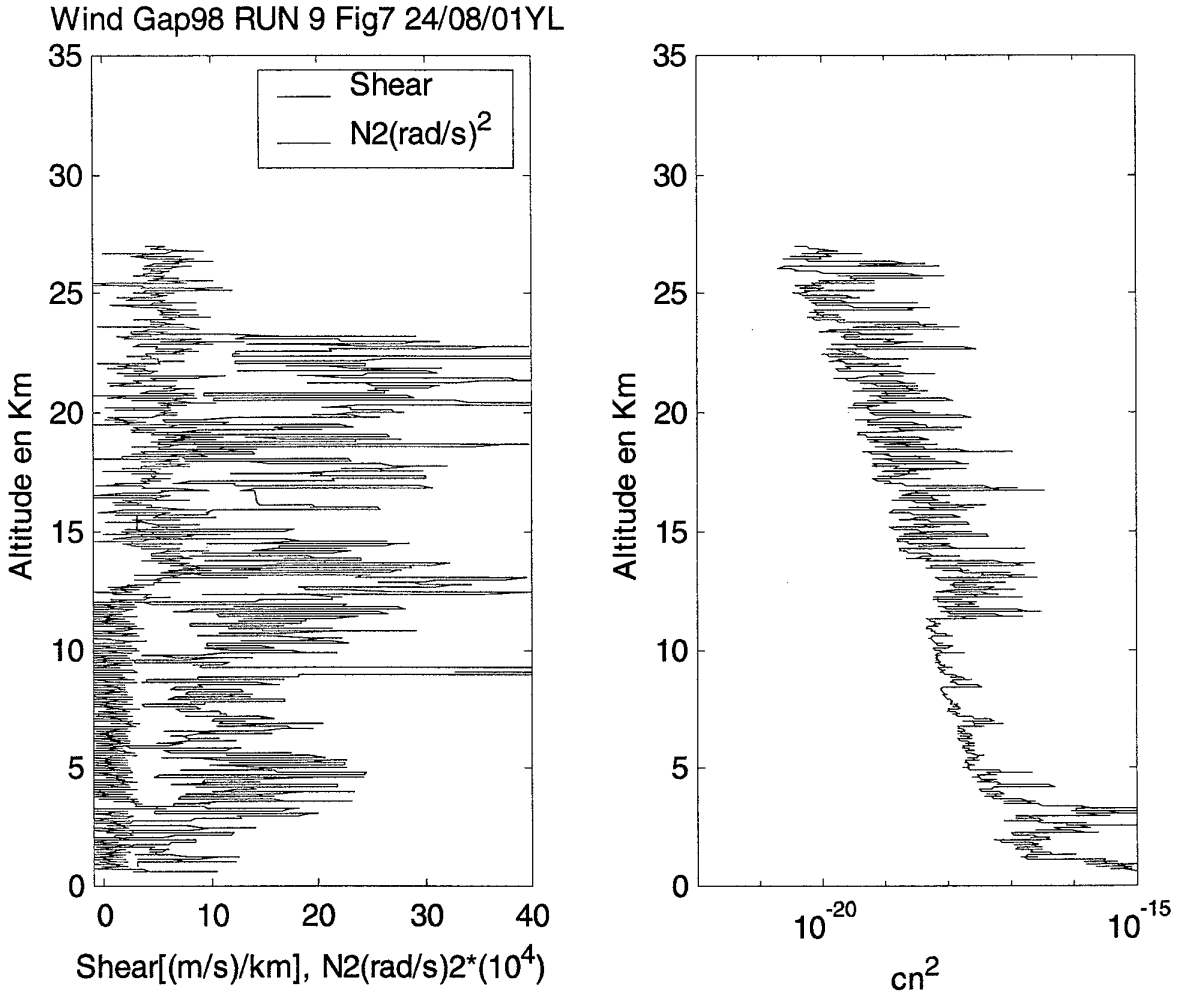
Wind Gap98 RUN 9 Fig7 24/08/01YL
Shear
N2(rad/s)2
Altitude en Km
Shear[(m/s)/km], N2(rad/s)2*(10^4)
cn2
10^-20
10^-15

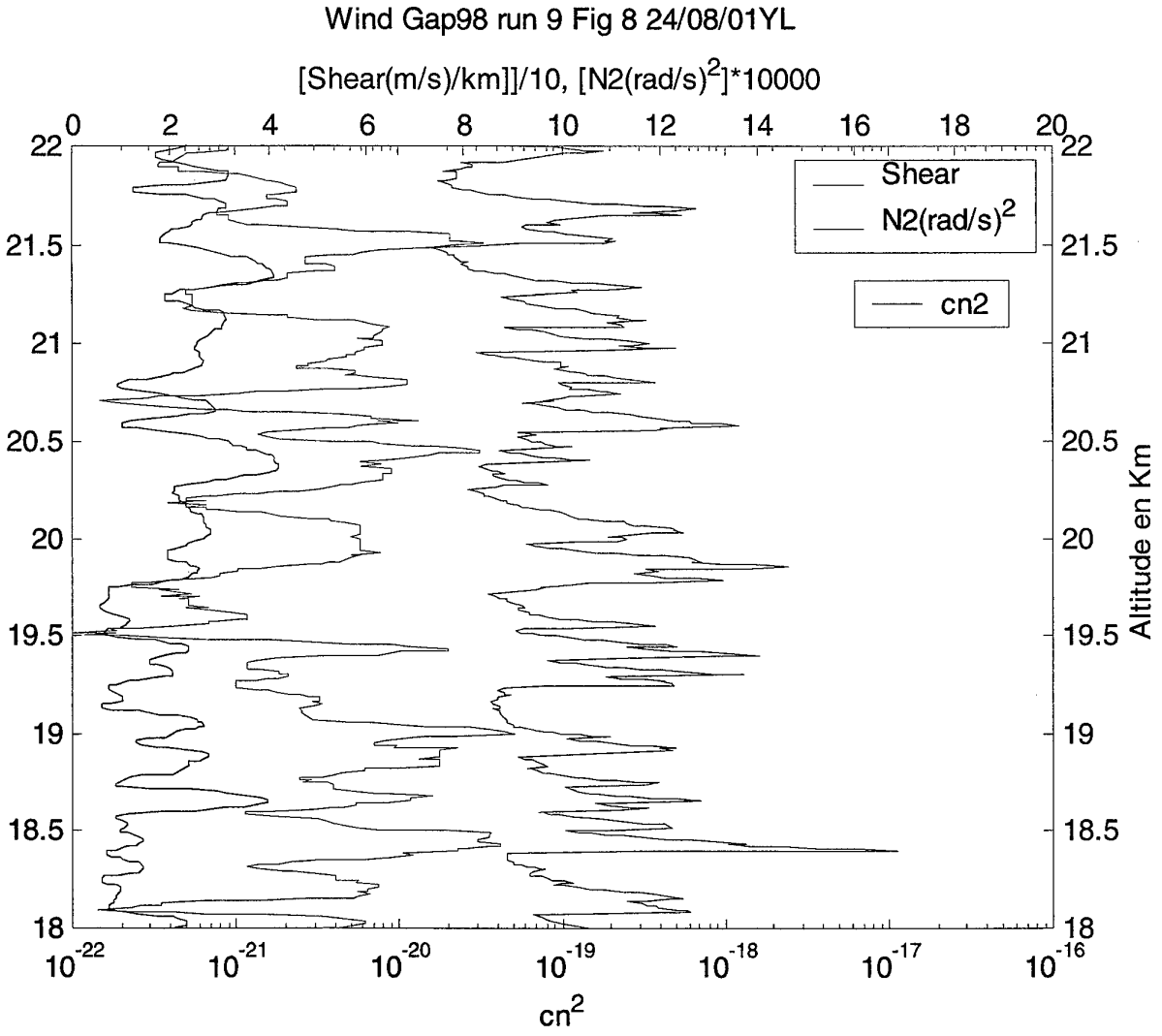
Wind Gap98 run 9 Fig 8 24/08/01YL
[Shear(m/s)/km]]/10, [N2(rad/s)2]*10000
Shear
N2(rad/s)2
cn2
Altitude en Km
cn2

GAP98- Graphs RUN n°10

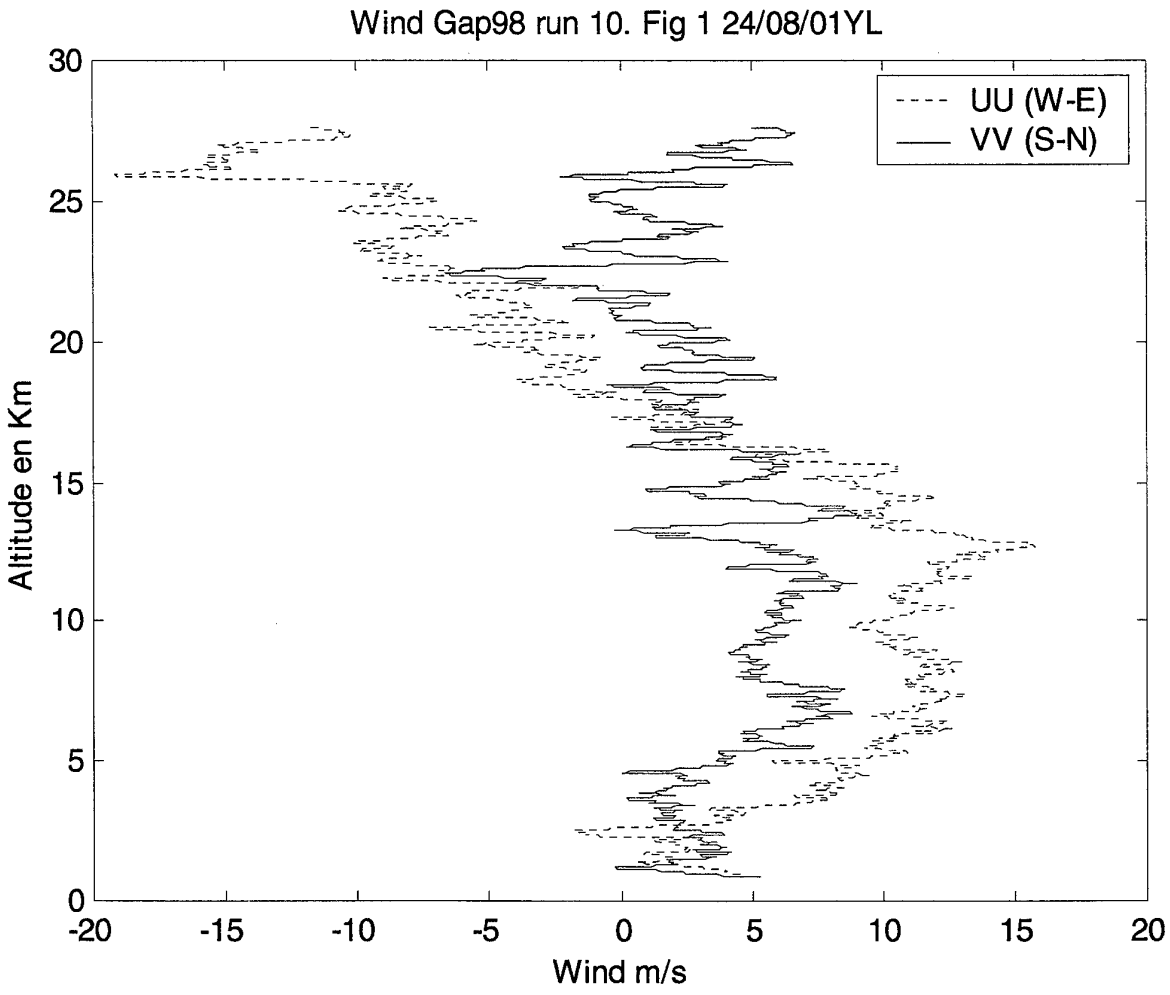
Wind Gap98 run 10. Fig 1 24/08/01YL
UU (W-E)
VV (S-N)
Altitude en Km
Wind m/s
30
25
20
15
10
5
0
-20
-15
-10
-5
0
5
10
15
20

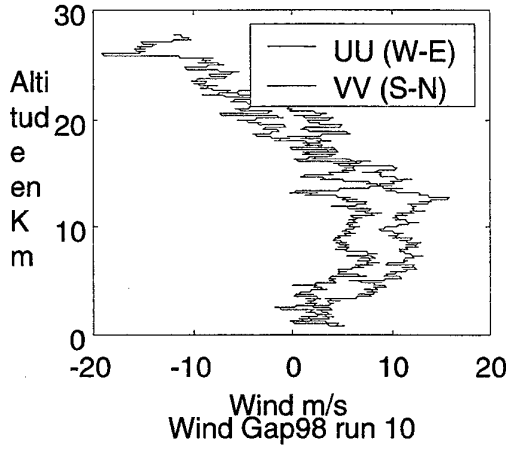
UU (W-E)
VV (S-N)
Altitude en Km
Wind m/s
Wind Gap98 run 10

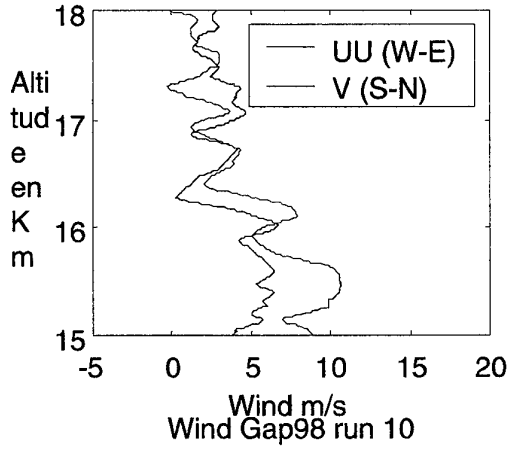
UU (W-E)
V (S-N)
Altitude en Km
Wind m/s
Wind Gap98 run 10

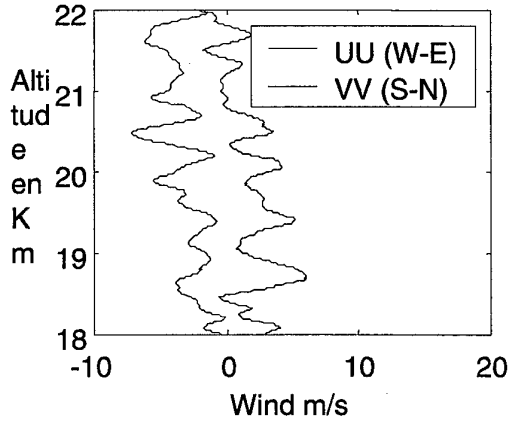
UU (W-E)
VV (S-N)
Altitude en Km
Wind m/s

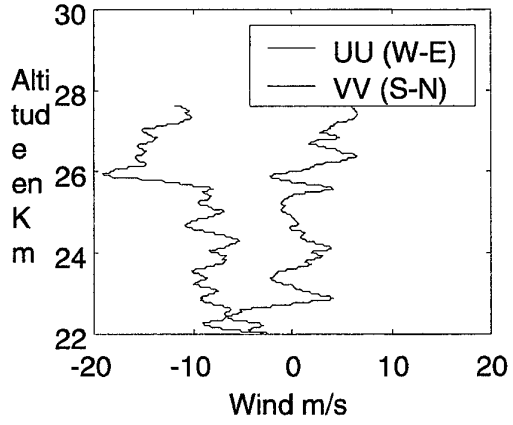
UU (W-E)
VV (S-N)
Altitude en Km
Wind m/s

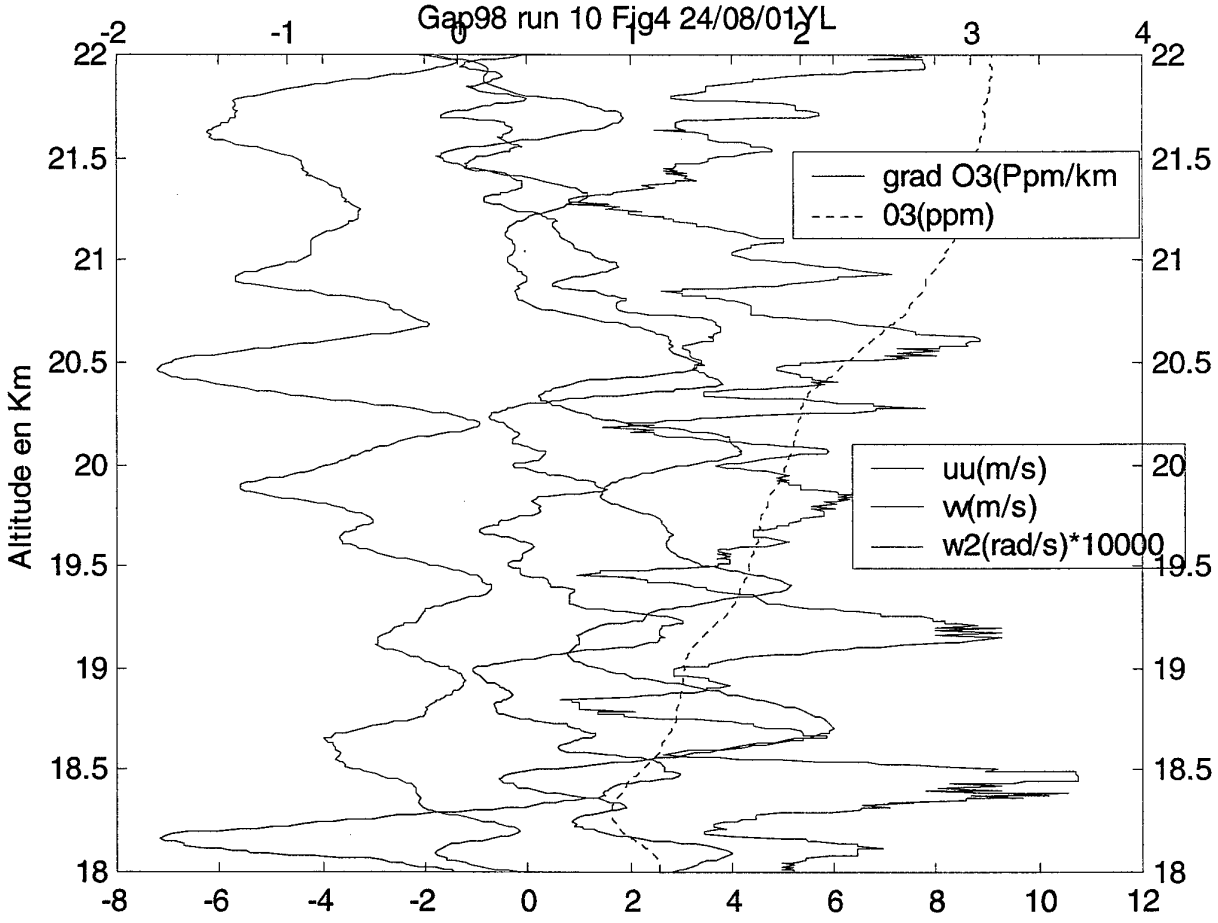
Gap98 run 10 Fig4 24/08/01YL
Altitude en Km
grad O3(Ppm/km
03(ppm)
uu(m/s)
w(m/s)
w2(rad/s)*10000

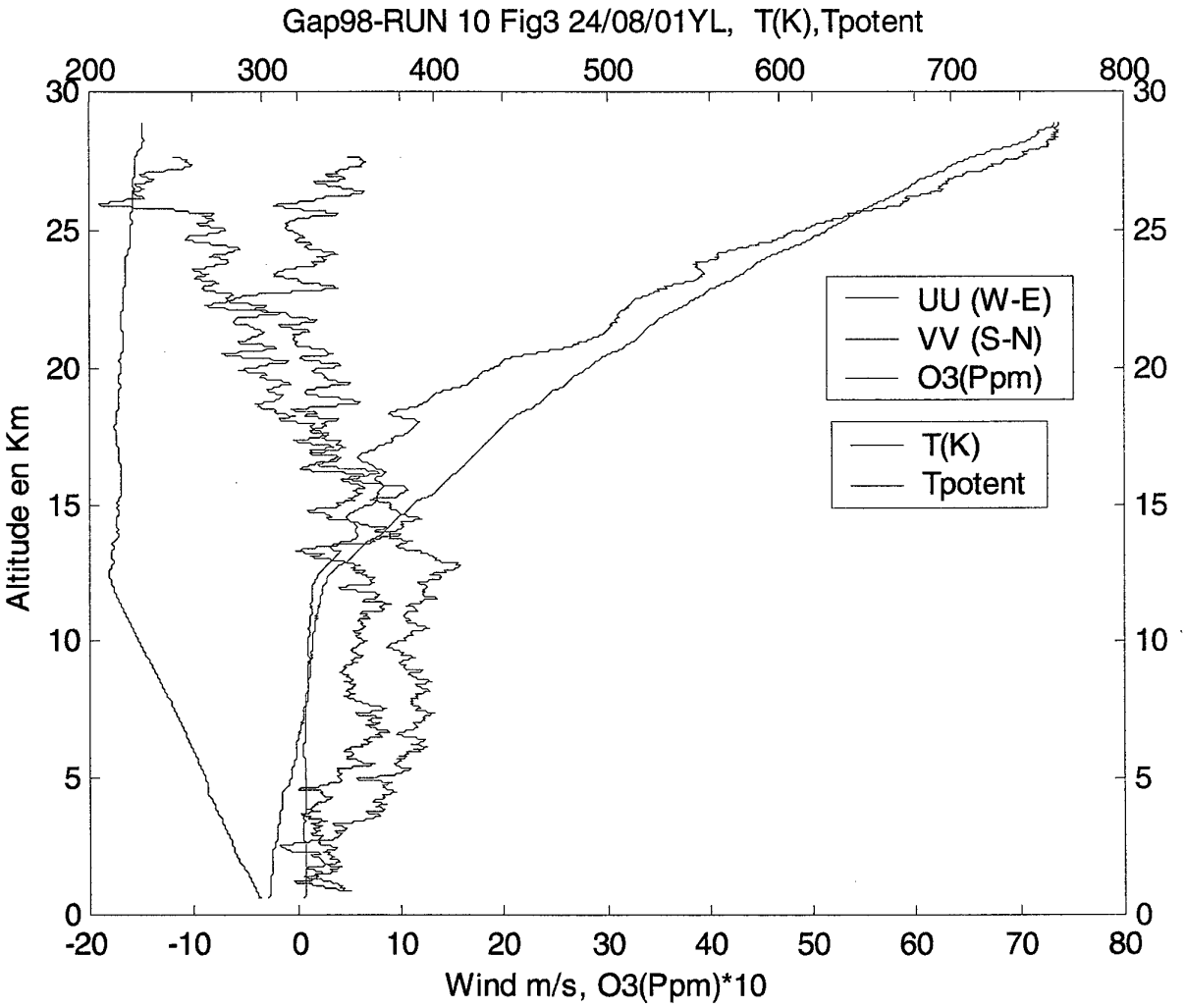
Gap98-RUN 10 Fig3 24/08/01YL, T(K),Tpotent
200
300
400
500
600
700
800
30
25
20
15
10
5
0
Altitude en Km
UU (W-E)
VV (S-N)
O3(Ppm)
T(K)
Tpotent
-20
-10
0
10
20
30
40
50
60
70
80
Wind m/s, O3(Ppm)*10

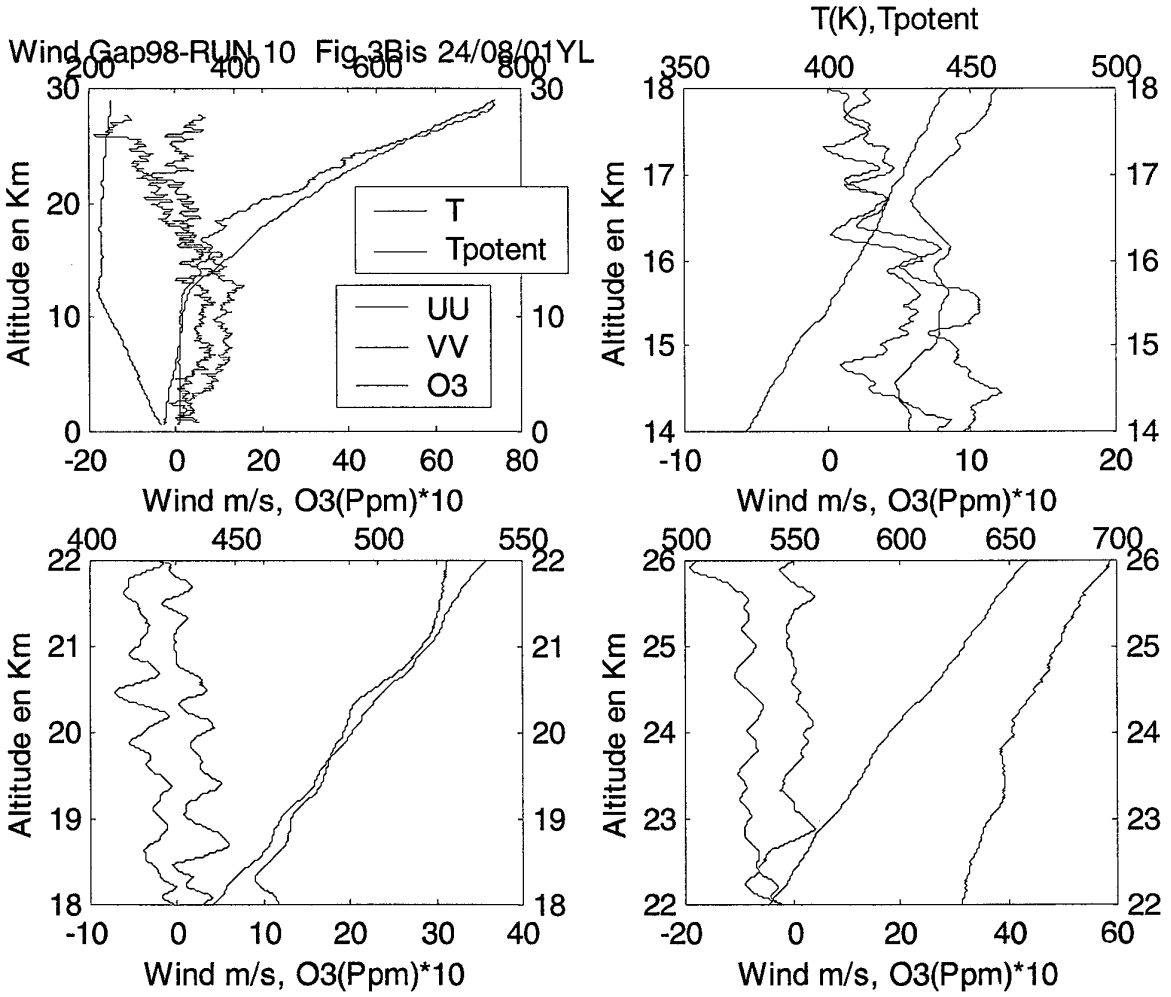
Wind Gap98-RUN 10 Fig 3Bis 24/08/01YL
Altitude en Km
Wind m/s, O3(Ppm)*10
T
Tpotent
UU
VV
O3
T(K), Tpotent
Altitude en Km
Wind m/s, O3(Ppm)*10
Altitude en Km
Wind m/s, O3(Ppm)*10
Altitude en Km
Wind m/s, O3(Ppm)*10

SANS MENTION
DE PROTECTION

SMP

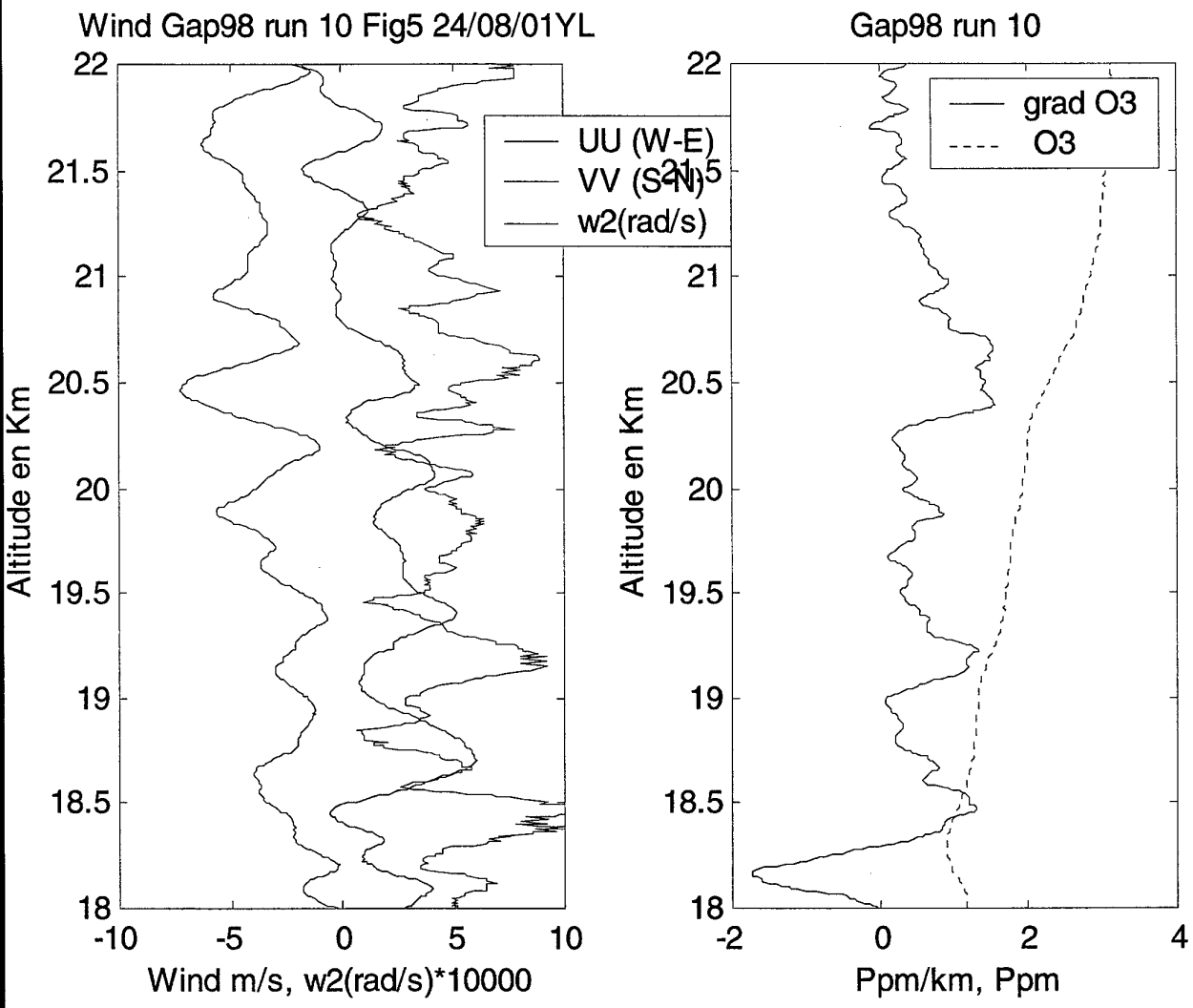

ONERA

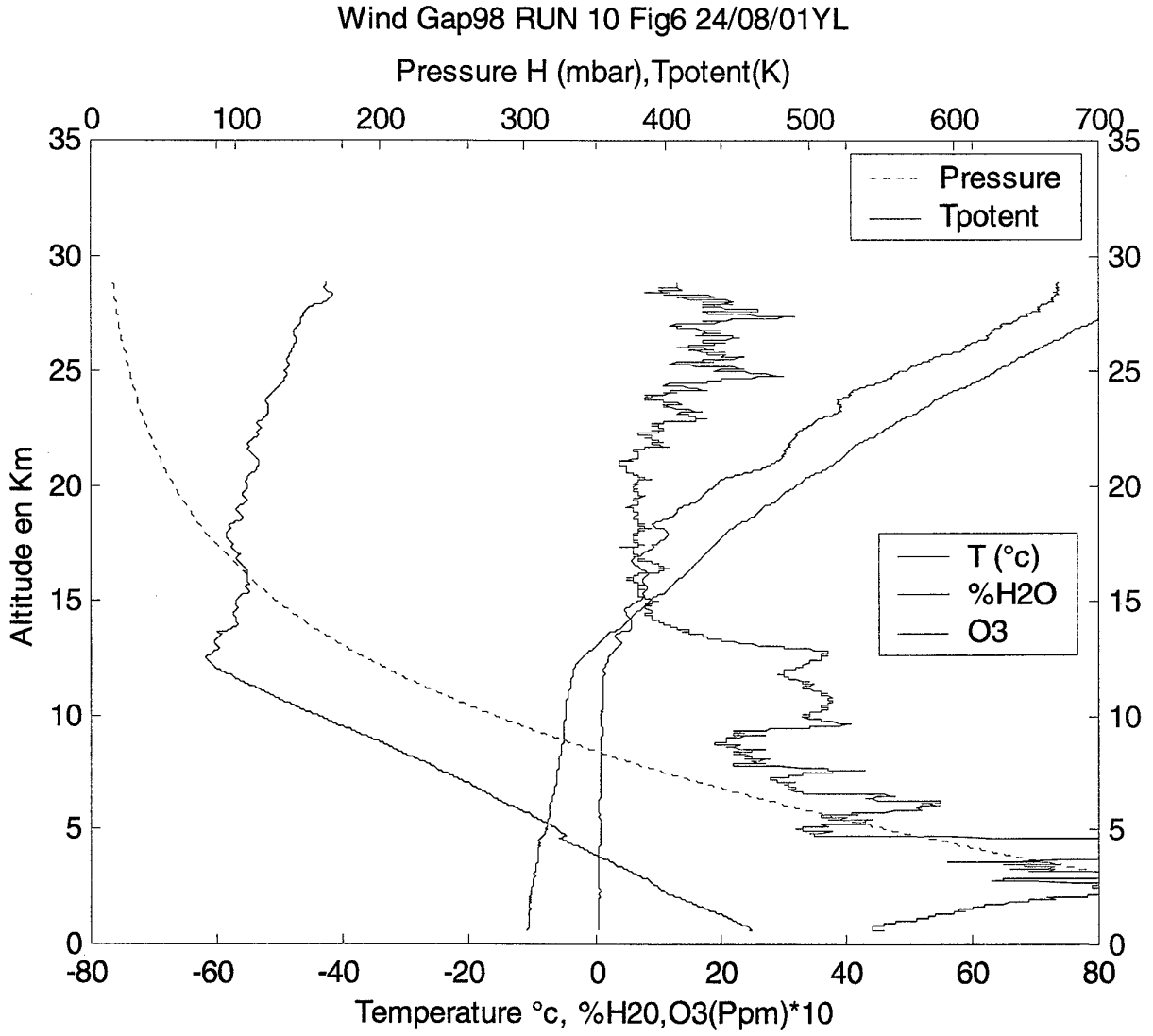
Wind Gap98 RUN 10 Fig6 24/08/01YL
Pressure H (mbar),Tpotent(K)
0
100
200
300
400
500
600
700
Pressure
Tpotent
T (°c)
%H2O
O3
Altitude en Km
35
30
25
20
15
10
5
0
-80
-60
-40
-20
0
20
40
60
80
Temperature °c, %H20,O3(Ppm)*10

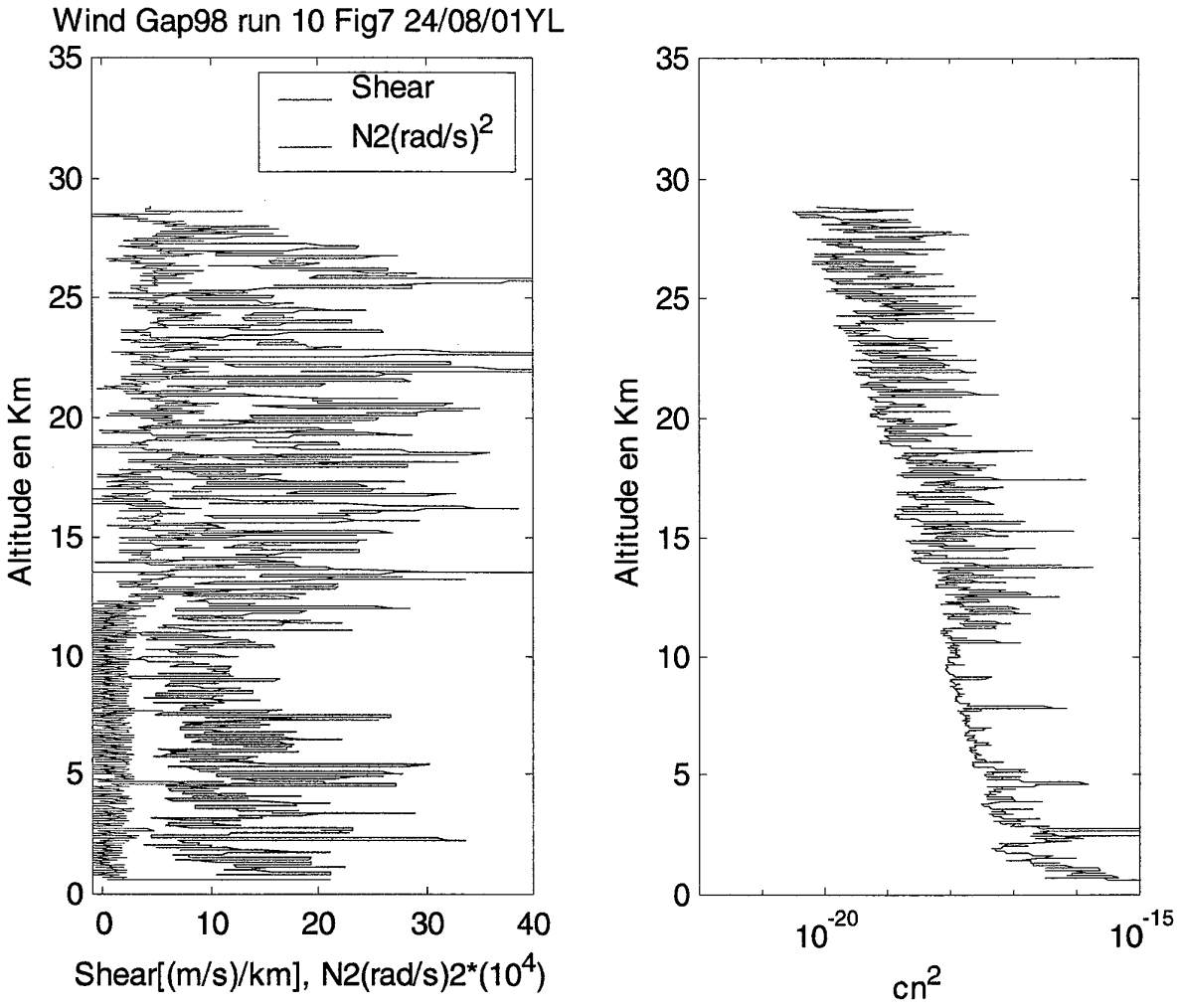
Wind Gap98 run 10 Fig7 24/08/01YL
Shear
N2(rad/s)2
Altitude en Km
Shear[(m/s)/km], N2(rad/s)2*(10^4)
cn2

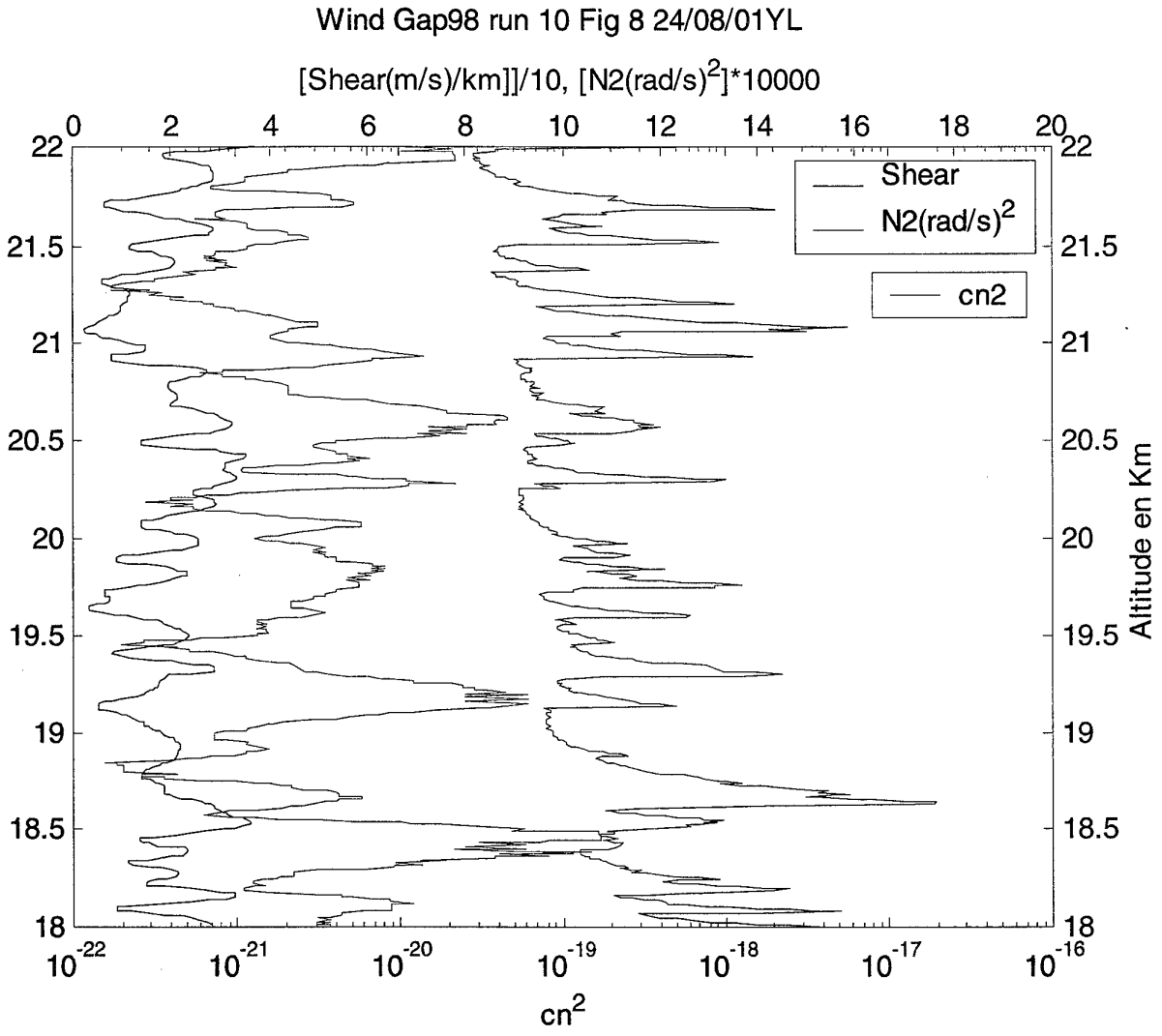
Wind Gap98 run 10 Fig 8 24/08/01YL
[Shear(m/s)/km]]/10, [N2(rad/s)2]*10000
Shear
N2(rad/s)2
cn2
Altitude en Km
cn2

GAP98- Graphs RUN n°11

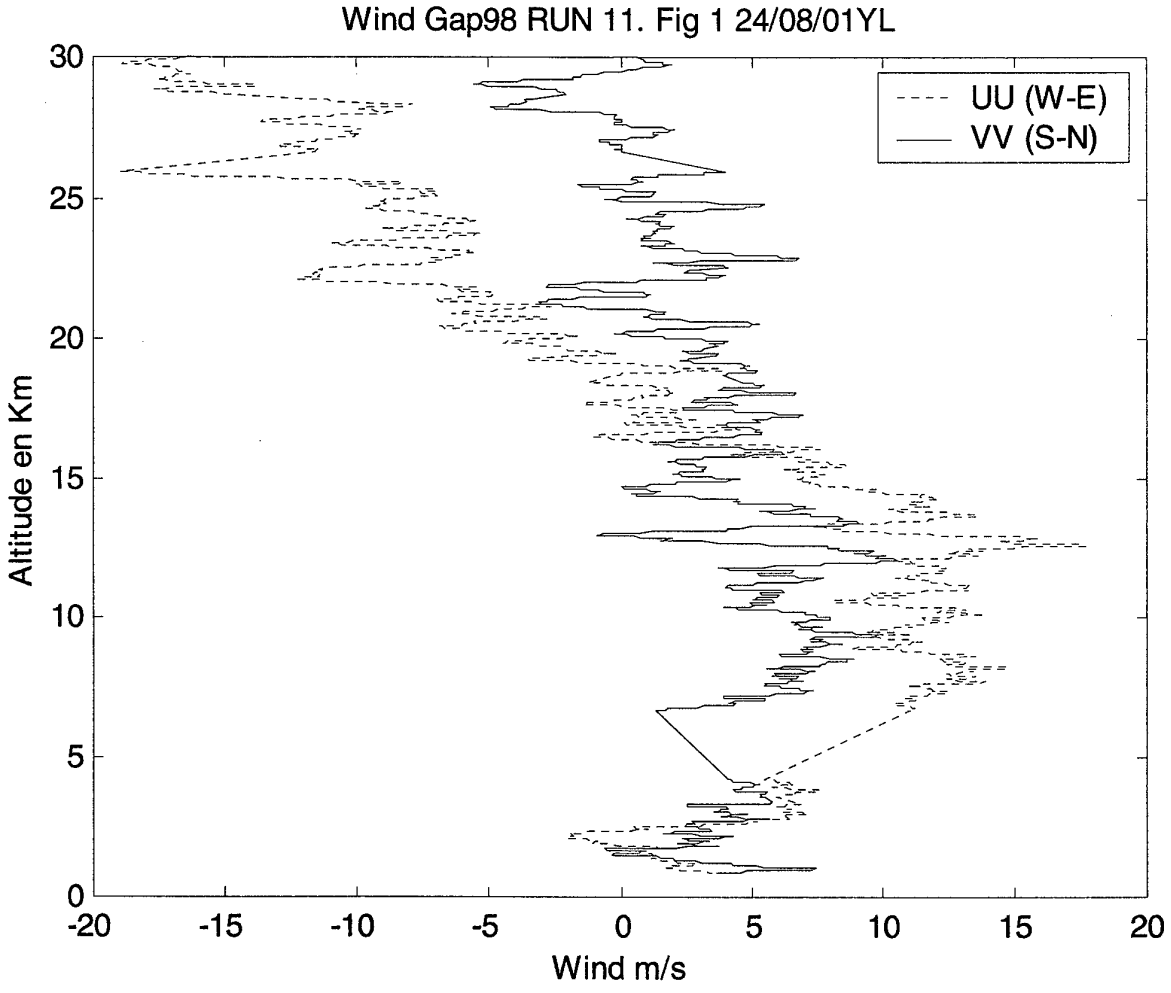
Wind Gap98 RUN 11. Fig 1 24/08/01YL
UU (W-E)
VV (S-N)
Altitude en Km
Wind m/s
30
25
20
15
10
5
0
-20
-15
-10
-5
0
5
10
15
20

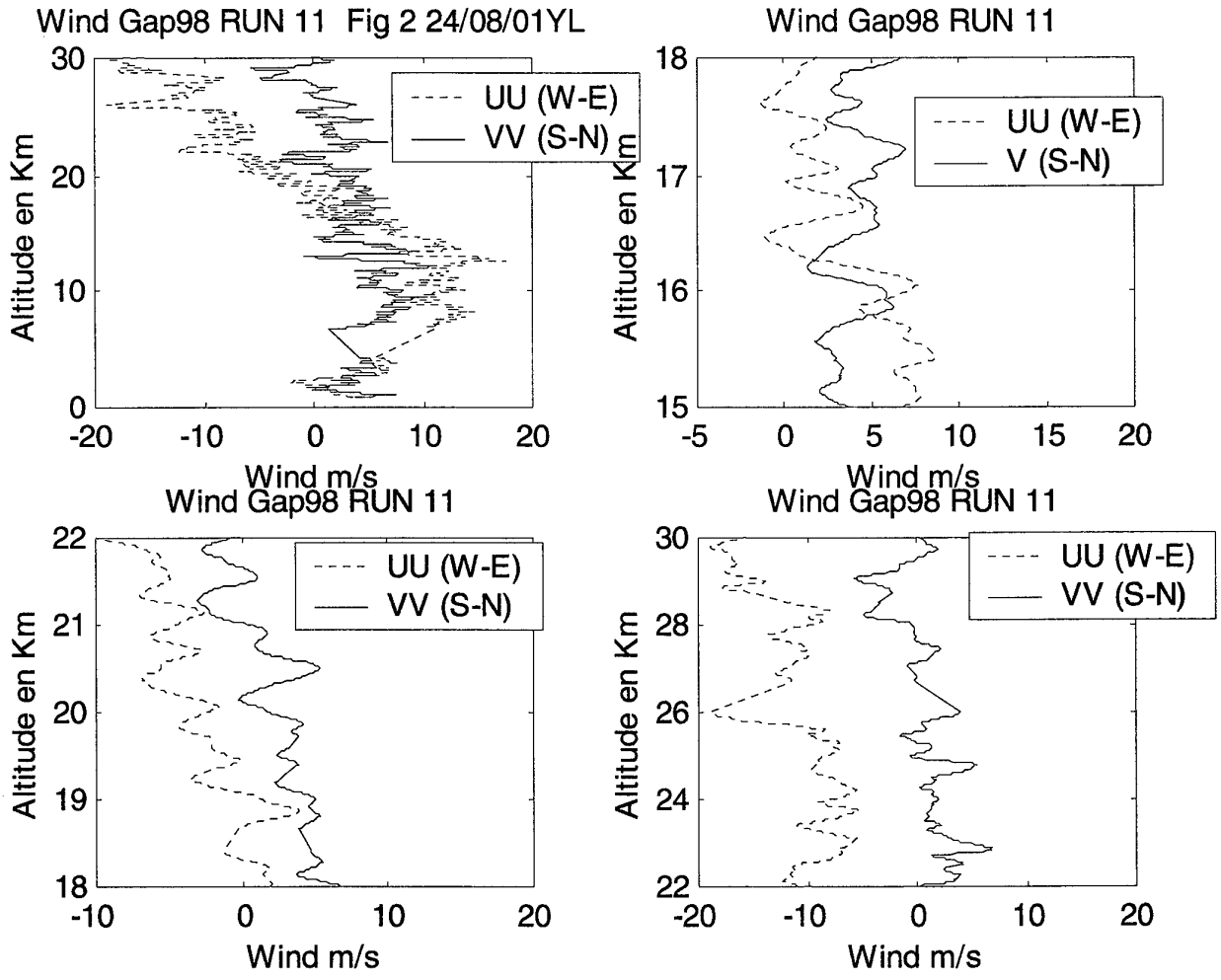
Wind Gap98 RUN 11 Fig 2 24/08/01YL
Altitude en Km
Wind m/s
UU (W-E)
VV (S-N)
Wind Gap98 RUN 11
Altitude en Km
Wind m/s
UU (W-E)
V (S-N)
Wind Gap98 RUN 11
Altitude en Km
Wind m/s
UU (W-E)
VV (S-N)
Wind Gap98 RUN 11
Altitude en Km
Wind m/s
UU (W-E)
VV (S-N)

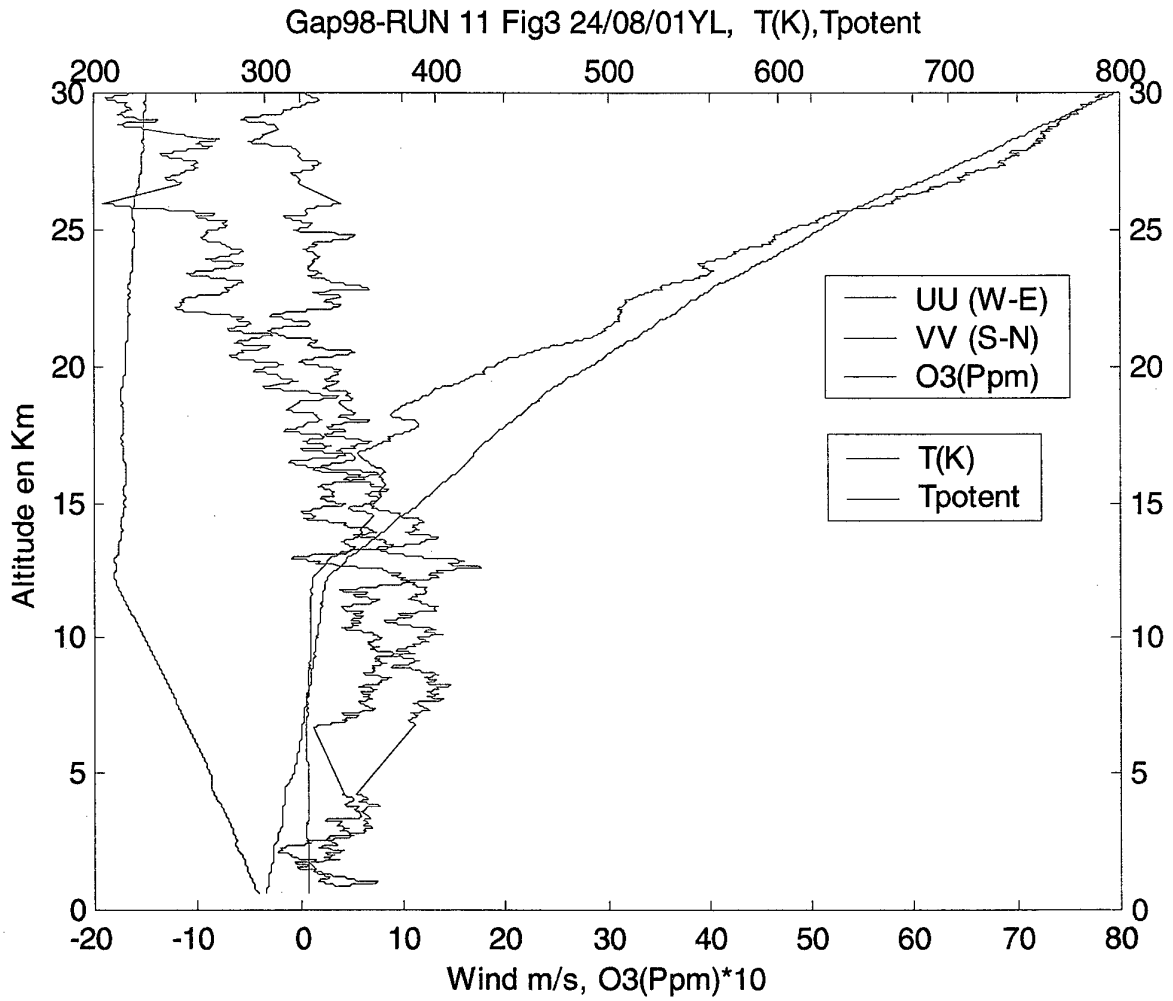
Gap98-RUN 11 Fig3 24/08/01YL, T(K),Tpotent
Altitude en Km
Wind m/s, O3(Ppm)*10
UU (W-E)
VV (S-N)
O3(Ppm)
T(K)
Tpotent

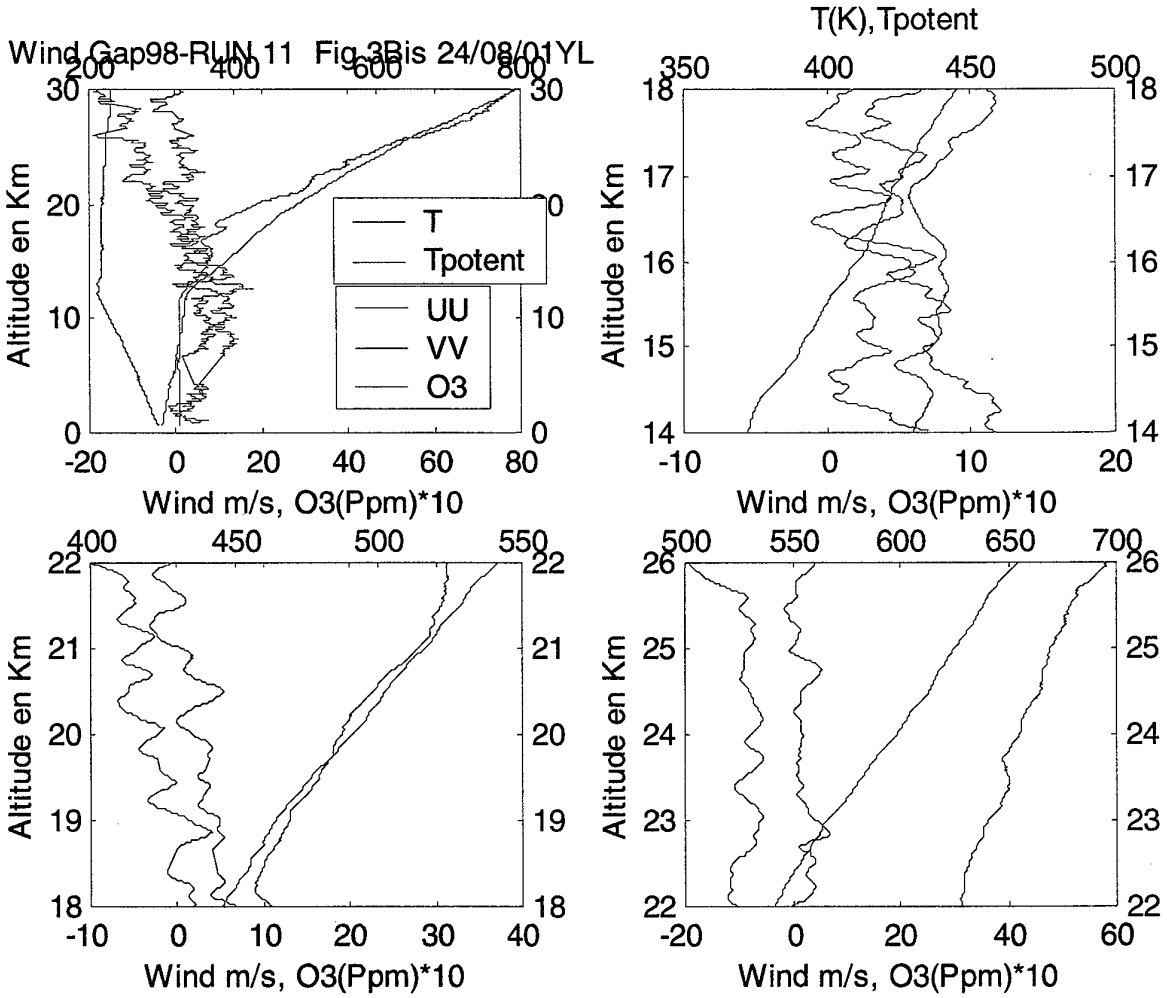
Wind Gap98-RUN 11 Fig 3Bis 24/08/01YL
Altitude en Km
Wind m/s, O3(Ppm)*10
T
Tpotent
UU
VV
O3
T(K),Tpotent

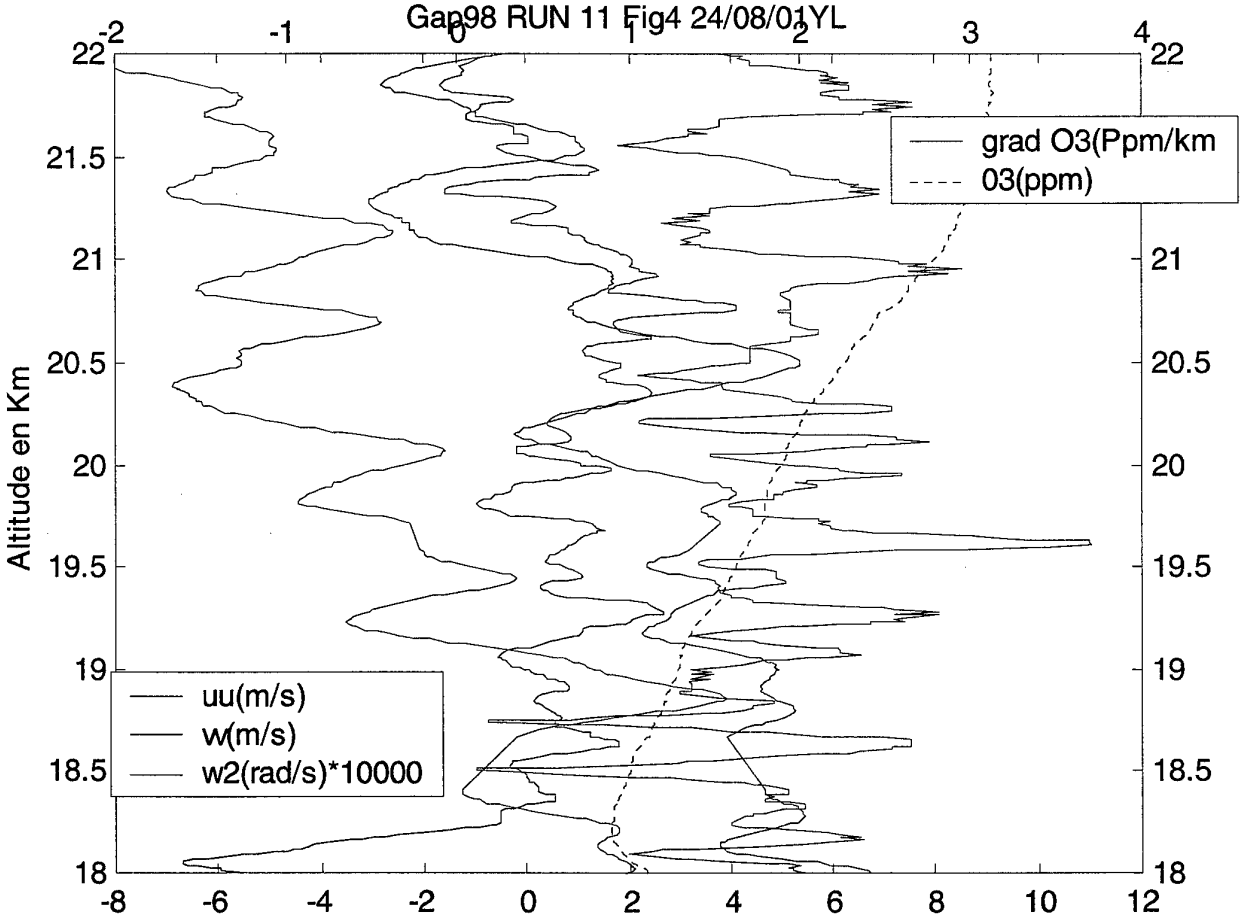
Gap98 RUN 11 Fig4 24/08/01YL
Altitude en Km
grad O3(Ppm/km
03(ppm)
uu(m/s)
w(m/s)
w2(rad/s)*10000
-2
-1
0
1
2
3
4
22
21.5
21
20.5
20
19.5
19
18.5
18
-8
-6
-4
-2
0
2
4
6
8
10
12

ONERA

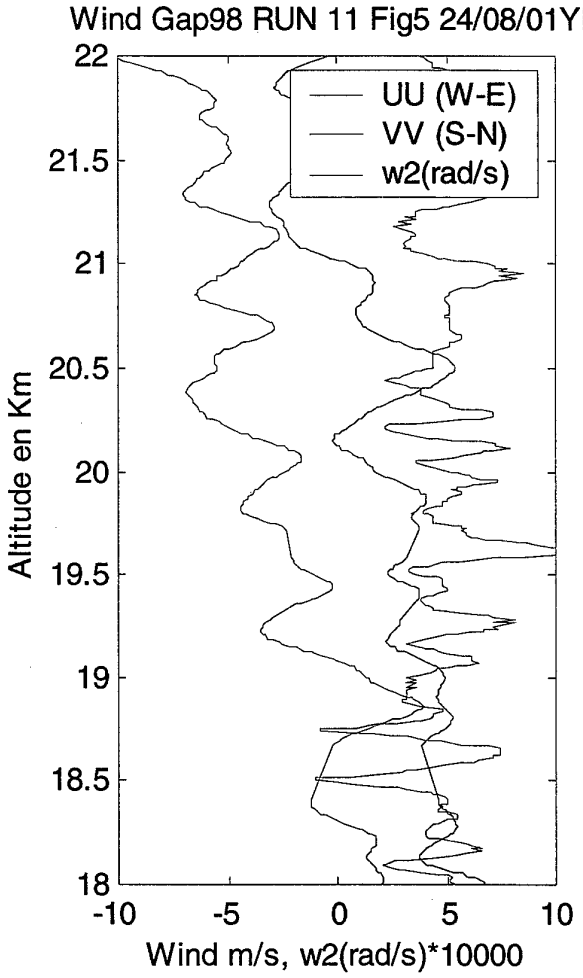
Wind Gap98 RUN 11 Fig5 24/08/01YL
UU (W-E)
VV (S-N)
w2(rad/s)
Altitude en Km
22
21.5
21
20.5
20
19.5
19
18.5
18
-10
-5
0
5
10
Wind m/s, w2(rad/s)*10000

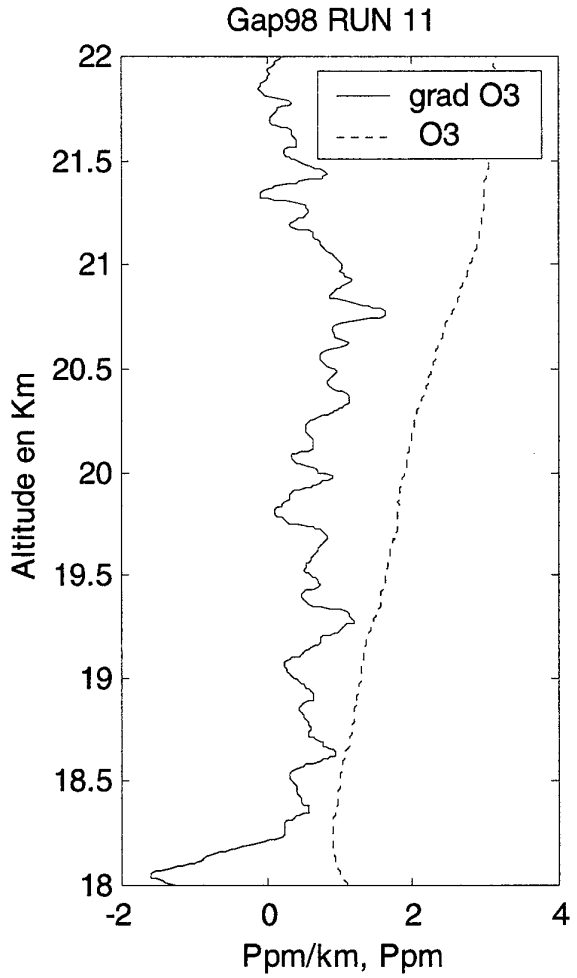
Gap98 RUN 11
grad O3
O3
Altitude en Km
22
21.5
21
20.5
20
19.5
19
18.5
18
-2
0
2
4
Ppm/km, Ppm

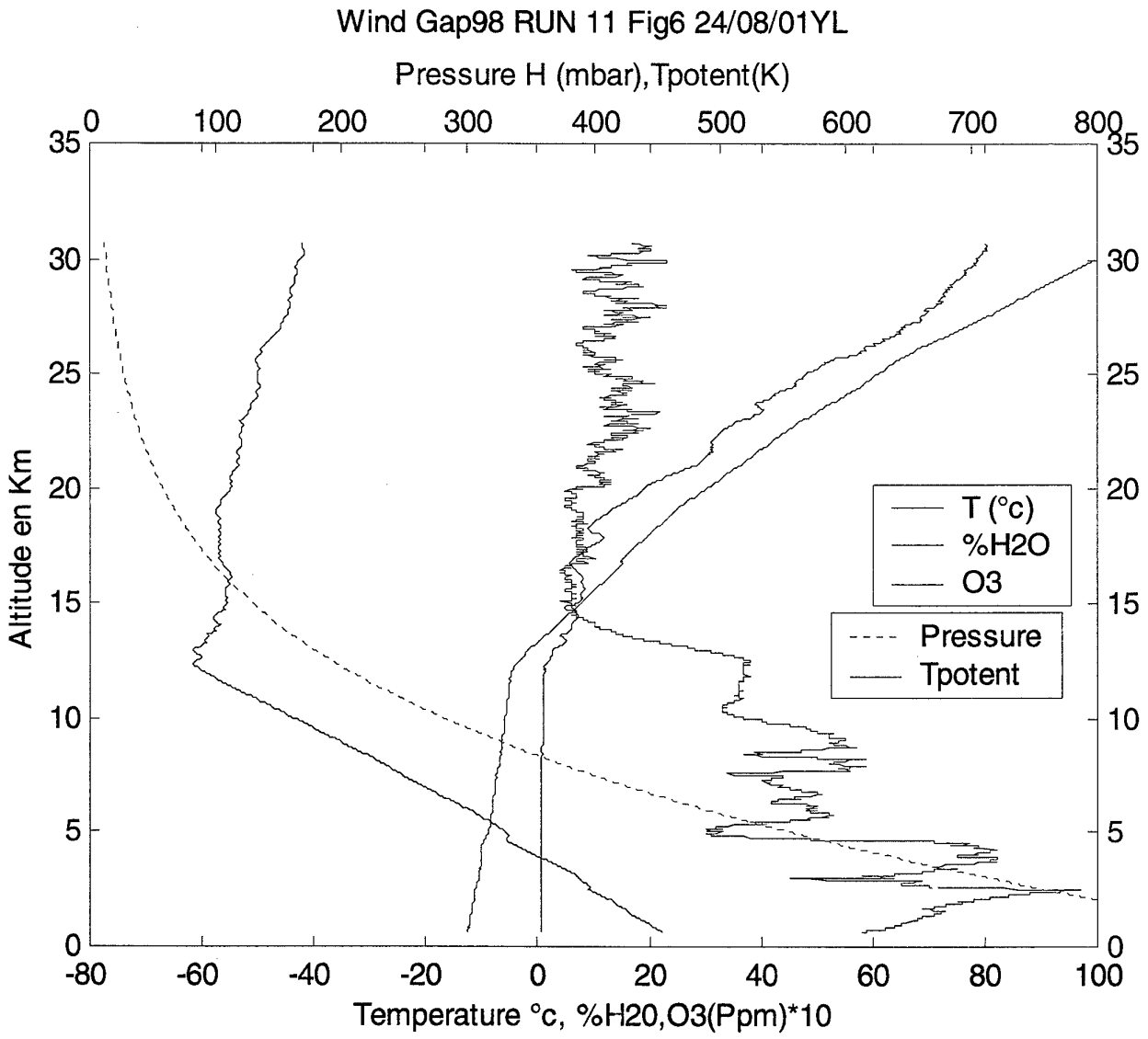
Wind Gap98 RUN 11 Fig6 24/08/01YL
Pressure H (mbar),Tpotent(K)
0
100
200
300
400
500
600
700
800
35
30
25
20
15
10
5
0
Altitude en Km
T (°c)
%H2O
O3
Pressure
Tpotent
-80
-60
-40
-20
0
20
40
60
80
100
Temperature °c, %H20,O3(Ppm)*10

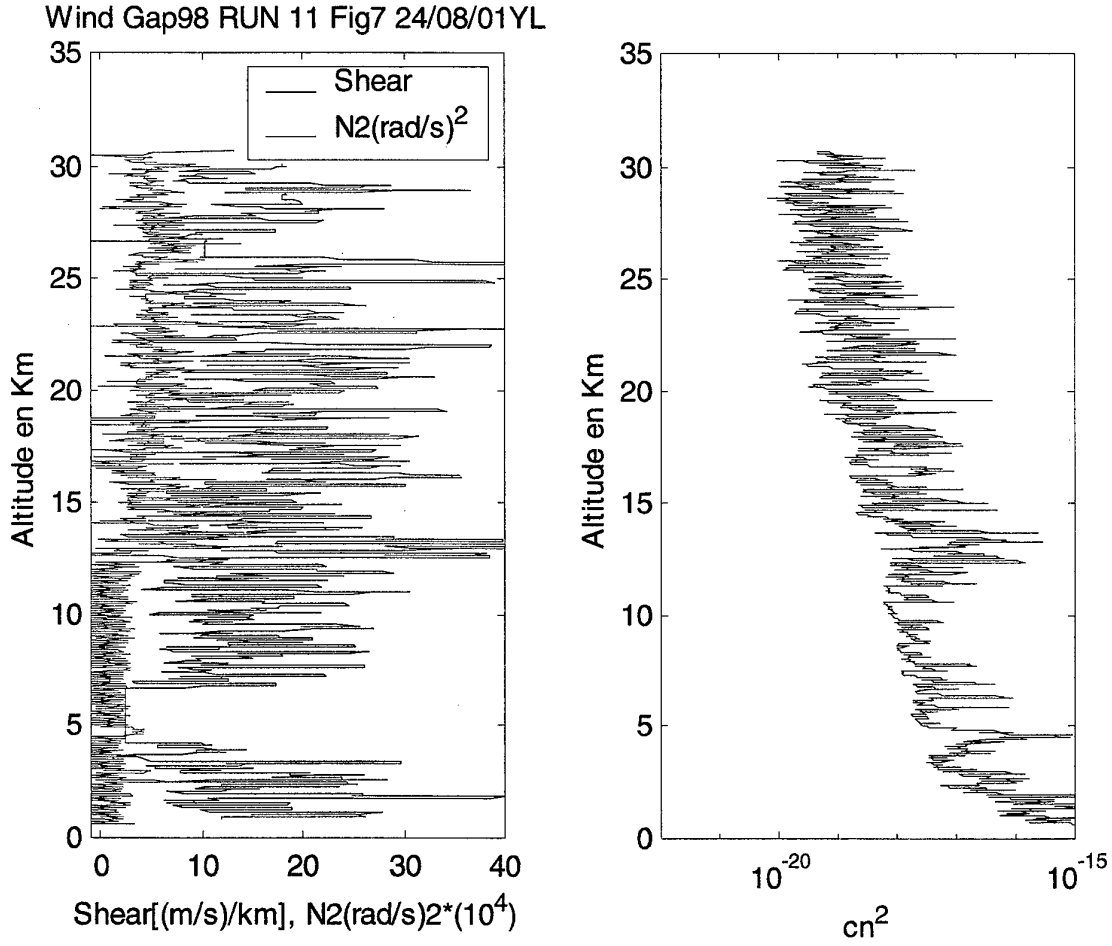
Wind Gap98 RUN 11 Fig7 24/08/01YL
Shear
N2(rad/s)2
Altitude en Km
Shear[(m/s)/km], N2(rad/s)2*(10^4)
cn2
10^-20
10^-15

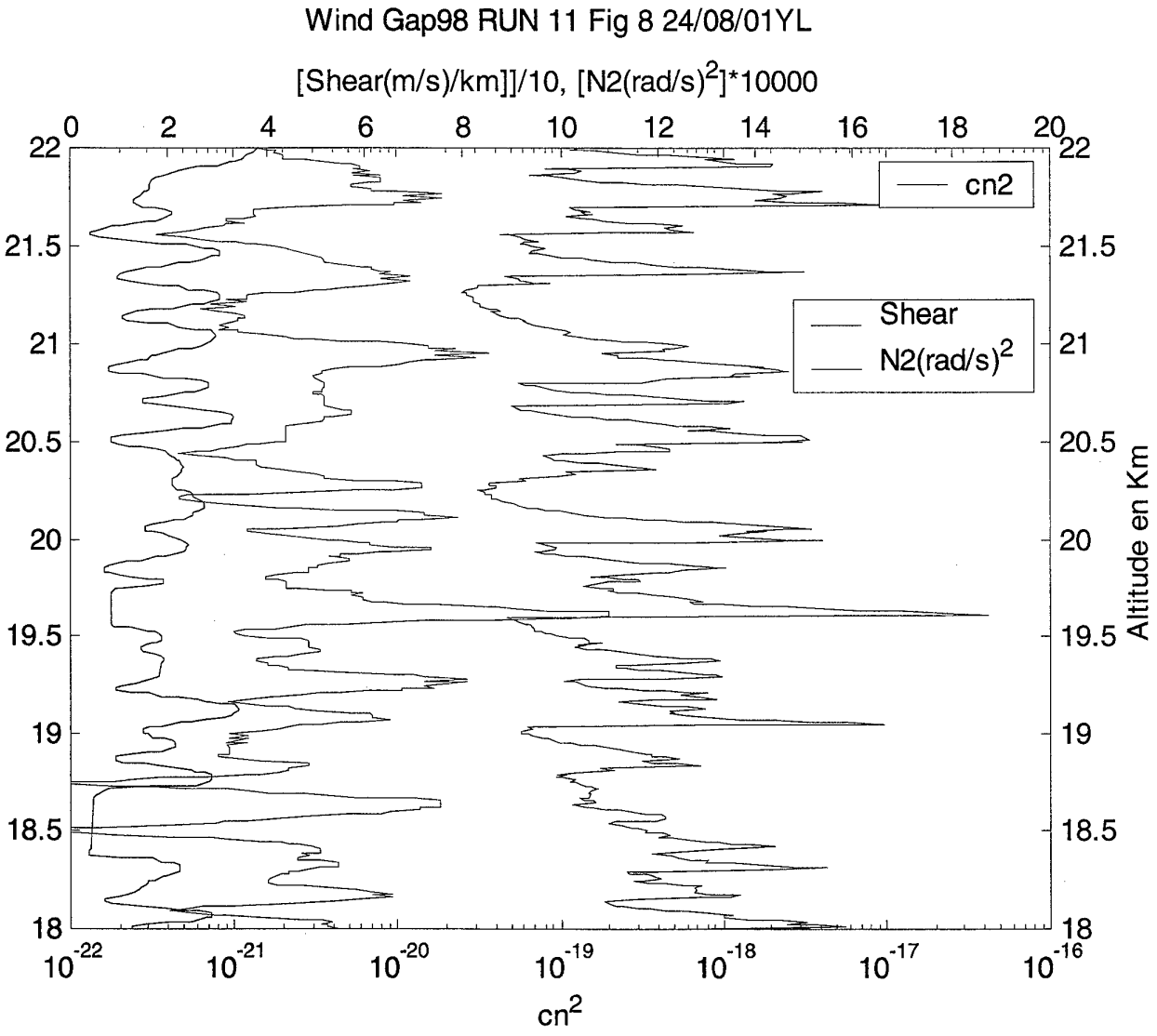
Wind Gap98 RUN 11 Fig 8 24/08/01YL
[Shear(m/s)/km]]/10, [N2(rad/s)2]*10000
0
2
4
6
8
10
12
14
16
18
20
22
21.5
21
20.5
20
19.5
19
18.5
18
cn2
Shear
N2(rad/s)2
Altitude en Km
10-22
10-21
10-20
10-19
10-18
10-17
10-16
cn2

GAP98- Graphs RUN n°12

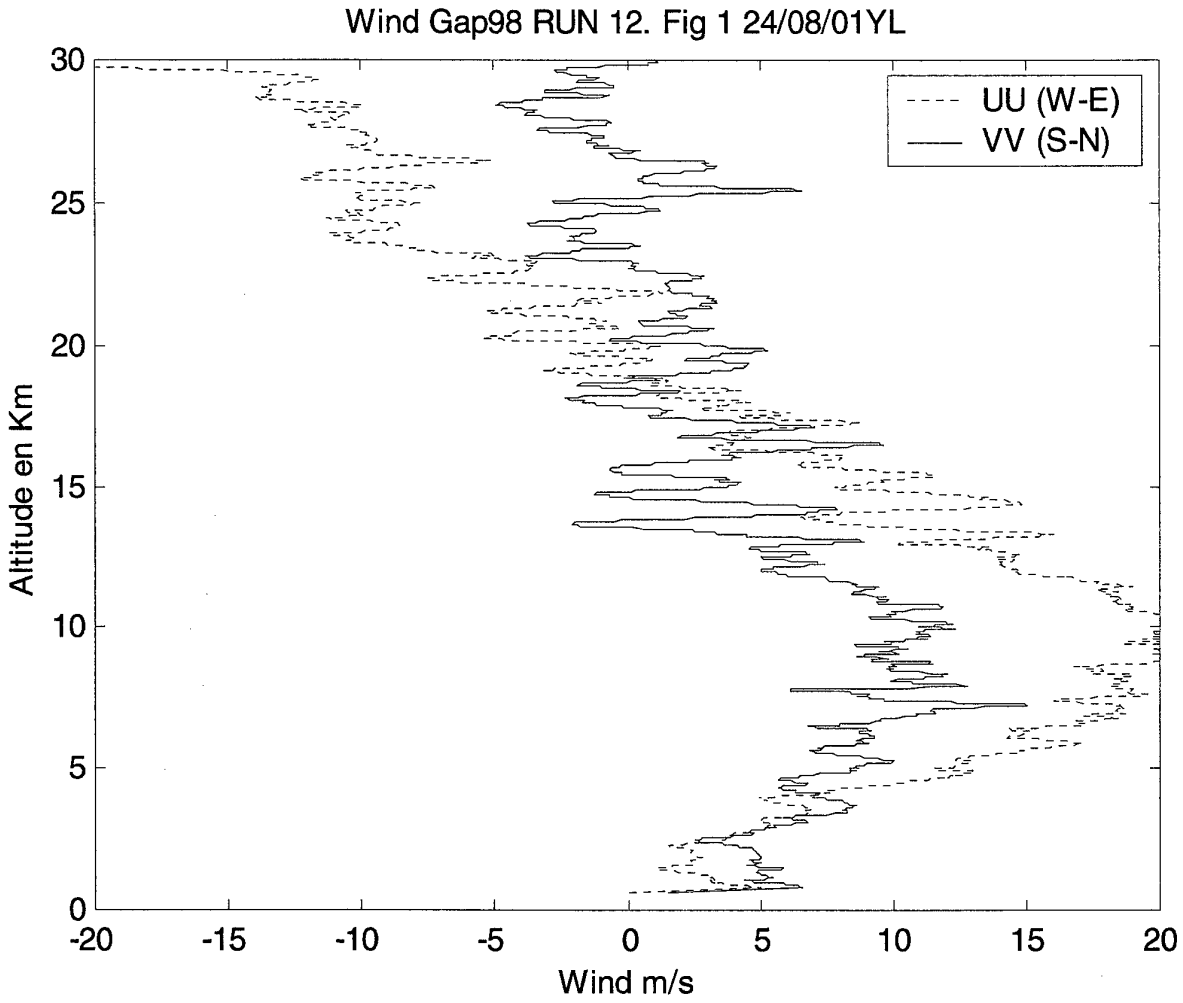
Wind Gap98 RUN 12. Fig 1 24/08/01YL
UU (W-E)
VV (S-N)
Altitude en Km
Wind m/s
30
25
20
15
10
5
0
-20
-15
-10
-5
0
5
10
15
20

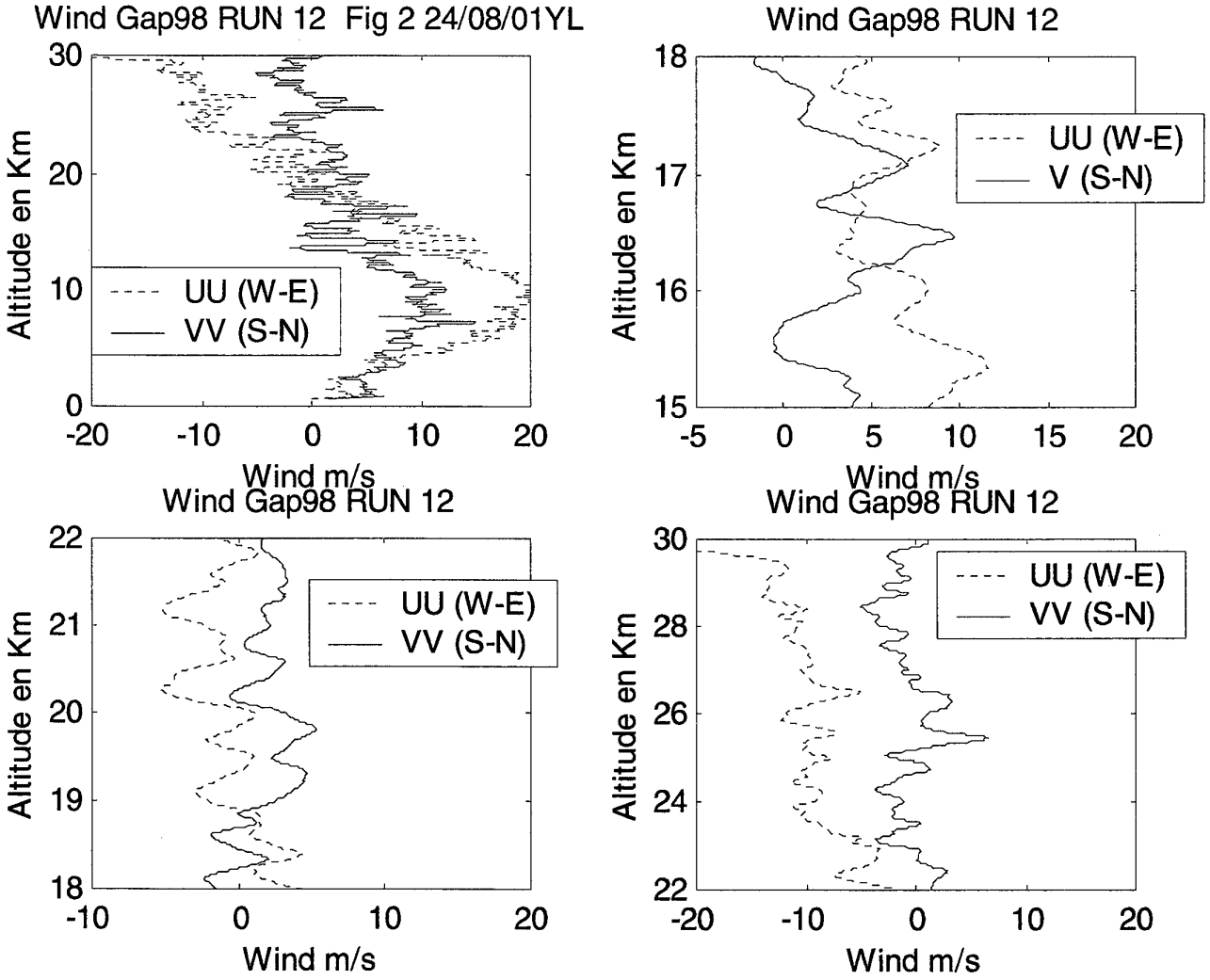
Wind Gap98 RUN 12 Fig 2 24/08/01YL
Altitude en Km
Wind m/s
UU (W-E)
VV (S-N)
Wind Gap98 RUN 12
Altitude en Km
Wind m/s
UU (W-E)
V (S-N)
Wind Gap98 RUN 12
Altitude en Km
Wind m/s
UU (W-E)
VV (S-N)
Wind Gap98 RUN 12
Altitude en Km
Wind m/s
UU (W-E)
VV (S-N)

ONERA

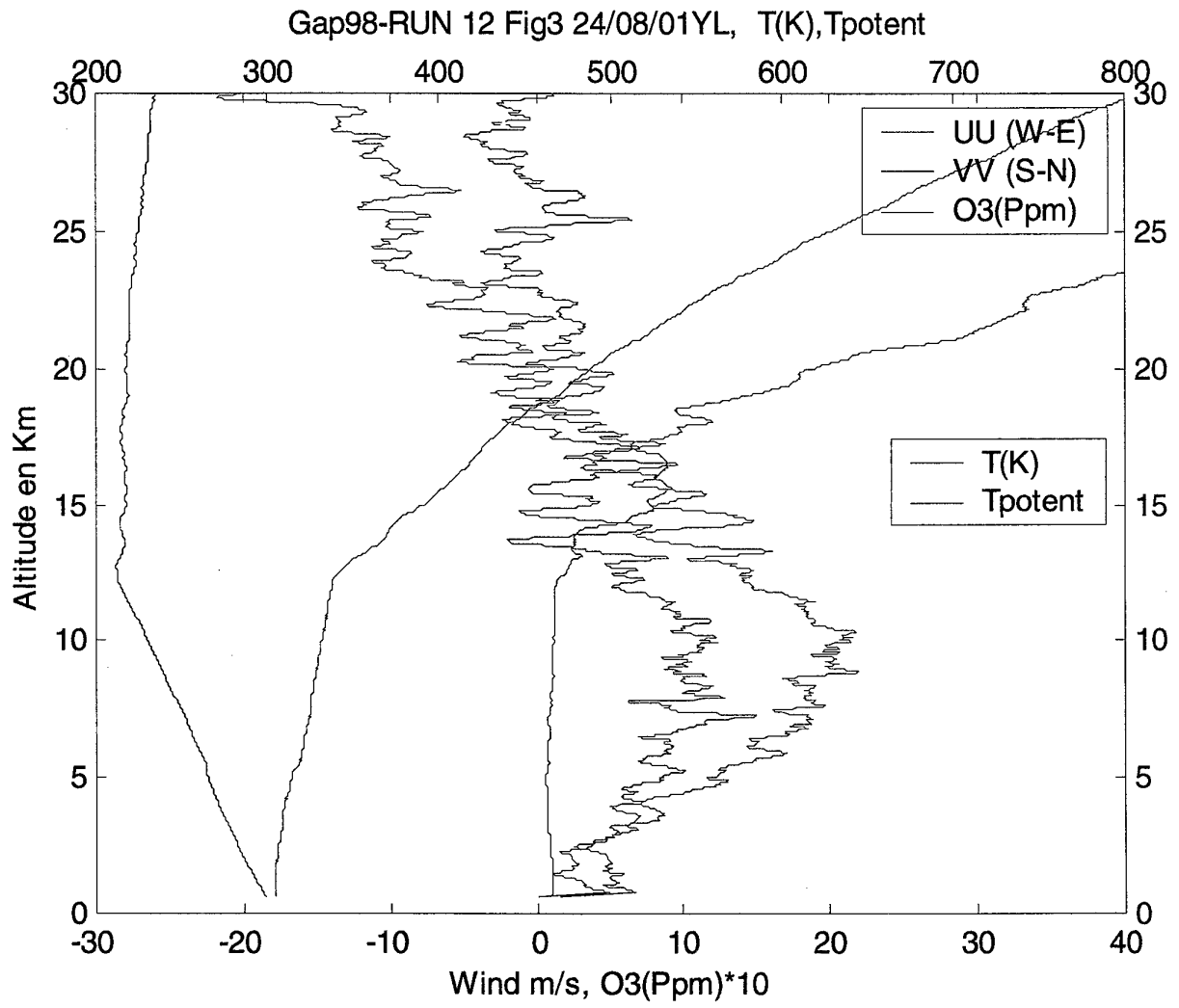
Gap98-RUN 12 Fig3 24/08/01YL, T(K),Tpotent
200
300
400
500
600
700
800
30
25
20
15
10
5
0
UU (W-E)
VV (S-N)
O3(Ppm)
T(K)
Tpotent
Altitude en Km
-30
-20
-10
0
10
20
30
40
Wind m/s, O3(Ppm)*10

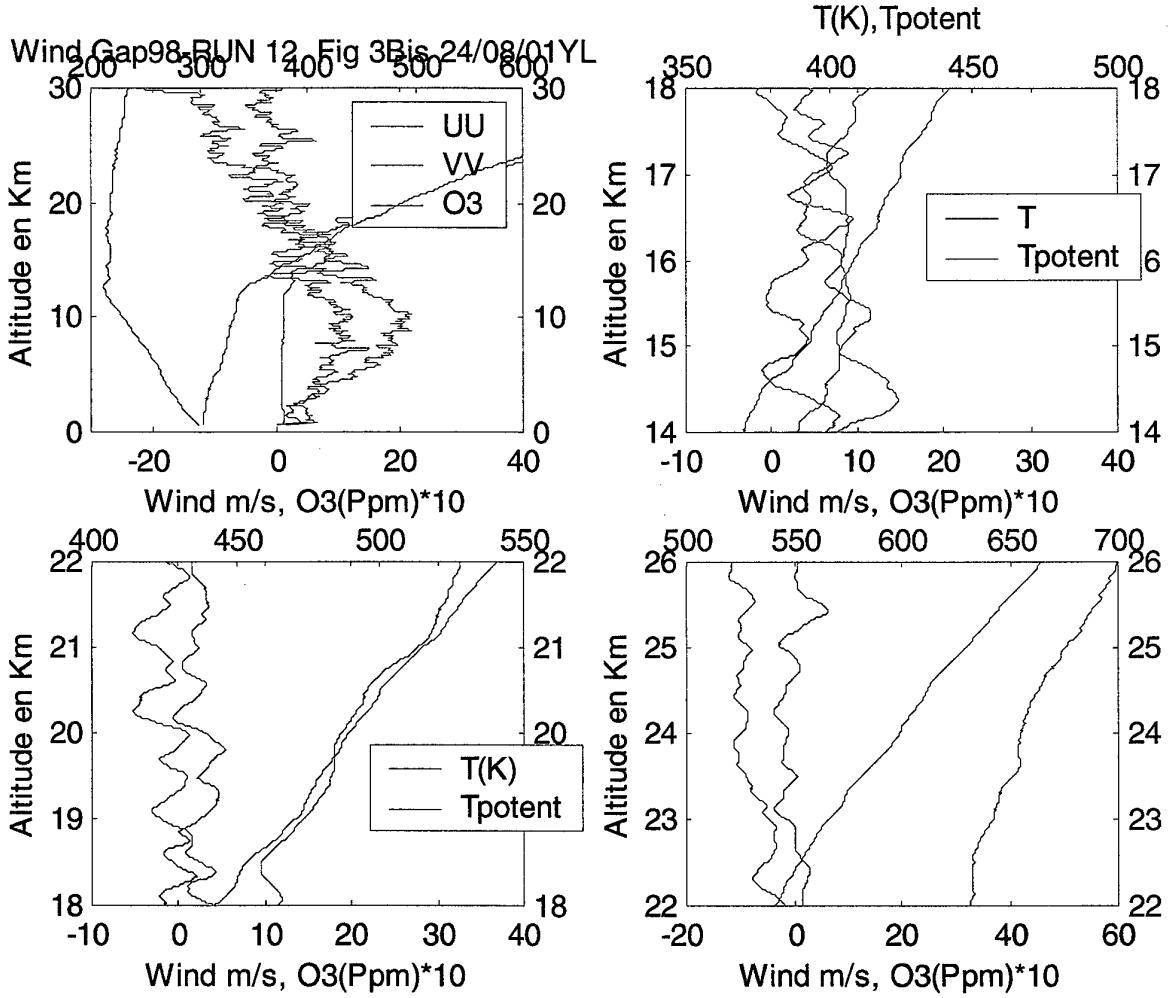
Wind Gap98 RUN 12 Fig 3Bis 24/08/01YL
Altitude en Km
Wind m/s, O3(Ppm)*10
UU
VV
O3
T(K),Tpotent
T
Tpotent
T(K)
Tpotent

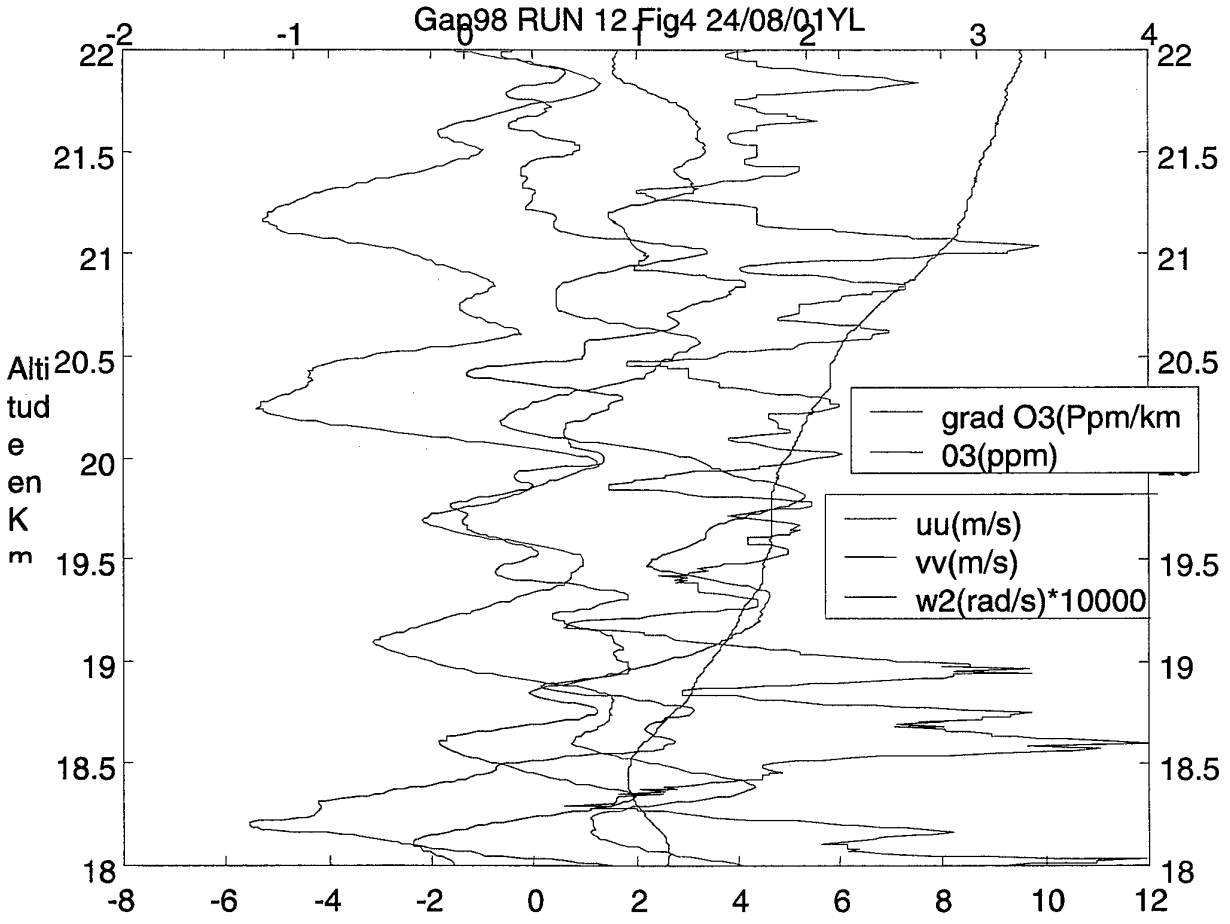
Gap98 RUN 12 Fig4 24/08/01YL
Altitude en Km
grad O3(Ppm/km
03(ppm)
uu(m/s)
vv(m/s)
w2(rad/s)*10000

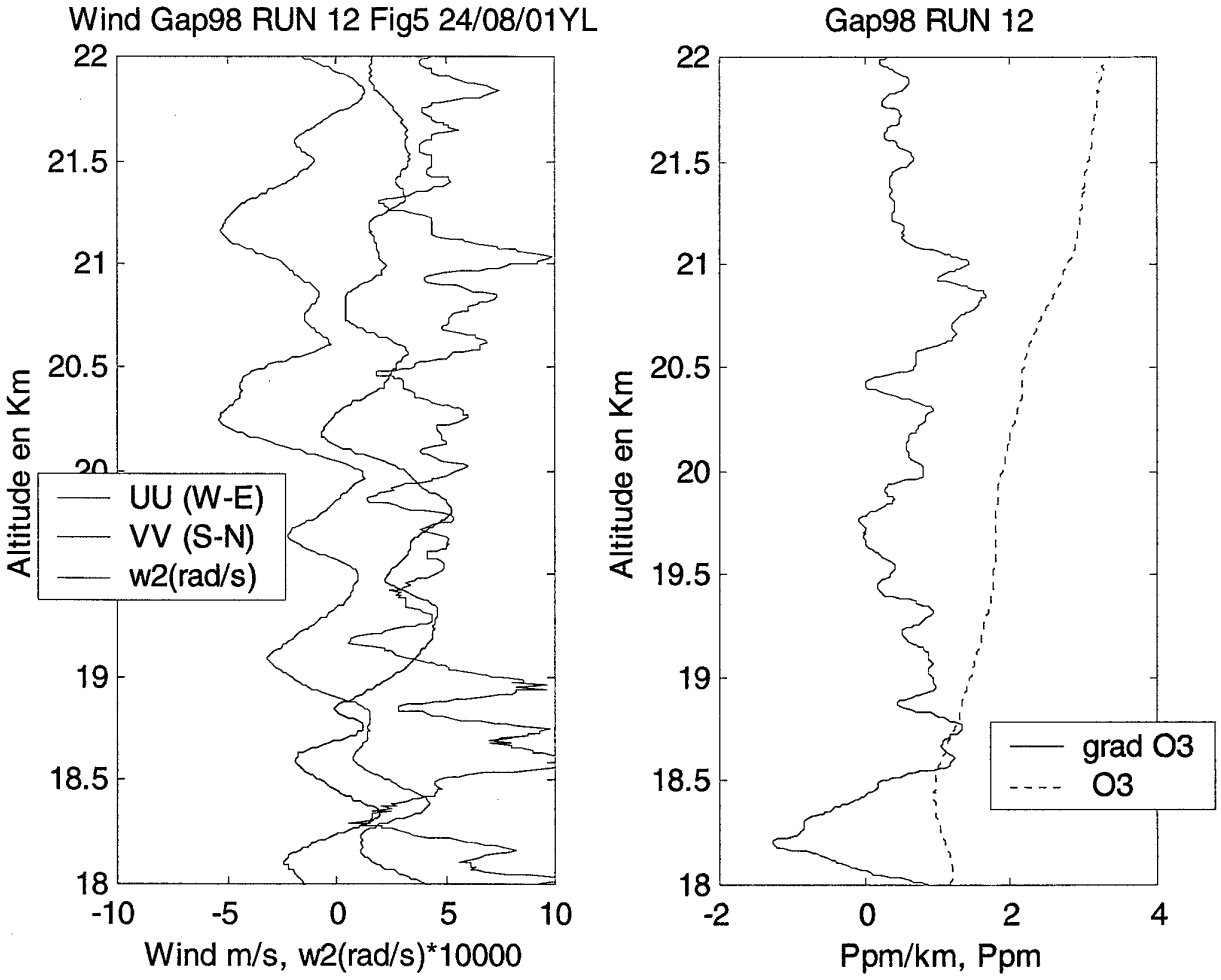
Wind Gap98 RUN 12 Fig5 24/08/01YL
Altitude en Km
22
21.5
21
20.5
20
19
18.5
18
UU (W-E)
VV (S-N)
w2(rad/s)
-10
-5
0
5
10
Wind m/s, w2(rad/s)*10000
Gap98 RUN 12
Altitude en Km
22
21.5
21
20.5
20
19.5
19
18.5
18
grad O3
O3
-2
0
2
4
Ppm/km, Ppm

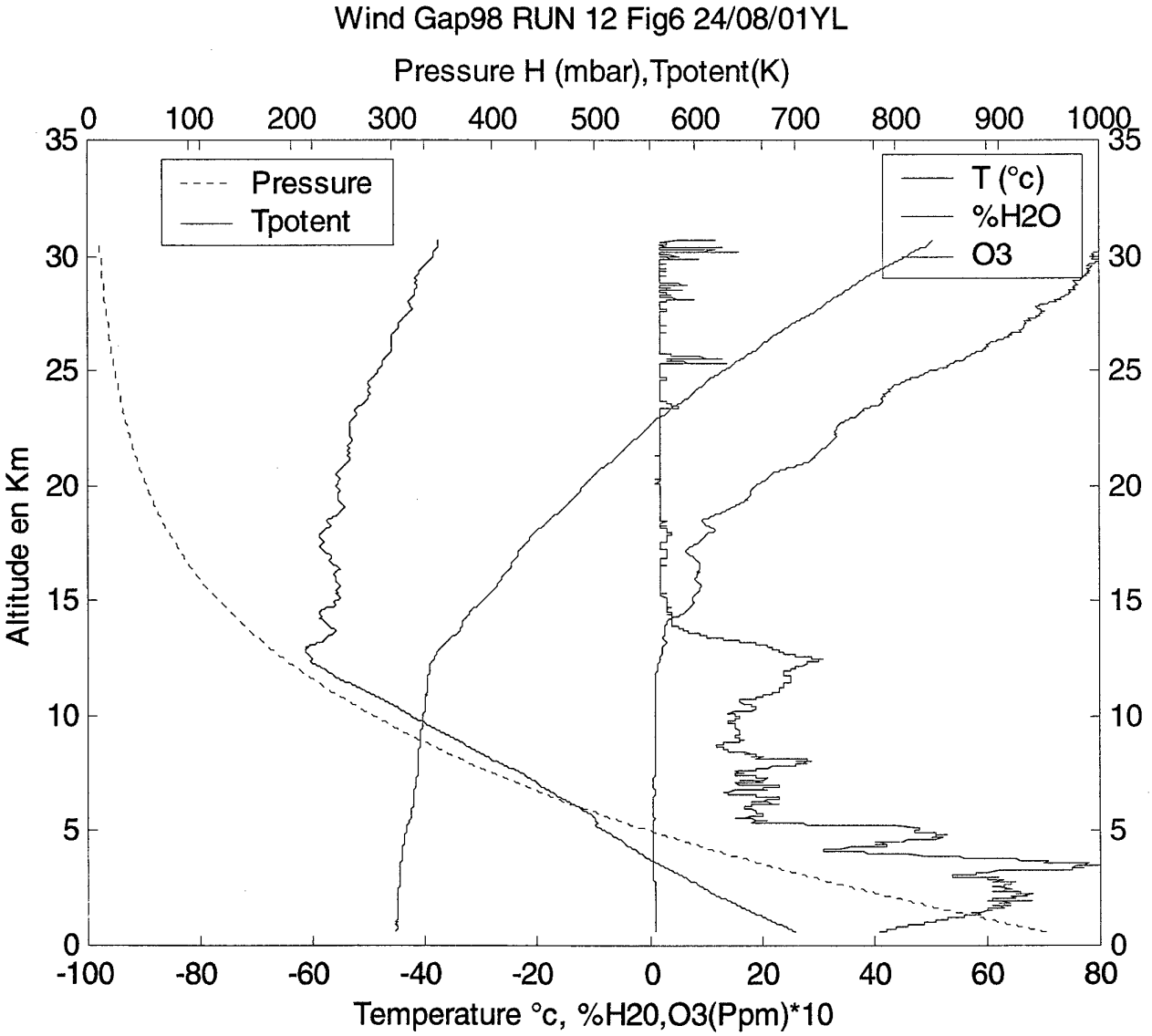
Wind Gap98 RUN 12 Fig6 24/08/01YL
Pressure H (mbar),Tpotent(K)
0
100
200
300
400
500
600
700
800
900
1000
Pressure
Tpotent
T (°c)
%H2O
O3
Altitude en Km
35
30
25
20
15
10
5
0
-100
-80
-60
-40
-20
0
20
40
60
80
Temperature °c, %H20,O3(Ppm)*10

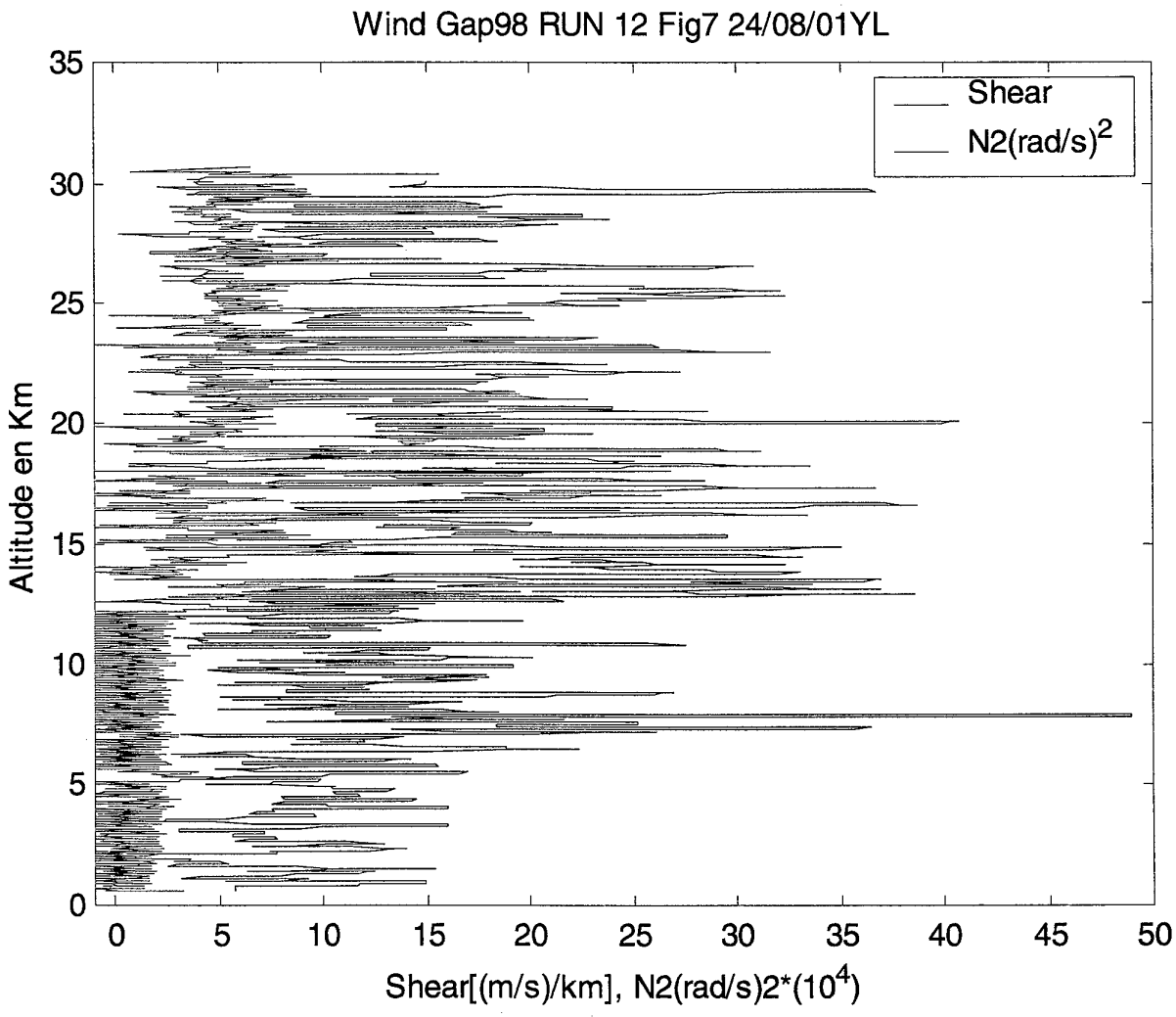
Wind Gap98 RUN 12 Fig7 24/08/01YL
Shear
N2(rad/s)2
Altitude en Km
0
5
10
15
20
25
30
35
0
5
10
15
20
25
30
35
40
45
50
Shear[(m/s)/km], N2(rad/s)2*(10^4)

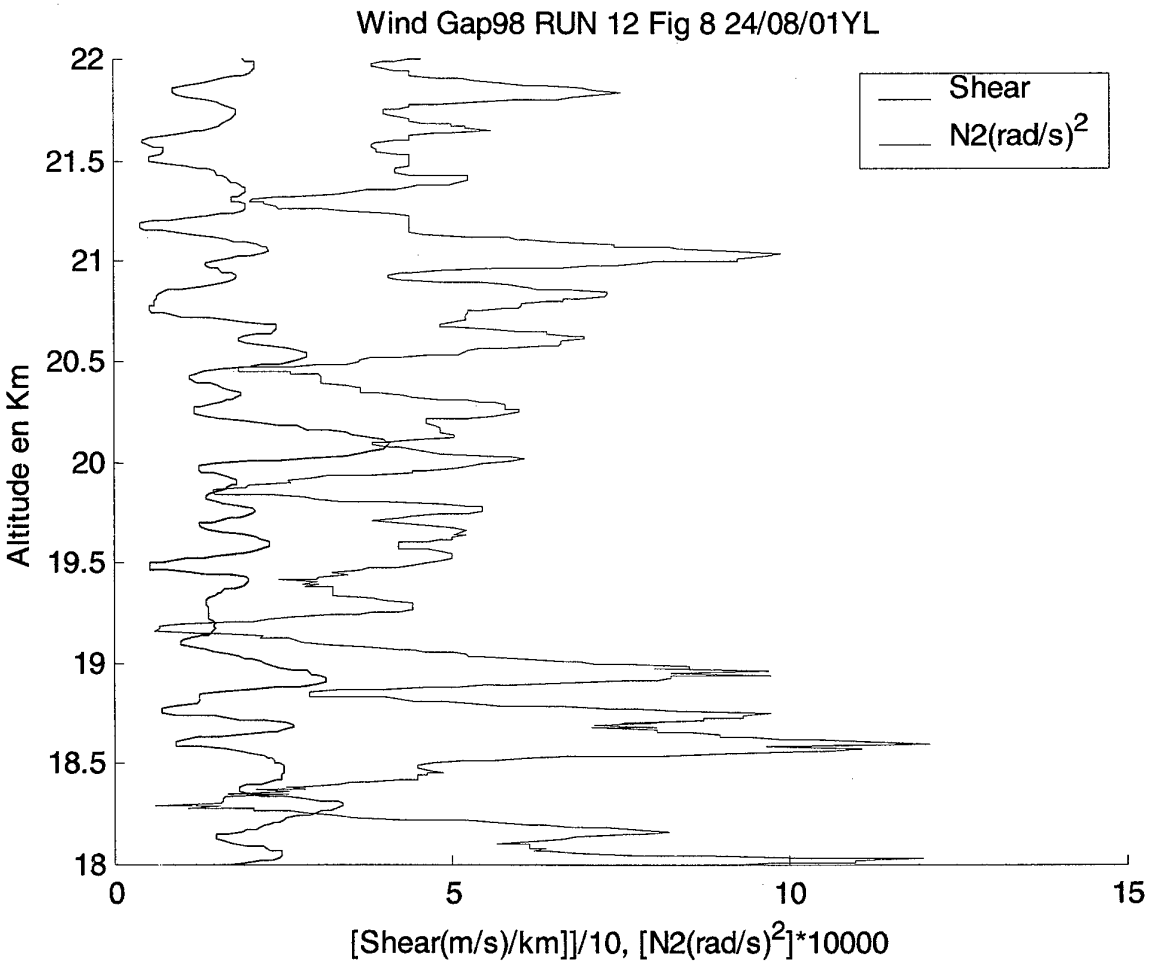
Wind Gap98 RUN 12 Fig 8 24/08/01YL
Shear
N2(rad/s)2
Altitude en Km
22
21.5
21
20.5
20
19.5
19
18.5
18
0
5
10
15
[Shear(m/s)/km]]/10, [N2(rad/s)2]*10000

GAP98- Graphs RUN n°14

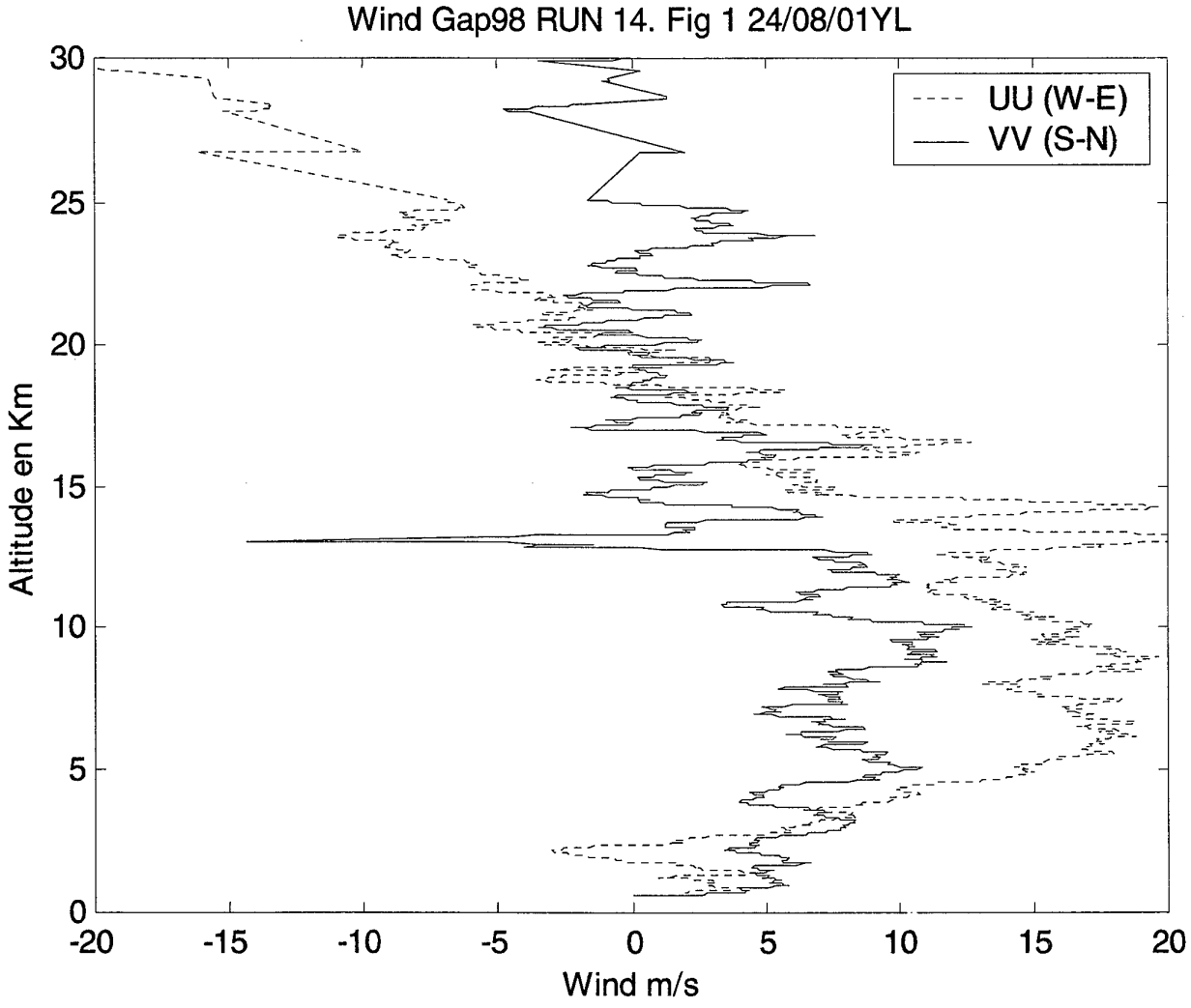
Wind Gap98 RUN 14. Fig 1 24/08/01YL
UU (W-E)
VV (S-N)
Altitude en Km
Wind m/s
30
25
20
15
10
5
0
-20
-15
-10
-5
0
5
10
15
20

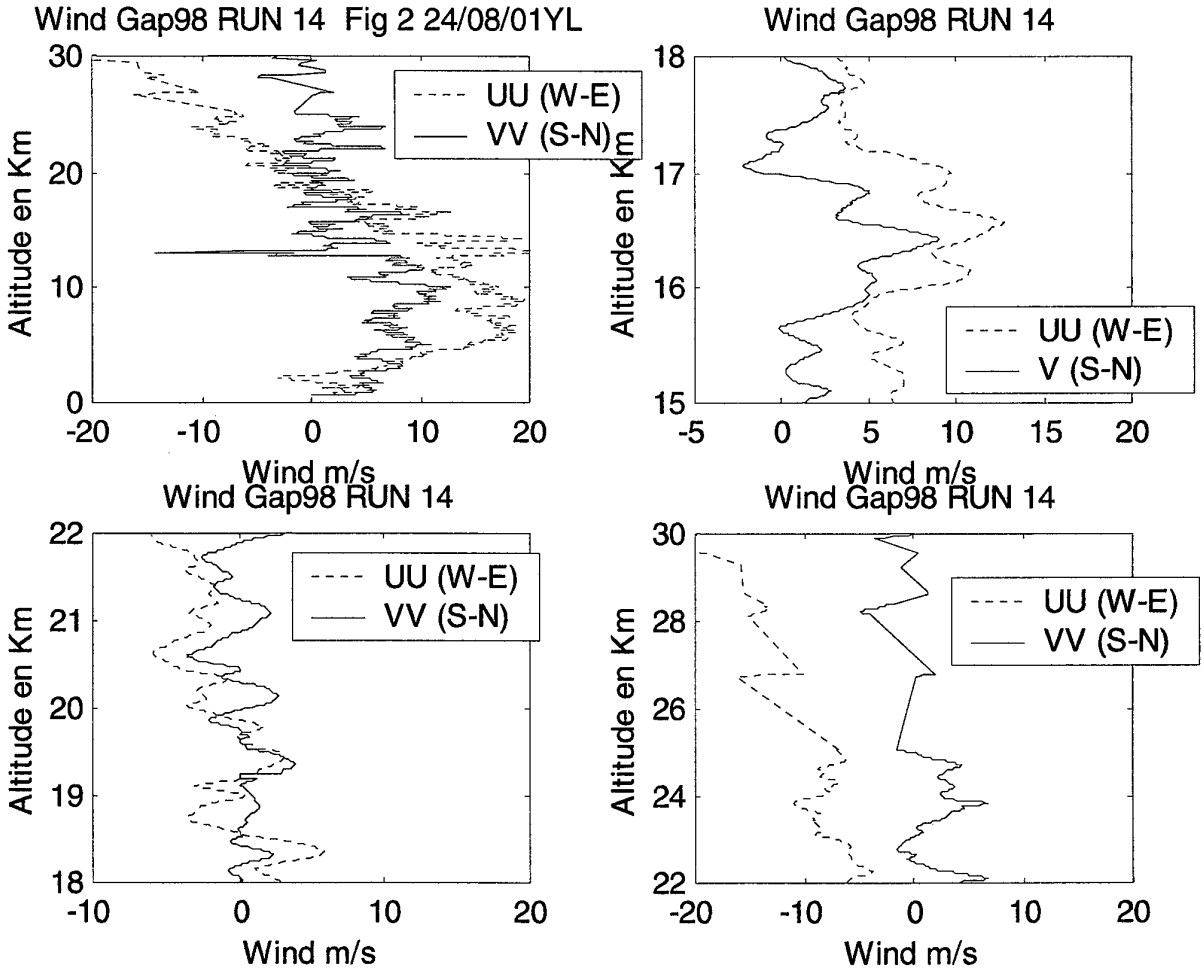
Wind Gap98 RUN 14 Fig 2 24/08/01YL
Altitude en Km
Wind m/s
UU (W-E)
VV (S-N)
Wind Gap98 RUN 14
Altitude en Km
Wind m/s
UU (W-E)
V (S-N)
Wind Gap98 RUN 14
Altitude en Km
Wind m/s
UU (W-E)
VV (S-N)
Wind Gap98 RUN 14
Altitude en Km
Wind m/s
UU (W-E)
VV (S-N)

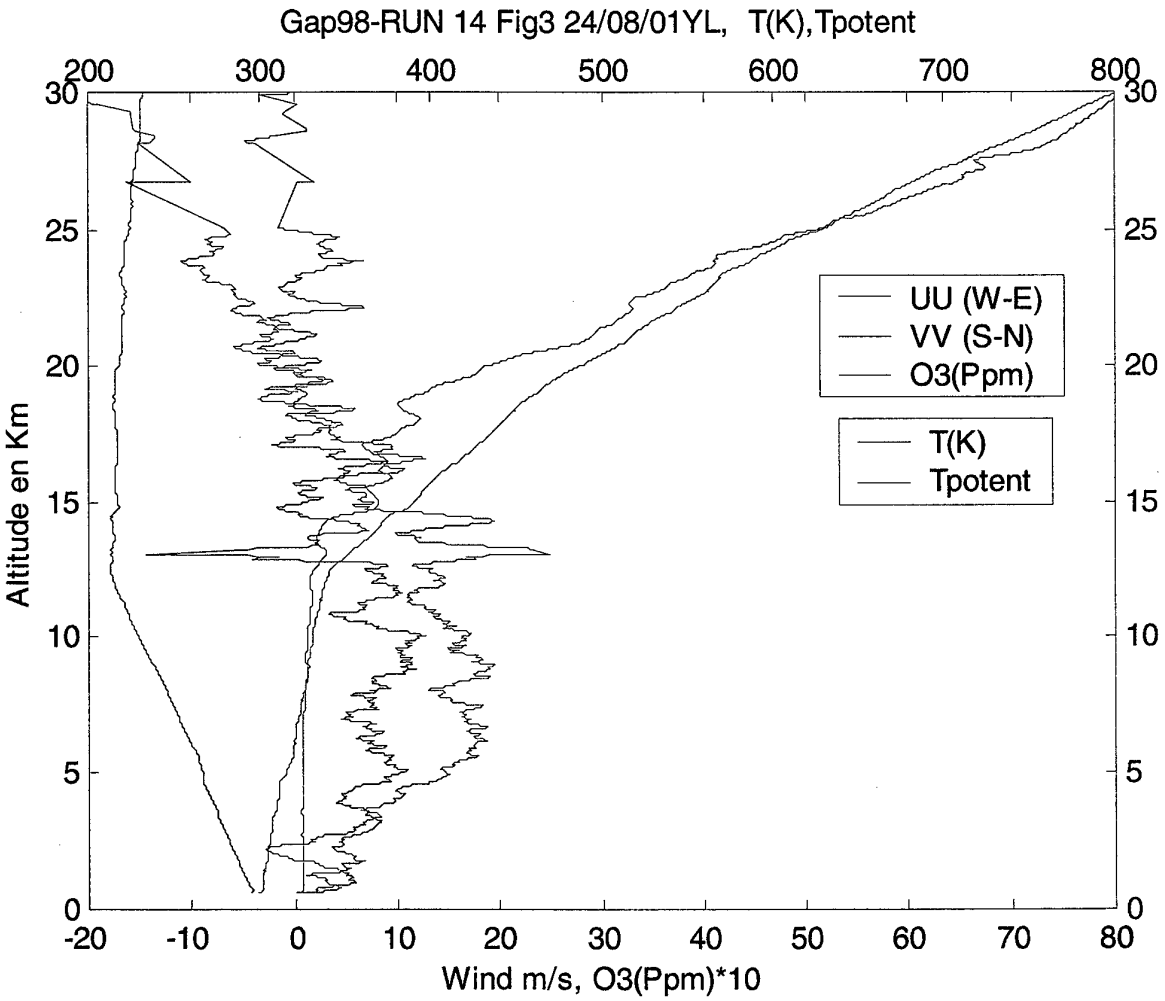
Gap98-RUN 14 Fig3 24/08/01YL, T(K),Tpotent
200
300
400
500
600
700
800
30
25
20
15
10
5
0
Altitude en Km
UU (W-E)
VV (S-N)
O3(Ppm)
T(K)
Tpotent
-20
-10
0
10
20
30
40
50
60
70
80
Wind m/s, O3(Ppm)*10

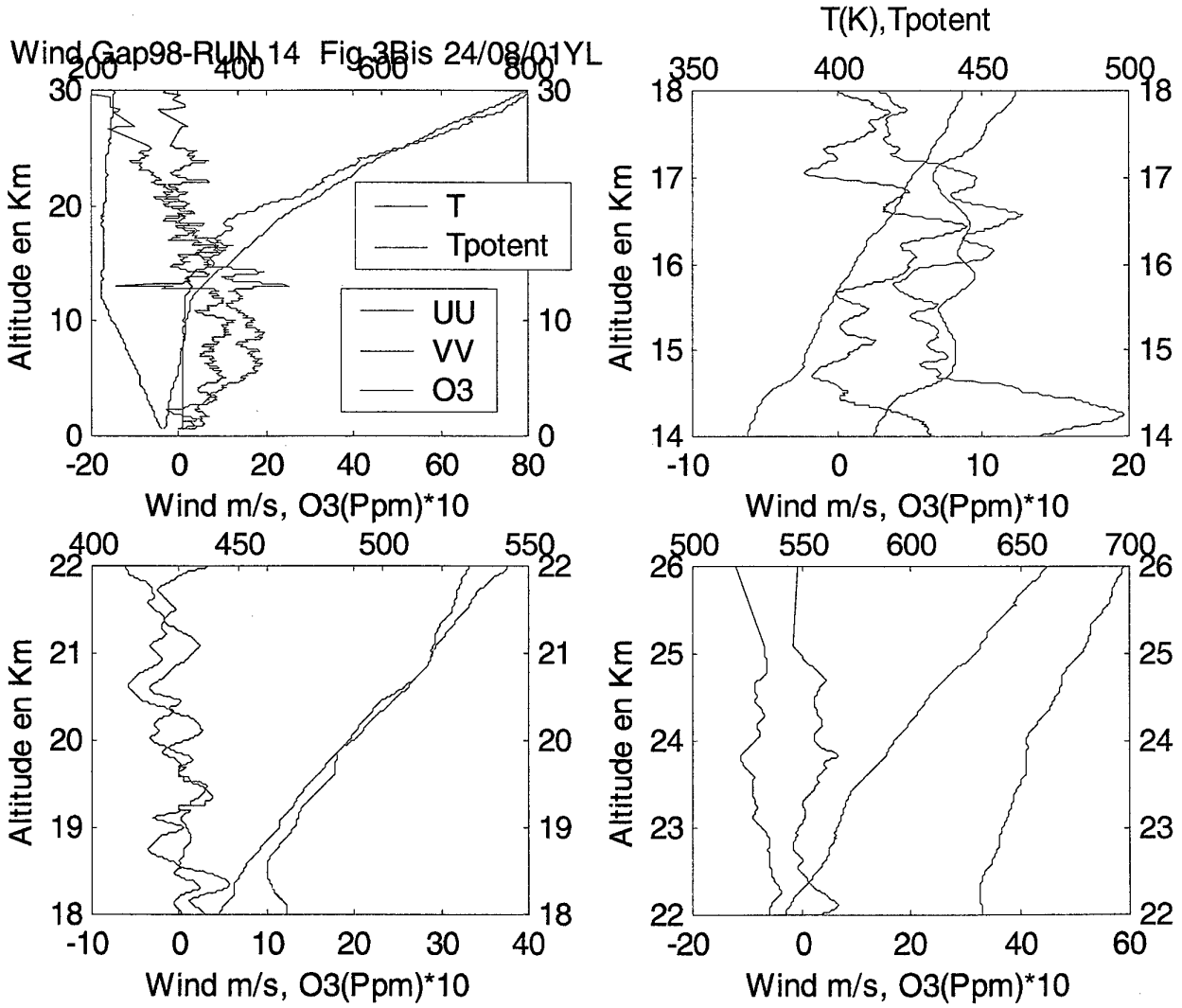
Wind Gap98-RUN 14 Fig 3Bis 24/08/01YL
Altitude en Km
Wind m/s, O3(Ppm)*10
T
Tpotent
UU
VV
O3
T(K),Tpotent

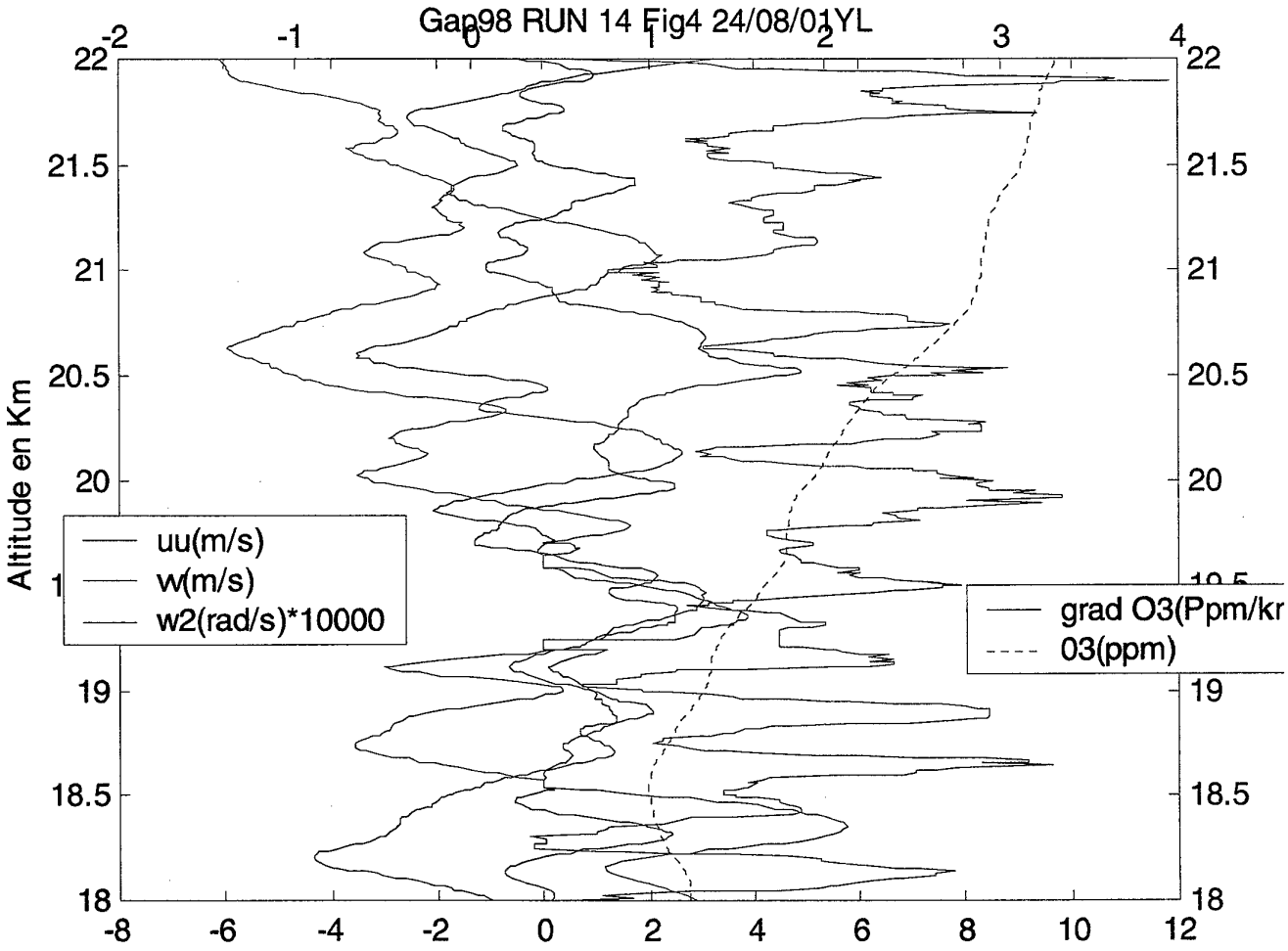
Gap98 RUN 14 Fig4 24/08/01YL
Altitude en Km
uu(m/s)
w(m/s)
w2(rad/s)*10000
grad O3(Ppm/kr
03(ppm)

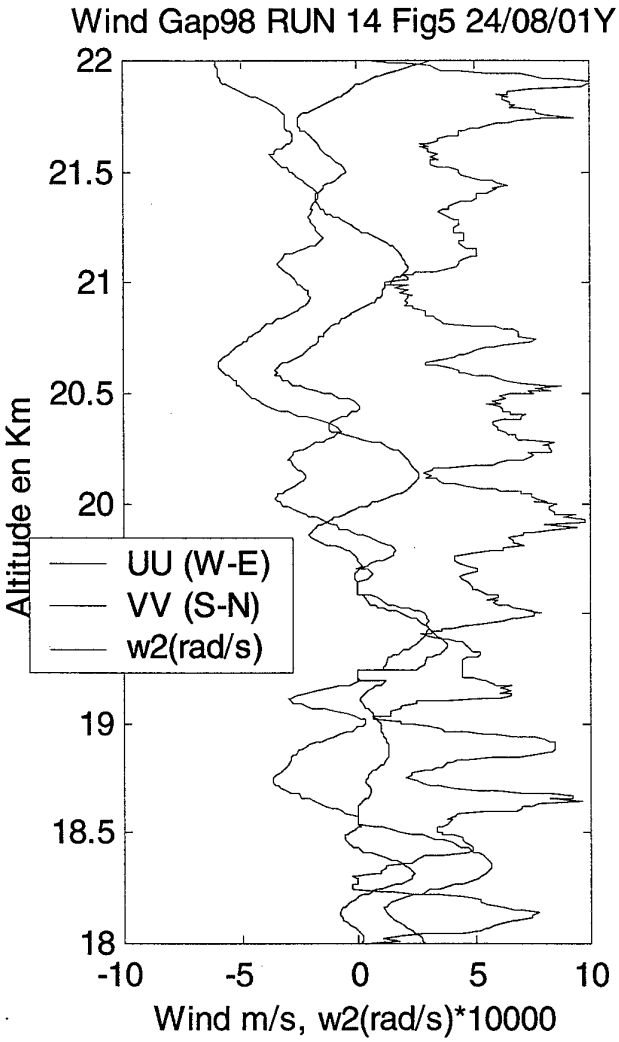
Wind Gap98 RUN 14 Fig5 24/08/01YL
Altitude en Km
22
21.5
21
20.5
20
19
18.5
18
UU (W-E)
VV (S-N)
w2(rad/s)
-10
-5
0
5
10
Wind m/s, w2(rad/s)*10000

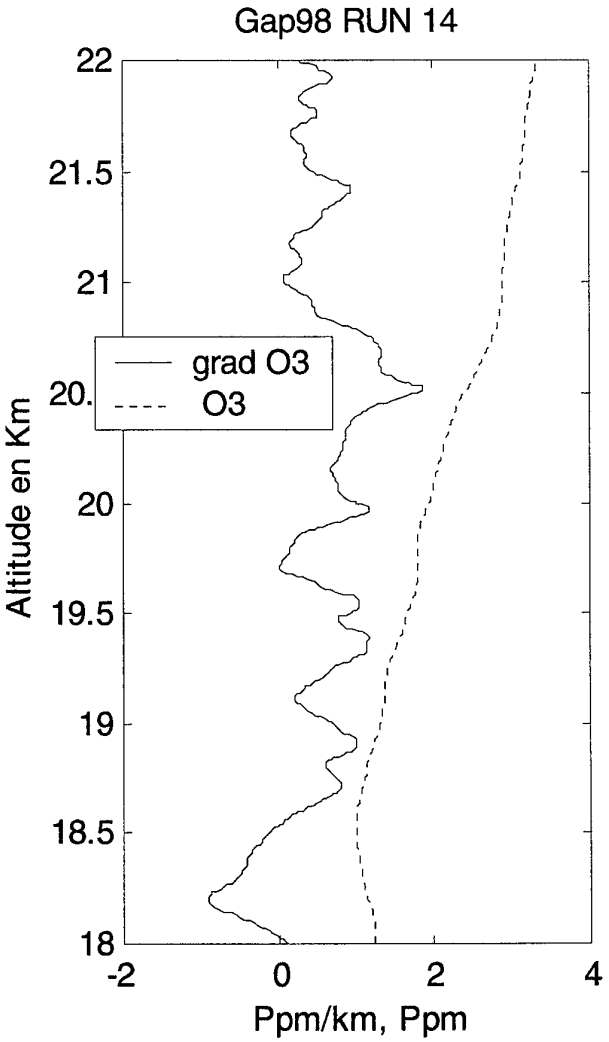
Gap98 RUN 14
Altitude en Km
22
21.5
21
20.
20
19.5
19
18.5
18
grad O3
O3
-2
0
2
4
Ppm/km, Ppm

ONERA

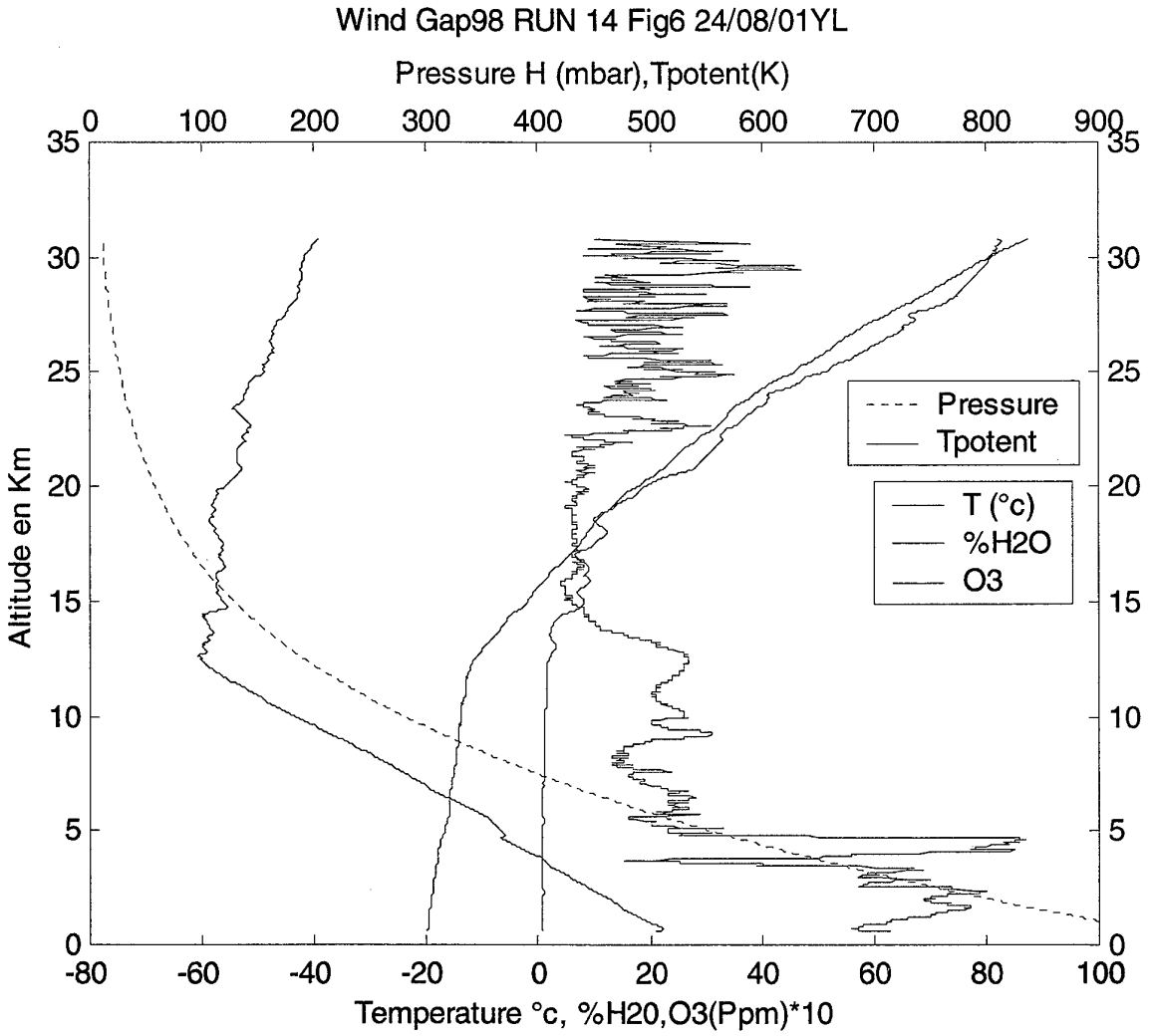
Wind Gap98 RUN 14 Fig6 24/08/01YL
Pressure H (mbar),Tpotent(K)
0
100
200
300
400
500
600
700
800
900
35
30
25
20
15
10
5
0
Altitude en Km
Pressure
Tpotent
T (°c)
%H2O
O3
-80
-60
-40
-20
0
20
40
60
80
100
Temperature °c, %H20,O3(Ppm)*10

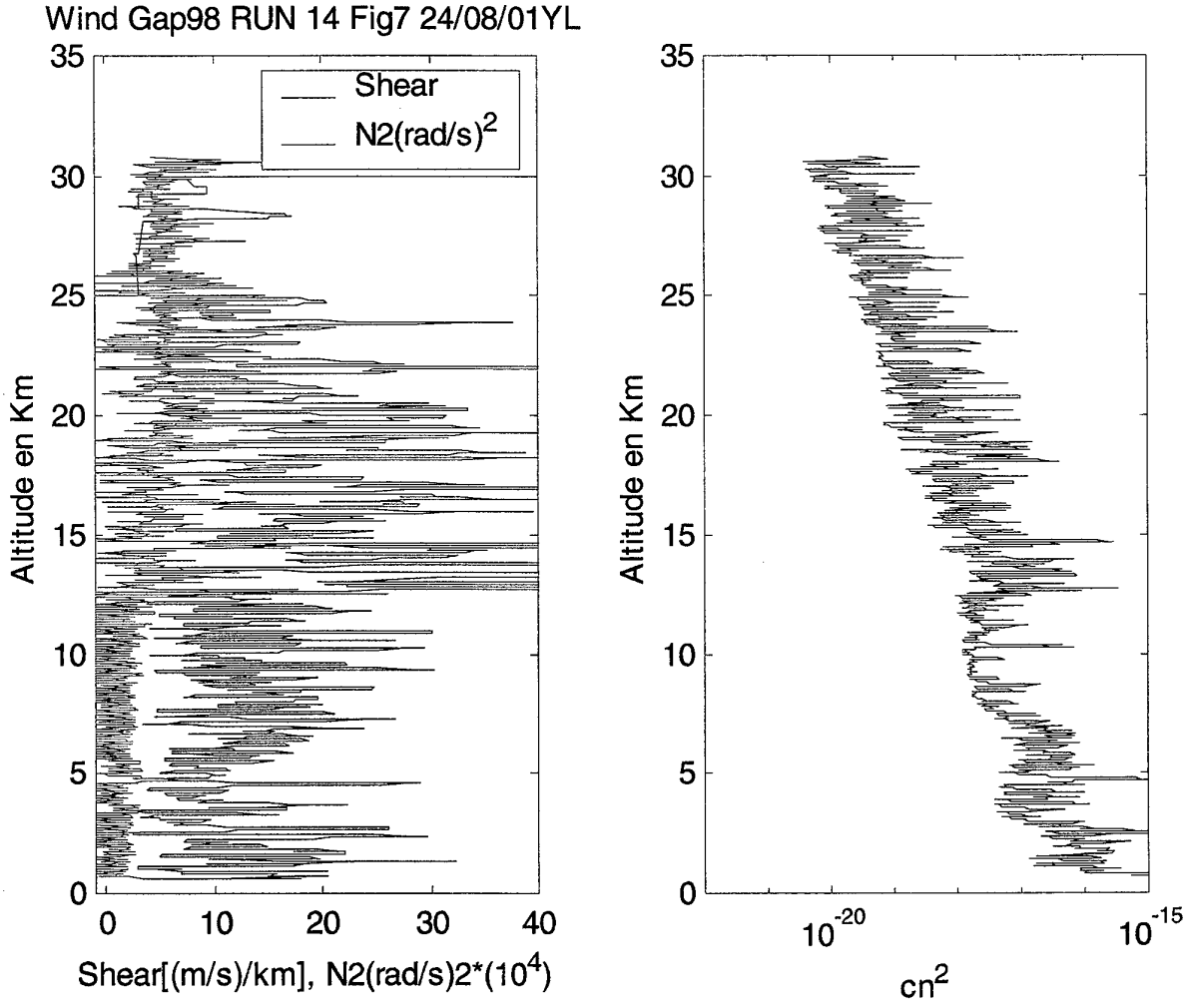
Wind Gap98 RUN 14 Fig7 24/08/01YL
Shear
N2(rad/s)2
Altitude en Km
Shear[(m/s)/km], N2(rad/s)2*(10^4)
cn2

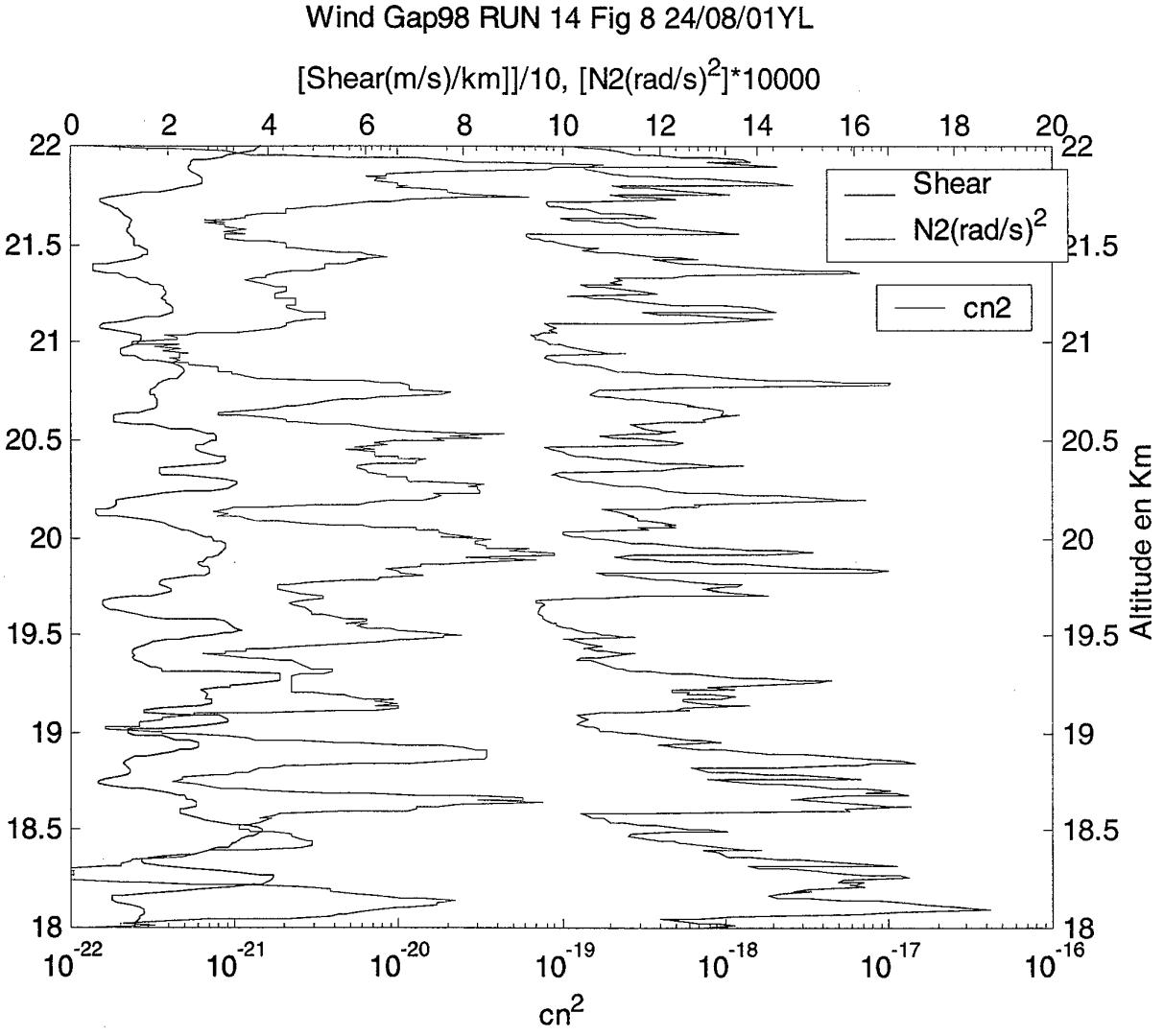
Wind Gap98 RUN 14 Fig 8 24/08/01YL
[Shear(m/s)/km]]/10, [N2(rad/s)^2]*10000
Shear
N2(rad/s)^2
cn2
Altitude en Km
cn^2

GAP98- Graphs RUN n°15

SANS MENTION
DE PROTECTION

SMP

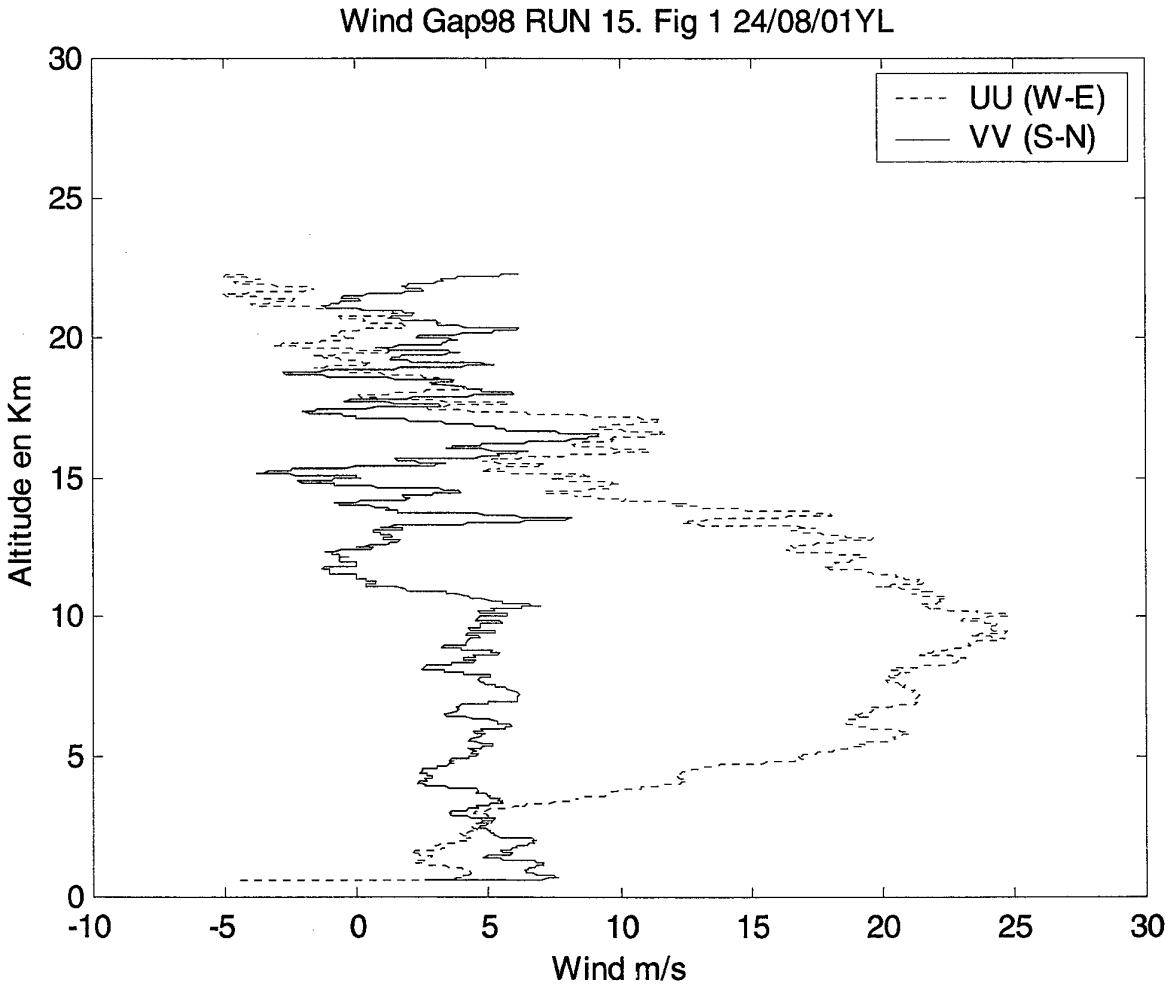

ONERA

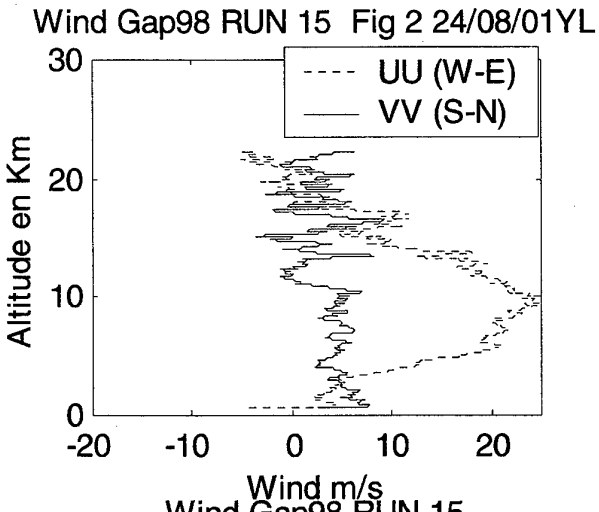
Wind Gap98 RUN 15 Fig 2 24/08/01YL
UU (W-E)
VV (S-N)
Altitude en Km
Wind m/s
30
20
10
0
-20
-10
0
10
20

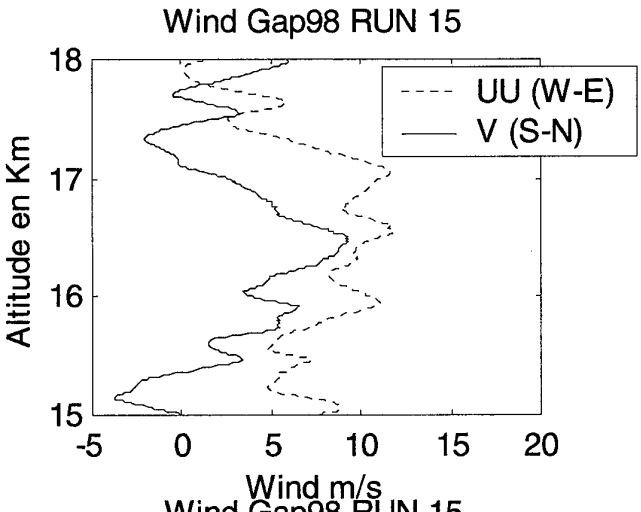
Wind Gap98 RUN 15
UU (W-E)
V (S-N)
Altitude en Km
Wind m/s
18
17
16
15
-5
0
5
10
15
20

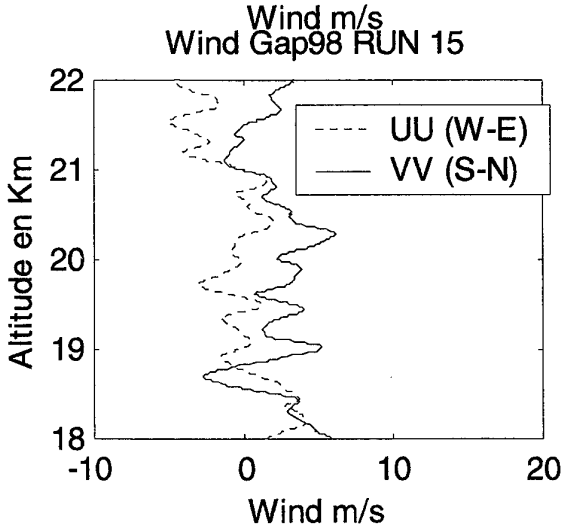
Wind Gap98 RUN 15
UU (W-E)
VV (S-N)
Altitude en Km
Wind m/s
22
21
20
19
18
-10
0
10
20

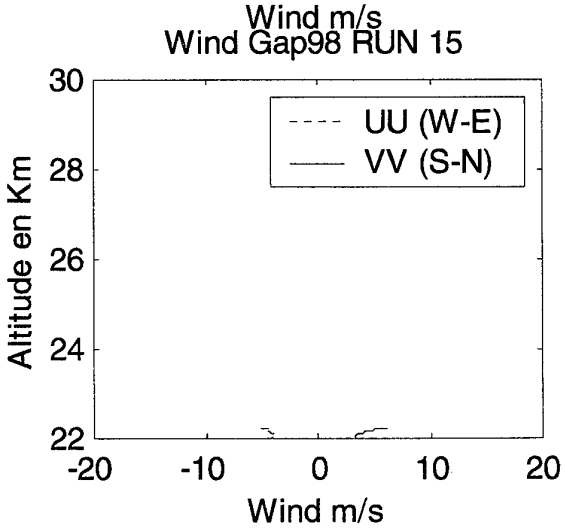
Wind Gap98 RUN 15
UU (W-E)
VV (S-N)
Altitude en Km
Wind m/s
30
28
26
24
22
-20
-10
0
10
20

ONERA

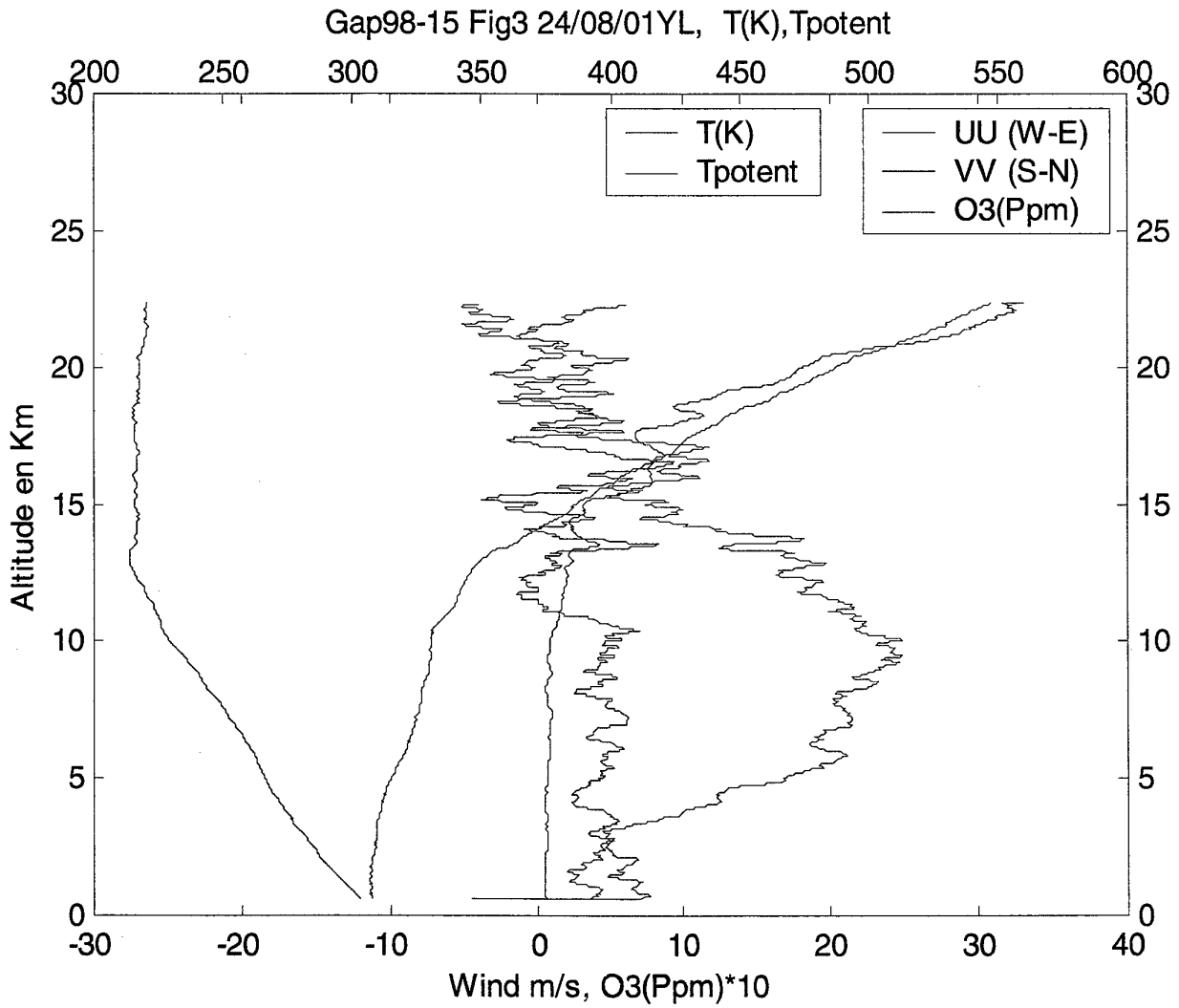
Gap98-15 Fig3 24/08/01YL, T(K),Tpotent
T(K)
Tpotent
UU (W-E)
VV (S-N)
O3(Ppm)
Altitude en Km
Wind m/s, O3(Ppm)*10
200
250
300
350
400
450
500
550
600
-30
-20
-10
0
10
20
30
40
0
5
10
15
20
25
30

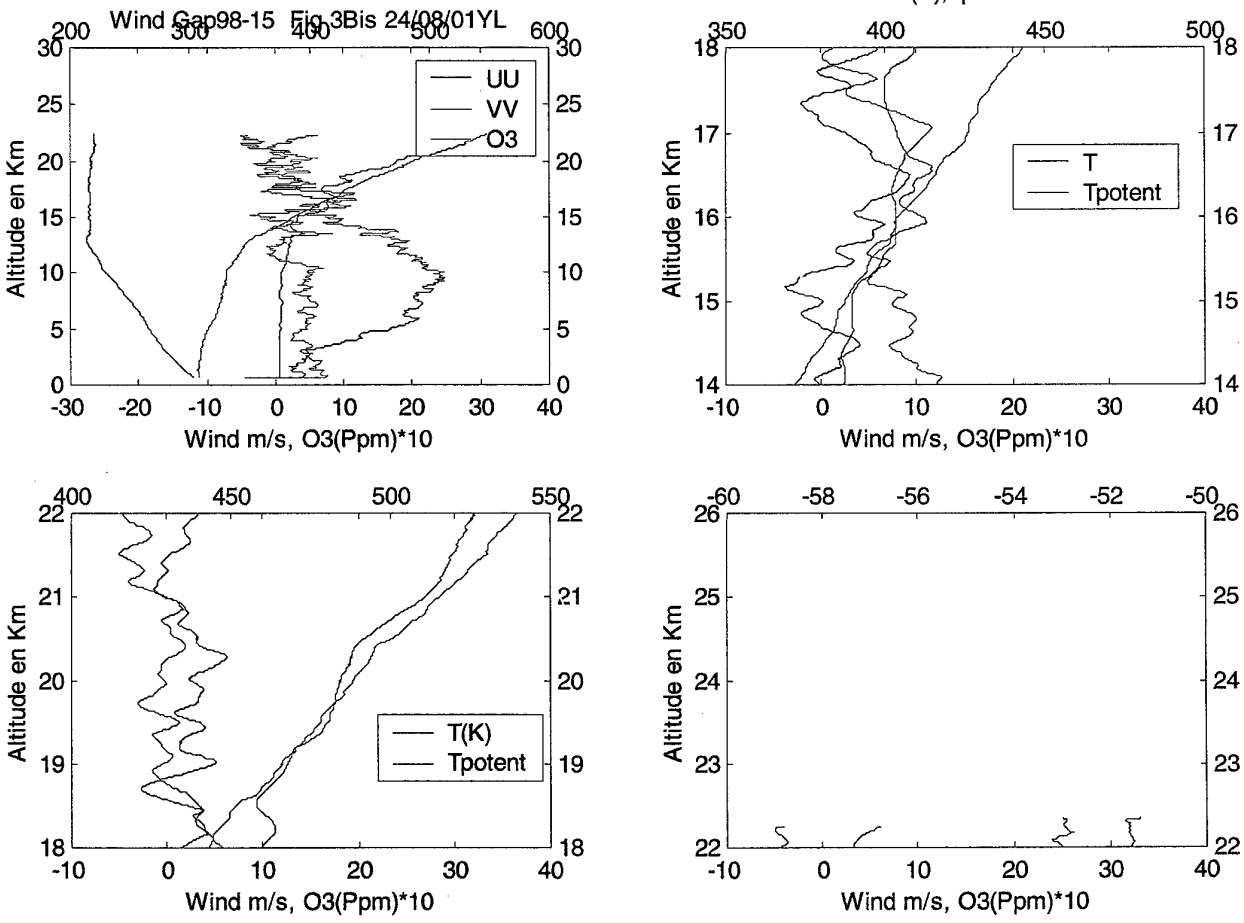
Wind Gap98-15 Fig.3Bis 24/08/01YL
UU
VV
O3
Altitude en Km
Wind m/s, O3(Ppm)*10
T(K),Tpotent
T
Tpotent
T(K)
Tpotent

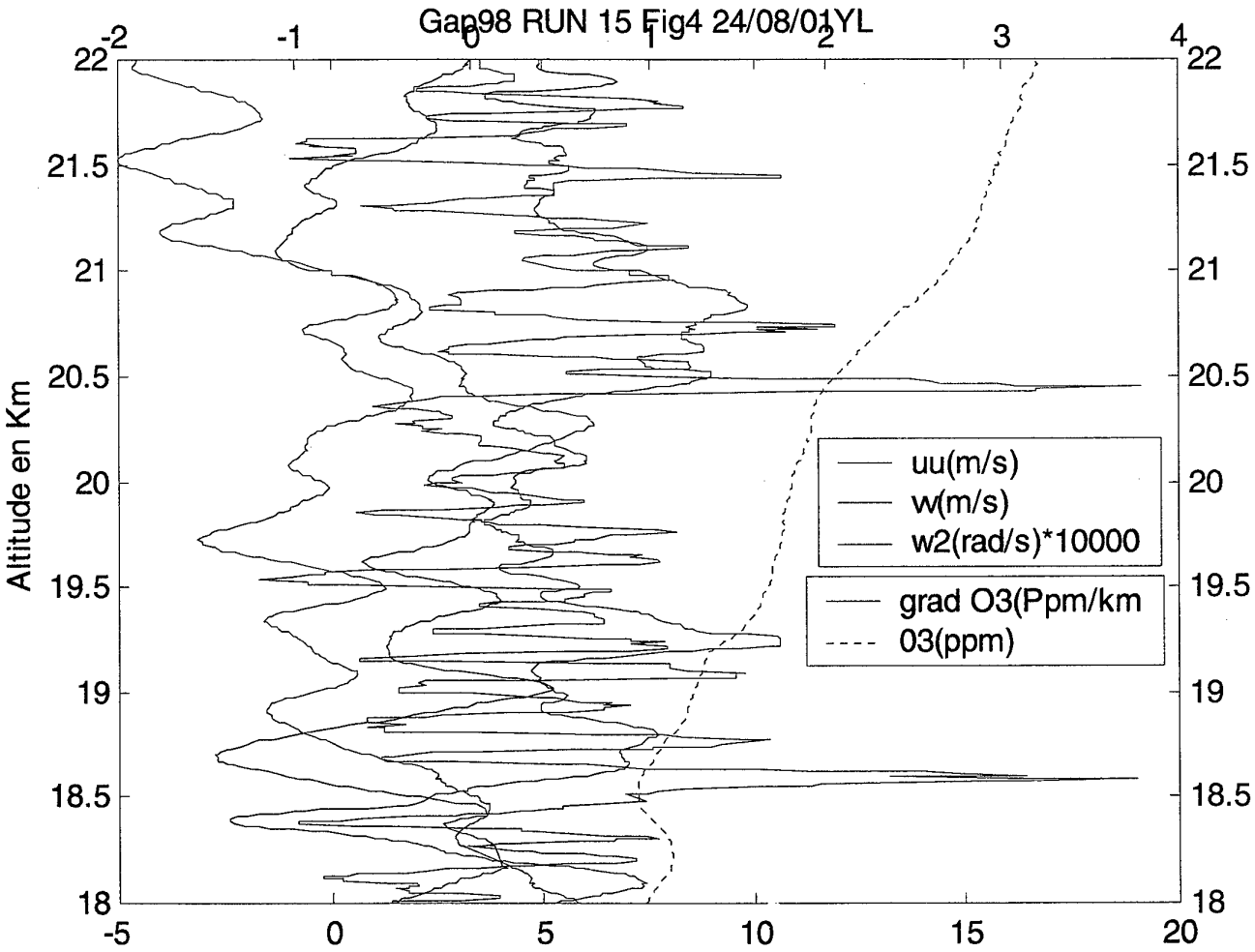
Gap98 RUN 15 Fig4 24/08/01YL
Altitude en Km
uu(m/s)
w(m/s)
w2(rad/s)*10000
grad O3(Ppm/km
03(ppm)

ONERA

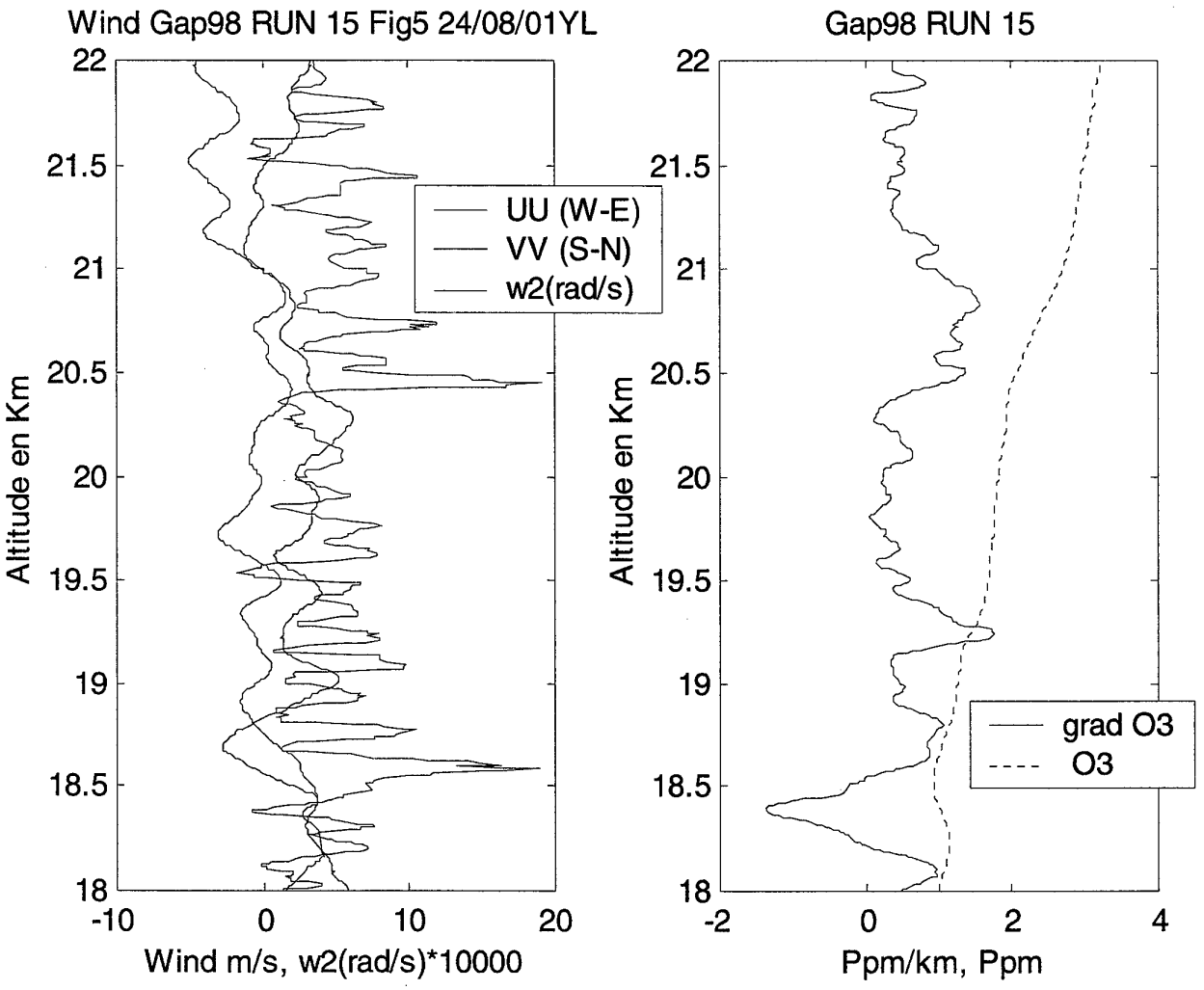
Wind Gap98 RUN 15 Fig5 24/08/01YL
Altitude en Km
22
21.5
21
20.5
20
19.5
19
18.5
18
-10
0
10
20
Wind m/s, w2(rad/s)*10000
UU (W-E)
VV (S-N)
w2(rad/s)
Gap98 RUN 15
Altitude en Km
-2
0
2
4
Ppm/km, Ppm
grad O3
O3

ONERA

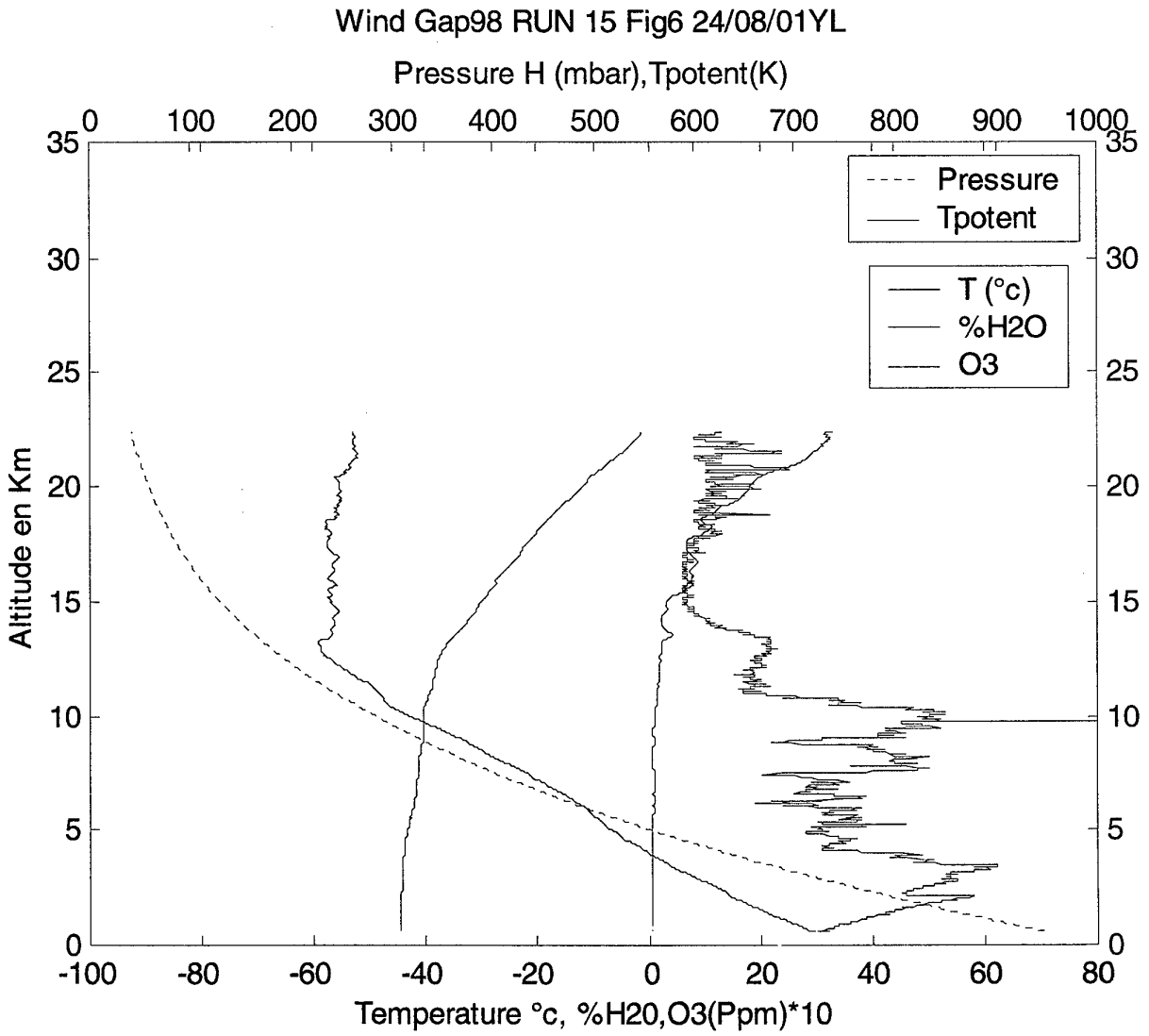
Wind Gap98 RUN 15 Fig6 24/08/01YL
Pressure H (mbar),Tpotent(K)
0 100 200 300 400 500 600 700 800 900 1000
Pressure
Tpotent
T (°c)
%H2O
O3
Altitude en Km
0 5 10 15 20 25 30 35
-100 -80 -60 -40 -20 0 20 40 60 80
Temperature °c, %H20,O3(Ppm)*10

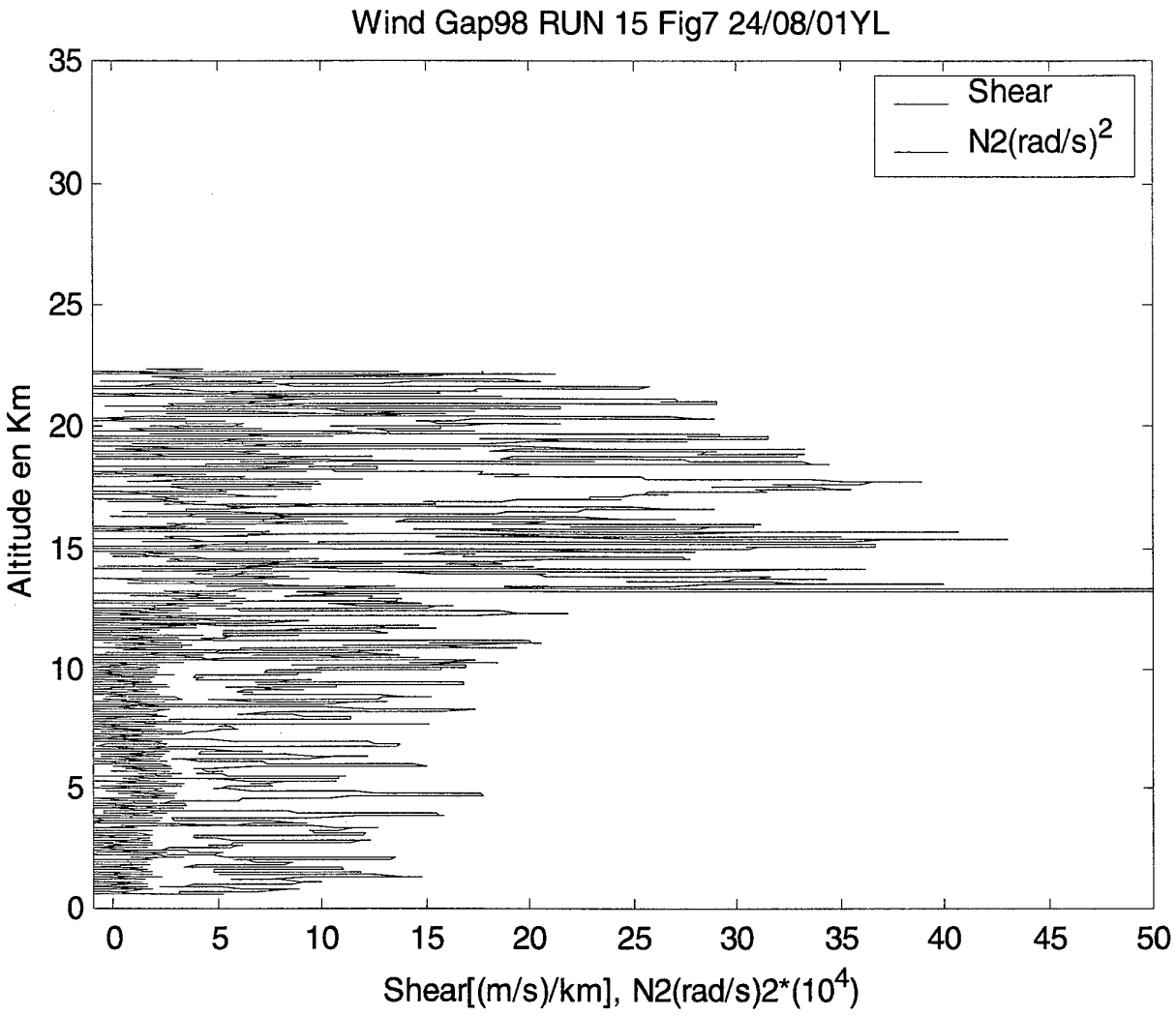
Wind Gap98 RUN 15 Fig7 24/08/01YL
Shear
N2(rad/s)2
Altitude en Km
0
5
10
15
20
25
30
35
0
5
10
15
20
25
30
35
40
45
50
Shear[(m/s)/km], N2(rad/s)2*(10^4)

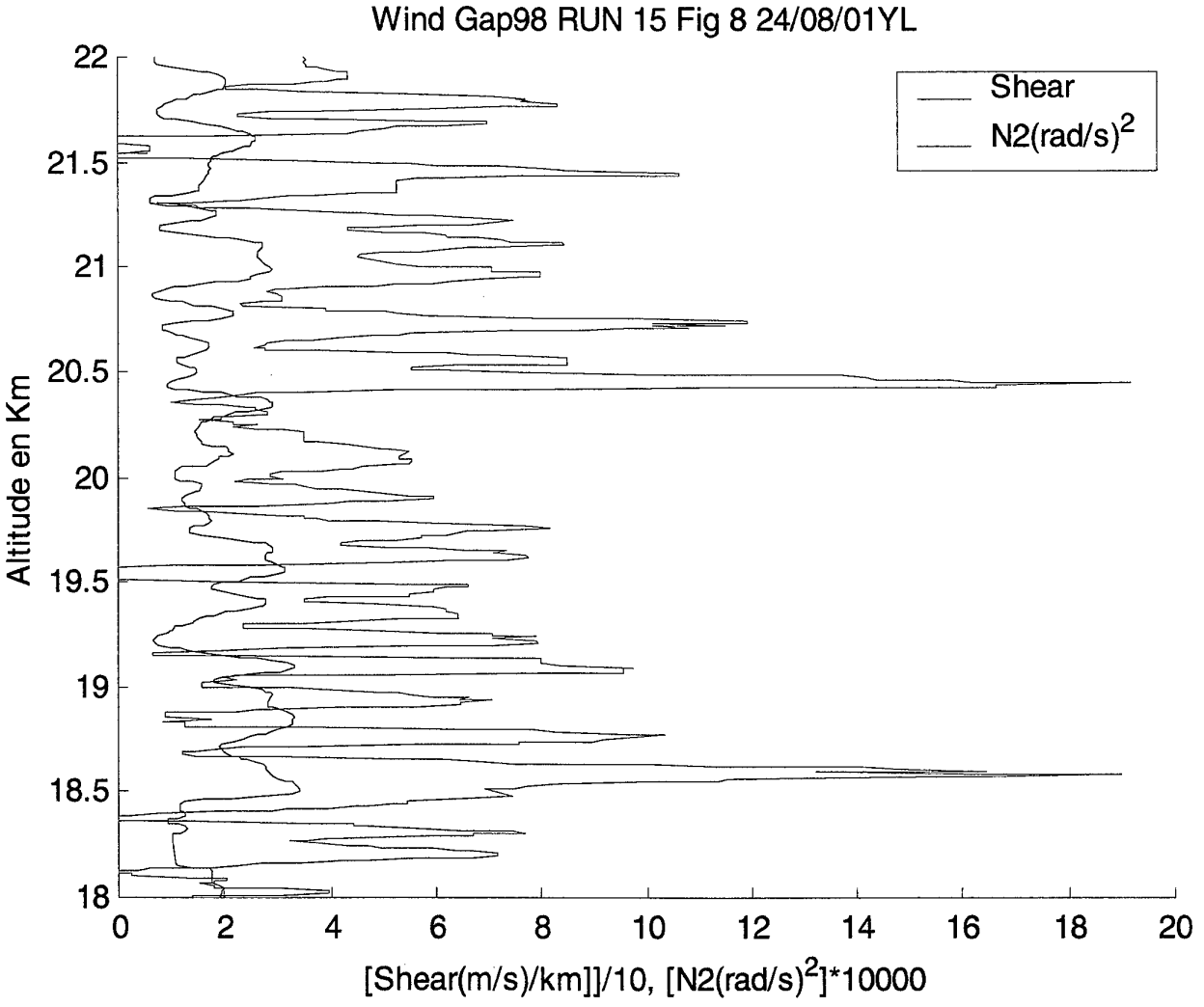
Wind Gap98 RUN 15 Fig 8 24/08/01YL
Shear
N2(rad/s)2
Altitude en Km
22
21.5
21
20.5
20
19.5
19
18.5
18
0
2
4
6
8
10
12
14
16
18
20
[Shear(m/s)/km]]/10, [N2(rad/s)2]*10000

GAP98- Graphs RUN n°16

ONERA

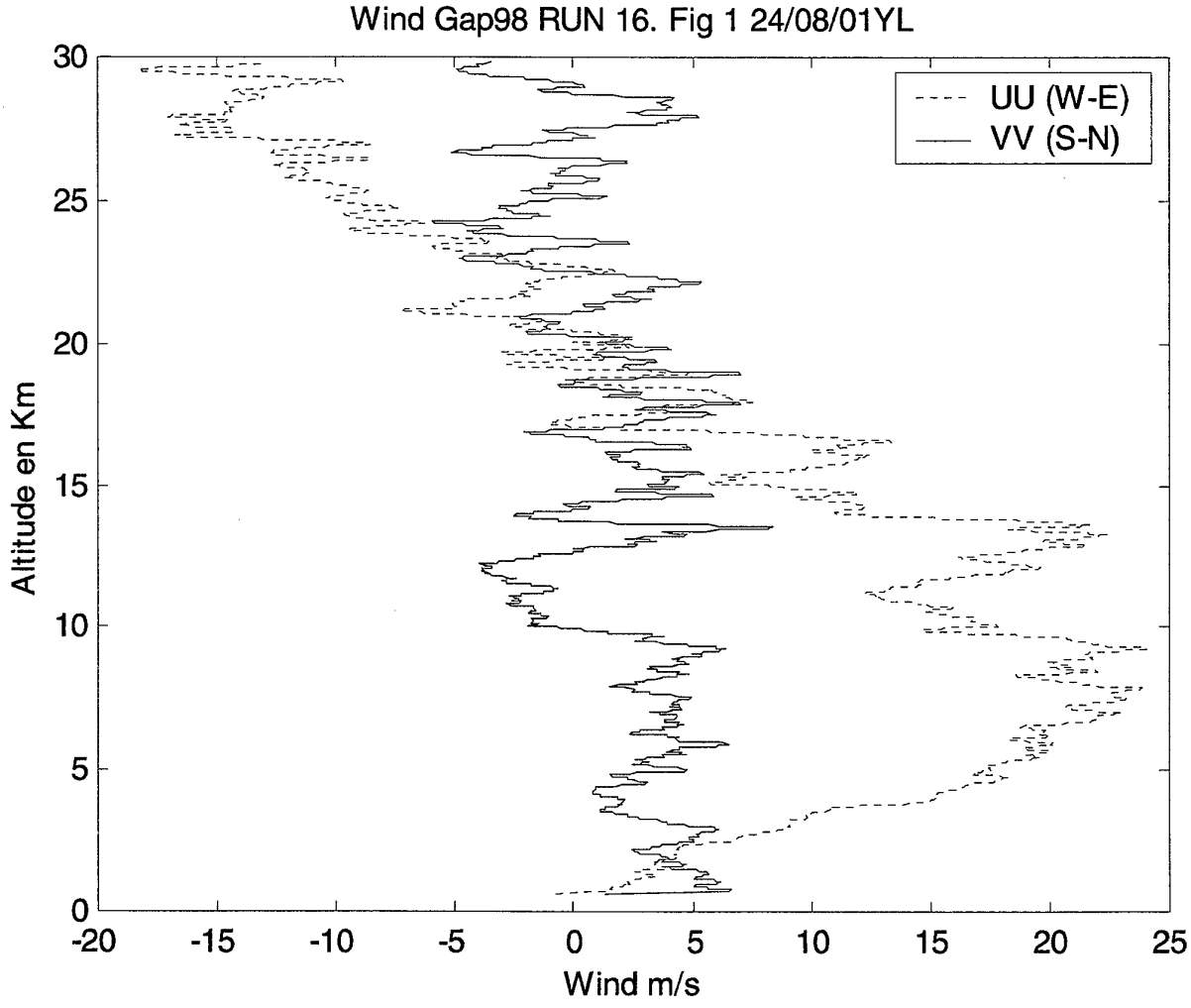
Wind Gap98 RUN 16. Fig 1 24/08/01YL
UU (W-E)
VV (S-N)
Altitude en Km
Wind m/s
30
25
20
15
10
5
0
-20
-15
-10
-5
0
5
10
15
20
25

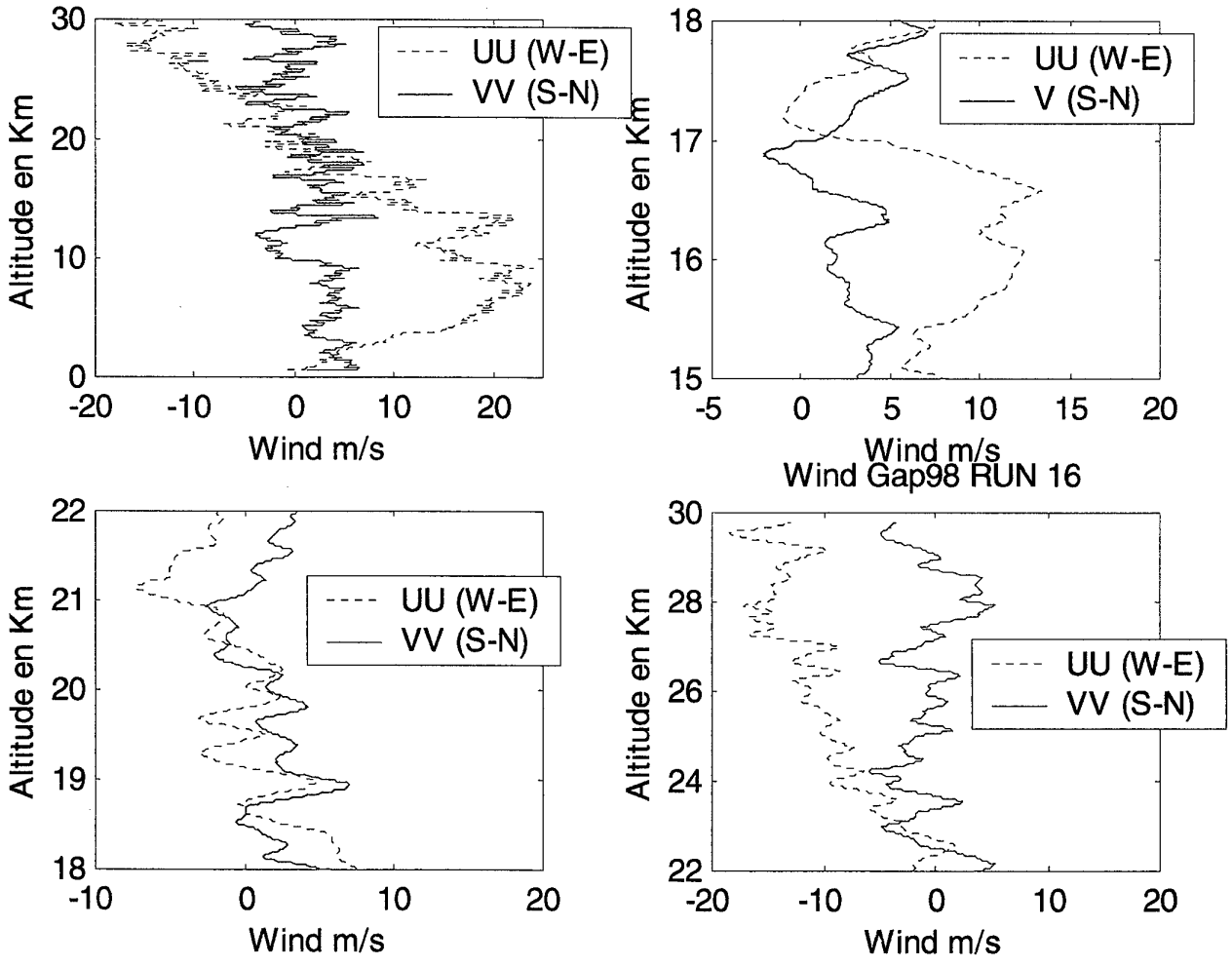
Altitude en Km
Wind m/s
UU (W-E)
VV (S-N)
V (S-N)
Wind Gap98 RUN 16

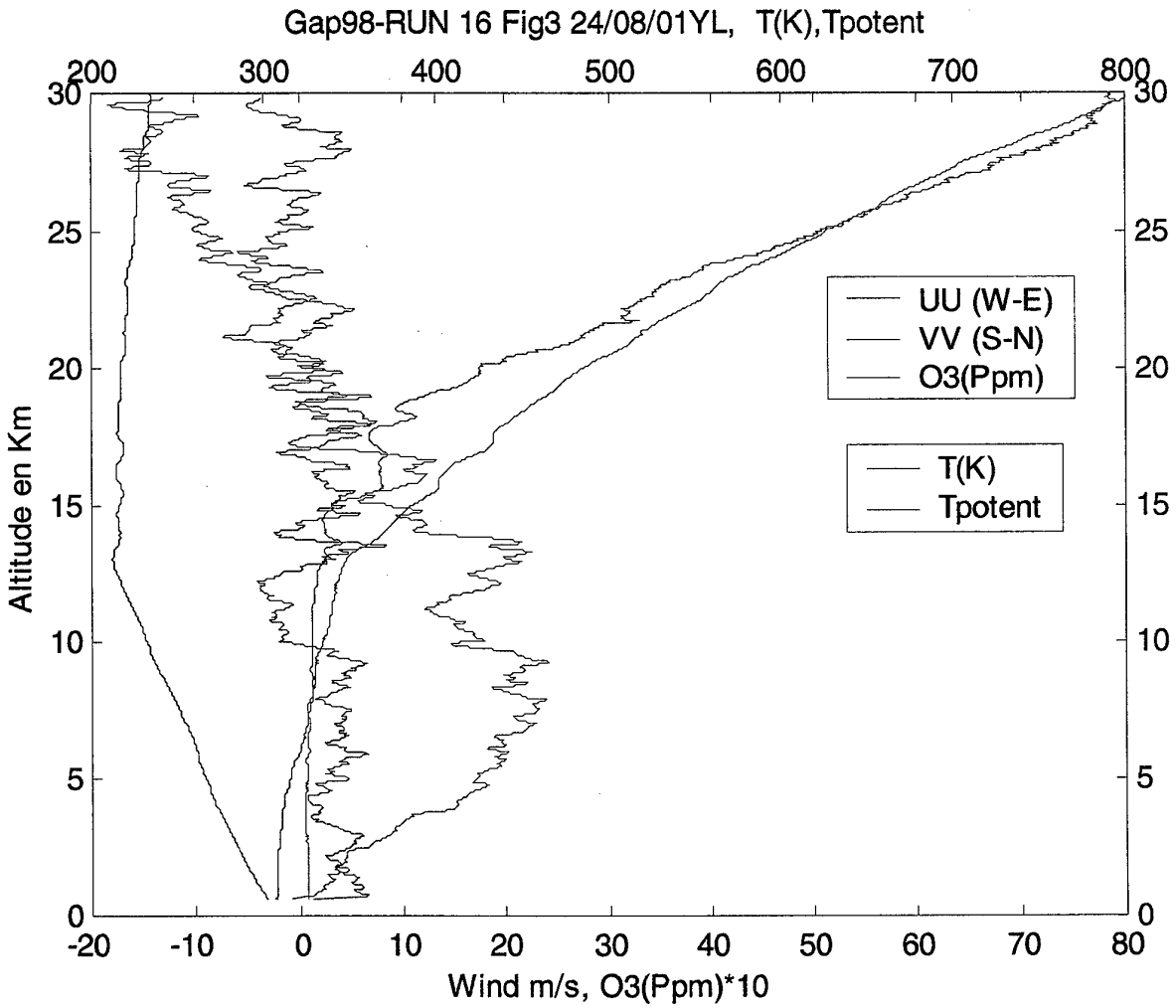
Gap98-RUN 16 Fig3 24/08/01YL, T(K),Tpotent
200
300
400
500
600
700
800
30
25
20
15
10
5
0
Altitude en Km
UU (W-E)
VV (S-N)
O3(Ppm)
T(K)
Tpotent
-20
-10
0
10
20
30
40
50
60
70
80
Wind m/s, O3(Ppm)*10

SANS MENTION
DE PROTECTION

SMP

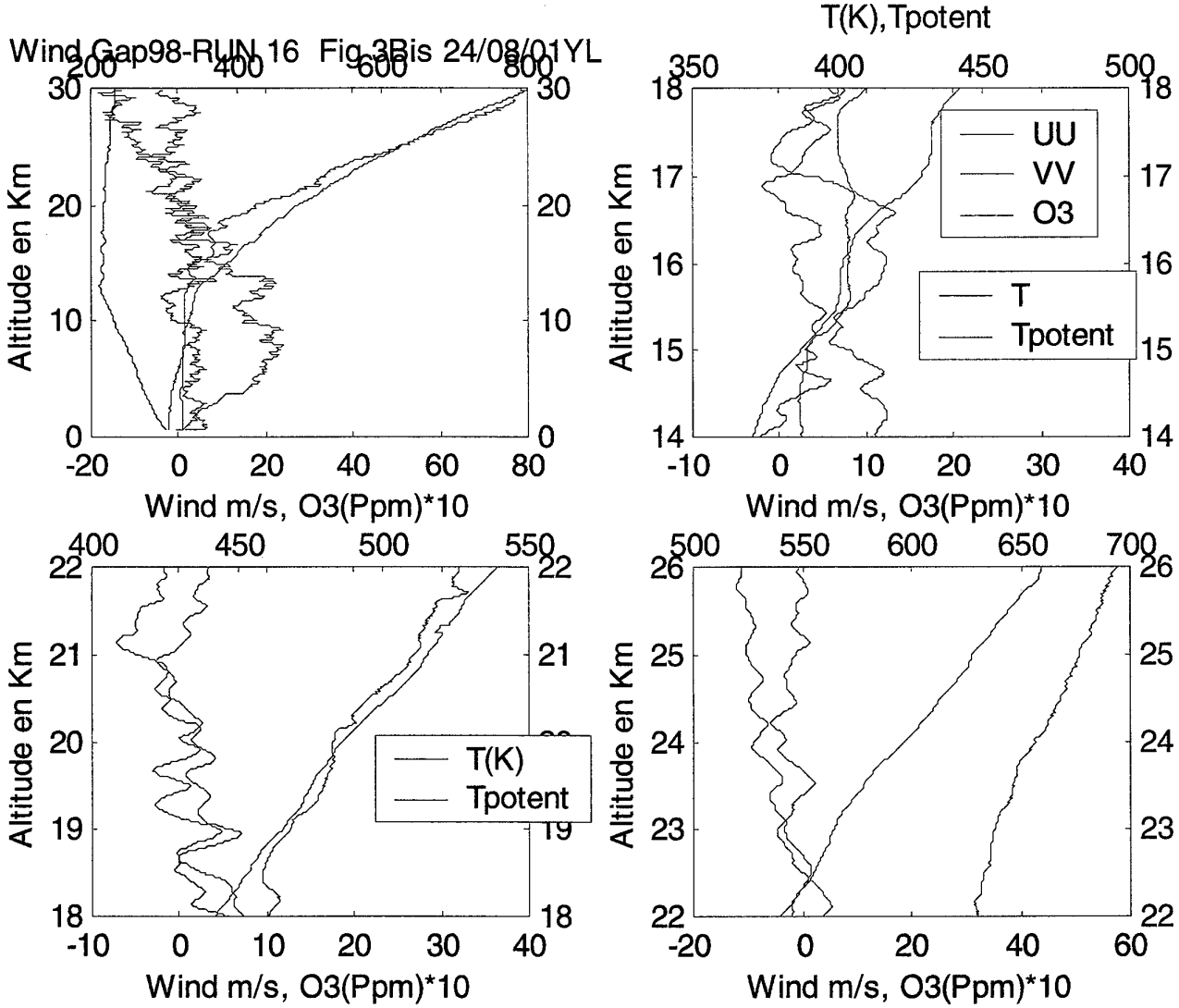

ONERA

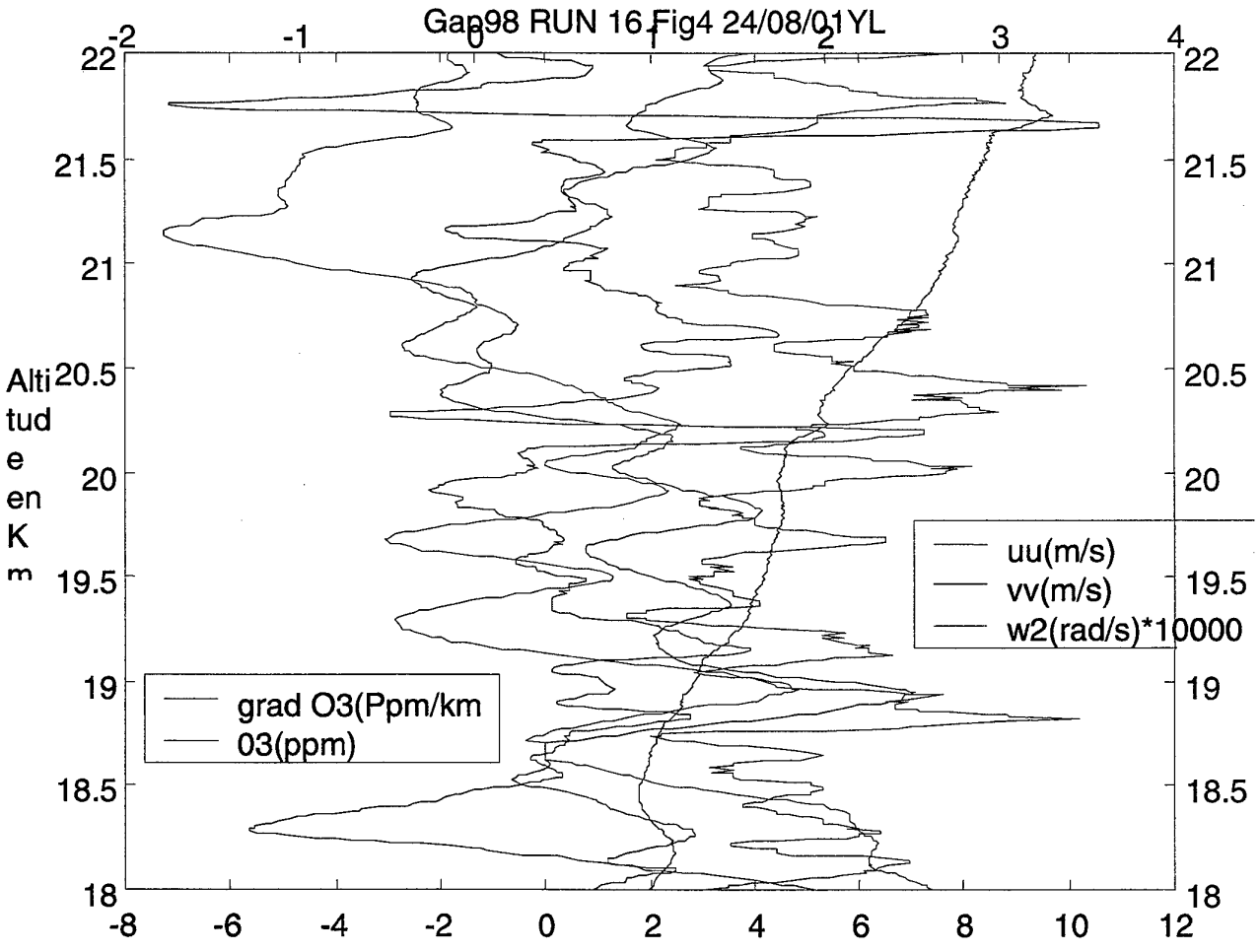
Gap98 RUN 16 Fig4 24/08/01YL
Altitude en Km
grad O3(Ppm/km
03(ppm)
uu(m/s)
vv(m/s)
w2(rad/s)*10000

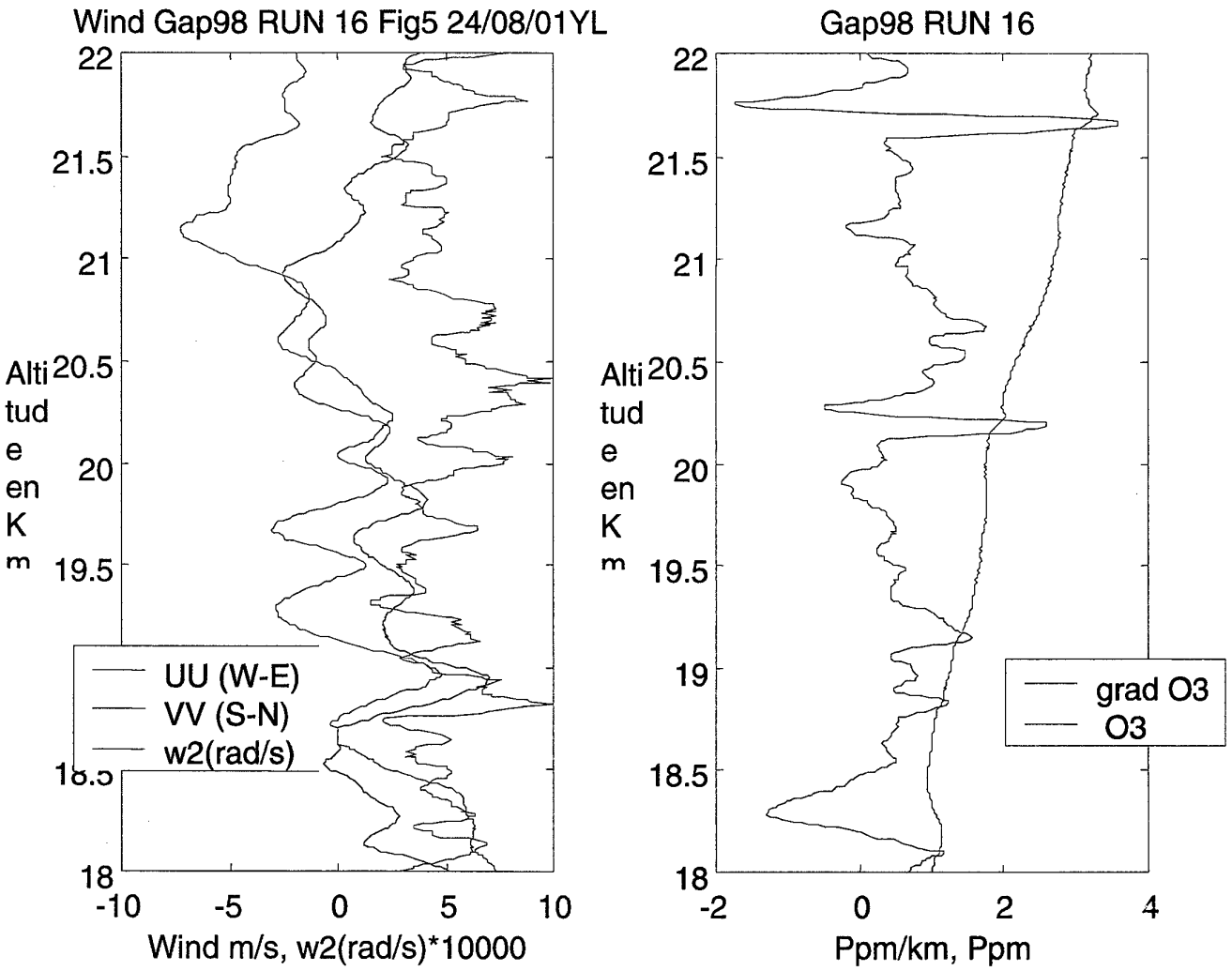
Wind Gap98 RUN 16 Fig5 24/08/01YL
Altitude en Km
22
21.5
21
20.5
20
19.5
18.5
18
UU (W-E)
VV (S-N)
w2(rad/s)
-10
-5
0
5
10
Wind m/s, w2(rad/s)*10000
Gap98 RUN 16
Altitude en Km
22
21.5
21
20.5
20
19.5
19
18.5
18
grad O3
O3
-2
0
2
4
Ppm/km, Ppm

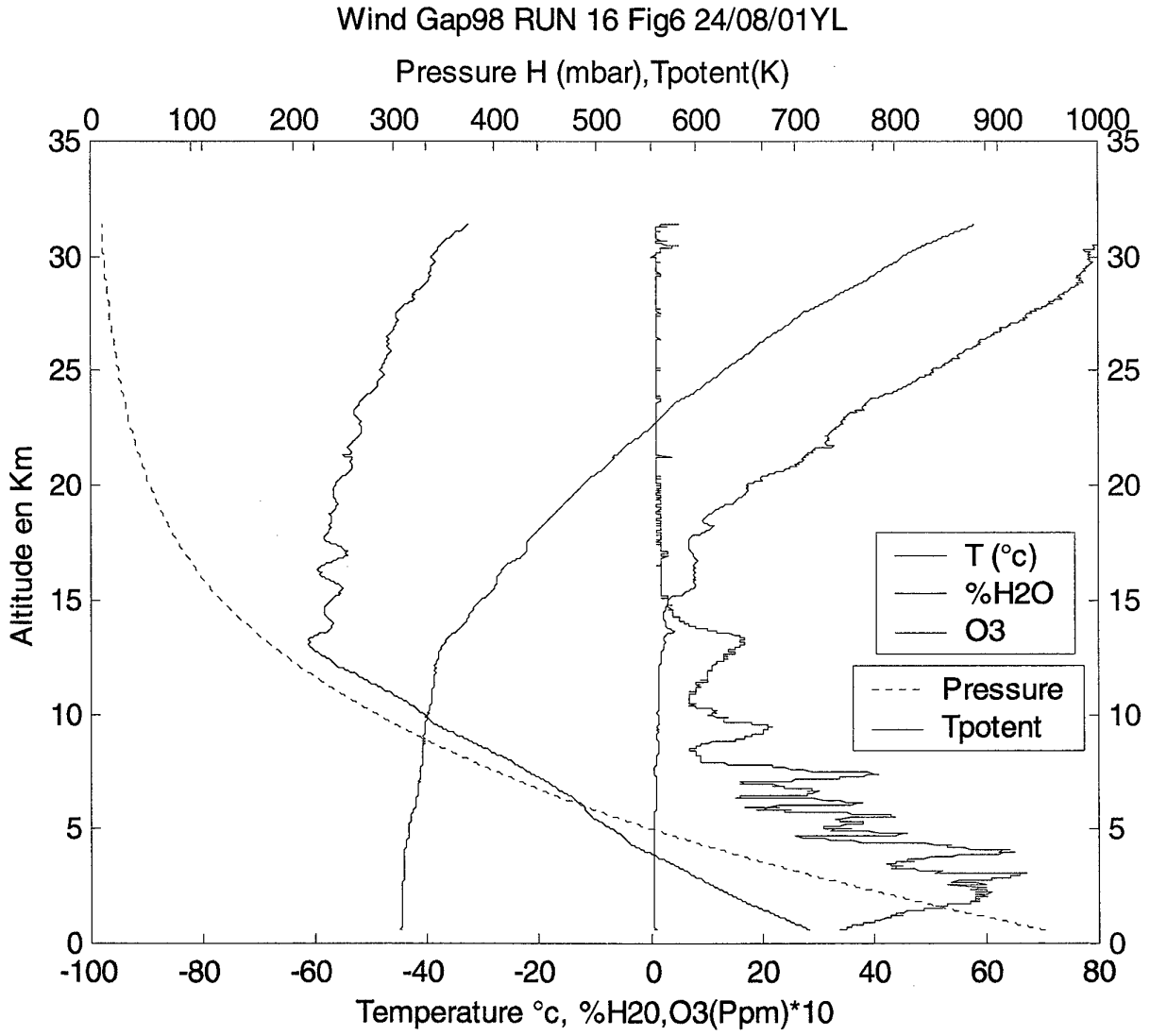
Wind Gap98 RUN 16 Fig6 24/08/01YL
Pressure H (mbar),Tpotent(K)
0
100
200
300
400
500
600
700
800
900
1000
Altitude en Km
35
30
25
20
15
10
5
0
T (°c)
%H2O
O3
Pressure
Tpotent
-100
-80
-60
-40
-20
0
20
40
60
80
Temperature °c, %H20,O3(Ppm)*10

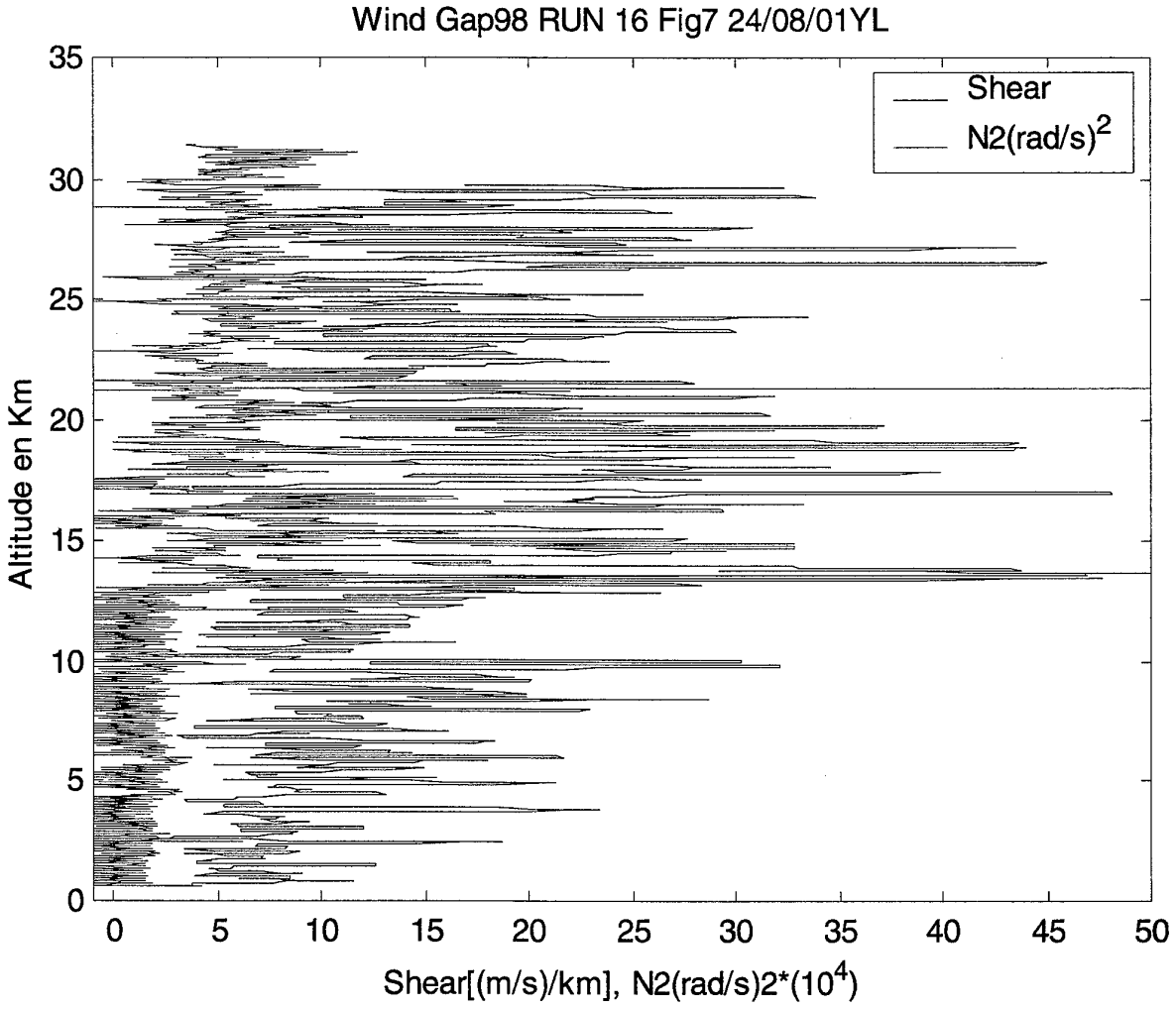
Wind Gap98 RUN 16 Fig7 24/08/01YL
Shear
N2(rad/s)2
Altitude en Km
0
5
10
15
20
25
30
35
0
5
10
15
20
25
30
35
40
45
50
Shear[(m/s)/km], N2(rad/s)2*(10^4)

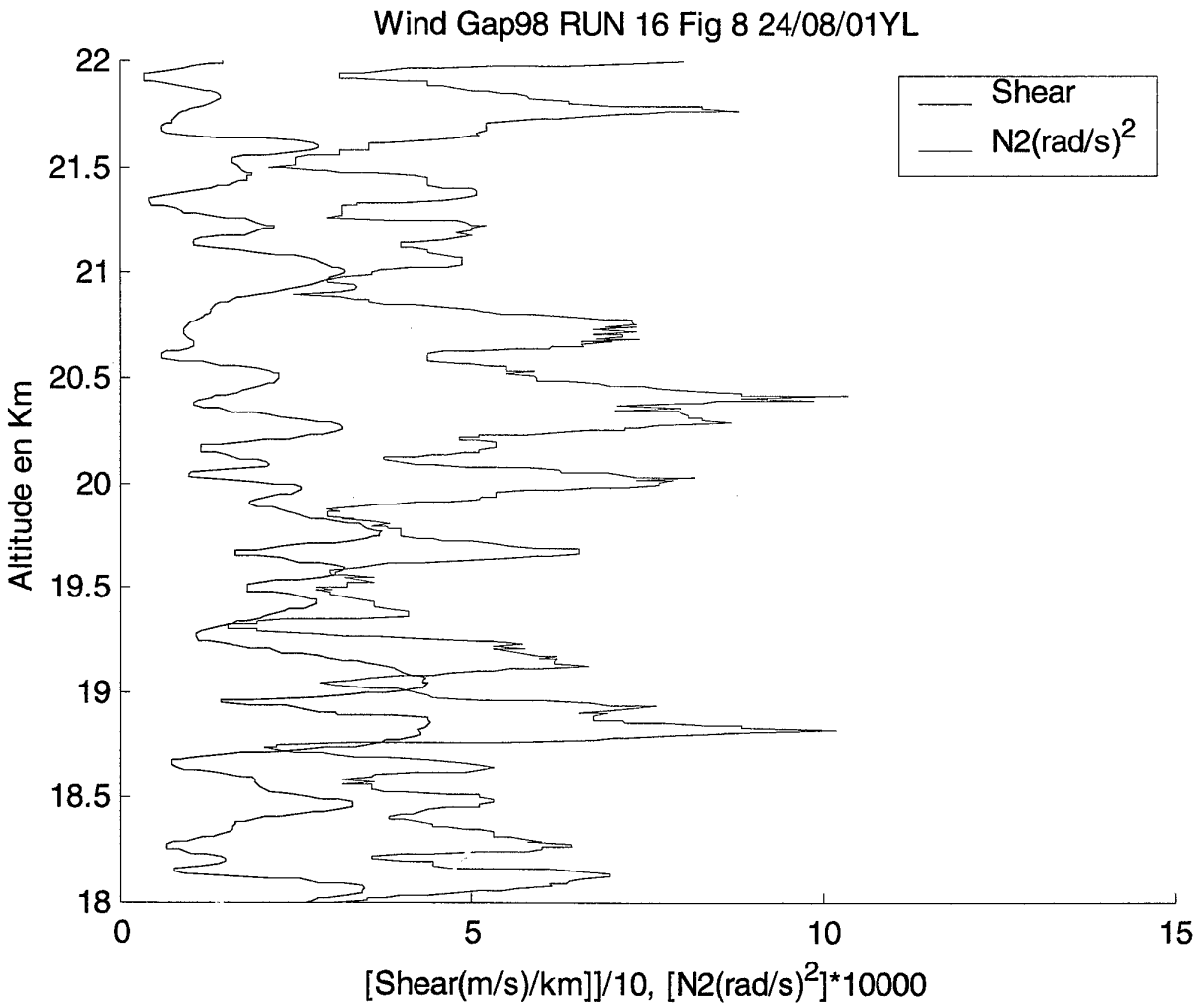
Wind Gap98 RUN 16 Fig 8 24/08/01YL
Shear
N2(rad/s)2
Altitude en Km
22
21.5
21
20.5
20
19.5
19
18.5
18
0
5
10
15
[Shear(m/s)/km]]/10, [N2(rad/s)2]*10000

APPENDIX 4
SECOND SET OF GRAPHS
RUNS 9, 10, 11, 14

We have nine figures for each run.

Figures X.4.1, X.4.2 and X.4.3 represent ozone gradient and concentration, wind components U and V and N2 (noted L2). Attention: L2 is in $(rad/s)^2$ *1000.

Figures X.8.1, X.8.2 and X.8.3 show the shear (wind gradient in [m/s]/km and divided by 10), cn2 and Richardson number.

Figure 9 shows cn2 as a function of shear.

We have detected some missing link on wind data
(RUN 9 from 15 to 17 km
RUN 10 none,
RUN 11 from 3 to 7 km, from 18.5 to 19.3 and 19.7 km and 27 km
RUN 14 at 19.3 km and 18.7 km

For each run we plotted 9 figures in the following order:

Figure 1 : Wind components UU (West –East) et VV (South-North) in the [0-35] km altitude range.
Figure 2 : Zoom in the [15-18] km, [18-22] km and [22-30] km altitude ranges.
Figure 3 : Plots of UU, VV, measured (T) and potential (Tpotent) temperatures, ozone concentration in the [0-35] km altitude range.
Figure 3bis : Same as 3 in the [15-18] km, [18-22] km and [22-30] km altitude ranges.
Figure 4 : Wind components UU (W-E) et VV (S-N); O3 concentration and gradient and N2 (square Brunt-Vaisala pulsation multiplied by 10000) in the [18-22] km altitude range.
Figure 5 : Same as Figure 4 but on two graphs.
Figure 6 : Curves of P (pressure), T, Tpotent, O3 and %humidity in the [0-35] km altitude range.
Figure 7 : Graphs of shear (wind gradient), N2 et cn2 (runs 9, 10, 11, and 14) in the [0-35] km altitude range.
Figure 8 : Same as Figure 7 but shear, N2 et cn2 (runs 9, 10, 11, and 14) in the [18-22] km altitude range.

APPENDIX 4
SECOND SET OF GRAPHS
RUN 9

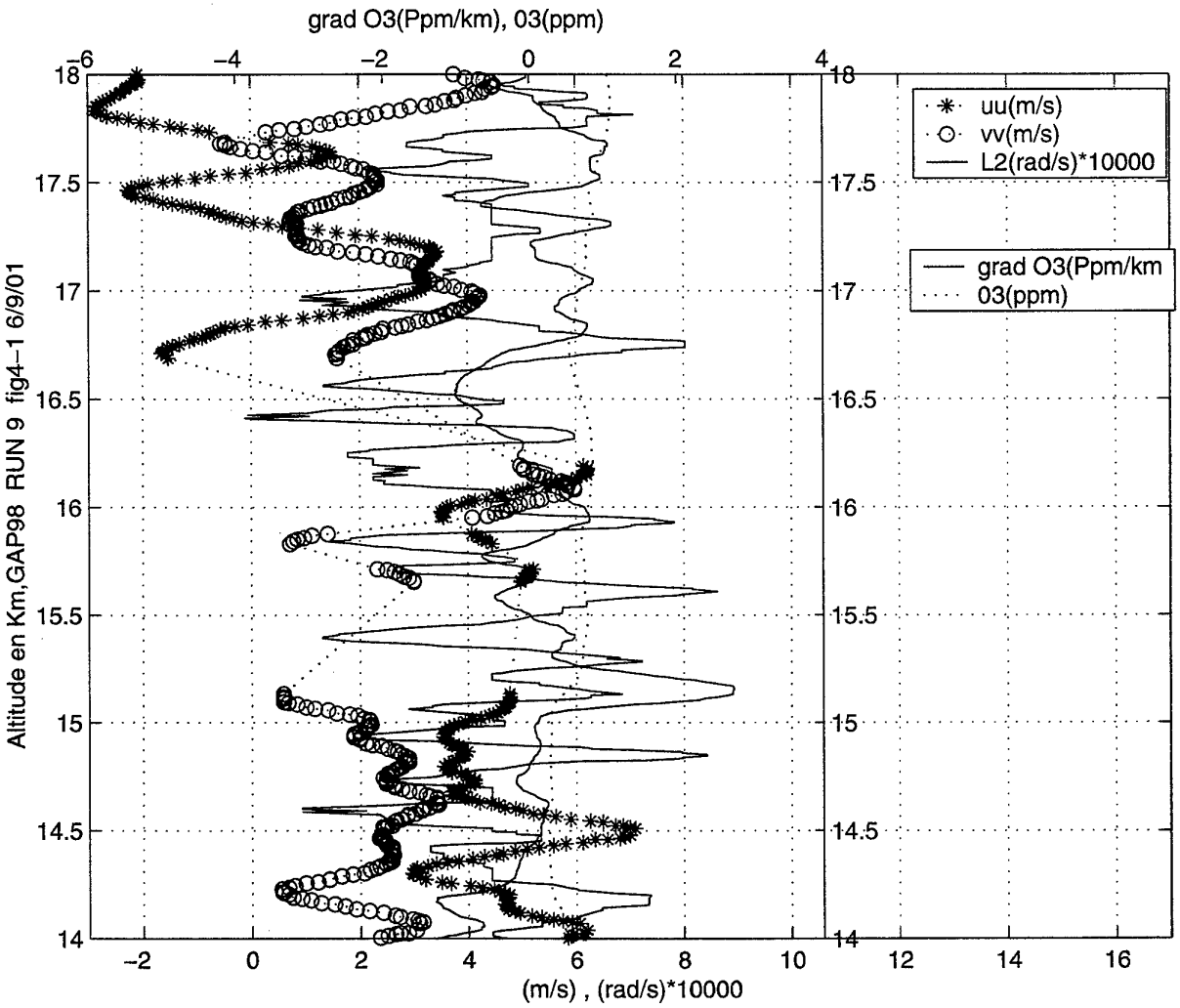

ONERA

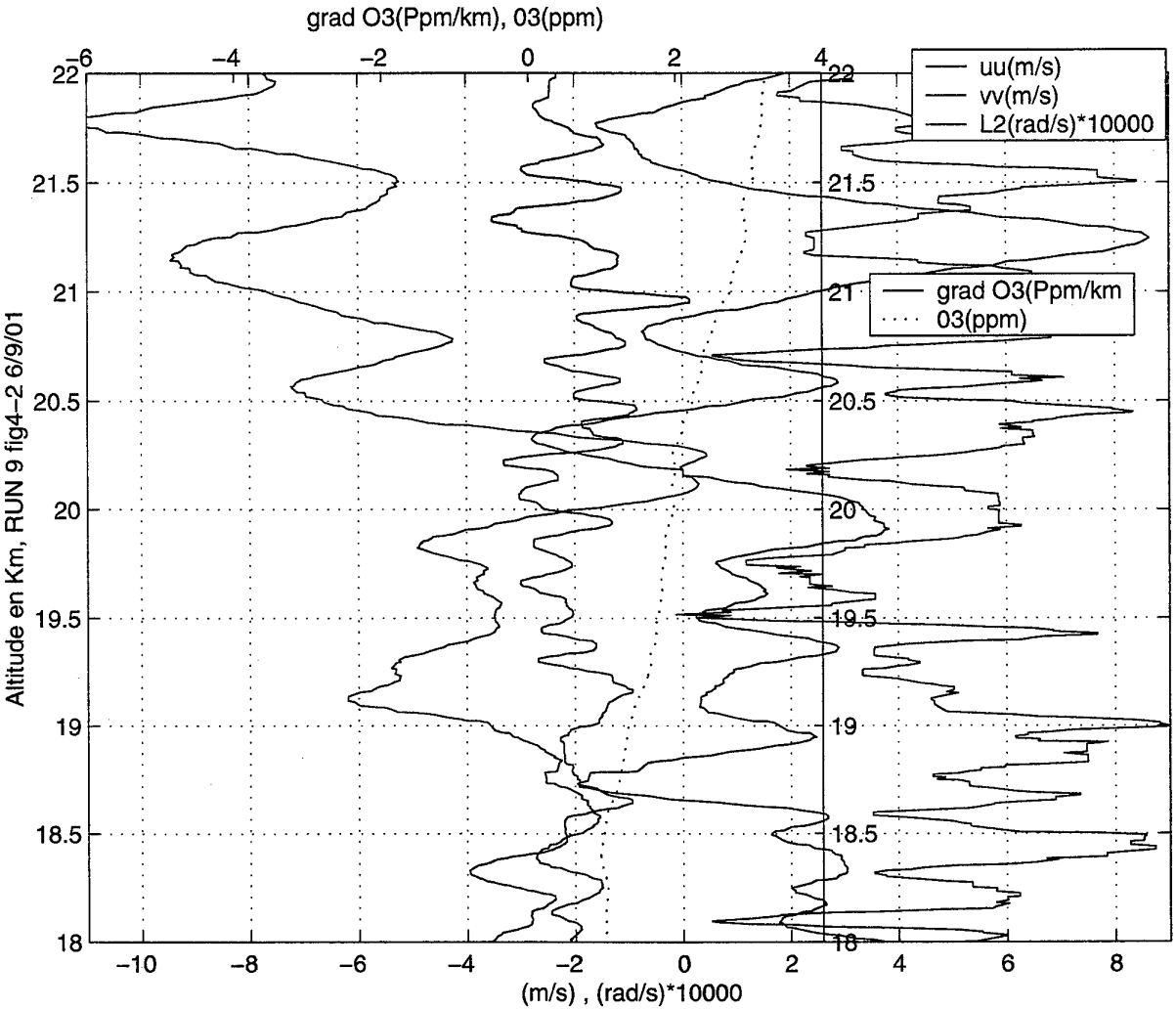
grad O3(Ppm/km), 03(ppm)
uu(m/s)
vv(m/s)
L2(rad/s)*10000
grad O3(Ppm/km
03(ppm)
Altitude en Km, RUN 9 fig4–2 6/9/01
(m/s) , (rad/s)*10000

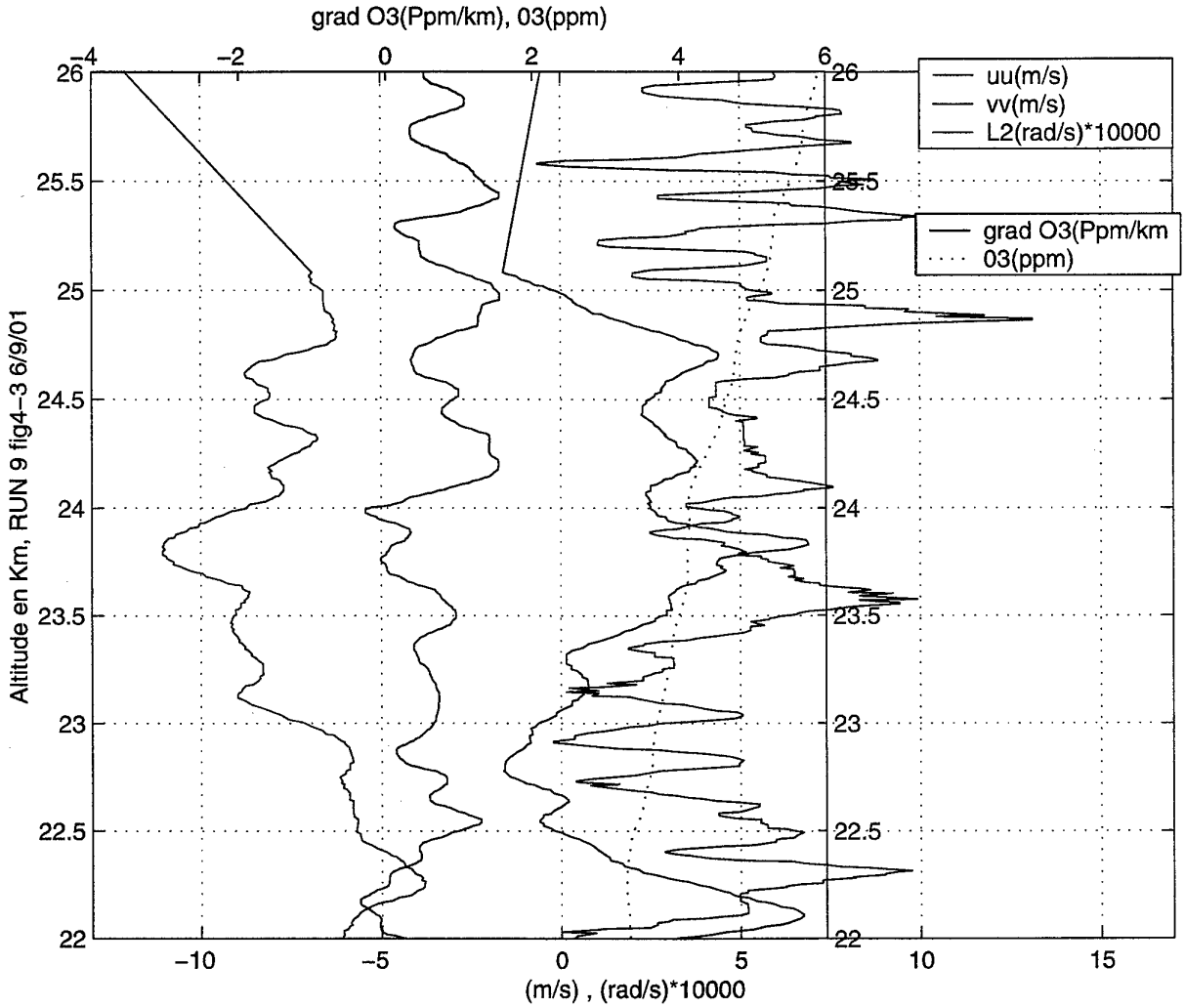
grad O3(Ppm/km), 03(ppm)
−4
−2
0
2
4
6
26
25.5
25
24.5
24
23.5
23
22.5
22
uu(m/s)
vv(m/s)
L2(rad/s)*10000
grad O3(Ppm/km
03(ppm)
Altitude en Km, RUN 9 fig4−3 6/9/01
−10
−5
0
5
10
15
(m/s) , (rad/s)*10000

ONERA

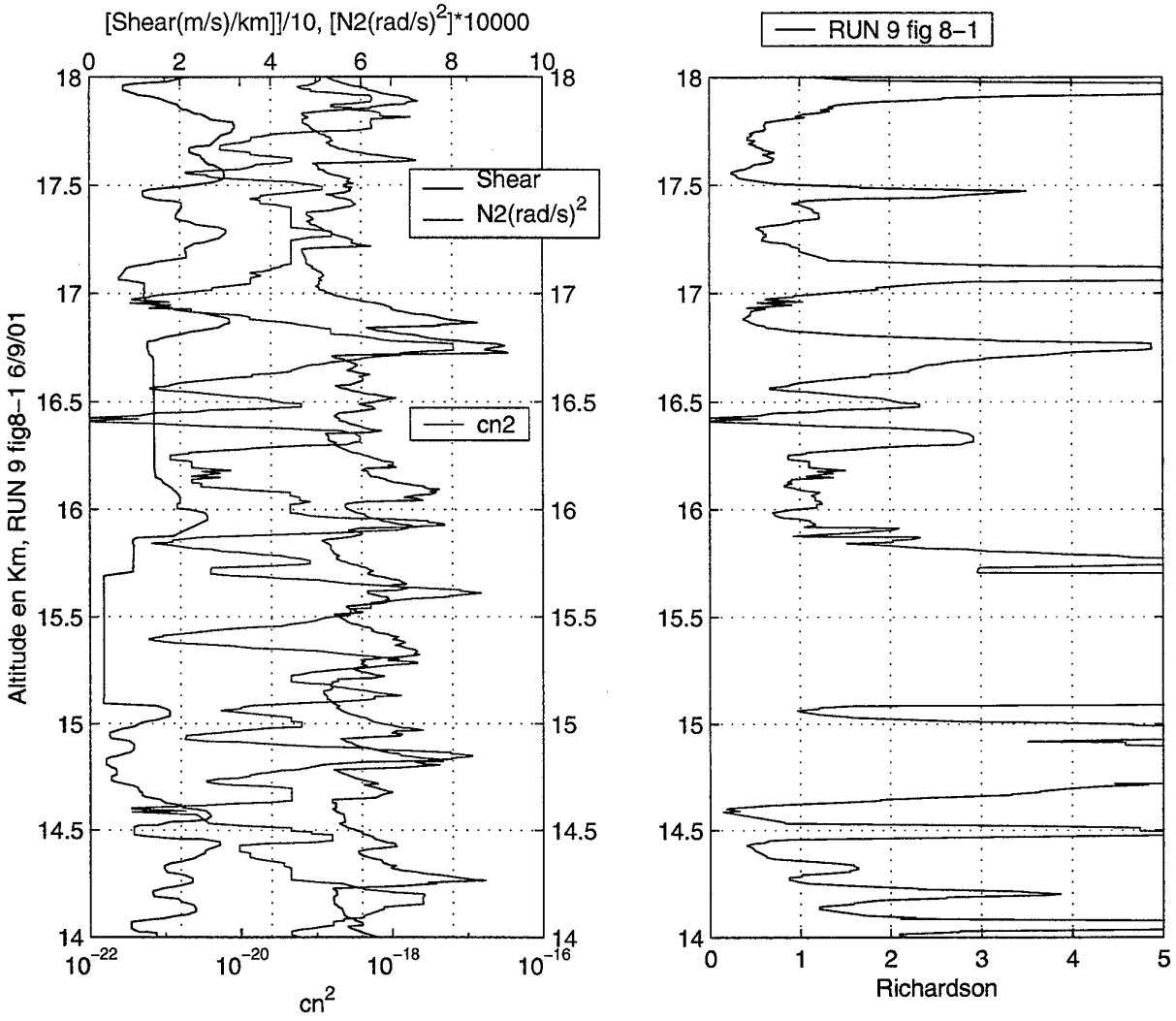
[Shear(m/s)/km]]/10, [N2(rad/s)2]*10000
Shear
N2(rad/s)2
cn2
Altitude en Km, RUN 9 fig8-1 6/9/01
cn2
RUN 9 fig 8-1
Richardson

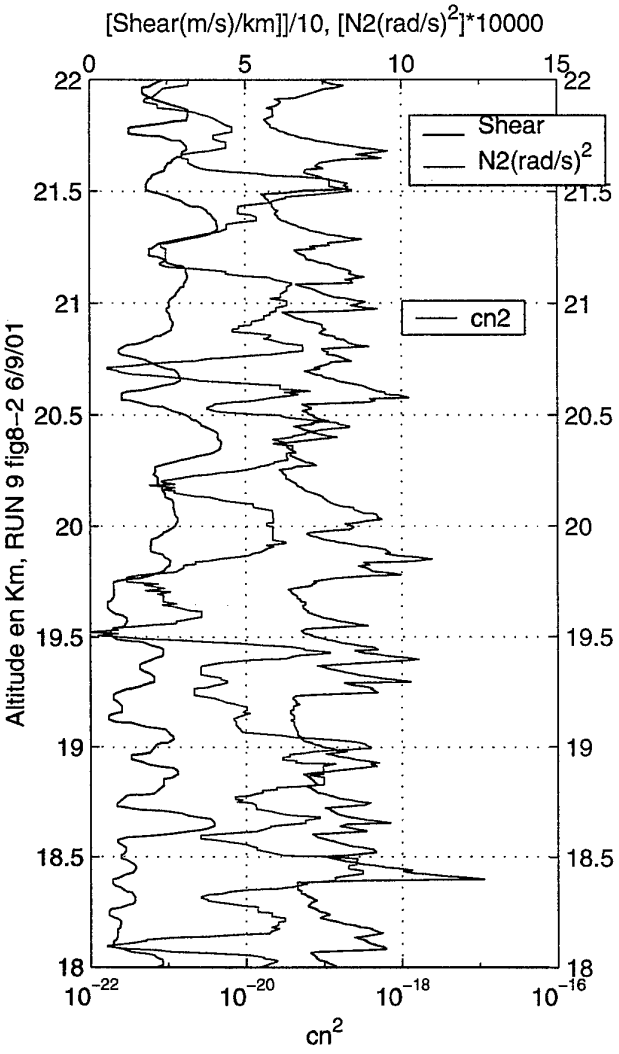
[Shear(m/s)/km]]/10, [N2(rad/s)2]*10000
Shear
N2(rad/s)2
cn2
Altitude en Km, RUN 9 fig8-2 6/9/01
cn2

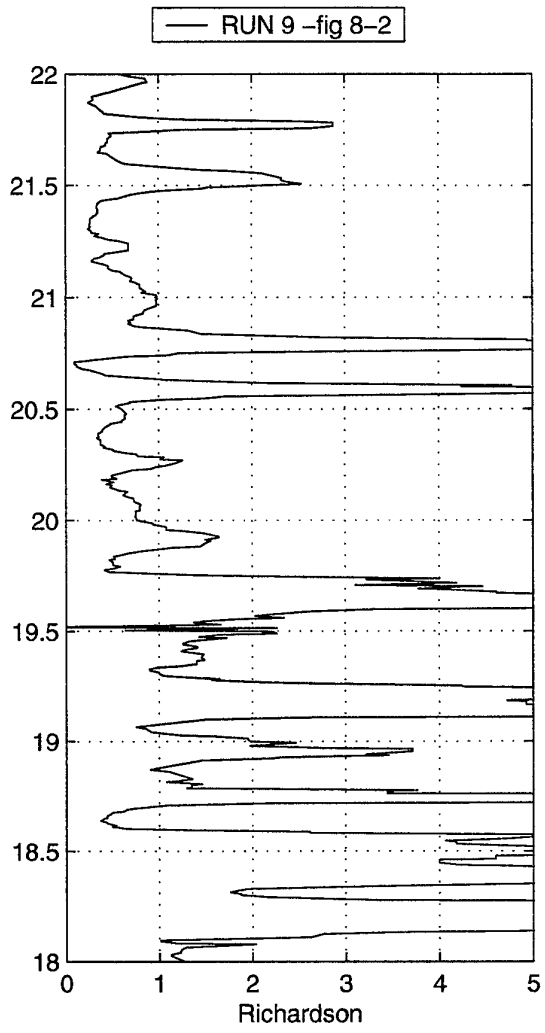
RUN 9 -fig 8-2
Richardson

ONERA

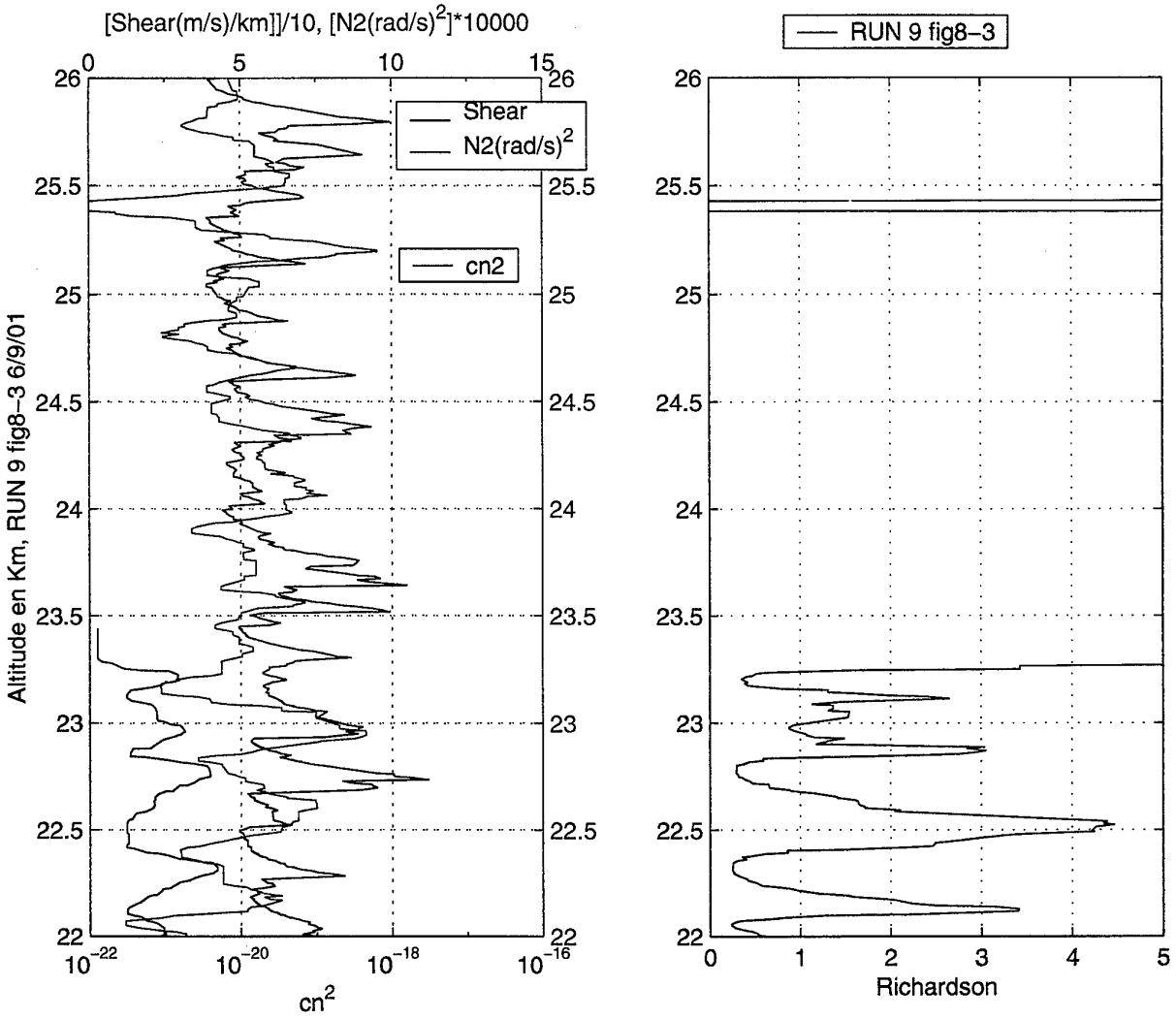
[Shear(m/s)/km]]/10, [N2(rad/s)^2]*10000
Shear
N2(rad/s)^2
cn2
Altitude en Km, RUN 9 fig8–3 6/9/01
cn^2
RUN 9 fig8–3
Richardson

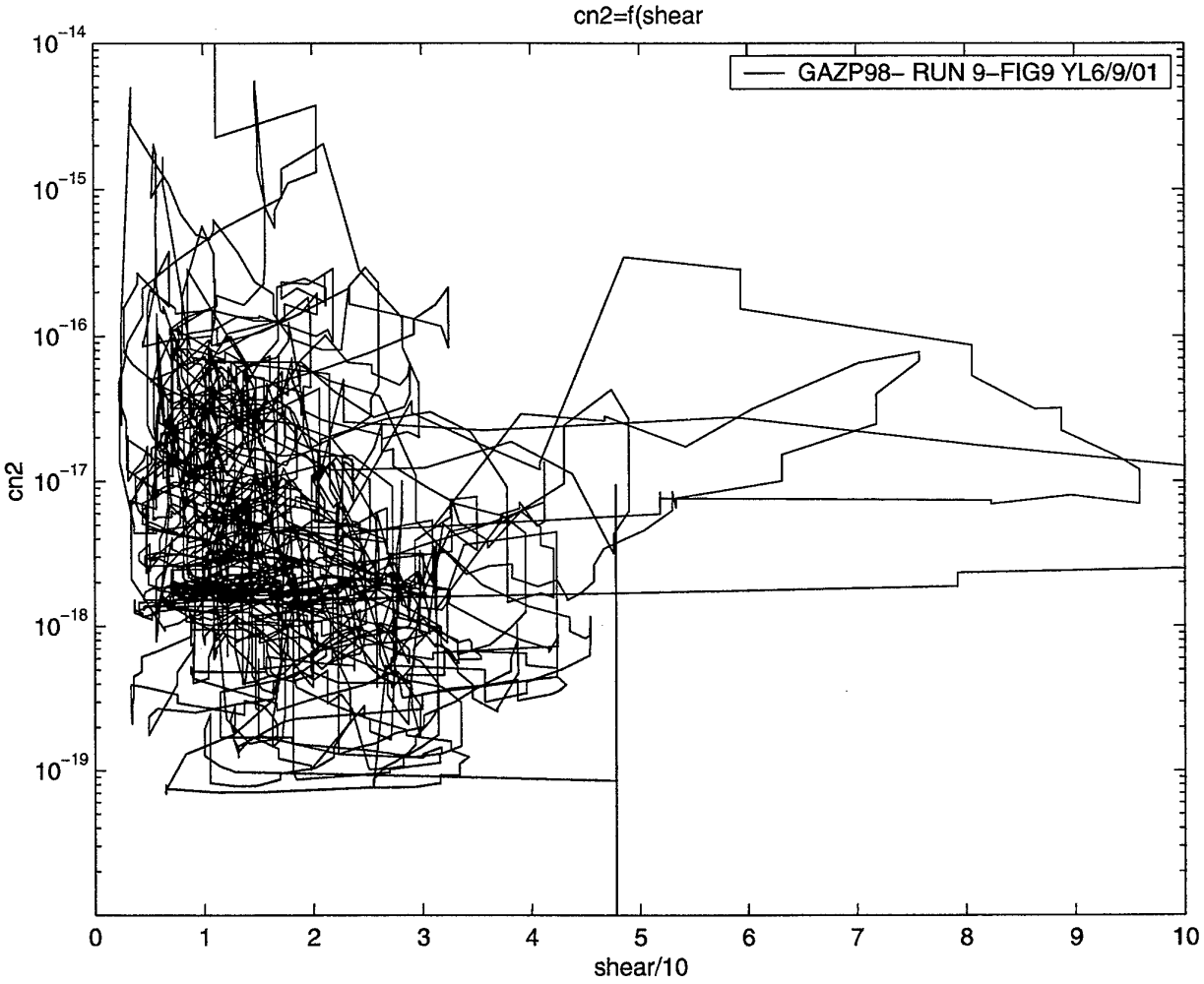
cn2=f(shear
GAZP98– RUN 9–FIG9 YL6/9/01
cn2
shear/10
10^{-14}
10^{-15}
10^{-16}
10^{-17}
10^{-18}
10^{-19}
0
1
2
3
4
5
6
7
8
9
10

APPENDIX 4
SECOND SET OF GRAPHS
RUN 10

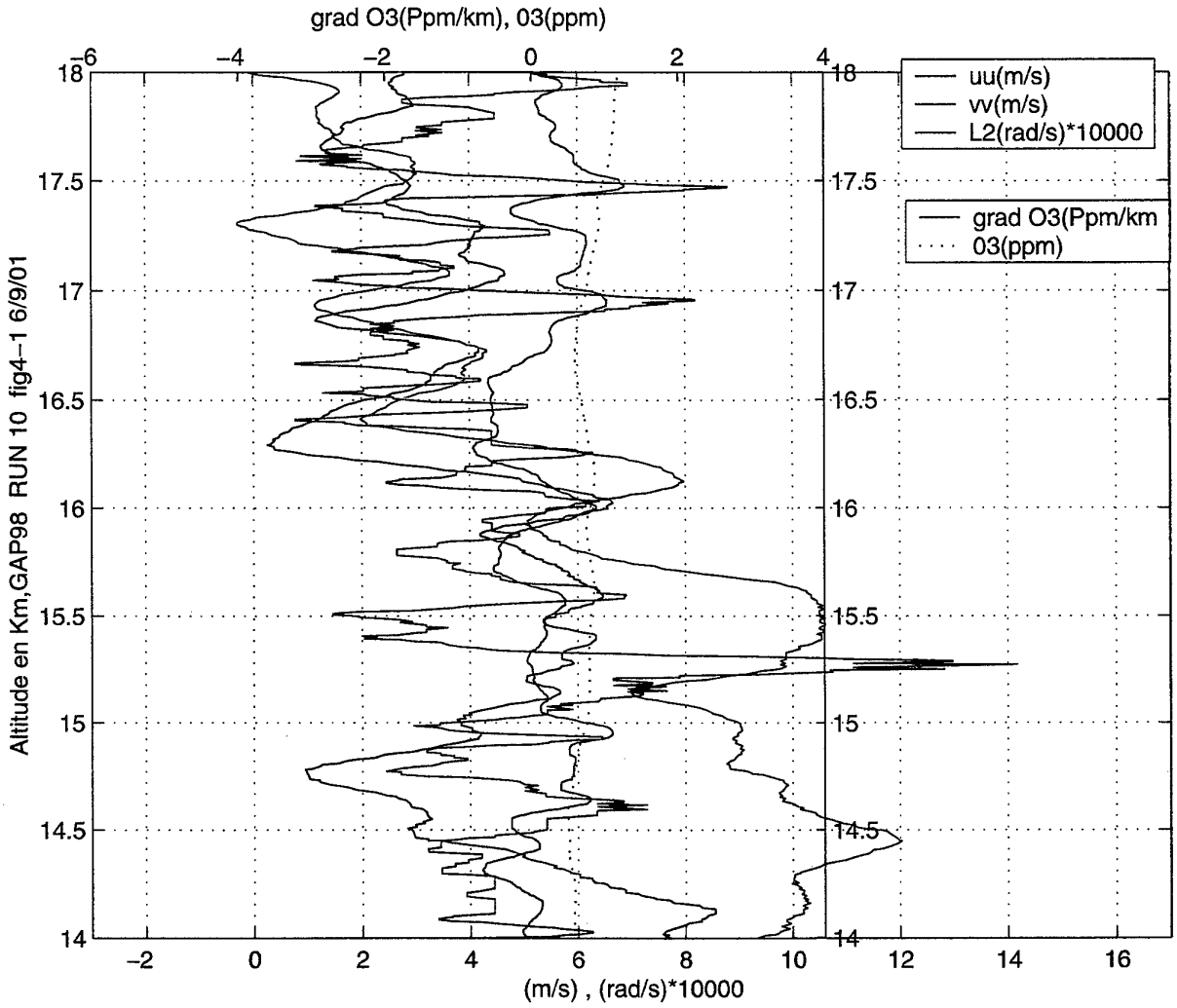
grad O3(Ppm/km), 03(ppm)
uu(m/s)
vv(m/s)
L2(rad/s)*10000
grad O3(Ppm/km
03(ppm)
Altitude en Km,GAP98 RUN 10 fig4-1 6/9/01
(m/s) , (rad/s)*10000

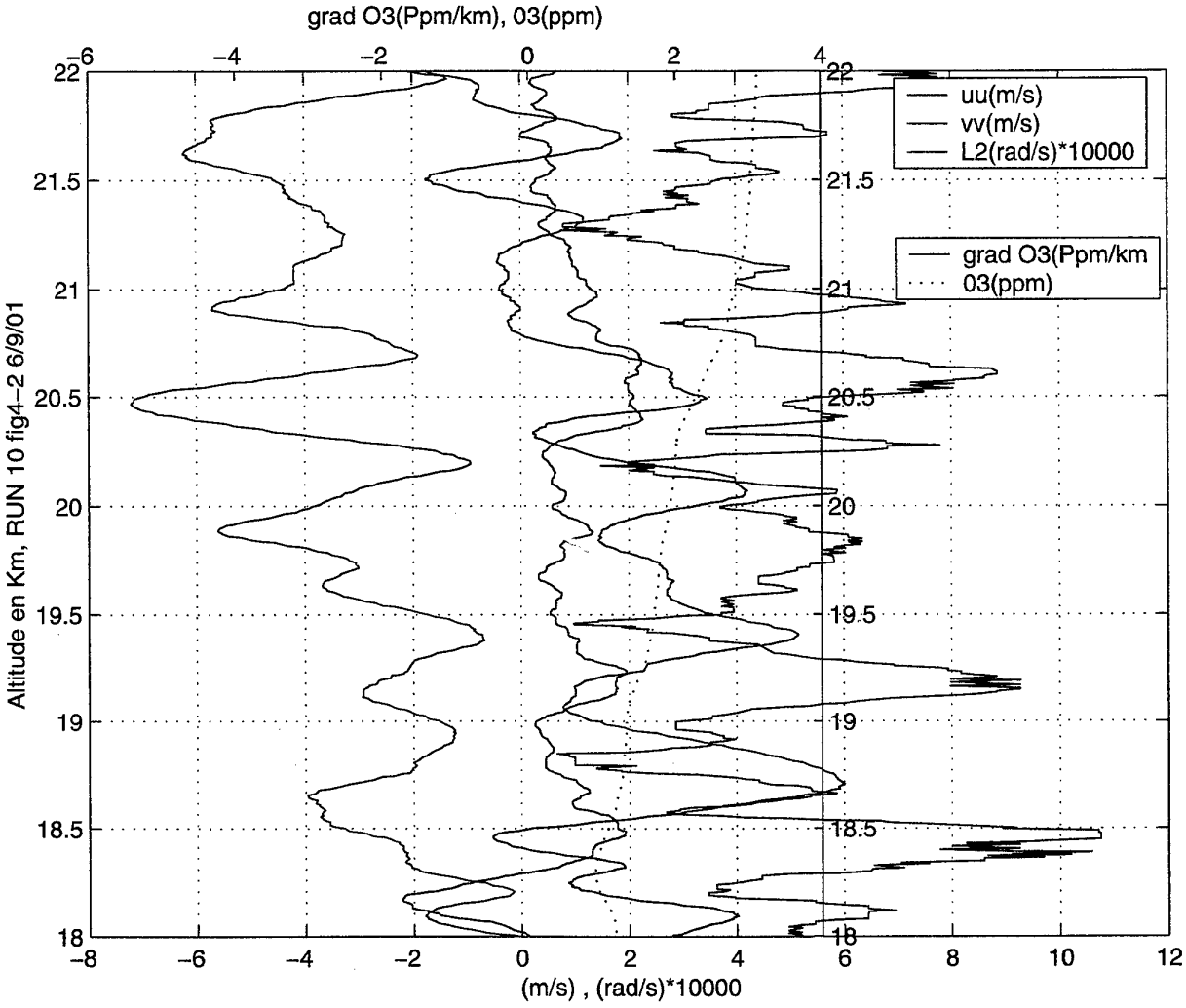
grad O3(Ppm/km), 03(ppm)
uu(m/s)
vv(m/s)
L2(rad/s)*10000
grad O3(Ppm/km
03(ppm)
Altitude en Km, RUN 10 fig4-2 6/9/01
(m/s) , (rad/s)*10000

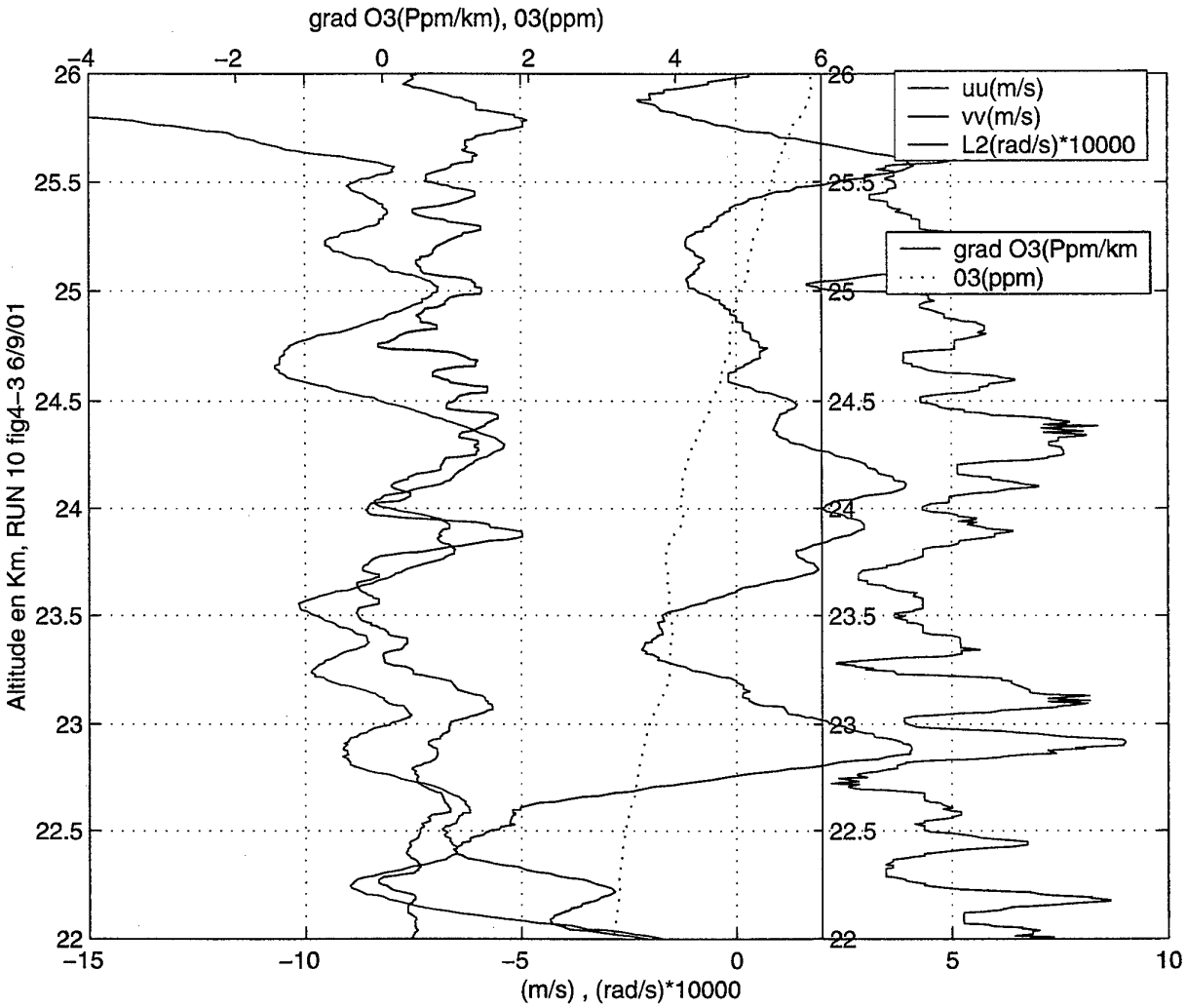
grad O3(Ppm/km), 03(ppm)
−4
−2
0
2
4
6
26
25.5
25
24.5
24
23.5
23
22.5
22
uu(m/s)
vv(m/s)
L2(rad/s)*10000
grad O3(Ppm/km
03(ppm)
Altitude en Km, RUN 10 fig4−3 6/9/01
−15
−10
−5
0
5
10
(m/s) , (rad/s)*10000

ONERA

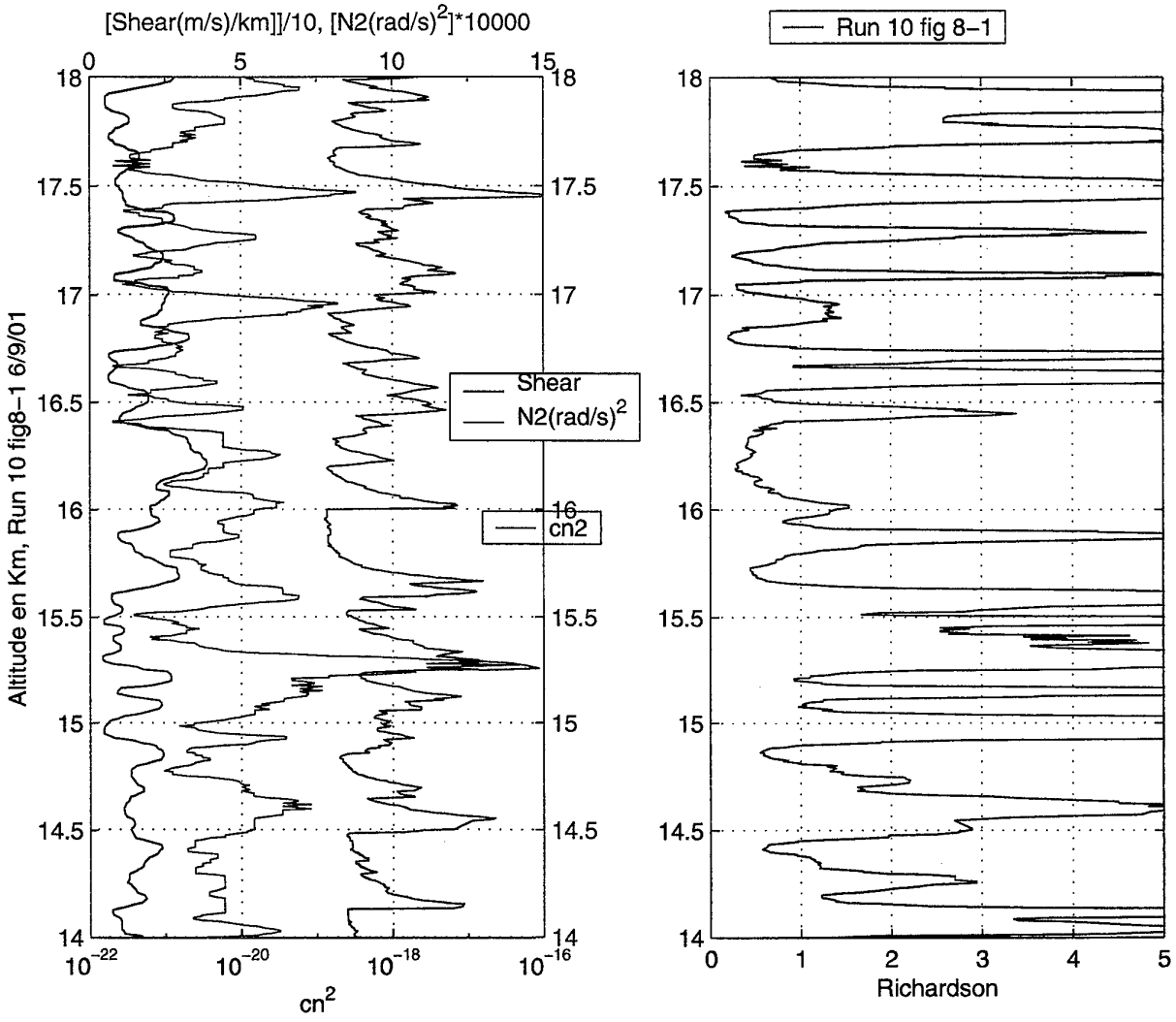
[Shear(m/s)/km]]/10, [N2(rad/s)2]*10000
Run 10 fig 8–1
Shear
N2(rad/s)2
cn2
Altitude en Km, Run 10 fig8–1 6/9/01
cn2
Richardson

ONERA

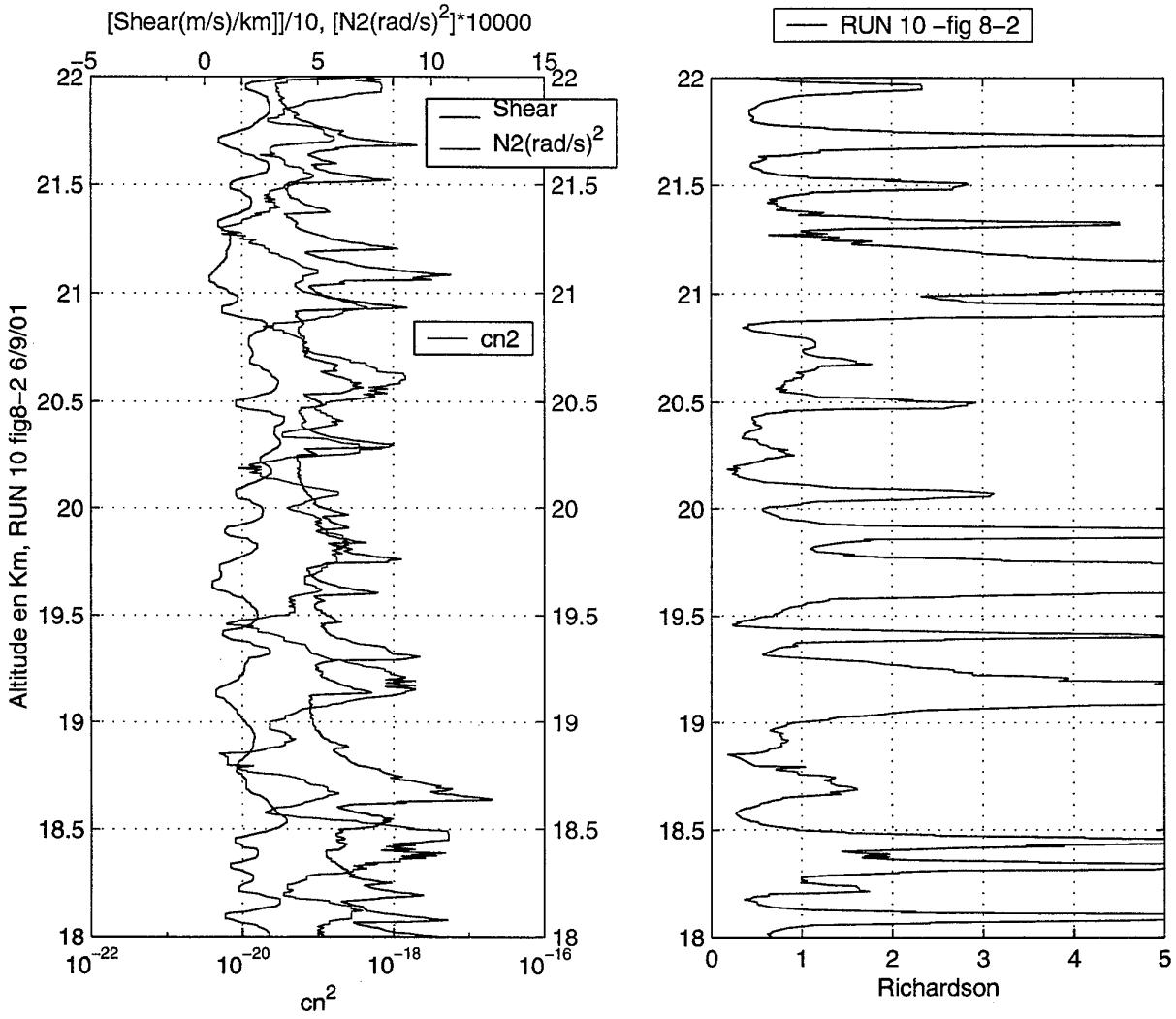
[Shear(m/s)/km]]/10, [N2(rad/s)2]*10000
Shear
N2(rad/s)2
cn2
Altitude en Km, RUN 10 fig8–2 6/9/01
cn2
RUN 10 –fig 8–2
Richardson

ONERA

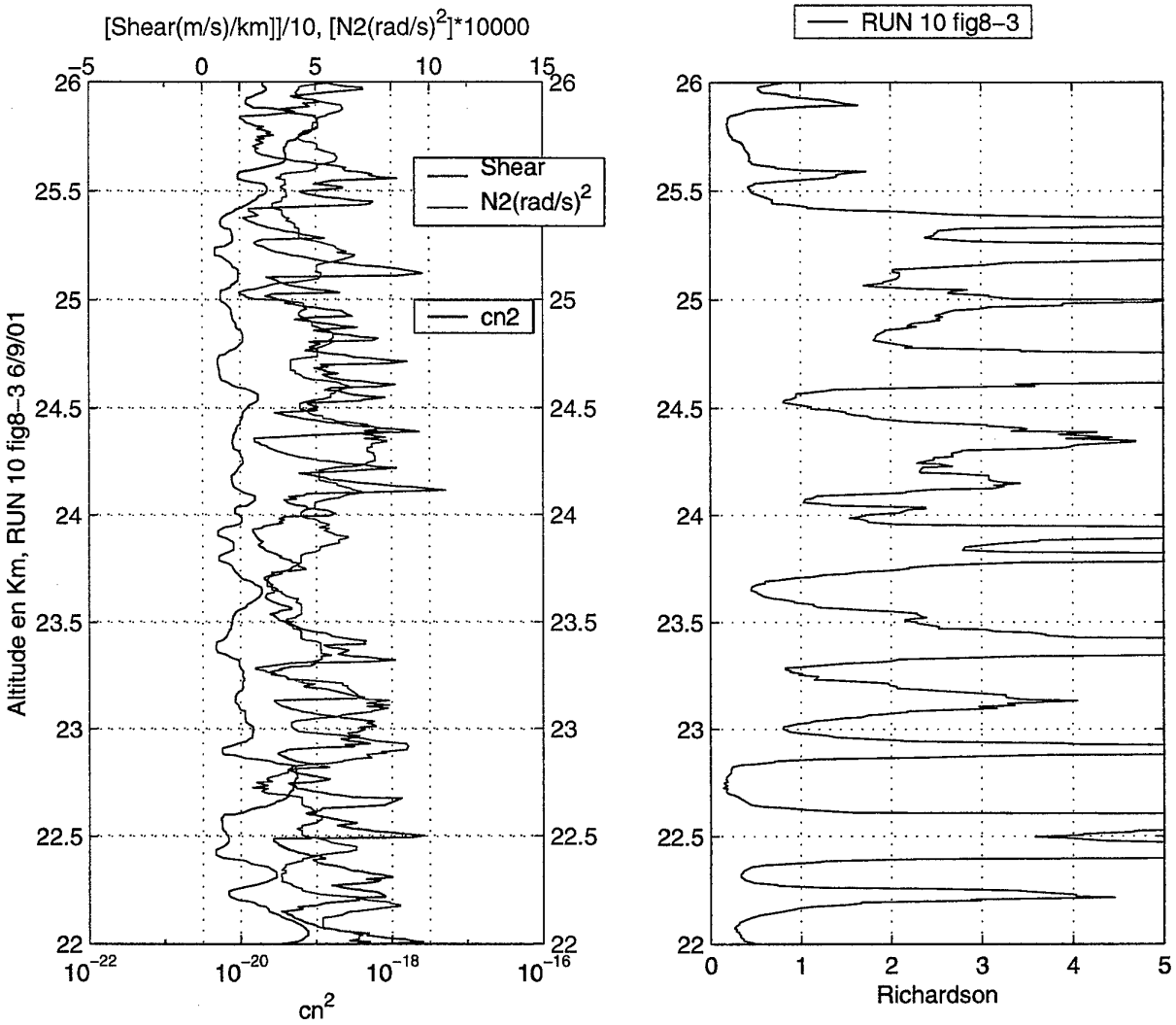
[Shear(m/s)/km]]/10, [N2(rad/s)2]*10000
Shear
N2(rad/s)2
cn2
Altitude en Km, RUN 10 fig8-3 6/9/01
cn2
RUN 10 fig8-3
Richardson

SANS MENTION
DE PROTECTION

SMP

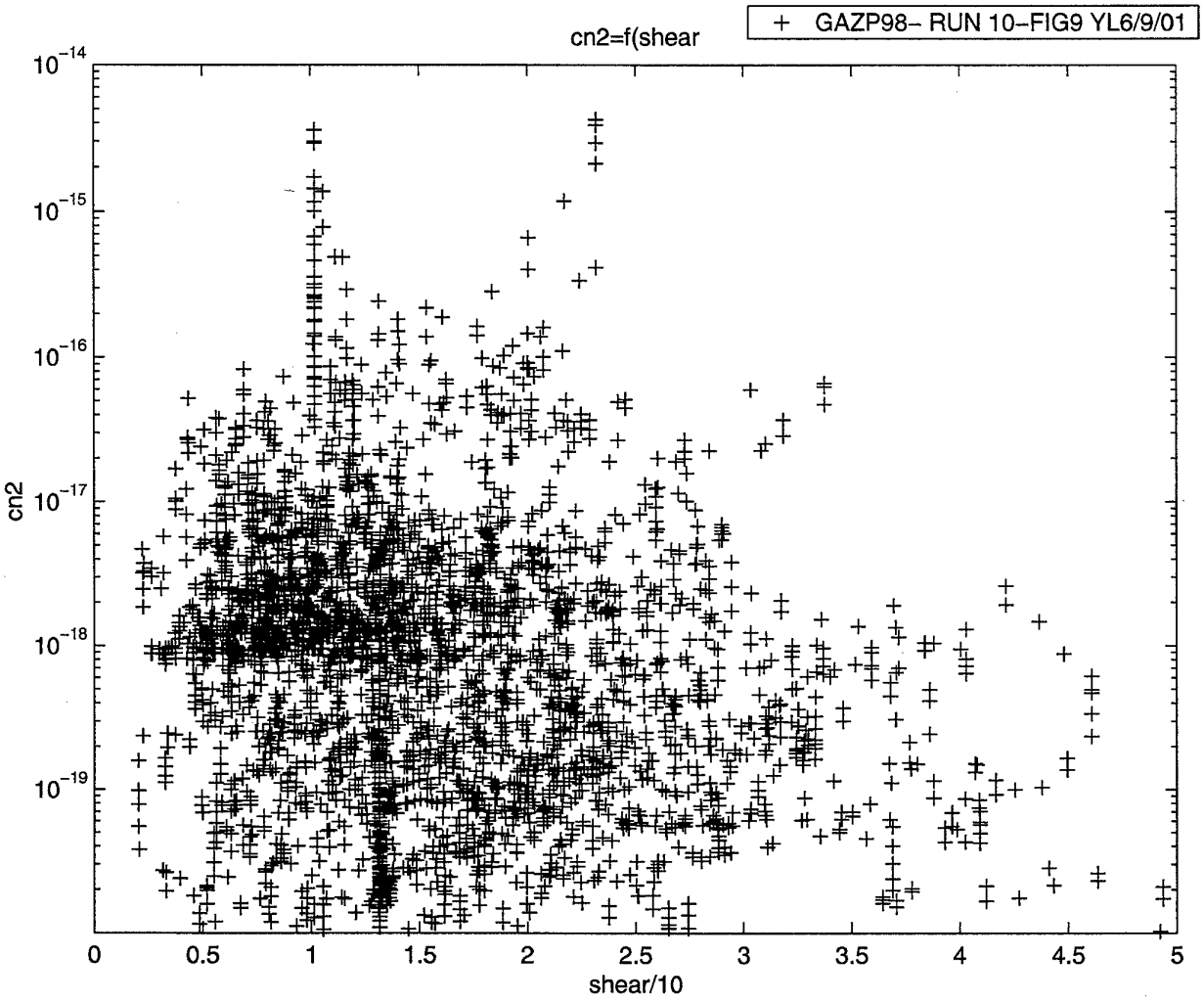

ONERA

APPENDIX 4
SECOND SET OF GRAPHS
RUN 11

SANS MENTION
DE PROTECTION

SMP

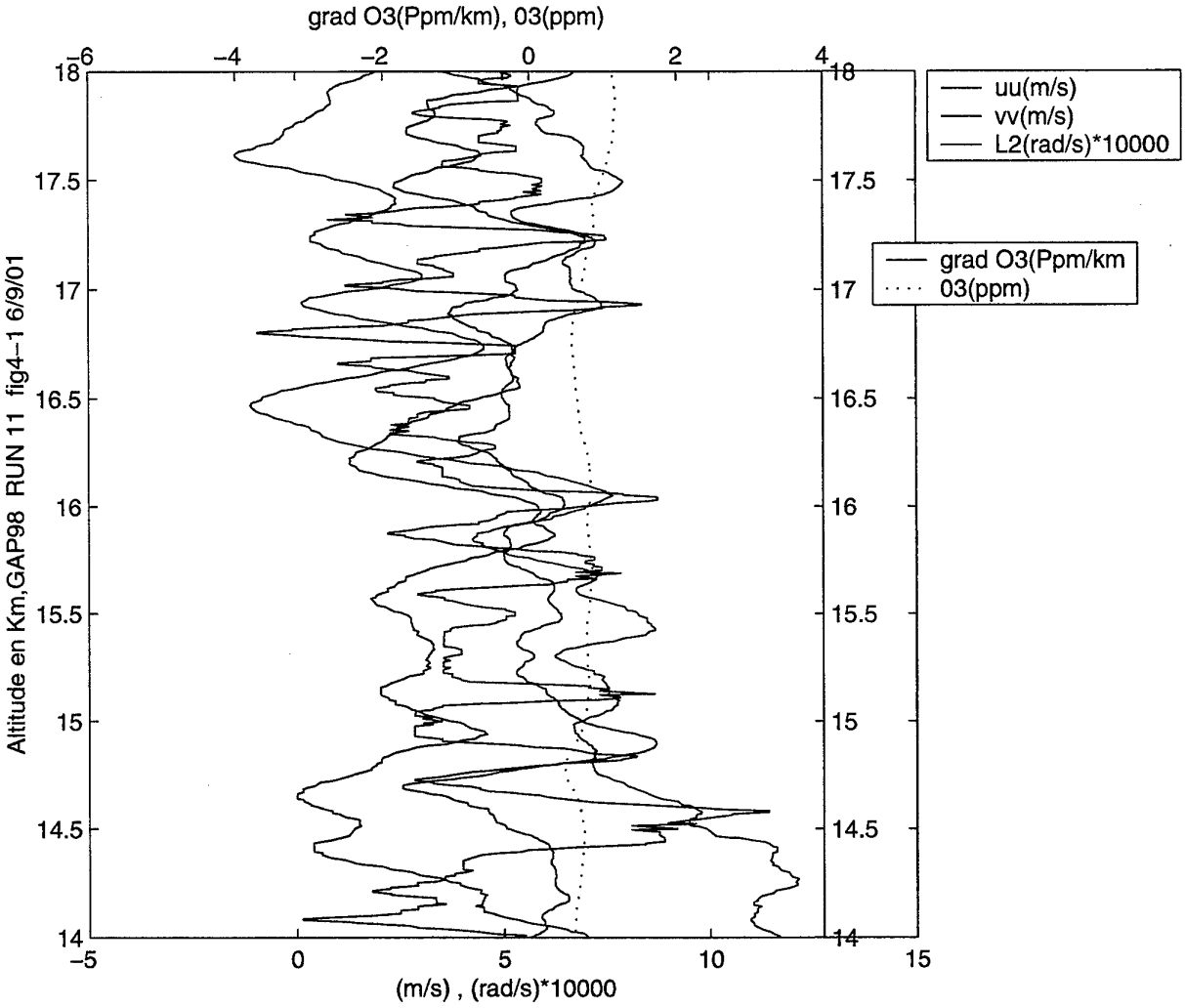

ONERA

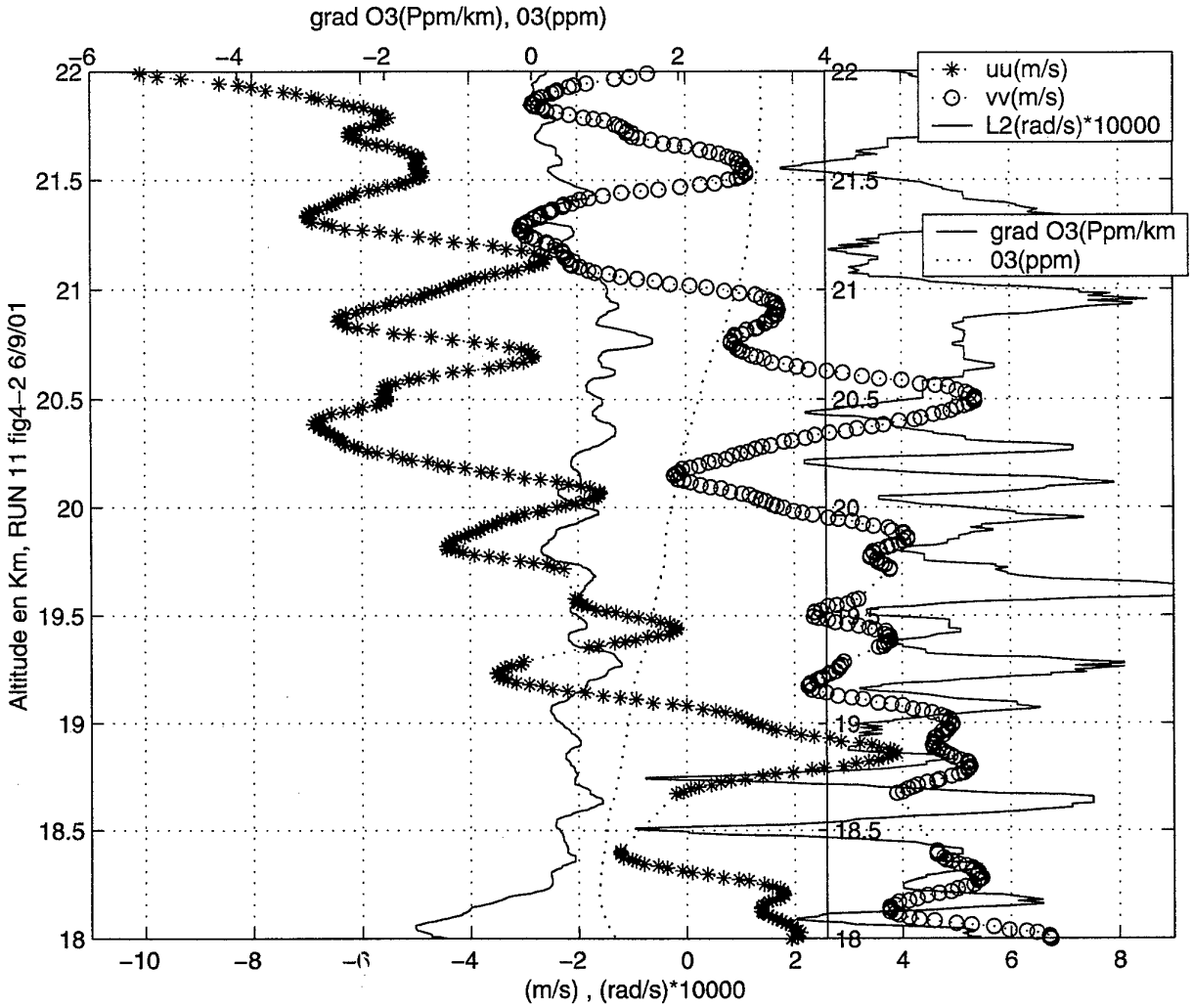
grad O3(Ppm/km), 03(ppm)
uu(m/s)
vv(m/s)
L2(rad/s)*10000
grad O3(Ppm/km
03(ppm)
Altitude en Km, RUN 11 fig4-2 6/9/01
(m/s) , (rad/s)*10000

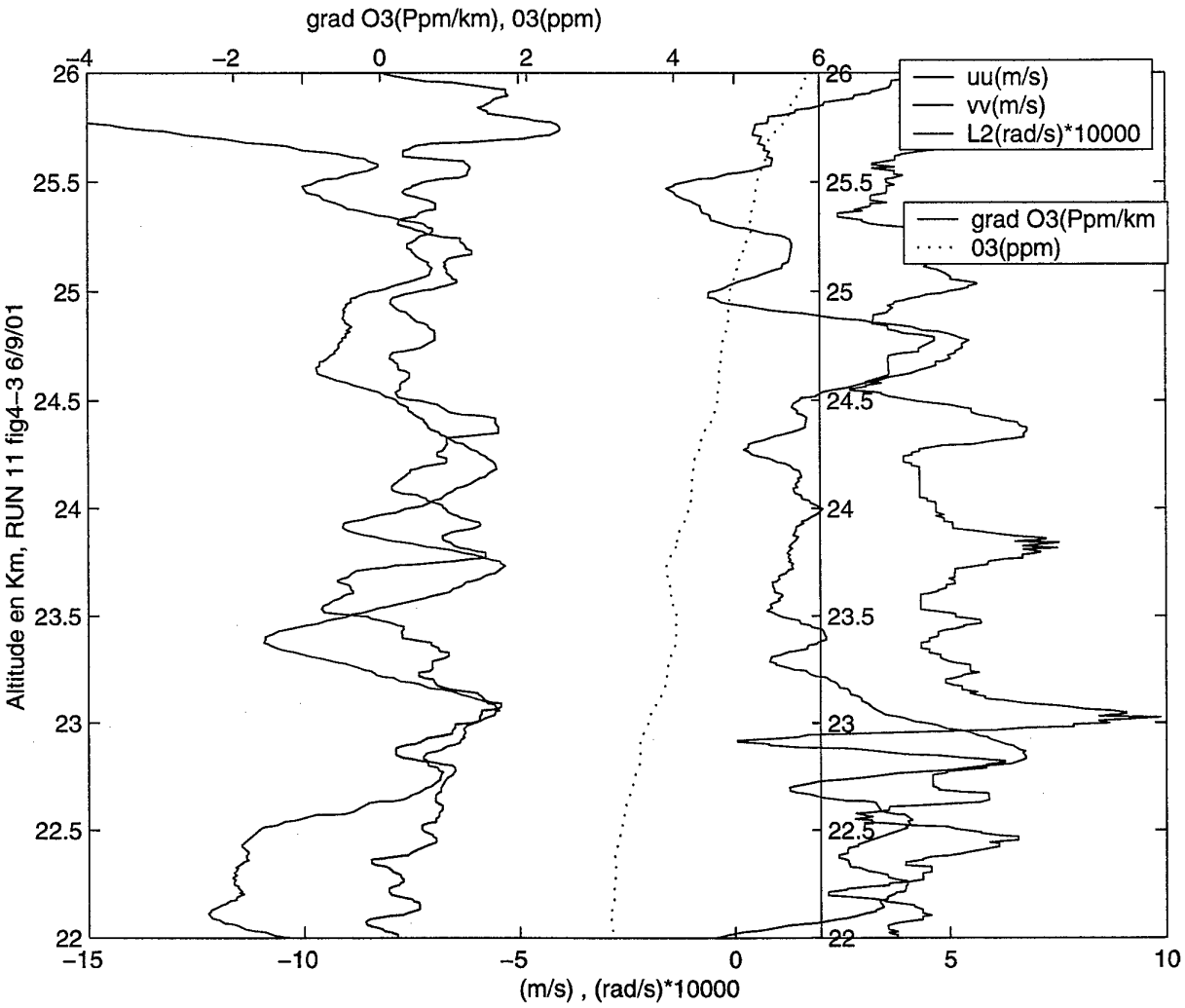
grad O3(Ppm/km), 03(ppm)
−4
−2
0
2
4
6
26
25.5
25
24.5
24
23.5
23
22.5
22
uu(m/s)
vv(m/s)
L2(rad/s)*10000
grad O3(Ppm/km
03(ppm)
Altitude en Km, RUN 11 fig4−3 6/9/01
−15
−10
−5
0
5
10
(m/s) , (rad/s)*10000

ONERA

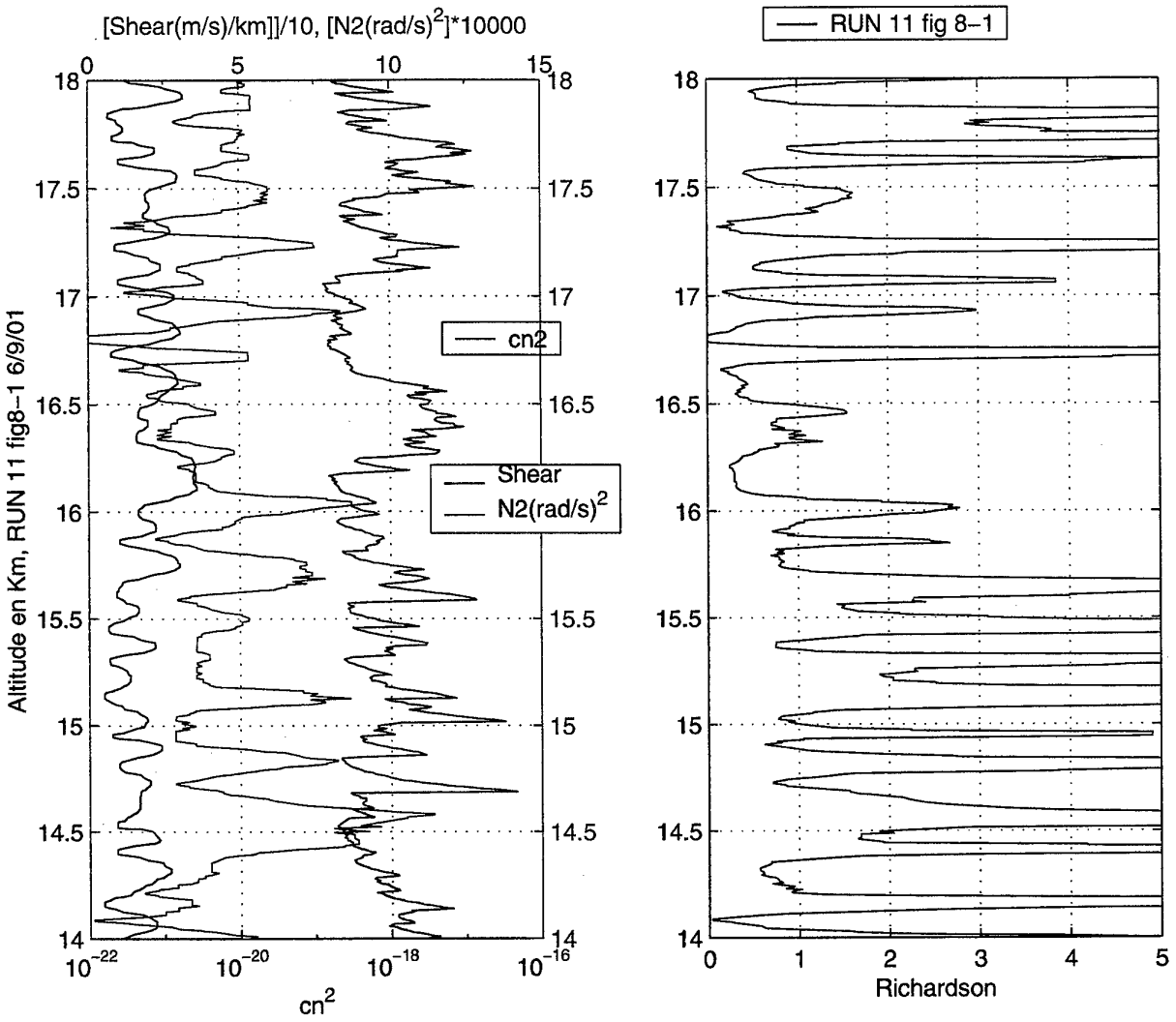
[Shear(m/s)/km]]/10, [N2(rad/s)2]*10000
cn2
Shear
N2(rad/s)2
Altitude en Km, RUN 11 fig8-1 6/9/01
cn2
RUN 11 fig 8-1
Richardson

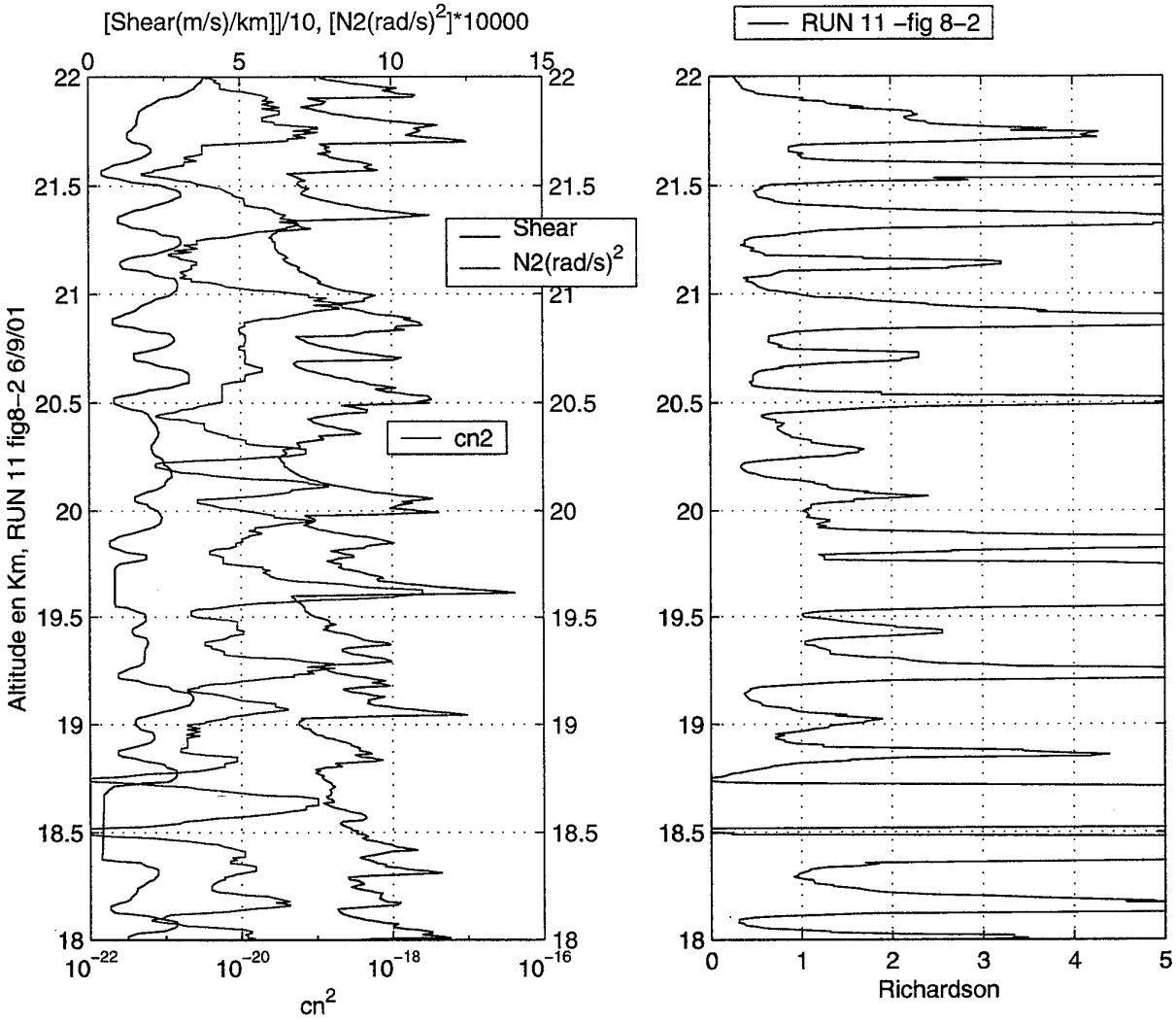
[Shear(m/s)/km]]/10, [N2(rad/s)^2]*10000
RUN 11 –fig 8–2
Shear
N2(rad/s)^2
cn2
Altitude en Km, RUN 11 fig8–2 6/9/01
cn^2
Richardson

ONERA

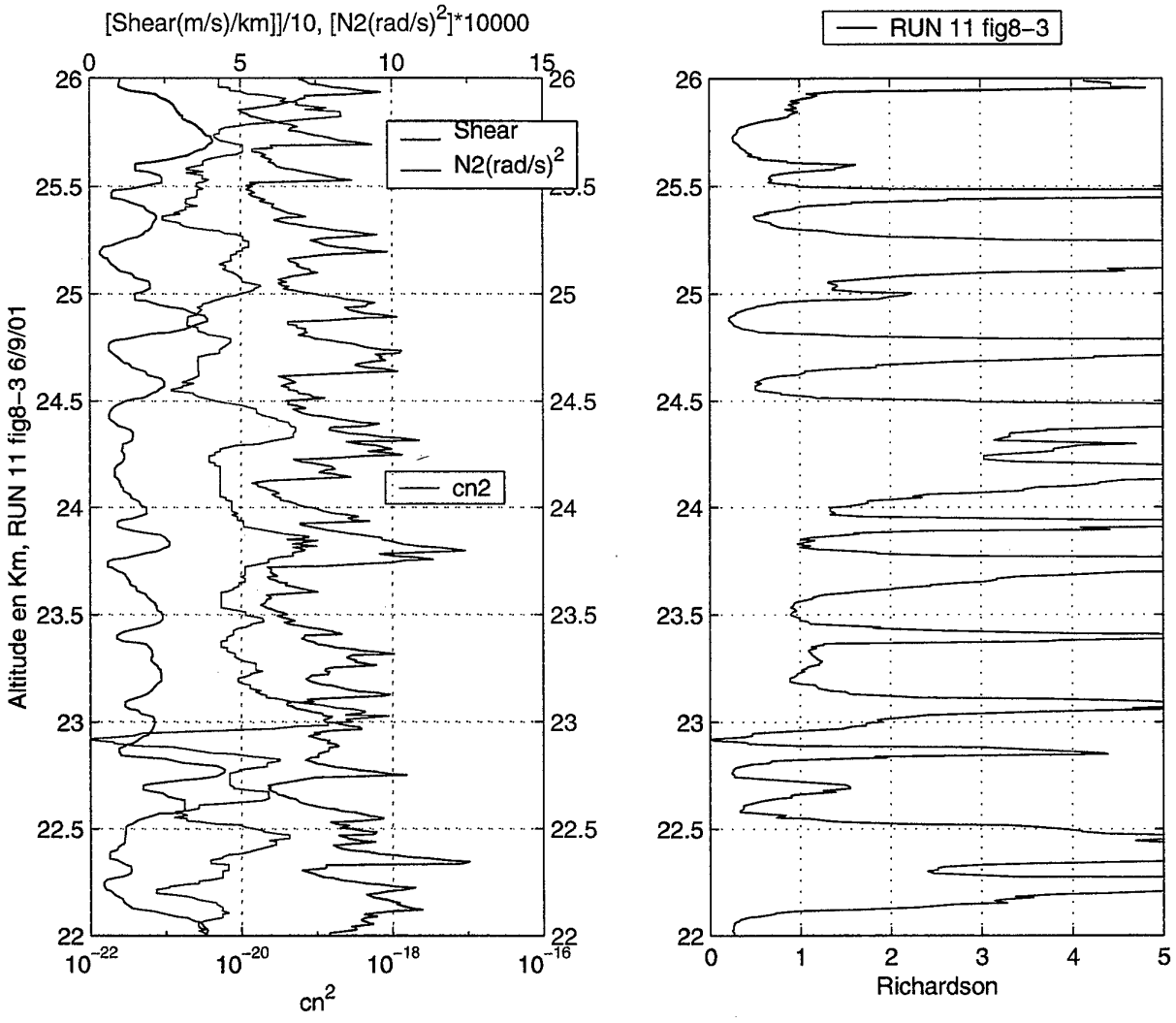
[Shear(m/s)/km]]/10, [N2(rad/s)^2]*10000
Shear
N2(rad/s)^2
cn2
Altitude en Km, RUN 11 fig8-3 6/9/01
cn^2
RUN 11 fig8-3
Richardson

ONERA

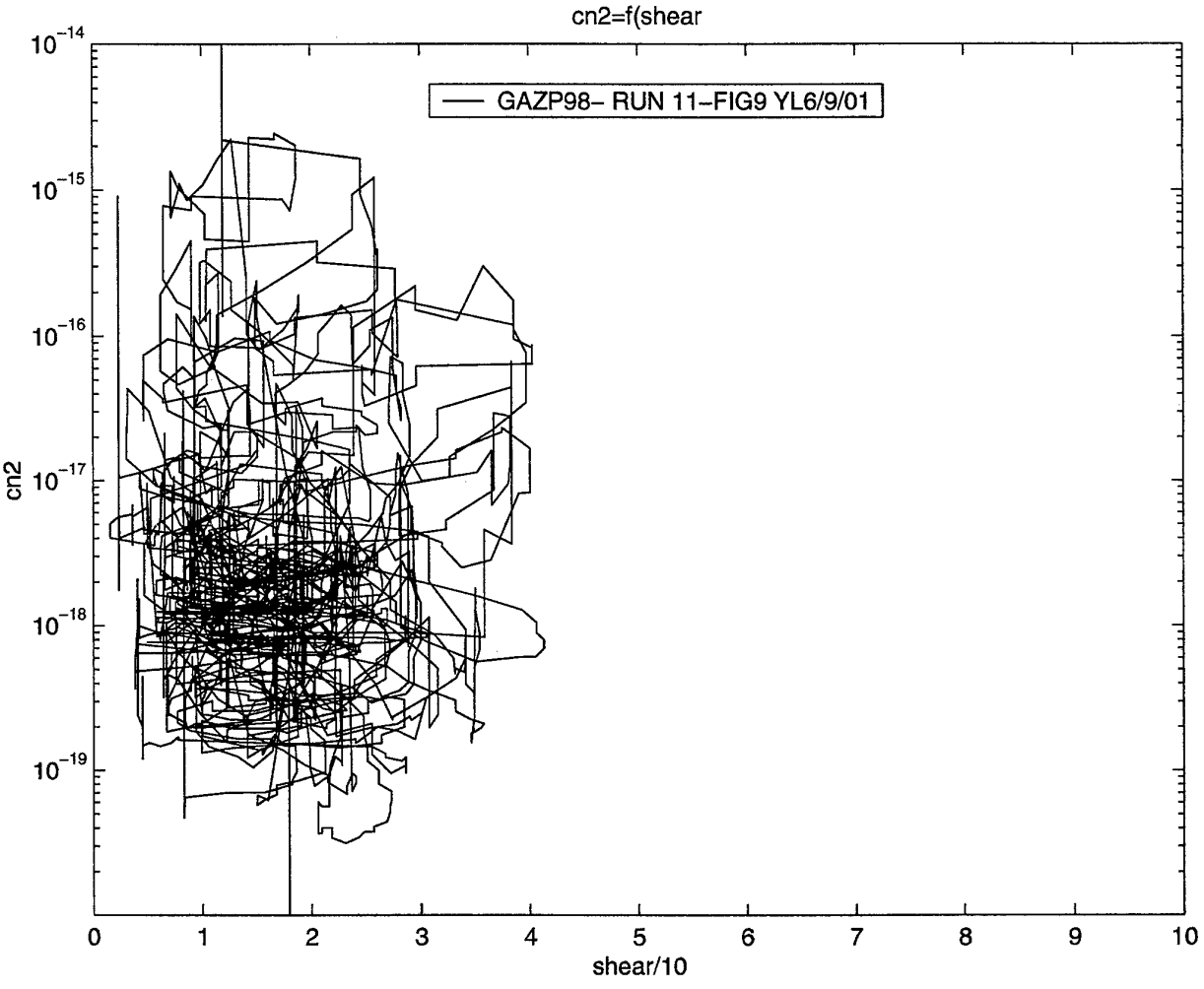
cn2=f(shear
GAZP98– RUN 11–FIG9 YL6/9/01
cn2
10^{-14}
10^{-15}
10^{-16}
10^{-17}
10^{-18}
10^{-19}
0
1
2
3
4
5
6
7
8
9
10
shear/10

APPENDIX 4
SECOND SET OF GRAPHS
RUN 14

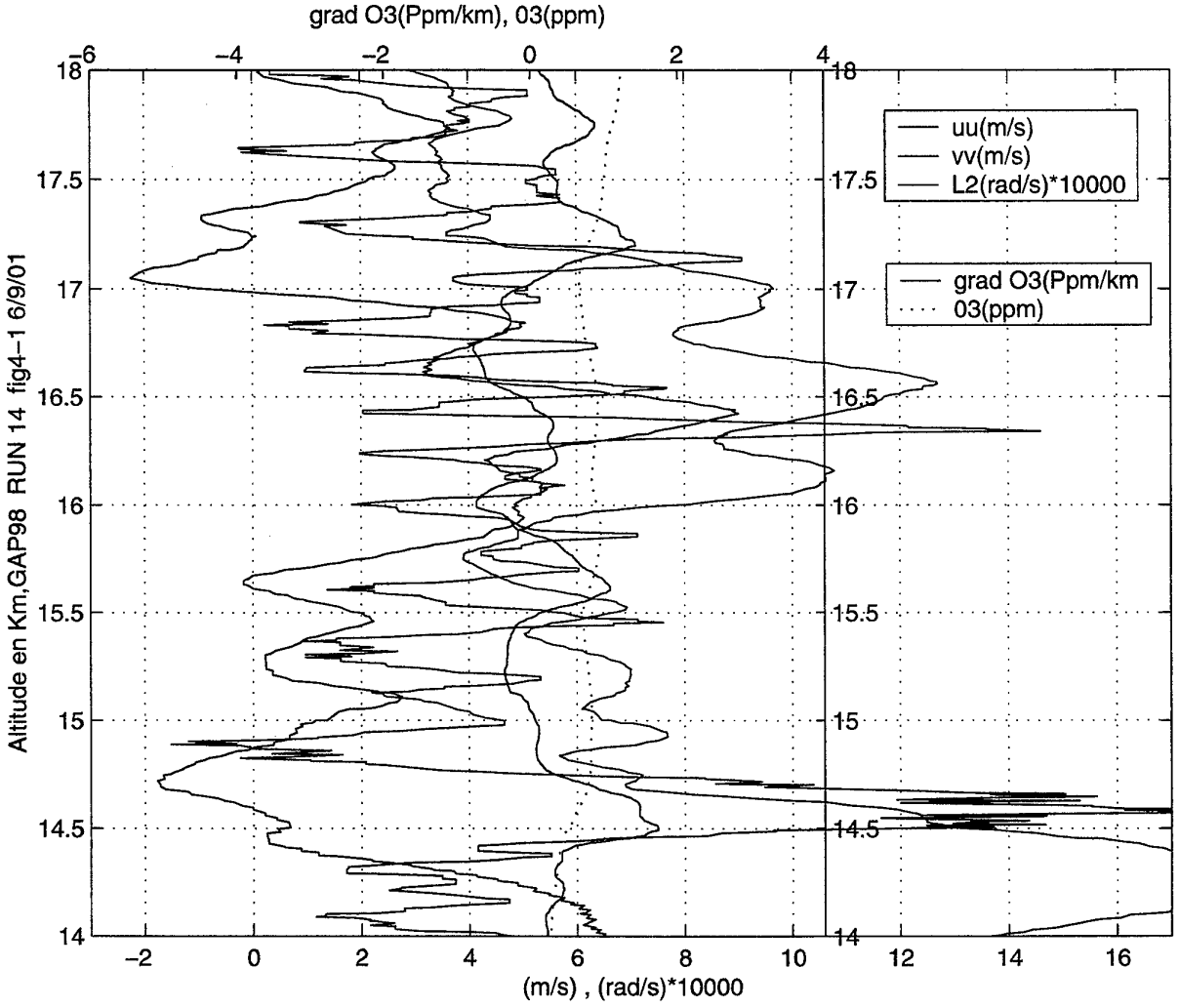
grad O3(Ppm/km), 03(ppm)
Altitude en Km,GAP98 RUN 14 fig4-1 6/9/01
(m/s) , (rad/s)*10000
uu(m/s)
vv(m/s)
L2(rad/s)*10000
grad O3(Ppm/km
03(ppm)

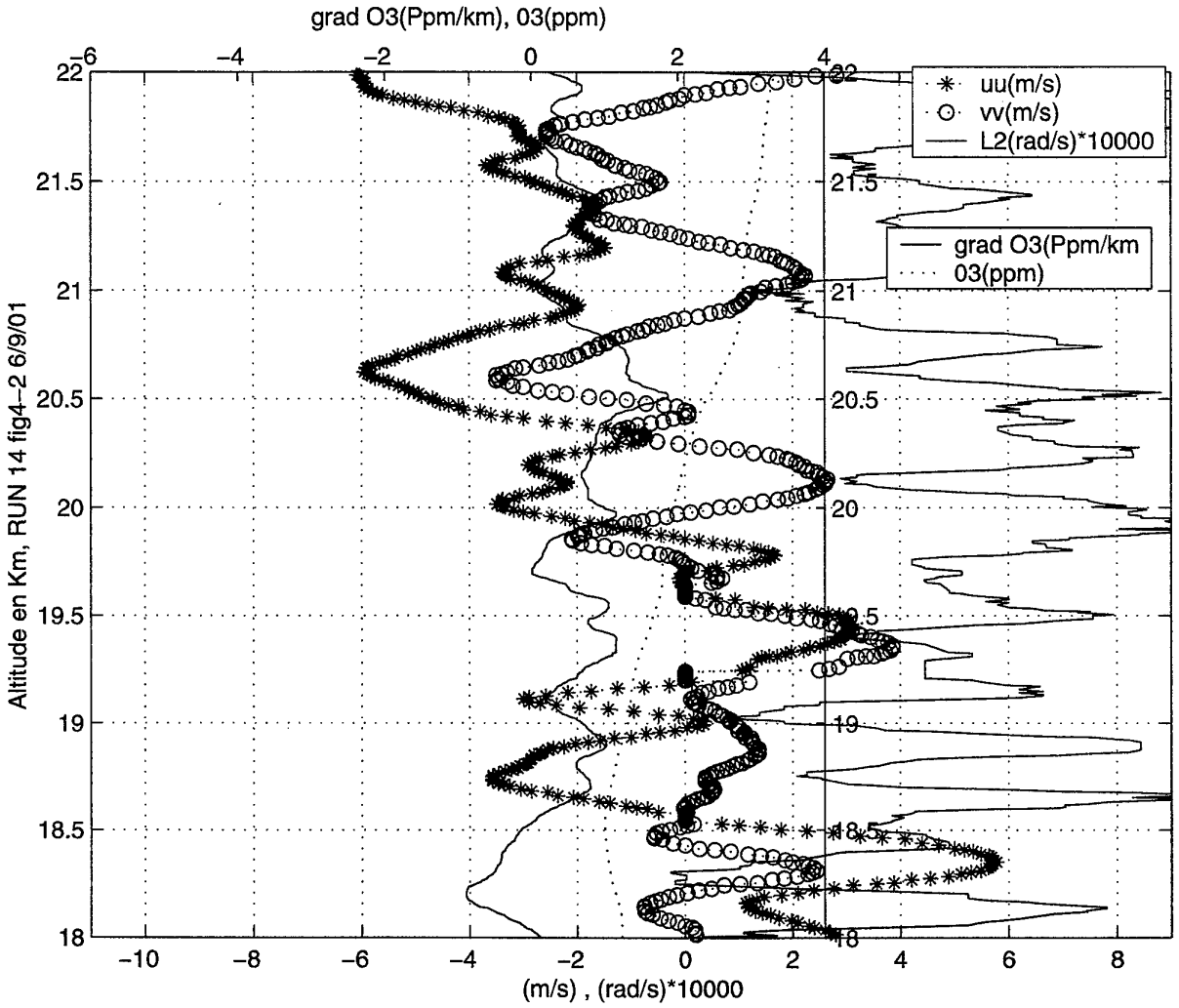
grad O3(Ppm/km), 03(ppm)
uu(m/s)
vv(m/s)
L2(rad/s)*10000
grad O3(Ppm/km
03(ppm)
Altitude en Km, RUN 14 fig4–2 6/9/01
(m/s) , (rad/s)*10000

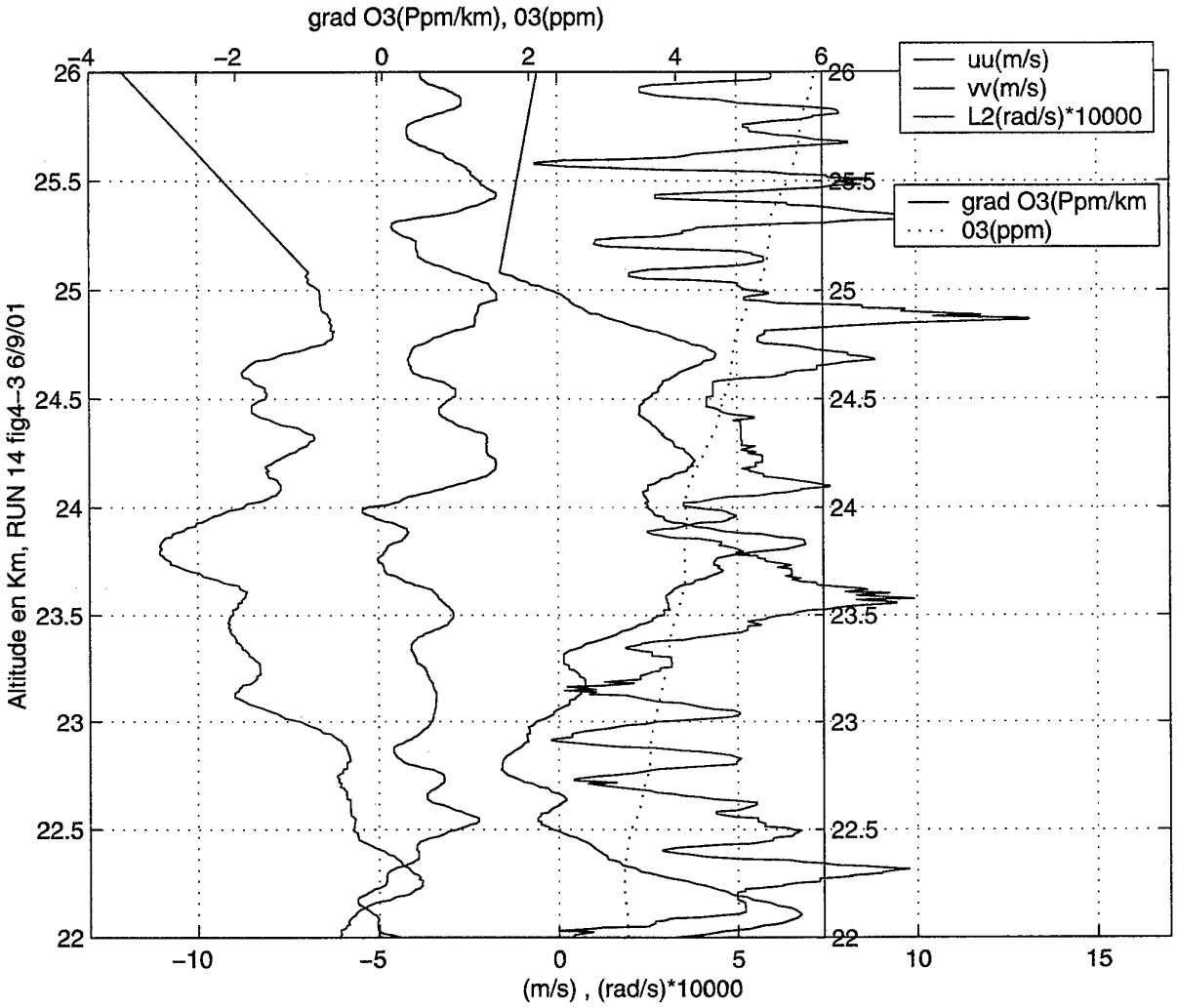
grad O3(Ppm/km), 03(ppm)
−4
−2
0
2
4
6
26
25.5
25
24.5
24
23.5
23
22.5
22
uu(m/s)
vv(m/s)
L2(rad/s)*10000
grad O3(Ppm/km
03(ppm)
Altitude en Km, RUN 14 fig4−3 6/9/01
−10
−5
0
5
10
15
(m/s) , (rad/s)*10000

ONERA

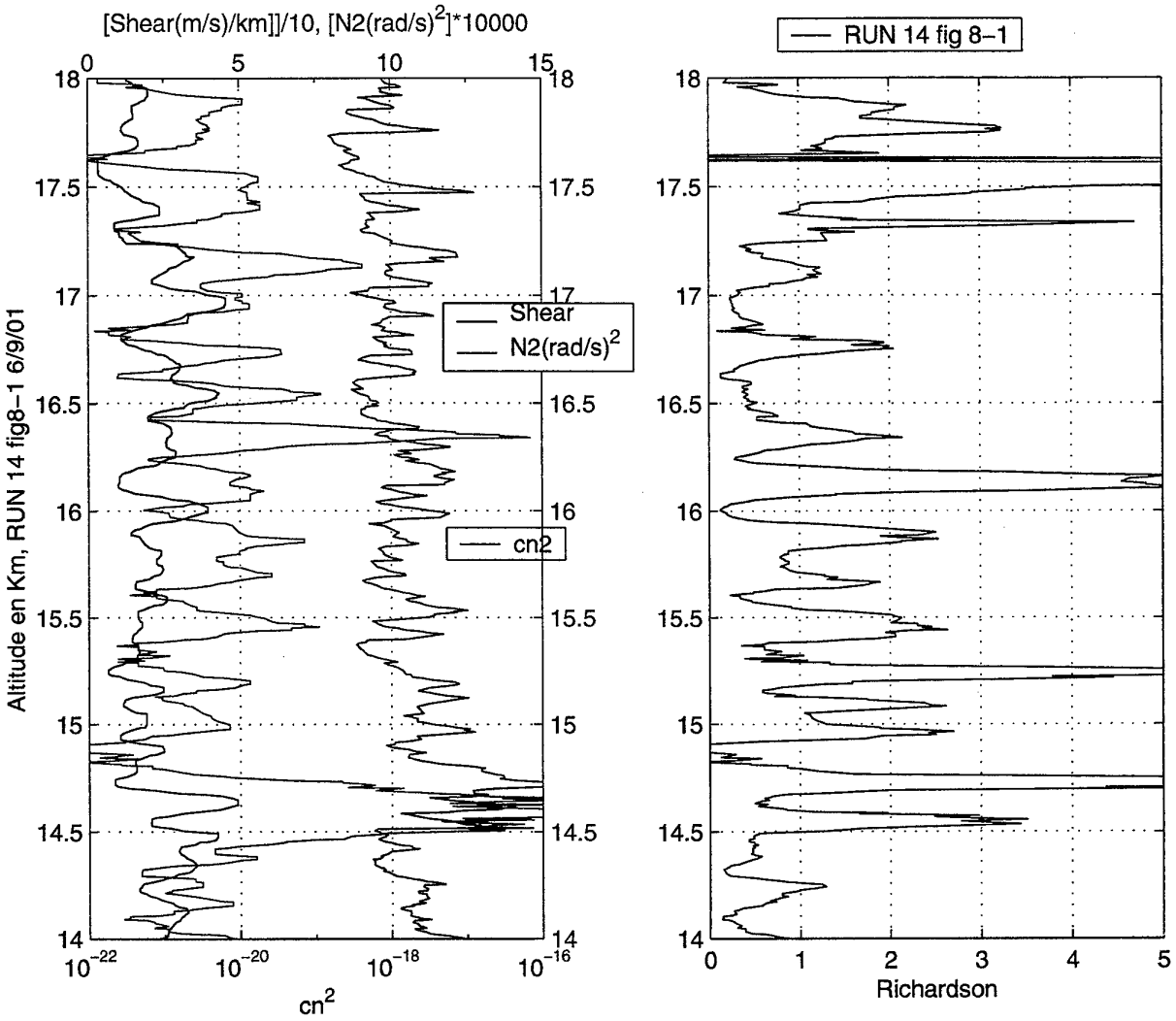
[Shear(m/s)/km]]/10, [N2(rad/s)2]*10000
Shear
N2(rad/s)2
cn2
Altitude en Km, RUN 14 fig8-1 6/9/01
cn2
RUN 14 fig 8-1
Richardson

ONERA

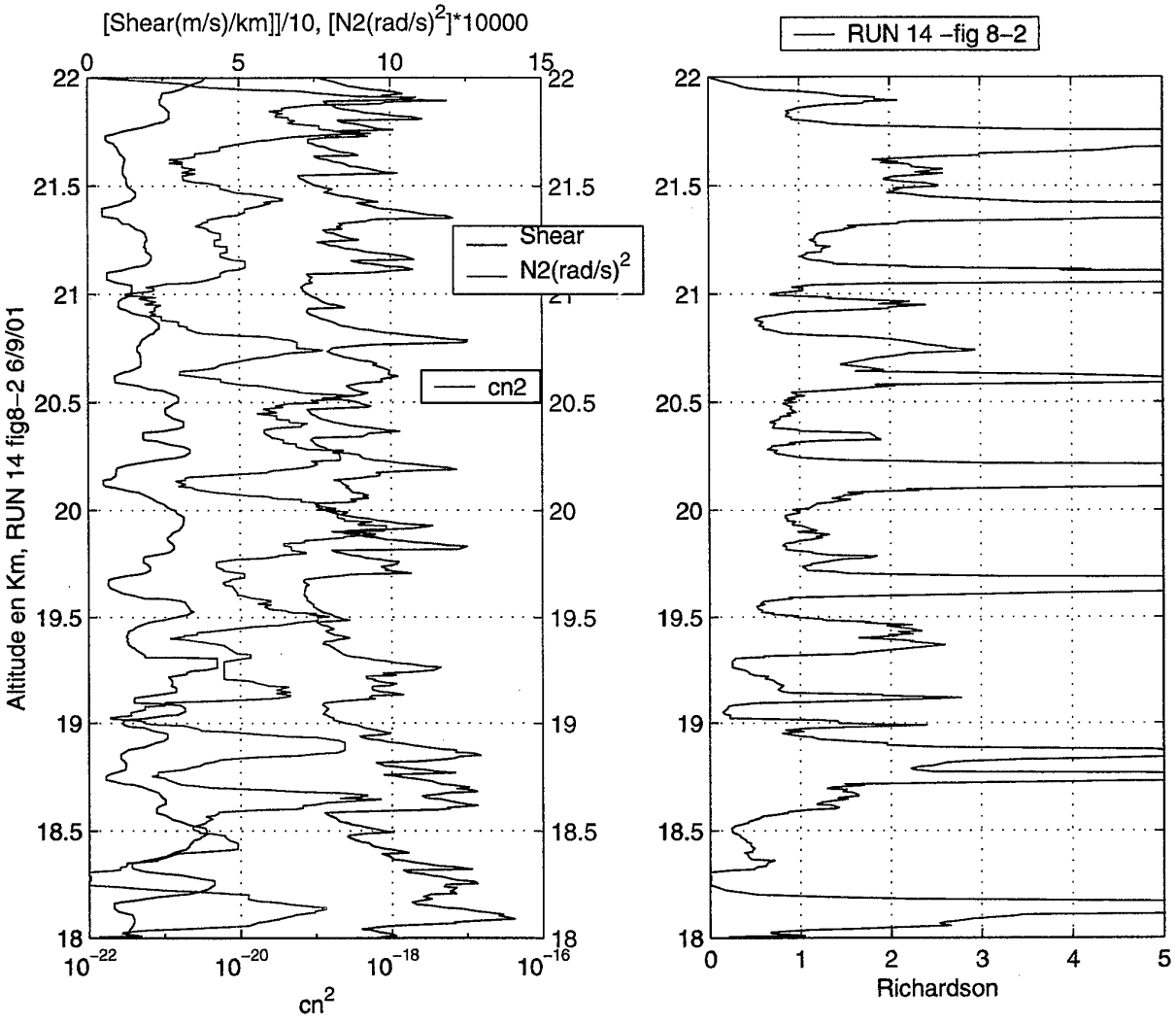
[Shear(m/s)/km]]/10, [N2(rad/s)2]*10000
RUN 14 –fig 8–2
Shear
N2(rad/s)2
cn2
Altitude en Km, RUN 14 fig8–2 6/9/01
cn2
Richardson

ONERA

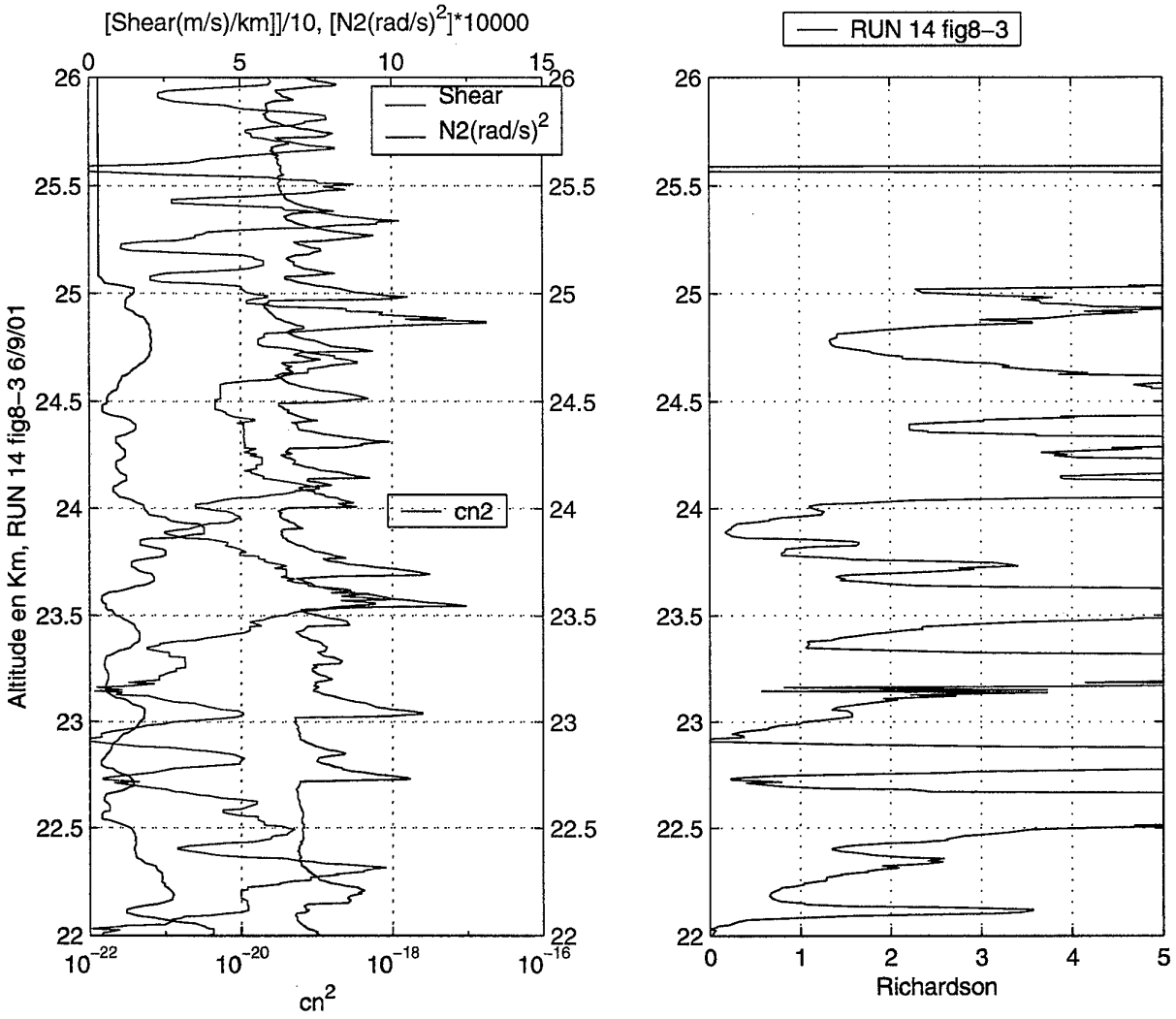
[Shear(m/s)/km]]/10, [N2(rad/s)^2]*10000
Shear
N2(rad/s)^2
cn2
Altitude en Km, RUN 14 fig8-3 6/9/01
cn^2
RUN 14 fig8-3
Richardson

ONERA

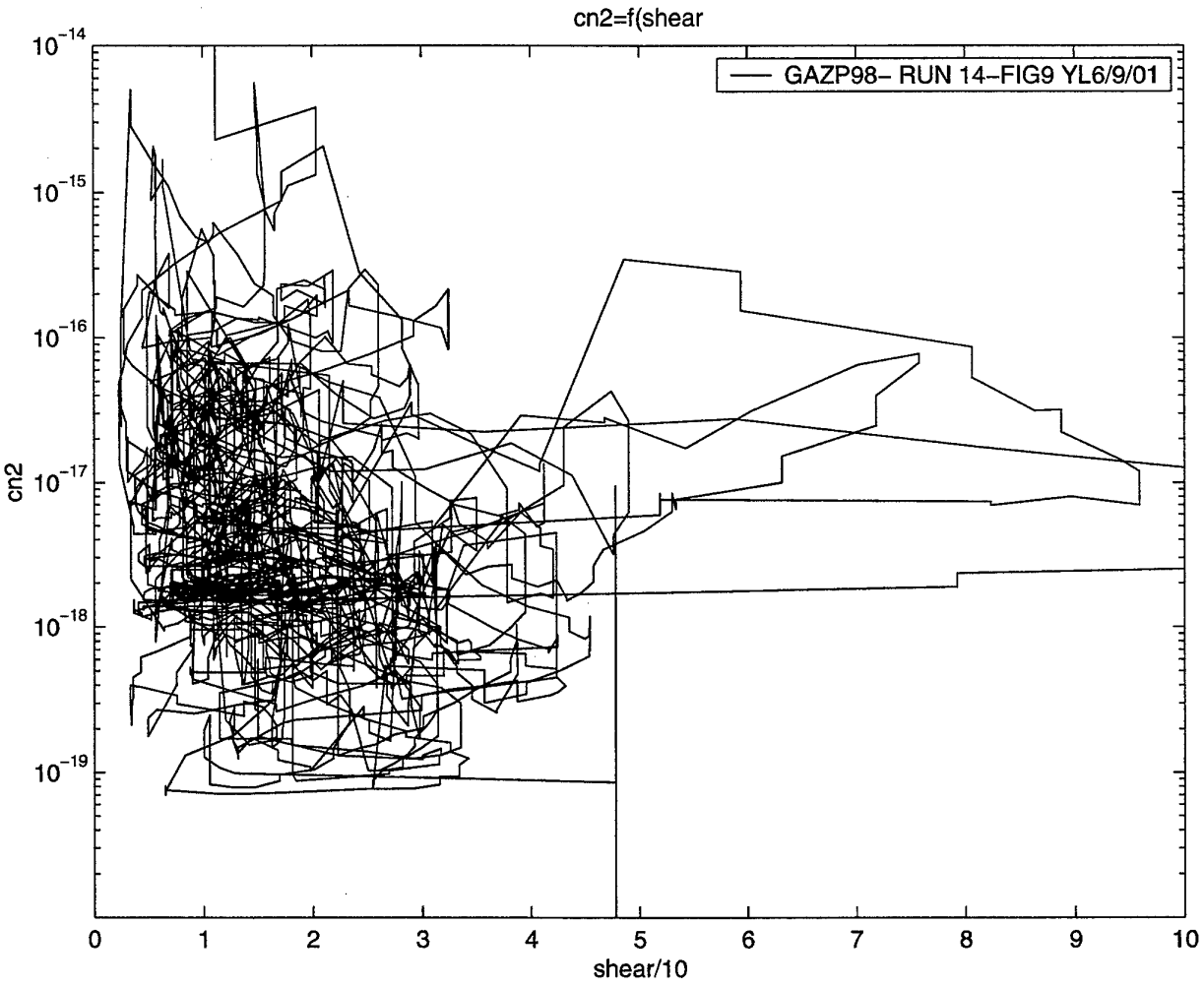
cn2=f(shear
GAZP98– RUN 14–FIG9 YL6/9/01
cn2
shear/10
10^{-14}
10^{-15}
10^{-16}
10^{-17}
10^{-18}
10^{-19}
0
1
2
3
4
5
6
7
8
9
10

APPENDIX 5
DESCRIPTION OF MEASUREMENTS FROM THE SERVICE D'AÉRONOMIE

SAOZ

The SAOZ instrument [4-5] consists of a UV-visible spectrometer allowing measurement of the vertical profiles of O_3, NO_2, OClO, BrO and IO by solar screening during the rise of the balloon in twilight from a ceiling close to 30 km. Controlled by a computer, it includes a pressure and temperature measurement, localization by Global Positioning System (GPS) and an Argos transmitter for its recovery on the ground after parachute descent. The total weight of 20 kg is designed for frequent and cheap flights under 5,000 and 10,000 m^3 balloons developed by the National Center of Space Studies (CNES). Numerous flights have been carried out since 1991 in France, Spain, Norway, Sweden and Brazil to study the ozone destruction and the chemistry of chlorine, bromine and iodine.

The list of SAOZ flights is given on web site http://www.aerov.jussieu.fr/~fgoutail/FlightList.html. Two flights including ozone measurements were made in June 1998 from the Gap launch base, on June 20 at sunrise and June 23 at sunset (see Figure 2). Dr. Goutail of the Service d'Aéronomie is in charge of the instrument.

EEC Ozone Probe

The Observatoire de Haute Provence station makes an atmospheric ozone survey by EEC probe every Wednesday. A survey was made on Wednesday June 24 during the trial runs. These measurements were provided by Mr. Vialle who is the measurement PI at the Service d'Aéronomie.

Stratospheric O_3 Lidar

The stratospheric ozone lidar used at OHP is a UV Dial Lidar [6-7] emitting at two wavelengths, one of which is absorbed by ozone. The laser pulses are scattered by atmospheric particles at various altitudes. Measurements are made by time-of-flight detection of the radiation scattered by the reflecting layers. Comparison of the range signals from the two-wavelength scattering laser gave an ozone measurement integrated on the probed column.

Measurements were made on the nights of June 19 and between June 21 and June 28.

The validity range of measurements in the 10 km to 45 km altitude range is supplied in the data file header and must be taken into account. The person in charge of these measurements is Dr. Godin of the Service d'Aéronomie.

Rayleigh Lidar

A Rayleigh lidar [8-12] provided temperature measurements with a spatial resolution of 75 m in the altitude range from 25 km to 70 km. The system detects scattering of laser pulses by Rayleigh molecules. The time-of-flight of the backscattered signal gives the distance from the probed layers. The measurements give access to atmospheric density which can be converted to temperature using the hydrostatic coefficients.

Measurements below 30 km can be wrong because of aerosols. Measurements were made nightly on June 19 and from June 21 to June 29. The measurement times are given in Figure 3. The measurements lasted approximately 5 hours, beginning at sunrise Dr. Hauchecorne of the Service d'Aeronomie was the leader of these measurements.

L'ONERA est le premier établissement de recherche français dans le domaine aéronautique et spatial, où il a pour mission de développer et d'orienter les recherches

L'ONERA est un organisme pluridisciplinaire qui décline ses projets de la recherche amont à leur aboutissement industriel. Ses « ingénieurs du ciel » imaginent, testent, simulent, modélisent et expérimentent les concepts nouveaux qu'ils livrent à l'industrie.

Depuis 50 ans au service de l'industrie aérospatiale civile et de défense

Les avions Airbus, Concorde, Mirage, Rafale ; les missiles Apache, ASMP et les lanceurs spatiaux Ariane ont bénéficié des travaux de l'ONERA.

Les clients et partenaires : Aerospatiale, CNES, DASA, Dassault, DGA, Matra Bae Dynamics, SNECMA, Thomson, etc. ainsi que les PME/PMI contribuent, au travers des projets menés en commun, à l'excellence scientifique et technique de l'ONERA.

Un nouvel élan pour un nouvel ONERA

Avec une organisation nouvelle, l'ONERA s'ouvre et s'adapte aux nouveaux besoins de l'industrie aéronautique et spatiale.
Les Grands Moyens Techniques regroupant ingénierie et bureaux d'études, les grands moyens de calcul et un parc de souffleries unique en Europe, apportent une assistance technique de haut niveau à une clientèle internationale.

Dix huit départements spécialisés sont répartis dans quatre branches scientifiques : Mécanique des fluides et énergétique, Physique, Matériaux et structures, Traitement de l'information et systèmes.

French aerospace research agency ONERA sets strategic research objectives and supports the development of research initiatives.

ONERA is a multidisciplinary organization, conducting upstream research projects that lead to industrial applications. Our scientists, engineers and technicians conceive, simulate, model and test solutions, which are then delivered to industry.

50 years at the cutting edge of civil and military aerospace research

ONERA has been involved in the development of a number of landmark aerospace projects, from the Airbus and Concorde jetliners, to Mirage and Rafale fighters, Apache and ASMP missiles and Ariane launch vehicles.
Our partners and customers include Aerospatiale, CNES (French space agency), DASA, Dassault, DGA (French arms-procurement agency), Matra BAe Dynamics, SNECMA and Thomson-CSF. We also team up with smaller companies on joint projects that have helped build Onera's reputation for scientific and technical excellence.

A revamped ONERA steps up the pace

ONERA has revamped its structures to keep pace with the fast-changing requirements of the aerospace industry.
We have set up a Technical Resources Division, grouping our design and engineering teams, large-scale computation facilities and an array of wind tunnels unique in Europe. By consolidating these resources in a single division, we can provide the high-level technical assistance demanded by customers from around the world.
ONERA has also set up four major scientific groups Fluid Mechanics and Energetics, Physics, Materials and Structures, Information Technology and Systems which are organized in 18 departments, each enjoying a wide degree of operational independence.

Office National d'Études et de Recherches Aérospatiales
BP 72 - 29 avenue de la Division Leclerc
92322 CHATILLON CEDEX
Tél. : +33 1 46 73 40 40 - Fax : +33 1 46 73 41 41
http://www.onera.fr